THE STRUCTURE AND STRENGTH OF CERTAIN Ni-Al-Ta AND Ni-Al-Hf ALLOYS

A Thesis

Submitted for the degree

of

DOCTOR OF PHILOSOPHY

in the

University of London

by

AHMET BALDAN

Department of Metallurgy and
Materials Science,
Imperial College of Science and
Technology,
London SW7

July 1978

ABSTRACT

The structure and mechanical properties of certain Ni-Al-Ta and Ni-Al-Hf alloys containing the γ' and β phases have been investigated. The alloy compositions were Ni - 28·75 at % Al - 2·5 at % Ta, Ni - 26·75 at % Al - 2·5 at % Ta, Ni - 20·0 at % Al - 7·5 at % Ta, Ni - 20·0 at % Al - 7·5 at % Hf and Ni - 22·5 at % Al - 5·0 at % Hf.

The structural and morphological aspects of the β martensite in the Ni-Al-Ta alloys have been studied using optical microscopy, transmission electron microscopy and X-ray diffraction. The main morphological feature of the β martensite in the solution treated condition is the presence of "self-accomodating" martensite plate groups. It appears that a multishear mechanism operates in the formation of β martensite.

The as-cast structure of the Ni - 28·75 at % Al - 2·5 at % Ta, Ni - 26·75 at % Al - 2·5 at % Ta, Ni - 20·0 at % Al - 7·5 at % Hf and Ni - 22·5 at % Al - 5·0 at % Hf alloys have shown eutectic-type regions which have been studied in terms of the structure and morphology. The eutectic regions of the hafnium-containing alloys consist of β plus Ni_3Hf which was shown to have a hexagonal structure with c = 6·042Å, a = 4·905Å, c/a = 1·23.

The correlation of the room temperature microhardness of γ phase as a function of tantalum and hafnium content has shown that hafnium hardened γ' phase more than did tantalum.

In the Ni - 20·0 at % Al - 7·5 at % Ta, Ni - 20·0 at % Al - 7·5 at % Hf alloys the flow stress is approximately constant up to about 700°C, and then falls with further increase in temperature. In the Ni - 68·75 at % Al - 2·5 at % Ta, Ni - 26175 at % Al - 2·5 at % Ta and Ni - 22·5 at % Al - 5·0 at % Hf alloys the flow stress increases with increasing temperature up to a certain temperature, then

falls with further increase in temperature.

In deformed γ' phase dislocations have been observed lying along the <111> directions, additional to the dislocations along the <110> directions. The stability of these dislocations in the γ' phase has been discussed in terms of elastic anisotropy. The higher strength of the γ' phase on the Al-rich side of stoichiometry compared to that of the Ni-rich side has been attributed to the presence of the dislocations along the <111> directions.

The flow stress behaviour of the alloys as a function of test temperature has been discussed in terms of volume fraction and flow stress behaviour of the β and γ' phases.

Stress relaxation and strain-rate cycling tests have been conducted to gain insight into the deformation behaviour of the alloys and an analysis of the data has been made in terms of "athermal" and thermally activated processes.

CONTENTS

CHAPTER 1

INTRODUCTION

Increasing attention has been paid to the so-called "superalloys", because of high-temperature strength and corrosion resistance. Nickel-base superalloys are the bulwark of high-temperature metallurgical technology in gas turbine, nuclear reactors, furnaces, and a great number of specialized modern products. With the advent of aircraft gas turbines requiring materials for longer periods of service, the better property requirements are beginning to dominate all gas turbine materials technology. During the last more than two decades γ' phase has been used as the precipitation hardener in nickel-rich nickel-aluminium alloys as high temperature engineering materials in the aero-space industry. However, because of the demand of the higher strength high-temperature materials, further research has been carried out on the Ni_3Al phase as the basis for alloy development. This phase has a high melting point and structural stability (an ordered face-centred cubic structure exists up to the melting point). It exists over a narrow range of composition but yet is capable of taking fairly substantial amounts of other elements into substitutional solid solution, the atoms of which can fit on either one or both of the individual sublattices of Ni_3Al ($L1_2$ structure). The mechanical behaviour of γ' is unusual in that the flow stress increases with increasing temperature to a maximum value, which occurs at a temperature in the range 500°C to 800°C[7,48,11,4]. The mechanical properties of γ' depend on both substitution behaviour of the alloying addition and the degree of non-stoichiometry. Considerable strengthening is achieved only when[4]

1) the alloying addition substitutes for aluminium and has a large size misfit parameter,

2) the alloy is aluminium-rich or stoichiometric.

The purpose of the present investigation has been to study the structural and mechanical properties of

nickel-based alloys treated mainly in the (γ' + β) phase field and to investigate the effects of the ternary additions, tantalum and hafnium, on the structure and mechanical properties.

Transmission electron microscopy, light microscopy and x-ray diffraction have been used as the main techniques for studying the structural and morphological features of the alloys. Compression and hardness testing have been used to study mechanical properties.

From this investigation it was hoped to determine the potentialities of achieving good elevated temperature properties by the solution of tantalum and hafnium based on γ' phase. For this purpose five different tantalum- and hafnium-containing alloys have been studied by changing the volume fractions of γ' and β phases, and Ta and Hf content. Alloys were studied in three different conditions:

i) as-cast
ii) homogenised at 1260°C for 48 hours and then water quenched
iii) homogenised at 1260°C for 48 hours and then water quenched plus aged at 1000°C for 3 days and then water quenched.

CHAPTER 2

2. REVIEW OF LITERATURE

2.1. The phase diagrams of the Ni-Al, Ni-Al-Ta, Ni-Al-Hf Systems

2.1.1. The Ni-Al phase diagram

The nickel-aluminium phase diagram was first investigated by Gwyer(1908)[1]. More detailed investigations were undertaken by Bradley and Taylor (1937)[2] using x-ray diffraction data to establish the composition range of the phases present at room temperature. Schram (1941)[3], using optical, magnetic, x-ray and hardness measurements, produced a detailed study of the Ni-NiAl system, showing the limits of the γ' field and the β(NiAl) phase. He also found that the hardness was a maximum for alloys in the two-phase Ni_3Al/NiAl region. The generally accepted Ni-Al phase diagram (Hansen, 1958)[4] is shown in fig. 2.1.

Nickel-rich β(NiAl) alloys are known to undergo a martensitic transformation (see sec. 2.8).

The γ' phase field exists over a narrow range of stoichiometry, approximately 3 at % wide at 1200°C. The β phase is stable over a wide composition range, from 41 to 54 at % Al at room temperature. The homogeneity range gradually widens with increasing temperature. The stoichiometric NiAl has a melting point at 1683°C; deviations from this composition result in a decrease in the liquidus temperature.

2.1.2. The Ni-Al-Ta system

The nickel-rich region of the Ni-Al-Ta ternary phase diagram around the pseudo-binary eutectic Ni_3Al-Ni_3Ta has been studied by Mollard et al (1974)[7]. A nominal composition of this eutectic has been found to be Ni-12·75 at % Al-11·86 at % Ta (fig. 2.2). The nickel-rich

corner of the Ni-Al-Ta diagram is shown in Fig. 2.2.

2.1.3. The Ni-Al-Hf system

The ternary system, Ni-Al-Hf, was first investigated by Markiv and Burnashova (1969)[9]. Fig. 2.3(a) shows an isothermal section of the diagram at 800°C. The highest solubility of Hf in Ni_3Al was found to be about 7 at % Hf. This ternary isothermal diagram relevant to the present work, contains a number of phases including γ', β and Ni_3Hf.

A computer analysis of the Ni-Al-Hf system based on a thermodynamic model has been carried out by Kaufman and Nesor (1975)[8] in order to predict the isothermal sections and liquidus projection. The data show a lower solubility of Hf in γ' (fig. 2.3(b)) than is shown by the isothermal section at 800°C determined by Markiv and Burnashova (1975)[9] (fig. 2.3(a)). The calculated diagram (fig. 2.3(b)) at 800°C shows some differences in the phase fields in the nickel-rich corner as compared with the experimentally determined isothermally diagram at 800°C (fig. 2.3(a)). This diagram will be compared with the present results in sec. 5.3.3.

2.2. Lattice parameters of γ' phase

The lattice parameters of the binary γ' phase have been determined by Aoki and Izumi (1975)[10] as a function of aluminium concentration. These workers found that the lattice parameter increases with increasing Al concentration (Table 2.1). The lattice parameter of the binary γ' at the stoichiometric composition has been determined to be 3·563Å.

Table 2.1

The lattice parameters of binary γ'

Alloy at % Al	Lattice parameter (Å)
23	3·558
24	3·560
25	3·563
26	3·567
27	3·570

The effect of third element alloy additions on the lattice parameters of Ni_3Al has also been determined by Guard and Westbrook (1959)[12], and by Curwick (1972)[11]. Curwick (1972)[11] has obtained data on the effect on the lattice parameters of Ni_3Al of various elements including tantalum. Fig. 2.4 shows the effects of tantalum in expanding the lattice parameter of Ni_3Al with increasing Ta concentration.

2.3. Lattice parameters of the β-NiAl phase

The physical properties of NiAl have been investigated by a number of workers. In the earliest x-ray investigation by Bradley and Taylor (1937)[2], the lattice parameter and density were measured between 45 at % and 61 at % Ni. They found that the density increased with increasing nickel content across the entire phase field, but the lattice parameter showed a maximum near the stoichiometric composition, which was 2·887Å (fig. 2.5). They explained this result in terms of different defect structures on either side of stoichiometry. The Ni-rich alloy accommodates the excess Ni atoms on Al sites; since Ni atoms are both smaller and heavier than Al atoms, this causes a reduction in lattice parameter and an increase in density. In the Al-rich alloys however, both atoms retain their ordered sites and the non-stoichiometry is

accommodated by vacant Ni sites in the lattice. This explains the sharp reduction in density and the fall in the lattice parameter.

Fig. 2.5 shows the lattice parameter versus composition curves obtained by the different workers. Some curves show maxima at lower nickel content, while Taylor and Doyle's curve shows a maximum at 50 at% Ni.

2.4. The Structure of Ni_3Al and its alloys

The binary intermetallic compound Ni_3Al is an ordered solid solution of aluminium in nickel having an $L1_2$ type structure. The $L1_2$ structure can be built up by four interpenetrating simple cubic lattices. Within this structure Al atoms occupy corner and Ni atoms face centre sites (fig. 2.6). Thus Ni_3Al consists of three nickel atoms at $(\frac{1}{2}, \frac{1}{2}, 0)$, $(\frac{1}{2}, 0, \frac{1}{2})$, $(0, \frac{1}{2}, \frac{1}{2})$ and an aluminium atom at (0, 0, 0).

It has been shown by using high temperature x-ray diffraction on single crystal specimens of Ni_3Al (Stoeckinger et al, 1970)[14] that it is still ordered up to 1320°C in both stoichiometric and nickel-rich specimens. This suggests that if disordering occurs it does so within 65°C of the melting point.

2.5. The Structure of NiAl

In the binary Ni-Al system (fig. 2.1) the β phase exists over a wide range of compositions from 41-54 at % Al at room temperature and the stoichiometric composition is given by NiAl 50 at % Al. At elevated temperatures the nickel-rich phase boundary extends to a composition of about 70 at % Ni, a value which is within 5 at % of the Ni_3Al phase boundary.

NiAl has a CsCl (B2) type crystal structure (fig. 2.7) with a lattice parameter at stoichiometry of 2·887Å[2]. This is an ordered structure consisting of two interpene-

trating simple cubic lattices of Ni and Al with their origins displaced by $(\frac{1}{2}, \frac{1}{2}, \frac{1}{2})$.

The fully ordered nature of stoichiometric NiAl is well documented and has been verified by x-ray measurements[15] and nuclear magnetic resonance[16,17]. At higher temperatures there has been some controversy, but it is generally accepted that the stoichiometric alloy is ordered up to, close to the melting point of 1638°C.

2.6. The alloying behaviour of Ni_3Al

Guard and Westbrook (1959)[12] carried out an investigation of the alloying characteristic of Ni_3Al. From an analysis of ternary phase diagram data they were able to deduce the substitution behaviour of a number of elements, namely that Co and Cu substitute for Ni, while Si, Ti, Mn and V substitute for Al and Cr and Fe for both species.

Rawlings and Staton-Bevan (1975)[18] published data concerning the substitution behaviour of ternary additions in γ' alloys. They pointed out that the substitution behaviour of the elements is determined by electronic rather than size considerations. According to their data Ta and Hf substitute for Al.

2.7. The operative slip systems in Ni_3Al

The Ni_3Al (the γ' phase) has an $L1_2$ type ordered fcc crystal structure. In fcc crystals, the normal slip occurs on {111} planes in <110> directions. These slip systems have been observed by a number of workers. In single crystals of γ', Davies and Stoloff (1965)[19]; Copley and Kear (1967)[20], and Thornton et al (1970)[32] have found that at low temperatures slip occurs on {111} <110> systems, but as the temperature is raised the tendency for cube slip {100} <110> increases. Transition from octahedral to cube slip has been shown by Staton-Bevan (1973)[45].

Muir (1975)[21] has found that the {110} or {112} type planes are possible slip planes. The dislocations which lie on these planes are aligned in <111> directions.

2.8. The martensite transformation in β NiAl

It was first observed by Guard and Turkalo (1960)[5] that the β phase undergoes a martensitic transformation on quenching to an acicular structure. Subsequently, Ball (1967)[6] also has reported a similar martensitic structure in NiAl. Rosen and Goebel (1968)[22] investigated the structure of the martensite in alloys containing 62 to 68 at % Ni using a combination of powder x-ray diffraction and diffractometry. They proposed a modified AuCu type crystal structure (FCT) with a c/a ratio of 0·86 (in the case of the alloy containing 34 at % Al) (fig. 2.8(a)). However, this modified L1o type structure cannot form directly from the high-temperature CsCl type structure. To facilitate this structure the hypothetical ordered NiAl structure was postulated at high temperature. However, this has not been proved experimentally.

The structure of the martensite has also been investigated by Enami et al (1973)[23] using electron microscopy. From the distribution of superlattice reflections the Ni-36·8 at % Al martensite has a crystal structure of the normal L1o type (CuAuI type) (fig. 2.8(b)) and this structure may be obtained from the high-temperature β phase with the CsCl type structure by the Bain distortion.

Chandrasekaran and Mukherjee (1974)[24] suggested that the NiAl martensite structure may be considered as a close packed structure corresponding to the 2H modulation (B19 structure) based on a CuAu type structure, similar to that reported for the martensitic transformation in the equiatomic Ti-Ni alloys.

The most detailed investigation of the structure of the martensite has been made by Moskovic (1974)[25] in a Ni-30·3 at % Al-6·6 at % Cr alloy on water quenching

from the solution treatment temperature (1300°C). The conclusions are summarised below:

i) The structure of the martensitic phase has two observed forms. Firstly, a body-centred tetragonal (BCT) crystal structure with c/a = 1,25 (fig. 2.8(b)) which is related to the parent β phase by an inverse Bain correspondence, as originally suggested by Enami et al (1973)[23]. The second structure, proposed by Moskovic is body-centred orthorhombic (BCO) with c/a = 1,25 and b/a = 1,1, which forms by a combination of shear and inhomogeneous shuffles.

ii) Moskovic (1974)[25] has suggested that the martensite is nucleated on super critical domains of Ni_3Al composition and has shown that the transformation may be suppressed by rapid quenching.

Smialek et al (1973)[26] determined the compositional dependence of the Ms temperature for NiAl (fig. 2.9). They found that:

i) a large deviation from stoichiometry (≈ 10 at pct) is needed before thermal martensite can be formed,

ii) that a large increase in Ms temperature occurs with increasing nickel content.

It was found[27] that rapid quenching is not a necessary condition for the formation of martensite in Ni-Al alloys but a condition of martensitic transformation is cooling from high temperatures at such rates that the excess nickel cannot be precipitated from the solid solution lattice.

Moskovic (1974)[25] has also shown that with increasing ageing time at 850°C the c/a ratio of the BCT structure decreased. It was shown that after 2 hours ageing at 850°C the equilibrium NiAl structure (B2) formed.

2.9. Twinning in NiAl martensite

Some workers have investigated the defect substructure by using x-ray data. Mohanty and Wert (1963)[28] suggested the existence of the twin faults on {211} planes by the fact that deformation caused the broadening of diffraction peaks in the cold worked stoichiometric NiAl. Mohanty and Schmidt (1970)[29] suggested that cold-worked NiAl was faulted on {110} planes from the evidence of peak-broadening. However, as was suggested by Ball (1967)[6], the presence of faults in NiAl powder deduced from x-ray data by the above workers, could be interpreted as being due to colonies of martensite produced by deformation during the preparation of the powder.

Transmission electron microscope investigations of the defect substructure of the NiAl martensite have been made by various workers. Enami et al (1973)[23] have shown that the NiAl martensite was internally twinned, and found $\{111\}_t$ $\langle 11\bar{2}\rangle_t$ transformation twins, corresponding to {110} planes in the β phase. The twinning system {101} <101> also has been confirmed by a number of other workers[30,24,25,21]. Muir (1975)[21] has claimed that the {110}<110> type twin also exist on the BCT β martensite.

2.10. Theories for the peak in the temperature dependence of the flow stress of γ′

The γ′ phase has attracted attention because of the unusual temperature dependence of the flow stress, which increases with increasing temperature to a peak value occurring, for polycrystals, in the range 350°C to 750°C.

Guard and Westbrook (1959)[12] first suggested that the observed flow stress peak may be due to strain ageing effects caused by C, O, N impurities or to diffusion controlled climb (Flinn, 1960)[31] involving the formation of sessile superlattice dislocations which acted as obstacles to successive glide.

Since the yield stress continues to change anomalously at temperatures much below 0·5 Tm, diffusion controlled mechanisms, such as strain ageing or thermally activated climb of superlattice dislocations, appear unlikely to be directly important. Also low strain rate sensitivity at low temperature (Thornton et al, 1970)[32] contradicts the above theories given by Guard and Westbrook (1956)[33], and Flinn (1960)[31].

Davies and Stoloff (1965)[19] found that the flow stress change with temperature was of a reversible nature. They have proposed a lattice resistance effect mechanism, which opposes dislocation motion. As the temperature is increased greater lattice forces are required to preserve the crystal structure, with the result that the proof stress increases until recovery processes become dominant.

Copley and Kear (1967)[20] have suggested that the dislocations in γ' are subjected to an increasing drag-stress with increasing temperature because of constriction of the Shockley partials. This was considered to arise from variations in the elastic anisotropy with temperature.

Alternatively, Thornton, Davies and Johnston (1970)[34] have explained the flow stress behaviour of Ni_3Al in terms of the observed dislocation structure during the deformation of polycrystalline, stoichiometric Ni_3Al, $Ni_3(Al,Ti)$, $Ni_3(Al,Ti,Cr)$, and have proposed that two mechanisms are responsible for the positive temperature dependence of the flow stress. At low temperatures, below approximately 0·6 Tp, they have suggested that there is an exhaustion of the mobile dislocation density by the formation of "Kear-Wilsdorf locks" (Kear and Wilsdorf, 1962)[35]. At high temperatures this is replaced by a "debris-hardening" mechanism. This debris hardening was thought to result from an interaction between octahedral {111} and cube {001} slip, the latter becoming easier with increasing temperature.

Therefore the role of cube slip is necessary if the anomalous temperature dependence of the flow stress is to be understood. As has been explained above, according to Thornton et al (1970)[34] it is the interaction of cube slip with octahedral slip that causes the increase in the flow stress, whereas the theory of Copley and Kear suggests that cube slip occurs because octahedral slip is abnormally difficult.

Staton-Bevan and Rawlings (1975)[36] have found five different deformation modes existed with increasing temperature (fig. 2.10) and they have proposed that the anomalous temperature dependence of the flow stress of Ni_3 (Al, Ti) results from an increase in the critical resolved shear stress for octahedral slip with increasing temperature and that the exact peak position is dependent on the onset of cube slip.

In his relaxation test on the Ni_3Al with iron additions, Nicholls (1974)[164] has proposed that the anomalous flow stress/temperature dependence results directly from a variation of the athermal stress with temperature, and he has also suggested that the increase in athermal stress results from an increase in the critical resolved shear stress for octahedral slip with temperature, due to a decrease in the separation of Shockel partials, as proposed by Staton-Bevan (1973)[45], and Copley and Kear (1969)[20].

Svetlov and Toloraiya (1975)[37] have investigated the temperature dependence of the yield stress on single crystal specimens of Ni_3Al with additions of 5 at % Ta, Hf, Nb and Ti. They have suggested that the mechanism of Kear and Wilsdorf (see sec. 2.13.2) operates. Since the energy of an antiphase boundary $\gamma_{(111)}$ is high in the octahedral plane, a superlattice dislocation gliding in plane (111) possesses high energy. The dislocation therefore tries to lower the energy by transferring to the cube plane, where $\gamma_{(111)} > \gamma_{(100)}$. This produces a resistant, blocked configuration of screw segments of dislocation

loops. The transition to the cube plane may be achieved by cross slip, which requires the formation of kinks at the leading dislocation. Since this is a thermally activated process on screw dislocations, the probability of cross slip increases with temperature. Thus, as the temperature rises, an ever-increasing number of screw segments of super-lattice dislocation loops emitted by a Frank-Read source goes over to the cube planes. An ever-increasing number of loops becomes blocked and can only be moved by an increase in force. This is reflected by the rising yield stress with increasing temperature.

2.11. The influence of alloying additions and temperature on the mechanical properties of γ'

The mechanical behaviour of Ni_3Al is unusual in that the flow stress increases with increasing temperature to a maximum value. Although alloying does not alter the temperature dependence of the flow stress, nevertheless the peak is displaced from its position for the stoichiometric Ni_3Al and the stress level of the peak is affected by ternary additions.

The effects of Ta and Hf additions on the flow stress of γ' have been investigated by several workers (11,38,39,37).

Curwick (1972)(11) has investigated the effect of ternary alloy additions including Ta on the temperature dependence of the critical resolved shear stress (CRSS) of stoichiometric γ'. He has found that Ta additions to Ni_3Al significantly increased the {111} <110> CRSS.

Doherty et al (1971)(38) have investigated the effect of Hf on the mechanical properties of stoichiometric Ni_3Al. The microhardness data has shown that the hardness has increased significantly with increasing Hf content (fig. 2.11).

Ramaswamy et al (1973)[39] and Svetlow and Toloraiya (1975)[37] have investigated the temperature dependence of the mechanical properties of Ni_3Al with additions of Ta and Hf. Fig. 2.12 shows the flow stress versus temperature curves of stoichiometric $Ni_3(Al,Hf)$. This figure shows that an increase in hafnium content from 2·5 to 5 at % has produced a notable increase in strength between room temperature and 900°C.

Aoki and Izumi (1975)[40] have also determined the influence of Ta on the yield stress of stoichiometric Ni_3Al. From their results the authors have concluded that the yield stress has increased almost linearly with the increase of Ta content at room temperature, and it has deviated from linearity at higher temperatures (fig. 2.13).

The effect of hafnium in increasing the value of the peak yield stress is greater than that of tantalum (fig. 2.14).

Rawlings and Staton-Bevan (1975)[18], in a review article, commented on the dependence of the room temperature yield stress (YS) of γ' on the concentration of ternary additions. They have found that the solid solution hardening ratio $(\Delta YS/\Delta C)^*$ is a strong function of the atomic misfit parameter ϵ[where $\epsilon = (d_A - d_I)/d_I$, d_A is the atomic diameter of the alloying element and d_I is the atomic diameter of the atom for which it substitutes] for elements substituting for Al in both stoichiometric and Al-rich alloys. The room temperature stress increment per atomic percentage alloying addition is shown in fig. 2.15. This figure shows that the strength increment due to ternary additions for stoichiometric and Al-rich γ' is approximately the same. In contrast there is very little strengthening associated with the same ternary additions in

$$* \frac{\Delta YS}{\Delta C} = \frac{\text{YS of ternary alloy - YS of binary } \gamma' \text{ having same degree of non-stoichiometry}}{\text{Atomic \% alloying addition}}$$

Ni-rich γ' alloys. This is so even when the misfit parameter is large (e.g. ε = 0,092 for Hf).

Aoki and Izumi (1976)[41] have investigated the solid solution hardening of γ' phase by ternary alloying additions in terms of the shear modulus parameter and size misfit parameter. For this they have measured and compared the variations of lattice parameter and shear modulus with the change of compressive yield stress. By applying a modified Fleisher's parameter, they have found that the defect hardening in Ni_3Al is a kind of a substitutional solid solution hardening, and both effects are controlled by the same mechanism, namely the elastic interaction between dislocations and solute atoms. Aoki and Izumi's work will be reconsidered in sec. 5.2.

2.12. The effect of non-stoichiometry on the mechanical properties of γ'

Rawlings and Staton-Bevan (1975)[18] have summarised most of the previous work on the effect of deviations from stoichiometry on the temperature dependence of the yield stress of γ'.

For a γ' alloy containing a given concentration of a given solute, changing the composition from Ni-rich to Al-rich has the following effects on the mechanical properties:

a) the room temperature yield stress YS_R is increased,

b) the peak yield stress YS_p is increased,

c) the value of $\Delta YS_p = YS_p - YS_R$ is increased,

d) the peak yield stress temperature T_p is decreased.

This is summarised schematically in fig. 2.16. Rawlings and Staton-Bevan (1975)[18] have suggested that the change in dYS/dT with the degree of non-stoichiometry must be associated with {111} <110> slip. Since γ' has

an ordered fcc, (a/2) <110> dislocations lying on {111} planes may dissociate into partial dislocations of the (a/6) <112> type. The degree of dissociation, which depends on the stacking fault energy, would undoubtedly affect the motion of the dislocations and hence dYS/dT.

Aoki and Izumi (1976)[41] have also investigated the effect of off-stoichiometry on the mechanical properties of γ' by taking into account the shear modulus misfit parameter and the size misfit parameter. They have found that the deviation from stoichiometry introduces some kind of "defect structure" into the γ' phase (Aoki and Izumi, 1975)[10]. As mentioned in sec. 2.11, by modifying Fleischer's parameter, they have found that the defect hardening resulting from deviations of stoichiometric composition is controlled by the elastic interaction between dislocations and solute atoms.

2.13. Dislocations in $L1_2$ Structures

In an ordered alloy, such as Ni_3Al or NiAl, the superlattice dislocation consists of two ordinary dislocations joined by an antiphase domain boundary (APB). One of these dislocations, when it moves through a superlattice, leaves a trail of disorder (APB). If two dislocations were to move in pairs, the second dislocation would recreate the original structure in its wake. The separation of the two unit dislocations (or "super-partials") is such that the value of the combined APB energy and elastic interaction energy is a minimum. The APB energy tends to draw the dislocations together whereas the elastic interaction between two dislocations causes them to repel each other.

In $L1_2$ structures the deformation occurs on the {111} planes along the <110> directions. It might energetically favourable for these dislocations to dissociate into two Shockley partials of the a/6 <112> type, separated by stacking fault (S.F.). Dissociated dislocations are said to be "extended". This dissociation may occur in

the (111) plane of the form:

$$\frac{a}{2}[\bar{1}01] \longrightarrow \frac{a}{6}[\bar{2}11] + \frac{a}{6}[\bar{1}\bar{1}2]$$

The extended superlattice dislocation consists of 4 Shockley partials connected by APB, with the leading and trailing pairs also connected by SF (fig. 2.17) such that the total energy of the configuration is a minimum.

Two types of dissociation of dislocations in $L1_2$ or Ni_3Al have been reported. Kear et al (1970)[147] have proposed that low energy {111} 1/3 <112> type stacking faults in $L1_2$ can be developed during plastic deformation. Cornwell et al (1969)[160], and Pak et al (1976)[161] have observed a/3 <211> type dislocations. On the basis of this observation it was proposed[160] that dissociation on (111) planes was of the type:

$$a[10\bar{1}] \longrightarrow \frac{a}{3}[2\bar{1}\bar{1}] + \frac{a}{3}[11\bar{2}]$$

Marcinkowski et al (1961)[201] have suggested that the a<110> superdislocation dissociates into two a/2 <110> superpartials and then further into 4 Shockley partials connected by a complex series of faults:

$$a[110] \longrightarrow \frac{a}{2}[110] + \frac{a}{2}[110]$$

2.14. Work hardening in $L1_2$ superlattices

The number of theories have been put to explain the work hardening behaviour of $L1_2$ superstructures. These theories may be classified as follows:

2.14.1. The "APB-tube" theory

The mechanism was first pointed out by Hirsch (1962)[42]. The idea was that a jogged superdislocation will create a tube of APB as the dislocation moves forward unless the jogs in the leading and trailing dislocation of the pair travel directly in line.

Vidoz et al (1962)[43] have suggested that when a gliding superdislocation crosses moving forest dislocations, the jogs on the super-partial will be arranged in such a way that they do not follow after one another when the superdislocation subsequently moves. This generates "pipes" of APB (fig. 2.18). They have suggested that the creation of APB tube exerts a considerable drag-stress on the superlattice dislocation which causes work hardening. This specific model proposed by Vidoz and Brown (1962)[43] (namely, producing tubular antiphase defects in the wake of jogs in the superlattice dislocations) has been observed in Cu_3Au (Kear, 1966)[44].

2.14.2. The Kear-Wilsdorf lock

Kear and Wilsdorf (1962)[35] have proposed that a screw dislocation on an octahedral plane would lower its energy if the leading super-partials were to constrict cross slip onto a cube plane and dissociate on a parallel octahedral plane (fig. 4.35). This is because in the $L1_2$ superlattice a screw dislocation pair can reduce its energy by changing the common plane from the slip plane to a cube plane (Flinn, 1960)[31]. Evidence of cross-slip onto cube planes has been found in Cu_3Au (Kear and Wilsdorf, 1962)[35] and Ni_3Al (staton-Bevan, 1973)[45].

Davies and Stoloff (1965)[19] have suggested that the work-hardening in ordered Cu_3Au was due to an exhaustion type of hardening. They developed a theory. As a super-lattice dislocation loop expands from a source, there is a finite probability that the screw component will cross-slip onto another {111} plane so that the antiphase boundary can lower its energy on a {100} plane. If cross-slip occurs a strong barrier will be created. This would produce an exhaustion of the mobile dislocation density and force other sources on parallel slip planes to operate, giving the observed fine slip lines.

Two mechanisms outlined above in this section explain an increase in work hardening rate with increasing temperature.

Since the constriction of the Shockley partials in fcc materials is thermally activated, the number of barriers formed would increase with increasing temperature, until the temperature was high enough for the locked dislocations to cross-slip back onto the octahedral slip plane.

The model proposed by Vidoz and Brown (1962)[43] requires slip in at least two intersecting systems. Kear (1966)[44] have found evidence for an increasing activity in secondary systems (APB-tube formation by jogs) in Cu_3Au. Since very little secondary slip had occurred, he suggested that even relatively small amounts of slip in secondary systems have a profound effect on the work hardening rate. These observations led him to suggest a new theory, which included aspects of both the APB-tube theory and the cross-slip theories. He suggested that jogs could be created in screw dislocations by a mechanism of localised cross-slip (fig. 4.35). When these jogged screw dislocations move forward, point defects or near edge dislocation dipoles would be created in their wake (Gilman and Johnson, 1962)[46] (fig. 4.36). This does not require intersecting slip and the rate of work hardening would largely depend on the intersection of glide dislocations with jog debris and antiphase defects.

Thornton et al (1970)[24] have proposed a similar debris hardening mechanism, which occurs at temperatures above 400°C. They have suggested that this debris hardening occurs by the intersection of octahedral and cube slip. At lower temperatures, an "exhaustion hardening" mechanism was proposed by the same workers, such as that produced by the Kear-Wilsdorf Lock.

2.15. The Operative slip systems in NiAl

In an ordered alloy, such as NiAl, the Burgers vector must be a unit vector of the superlattice, to preserve the ordered arrangement of atoms and the defect is referred to as a superdislocation[54,55]. Super-dislocations are normally dissociated into two or more

"superpartial" dislocations.

The normal criterion for choosing the slip direction is that slip occurs in the most close packed direction, i.e. with the shortest Burgers vector. The shortest vector in the BCC structure is 1/2 a<111>. But there has been controversy over which slip systems are operative in NiAl. Ball and Smallman (1966)[49] have determined the operative slip system on single crystal and polycrystalline stoichiometric NiAl, using electron microscopy. They have shown that the <100> {011} slip system operates in NiAl. They have also shown theoretically that a<100> dislocations are energetically more favourable than the a<111> dislocations originally predicted by Rachinger and Conttrell (1956)[56].

Pascoe (1966)[57] has found that at low temperatures the most closely packed plane, (110), was the slip plane, but an increase of temperature permitted slip on any plane that contained an [001] direction. It was also found that deviations from stoichiometry on the excess nickel side had no effect on the operative slip system. He has claimed some evidence for <111> slip on {132} at low temperatures and for <110> $\{1\bar{1}0\}$ slip above 700°K.

2.16. Precipitation in the β-NiAl Phase

Little work has been done on the precipitation of the γ' in the NiAl phase until the work of Maskovic (1974)[21] and of Muir (1975)[25].

Litvinov et al (1971)[27] have briefly investigated the γ' precipitation in the NiAl phase. They have found that the γ' precipitation occurred in the form of rosettes and precipitated mainly on the boundaries of grains and subgrains, which has been confirmed by Shklyar et al (1971)[52] and Arkhangel's Kaya et al (1972)[53].

Russell and Edington (1972)[47] have investigated the precipitation behaviour of a Ni-36 at % Al binary alloy by using optical and electron microscopy. After ageing at

875°C, they have observed a duplex precipitate structure. Firstly, a stable incoherent precipitate formed as a continuous film along the grain boundaries and as coarse rods (20μ x 1μ x 1μ) in the matrix. Secondly, from the diffraction evidence, the presence of fine plate-like precipitates on {110} planes was deduced. It was assumed that these fine precipitates formed during quenching from the ageing temperature.

Moskovic (1974)[25] has investigated the precipitation of γ' in β phase in detail using a Ni-6 at % Cr-24 at % Al alloy. By ageing this alloy for various times at 850°C, it was found that initially the precipitate structure was FCT (e.g. after 10 minutes ageing at 850°C c/a = 0,976). The tetragonality has diminished with increasing ageing time. After 2 hours ageing at 850°C, the Ni_3Al precipitates had the equilibrium $L1_2$ structure. It has also been observed in specimens, solution treated at 1300°C, and aged at 850°C, that fine plate-like Ni-rich precipitates formed on {110} matrix planes during quenching from the solution treated temperature, and during the ageing at 850°C. Muir (1975)[21] has also shown evidence for a fine dispersion of plates on {110} in the martensitic phase of Ni-Al alloys.

2.17. The mechanical properties of NiAl

The earliest study of the mechanical properties of NiAl was the comprehensive survey of hardness as a function of temperature and composition by Westbrook (1956)[33]. Hardness isotherms showed a minimum at the stoichiometry composition at all temperatures up to 800°C (fig. 2.19).

Ball and Smallman (1966)[49] investigated the mechanical properties of polycrystalline and single crystal specimen of NiAl as a function of testing temperature and composition. At low temperatures the polycrystalline specimen failed in a brittle manner along grain boundaries after little or no plastic deformation, but a marked increase in ductility occurred at an homologous temperature

of 0·45 Tm. The strength of single crystals depended strongly upon orientation.

It was shown by Pascoe and Newey (1968)[50] that the flow stress of NiAl was strongly sensitive to temperature in two regions (fig. 2.20). They concluded that both polycrystals and single crystals exhibited a three stage temperature dependence of the yield stress.

Stage 1. Low temperatures (up to about 400°K). The proof stress is strongly temperature dependent. The most likely rate-controlling mechanism is the overcoming of the Peierls barrier, the process being thermally activated. The strain rate sensitivity of the flow stress is high. The activation volume is small ($\approx 5b^3$).

Stage 2. Intermediate temperature (between 400°K-700°K). The proof stress is essentially independent of temperature. The strain rate sensitivity is low. The deformation process is most likely to be controlled by the interaction of dislocations with solute atoms. Work hardening increases with decreasing temperature.

Stage 3. High temperatures (above 700°K and up to 1300°K). The proof stress is again temperature dependent and highly strain rate sensitive. The work hardening rate is low. The high-temperature deformation of polycrystals is complex. Climb of dislocations around obstacles appear to be at the dominant process in near stoichiometric alloys.

The effect of grain size on the mechanical properties of NiAl was investigated by Pascoe and Newey (1968)[50]. They found that it had little influence on the room temperature proof stress.

As mentioned earlier, the results of Westbrook (1956)[33] shows that the strength of NiAl increases with increasing deviation from stoichiometric composition (fig. 2.19). The results of Ball and Smallman (1966)[49], and Pascoe and Newey (1968)[50] also show that the flow

stress increases in the following way:

Stoichiometric NiAl < Ni-rich NiAl < Al-rich NiAl

They have suggested that the greater hardening in the Al-rich compositions would be attributed either to a greater dilation or slight tetragonality of the strain field associated with a vacancy compared with a substitutional Ni atom; but this disagrees with Westbrook's hardness data (fig. 2.19) which indicated for 700°C and lower that the vacancies were the more effective hardeners.

The effect of alloying elements on the mechanical properties of NiAl has not been investigated systematically, but some information is available regarding the effect of Ti, Zr, Nb and Mo additives. Zr and Ti were observed to increase the room temperature strength of NiAl. The addition of 2 wt % Mo more than doubled the room temperature strength, whilst the addition of 1 wt % Mo almost doubled the strength of NiAl at 915°C[51].

2.18. The mechanical properties of γ'-β alloys

Very little work has been carried out on the mechanical properties of these two-phase alloys. The mechanical properties of NiAl containing Ni_3Al were investigated by Guard and Turkalo (1960)[5], and Litvinov et al (1971)[27]. The latter workers made some hardness measurements on the specimens, which were aged at 720°C and then slowly cooled to room temperature. They have found a large increase in hardness after ageing treatment, compared to that of the homogenised condition. They have concluded that this increase was caused by the Ni_3Al precipitate particles on the grain boundaries.

Russell and Edington (1972)[47] have investigated an aged condition of a 64 at % Ni alloy. They have found a considerable increase inductility at low temperature for this alloy compared with a single phase alloy of the NiAl matrix composition, of a similar grain size. They have

found also a significant increase in strength with temperature compared to single phase β phase and the flow stress remained essentially independent of temperature in the temperature range 0-700°C (fig. 2.21). They have suggested that the increase in strength by ≈ 20% was due to the presence of the coarse Ni_3Al precipitate in the NiAl matrix. Ageing time had little effect on room temperature hardness.

Moskovic (1972)[25] has investigated the mechanical properties of a Ni-30·3 at % Al-6·6 at % Cr alloy; he has aged this alloy for 2 hours at 850°C and produced 50% volume fraction of incoherent rod shaped γ′ precipitates. He has determined 0·2% flow stress as a function of temperature (fig. 2.22) and divided this curve into two regions. Below approximately 750°C, there is a small decrease in the 0·2% flow stress with increased temperature. The mechanism of deformation was suggested to be controlled by the interaction of dislocations with solute atoms, as in the case of NiAl. In the higher temperature range, the 0·2% flow stress falls off steeply with increasing temperature. In this temperature range the flow stress is highly strain rate sensitive. He has suggested that diffusion controlled glide was the deformation controlling mechanism.

Tsipas (1975)[48] has worked on Ni-23·5 at % Al-2·0 at % Hf-2·0 at % Co alloy. In the 20% γ′ containing alloys, he has found similar behaviour; the flow stress was independent of temperature up to 700°C (fig. 2.23). He has suggested that the rate controlling mechanism up to 700°C was the stress necessary to move dislocations through the β matrix which has been strengthened by the presence of γ′ precipitate.

2.19. Deformation Mechanisms

Plastic deformation is a consequence of the movement of dislocations through the crystal lattice under the action of an applied stress. The fact that significant

stresses are required to induce plasticity implies that the dislocations encounter obstacles to their motion. Plastic deformation of crystalline materials has long been established as a thermally activated process dependent on time, temperature and strain-rate. This basic concept was first proposed as early as by Becker (1925)[59] and it was soon realised that thermally activated flow was a typical rate process.

The deformation mechanisms are those athermal and thermally activated processes which determine the stress at which plastic deformation commences. In the case of a long range barrier (athermal), the interaction force with a dislocation varies slowly with the position of dislocation, and extends over distances of ten atomic diameters or more, e.g. forces due to dislocations on parallel slip planes, grain boundaries, and large second phase particles. In the case of a short range barrier (thermally activated), the force, resisting the glide of a dislocation past the barrier, increases rapidly with the proximity of the dislocation to the obstacle, and is effective over a small area of slip plane only, e.g. forces due to forest dislocations, asymmetric point defects etc. or from alternate low and high energy configurations of the dislocation core (Peierls-Nabarro barrier).

Possible thermally activated mechanisms include overcoming the Peierls-Nabarro force (the friction stress in the slip plane), dislocation intersections, cross-slip of screw dislocations, movement of jogged screw dislocations (Conrad, 1966; Evans, 1968; Little, 1974)[60,61,62]. If one mechanism only controls the deformation it is possible, by determining the strain rate sensitivity of the flow stress and stress relaxation characteristics of compression specimens, to discover what the mechanism is by calculating the activation volume and enthalpy for deformation and the thermally activated component of the flow stress over a range of temperatures.

Investigations to determine the controlling mechanism of the thermally activated deformation on γ' phase have been carried out by a number of workers. Thornton et al (1970)[32], Randall (1971)[63] and Nicholls (1974)[64] have investigated deformation mechanisms of the γ' phase. Nicholls (1974)[64] has found at least five modes of deformation, depending on the temperature, that occur in γ' (Ni_3Al.10 at % Fe). These are summarised below:

A) <0·23 Tp - Overcoming Peierls barriers.
Motion of jogged screw dislocations.

B) 0·23-0·41 Tp - Motion of jogged screw dislocations.

C) 0·41-0·64 Tp - Cross-slip between octahedral and cube planes.

D) 0·64-0·84 Tp - Cross-Slip.
Motion of jogged screw dislocations.
Intersection of dislocation dipoles.

E) >0·84 Tp - Recovery processes.

At temperatures below 600°C, the flow stress of γ' shows a very low strain rate sensitivity. By testing binary single crystal specimens, Copley and Kear (1965)[19] found that the specimens tested at 21°C and 429°C showed no strain-rate sensitivity and only a slight response was obtained from the specimen tested at 592°C. Davies and Stoloff (1965)[19] also found a similar behaviour in polycrystalline γ' phase. Thornton et al (1970)[32] found two types of response to changes in strain-rate sensitivity of binary Ni_3Al and a 2 at % Cr alloy. Below 400°C there was little response, but above 400°C a response typical of fcc metals was obtained. A similar behaviour was observed by Nichols (1974)[64] on polycrystalline Ni_3Al.10 Fe.

Pascoe and Newey (1971)[65], working on polycrystals of Ni-rich (43 at % Al) and near-stoichiometric (48·9 at % Al) NiAl phase, found that the strain-rate sensitivity was greatest where the flow stress was strongly dependent on temperature, namely below 400°K and above 700°K, and low in the intermediate temperature region.

2.20. Experimental Determination of Activation Parameters

Experimental studies of thermally activated deformation are usually directed at evaluating the thermal and athermal components of the applied stress, τ^*, τ_μ, and also the activation volume, V^*, activation energy, together with their variation with stress, strain, temperature etc. The principal aim is to identify the rate-controlling mechanism from these experimentally determined parameters. In the past a number of methods available for their determination have appeared in the literature[73,74,162,163]. Some of these are described in the following sections.

2.20.1. Determination of Thermal and Athermal Stress Components

An essential first step in any thermal activation analysis is an accurate determination of τ^* and τ_μ. These quantities may be determined by the following methods:

Stress Relaxation

If a specimen is plastically deformed in a hard testing machine and the crosshead movement arrested, the sample continues to deform with a diminishing strain-rate at decreasing stress (fig. 2.24). This phenomenon is known as stress relaxation and continues as long as the applied stress exceeds the athermal stress. Thus the athermal stress, τ_μ, may in principle be determined as the asymptotic stress level approached after long relaxation times. Theoretically it would take infinite time for complete relaxation to occur, and in practice rapid completion of relaxation occurs only under certain conditions, e.g. at low effective stresses. A method is the decre-

mental unloading technique[163] which facilitates rapid evaluation of τ_μ. In this method, fig. 2.25, the specimen is decrementally unloaded until a stress is found at which no relaxation occurs for an arbitrary period. At this point the applied stress should be exactly balanced by the athermal stress. It should be pointed out that the method fails if either dynamic strain-aging or recovery occur at the test temperature.

Relaxation curve has been analysed by a number of workers[73,74,162] and two empirical equations have been evaluated to fit the time dependent stress relaxation test:

$$\sigma - \sigma_o = \lambda \ln a - \lambda \ln(t+a) \quad \text{[Feltham (1965, 1969)]}^{(73,74)} \qquad (1)$$

$$\sigma - \sigma_\mu = K(t+a)^{-\frac{1}{m-1}} \quad \text{[Li (1967)}^{(162)}\text{]} \qquad (2)$$

where σ_o is the flow stress at time t = o
λ and a are constants
m is the effective stress exponent of the Johnston and Gilman equation[202].

If the athermal stress is assumed to be constant during the relaxation period, then Feltham's equation yields[164]

$$\frac{d\tau^*}{d\ln\dot{\gamma}} = \frac{d\sigma^* . \cos\theta . \cos\phi}{d\ln\dot{\varepsilon}} = \frac{d\sigma . \cos\theta . \cos\phi}{d\ln(-\dot{\sigma})} = \lambda = \frac{KT}{V^*} \qquad (3)$$

for a polycrystalline material it may be expressed as:

$$\frac{d\sigma}{d\ln(-\dot{\sigma})} = \lambda = \frac{2KT}{V^*} \qquad (4)$$

where $\cos\theta . \cos\phi$ is the Schmidt factor
K and T are Boltzman's constant and absolute temperature
$\dot{\varepsilon}$ is the strain rate
$\dot{\gamma}$ is the shear strain rate

Activation volume, V^* can thus be determined from the equation (4); however the emiprical nature of Feltham's equation may result in the variation of σ_μ which is

assumed to be constant during the relaxation period for evaluating V*. Feltham's equation has been used successfully to determine the thermal and athermal stress components of the flow stress in γ' phase[64].

2.20.2. Strain-rate cycling test

In the strain-rate cycling test the strain rate is changed by a given factor, to find the change in stress increment (fig. 2.26). If equation (2) (in Appendix 1) is differentiated with respect to the effective stress, one may obtain:

$$V^* = -\left(\frac{\partial \Delta G}{\partial \tau^*}\right)_T = KT\left[\frac{\partial \ln(\dot{\epsilon}/\dot{\epsilon}_o)}{\partial \tau^*}\right]_T \qquad (5)$$

provided that $\dot{\epsilon}_o$ and τ_μ are constant during the strain-rate cycling test and only one type of dislocations are moving, then

$$V^* = \frac{KT}{\alpha}\left[\frac{\Delta \ln \dot{\epsilon}}{\Delta \sigma}\right]_T \quad \text{for small values of } \Delta\sigma. \qquad (6)$$

where α is the Schmidt factor and often taken as 1/2 for polycrystalline material. Eq. (6) enables the activation volume to be determined by changing the strain rate during a constant temperature compression test and measuring the stress change $\Delta\tau (= \Delta\tau^*)$ produced.

The parameter $\left[\frac{\Delta\sigma}{\Delta \ln \dot{\epsilon}}\right]_T = \lambda$ is called the strain-rate sensitivity.

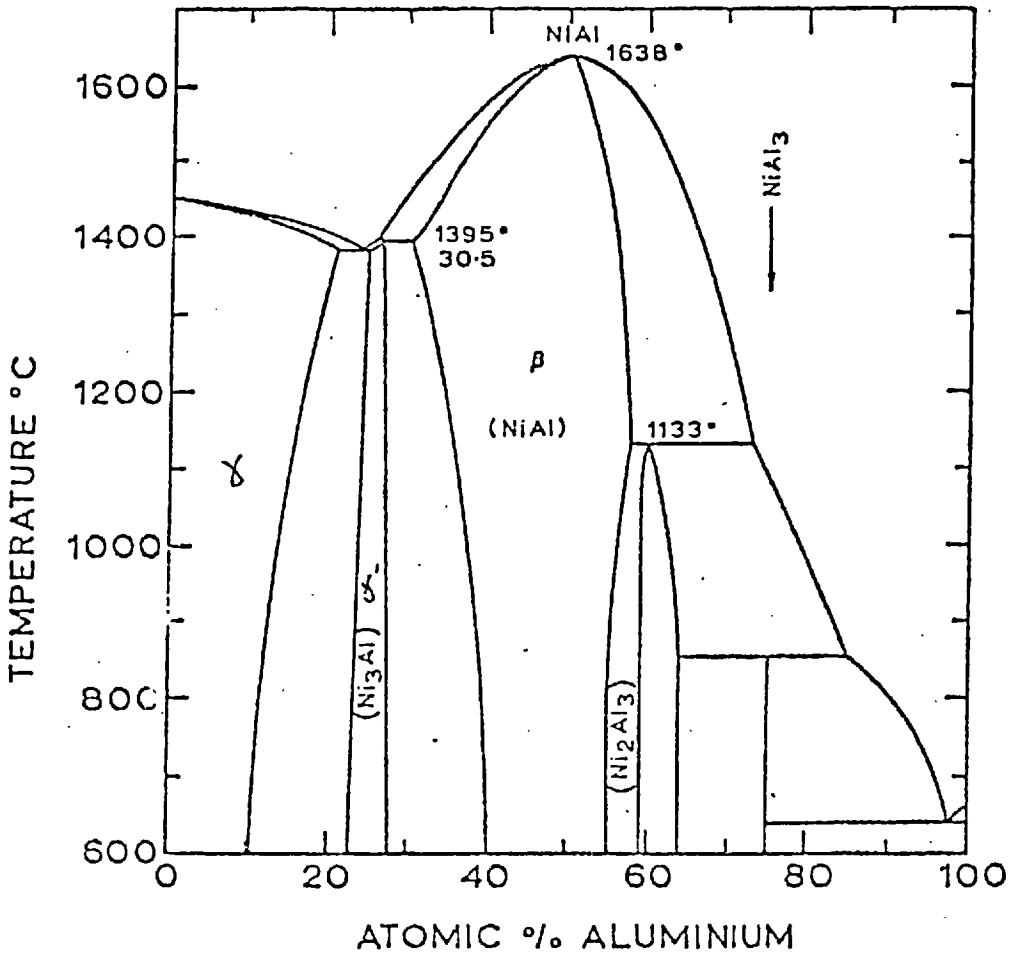

Fig. 2.1 The Nickel-Aluminium phase diagram.

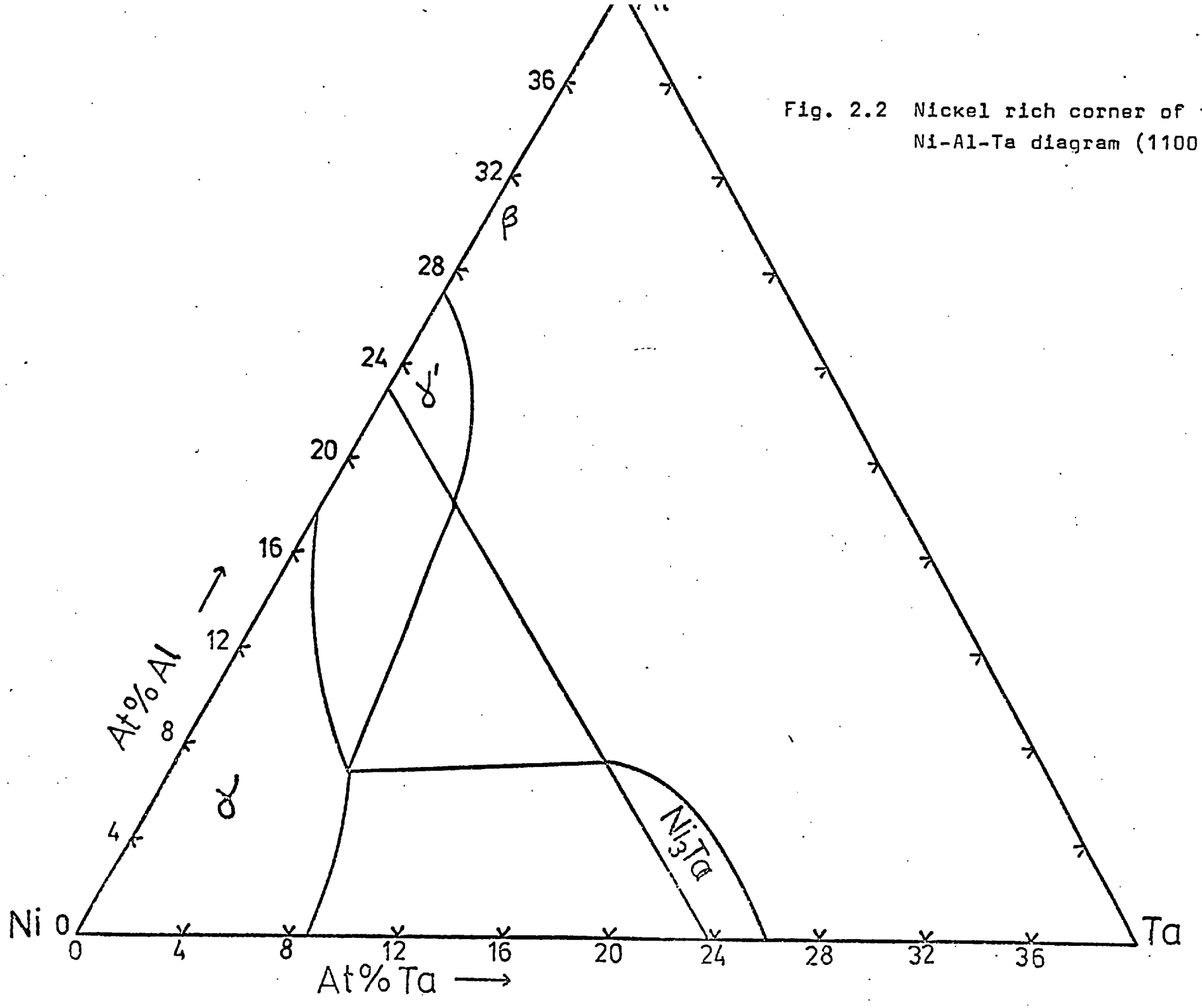

Fig. 2.2 Nickel rich corner of the Ni-Al-Ta diagram (1100°C).

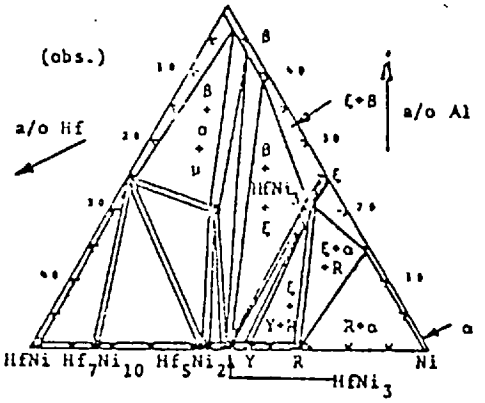

Fig. 2.3(a) Ni-Al-Hf ternary phase diagram (ref. 9).

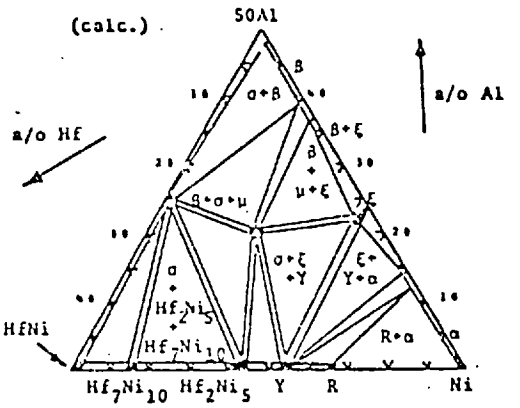

α-Ni_2AlHf
μ-$Ni_{64}Al_{20}Hf_{16}$
ζ-Ni_3Al
Y-Ni_7Hf_2
R-Ni_5Hf
β-bcc
α-fcc

Fig. 2.3(b) The Ni-Al-Hf phase diagram calculated from thermodynamic data (ref. 8).

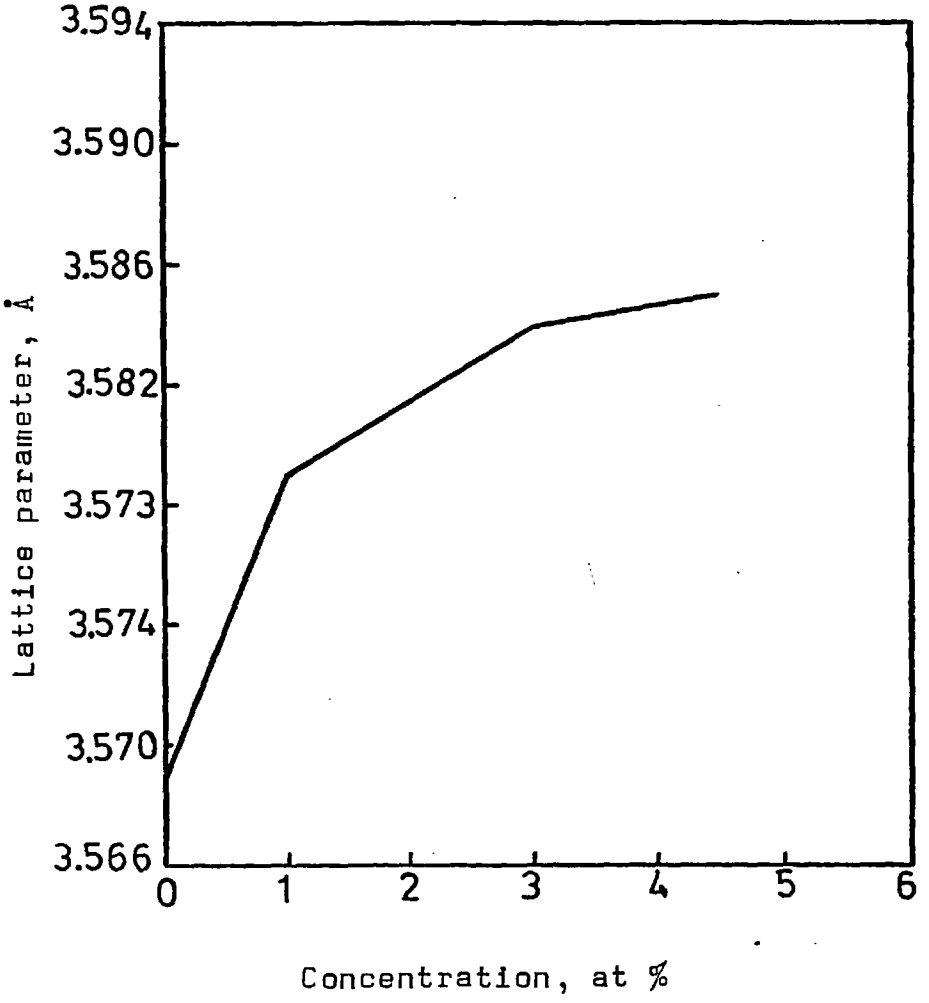

Fig. 2.4 The effect of tantalum on the $L1_2$ superlattice parameter of $Ni_3(Al,Ta)$ (ref. 11).

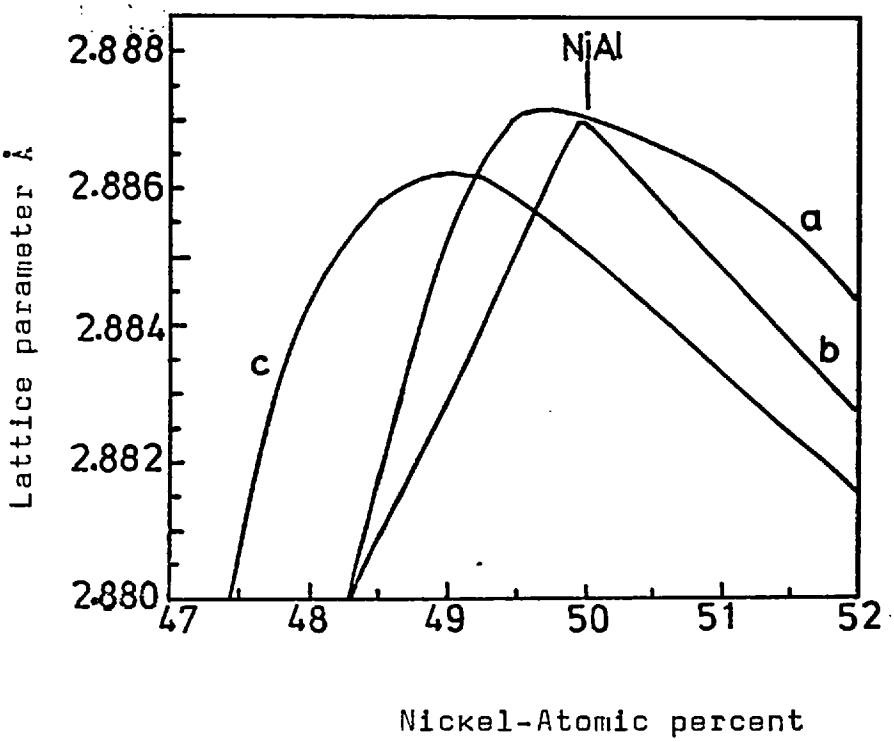

Fig. 2.5 The variation in lattice parameter with composition for NiAl (ref. 13)

a) Bradley and Taylor
b) Taylor and Doyle
c) Guseva

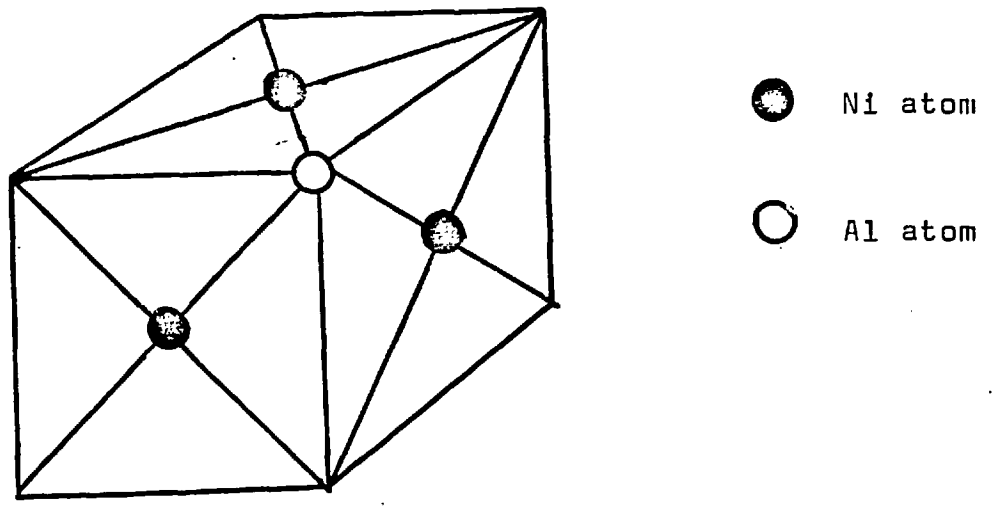

Fig. 2.6 The unit cell of binary Ni_3Al

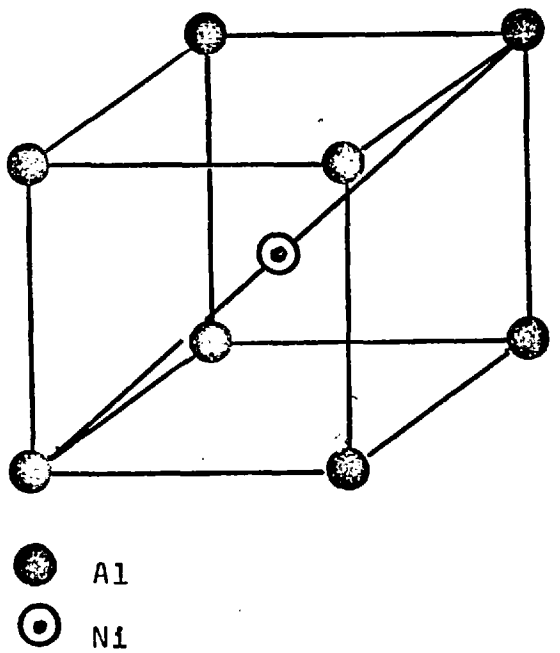

Fig. 2.7 The unit cell of NiAl

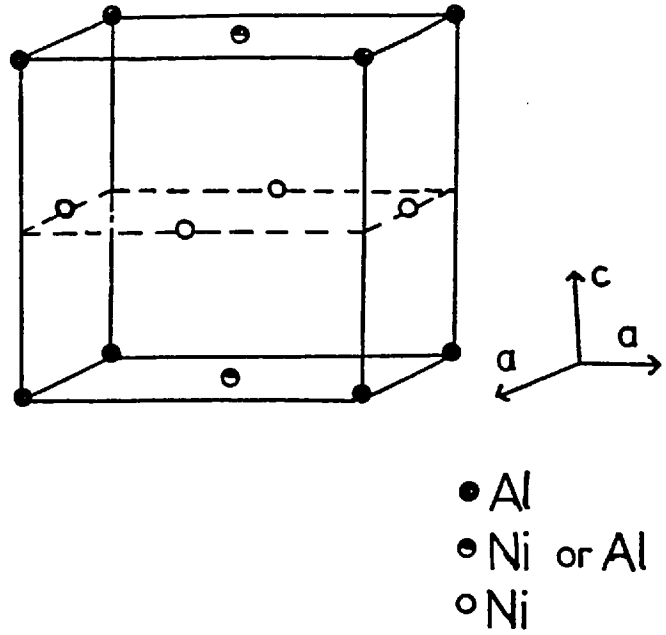

Fig. 2.8(a) The structure of NiAl martensite proposed by Rosen and Goebel (1968)[22].

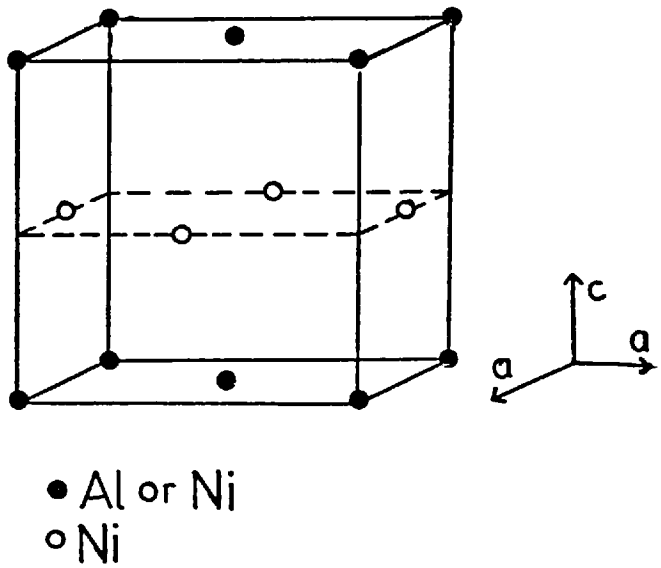

Fig. 2.8(b) The structure of NiAl martensite proposed by Enami et al (1973)[23] and Moskovic (1974)[25].

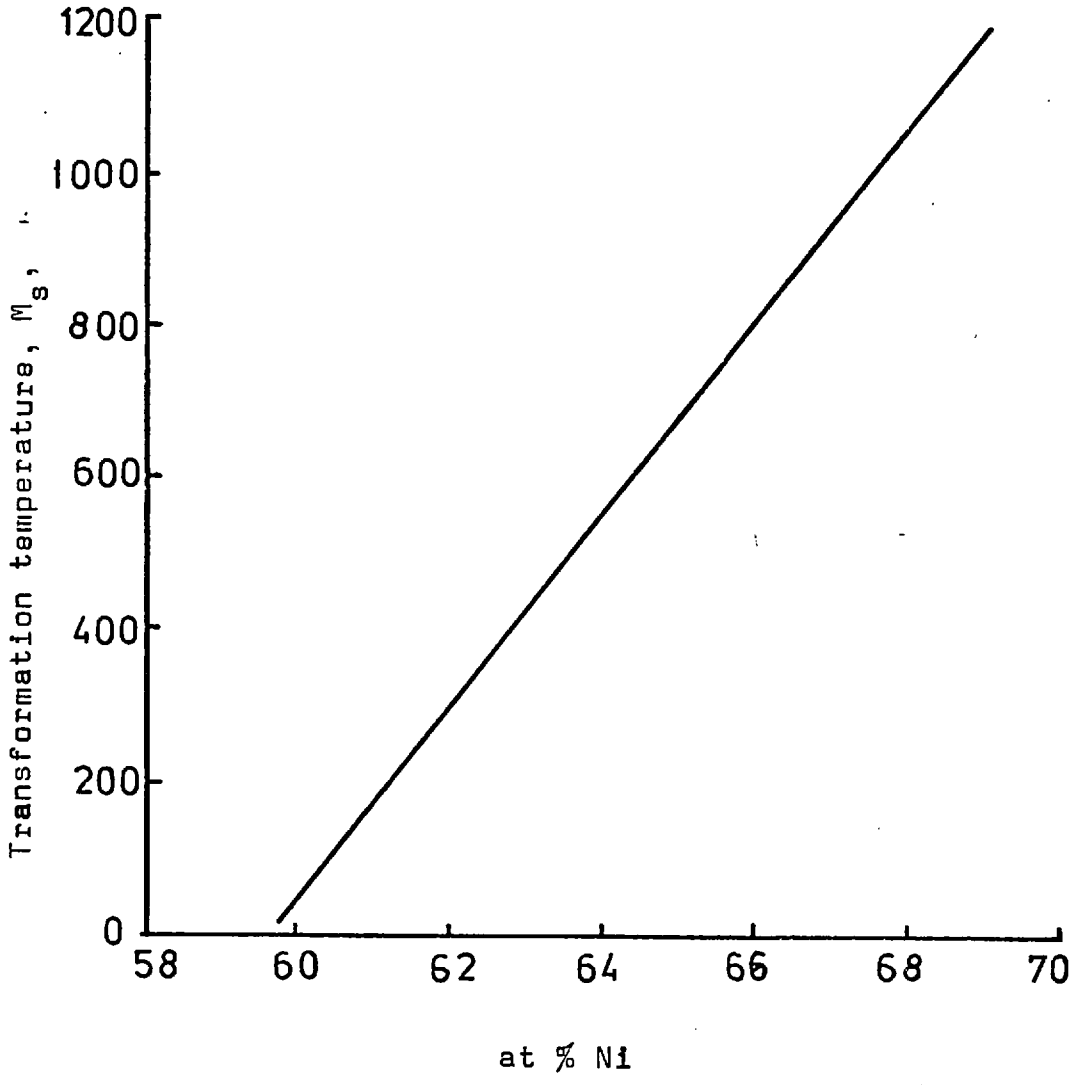

Fig. 2.9 Compositional dependence of Ms temperatures for NiAl martensite (ref. 26).

Fig. 2.10 Deformation behaviour of Ni_3Al (5·1 at % Ti) (Staton-Bevan, 1973)[45]

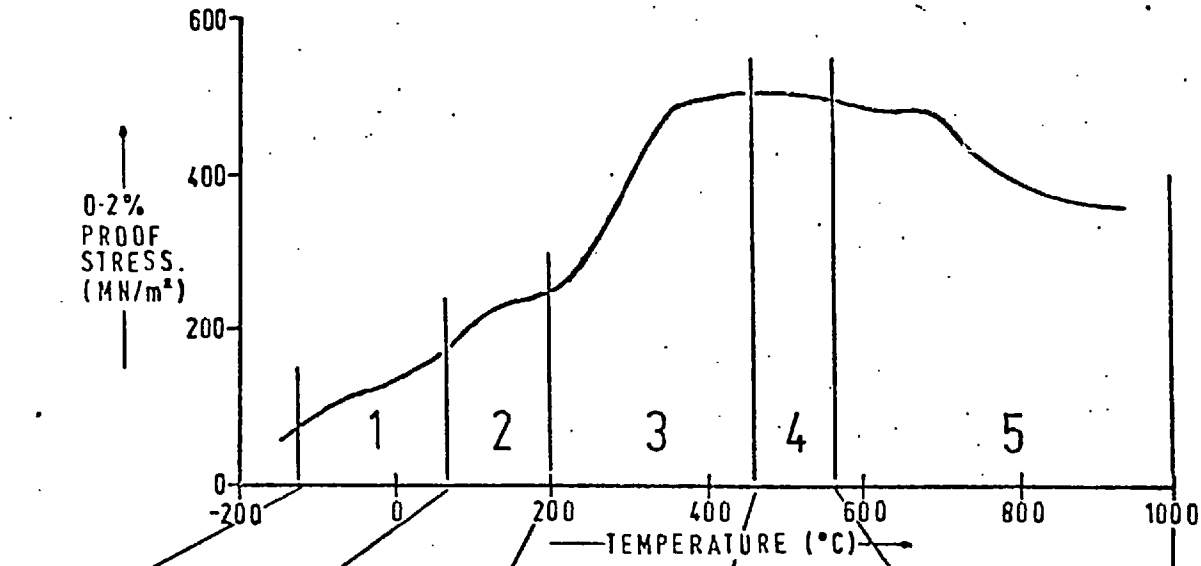

	0·21–0·38 Tp.	0·38–0·61 Tp.	0·61–0·93 Tp.	0·93–1·06 Tp.	<1·06 Tp.
SLIP-LINE ANALYSIS.	Coarse slip-lines on octahedral slip planes.	Dense packets of coarse slip-lines on octahedral planes.	Very fine closely spaced slip lines on the primary octahedral plane only	Slip-lines on both primary octahedral and cube slip-plane	Bands of slip-lines corresp. to slip on cube planes only.
TRUE STRESS/TRUE STRAIN DEPENDENCE.	Low work-hardening rates increasing gradually with strain.	High W.H. rates increasing rapidly with temperature and strain.	Very high W.H. rates decreasing with an increase in strain.	W.H. rate decreases with increasing temperature to low, often -ve, values.	W.H. rates exhibit a complexed temperature dependence.
ELECTRON MICROSCOPY. NO EVIDENCE OF DISLOCATIONS ON THE PRIMARY CUBE SLIP PLANE.	Screw dipoles on the primary octahedral plane. Edge loop debris Cross-slip onto cube planes unfavourable.	Cross-slip of screw dislocation. Edge dipoles in regions of high stress.	Much cross-slip resulting in edge dipole formation.	Transition region.	Primary and secondary cube slip. Near edge dipoles on the primary cube slip plane. Some dipoles collapse to loops. No octahedral slip.

SPECIMEN - Ni rich Ni_3Al (5·1 at.%Ti) - Single crystals.

ORIENTATION - $[\bar{1}32]$ Compression Axis.

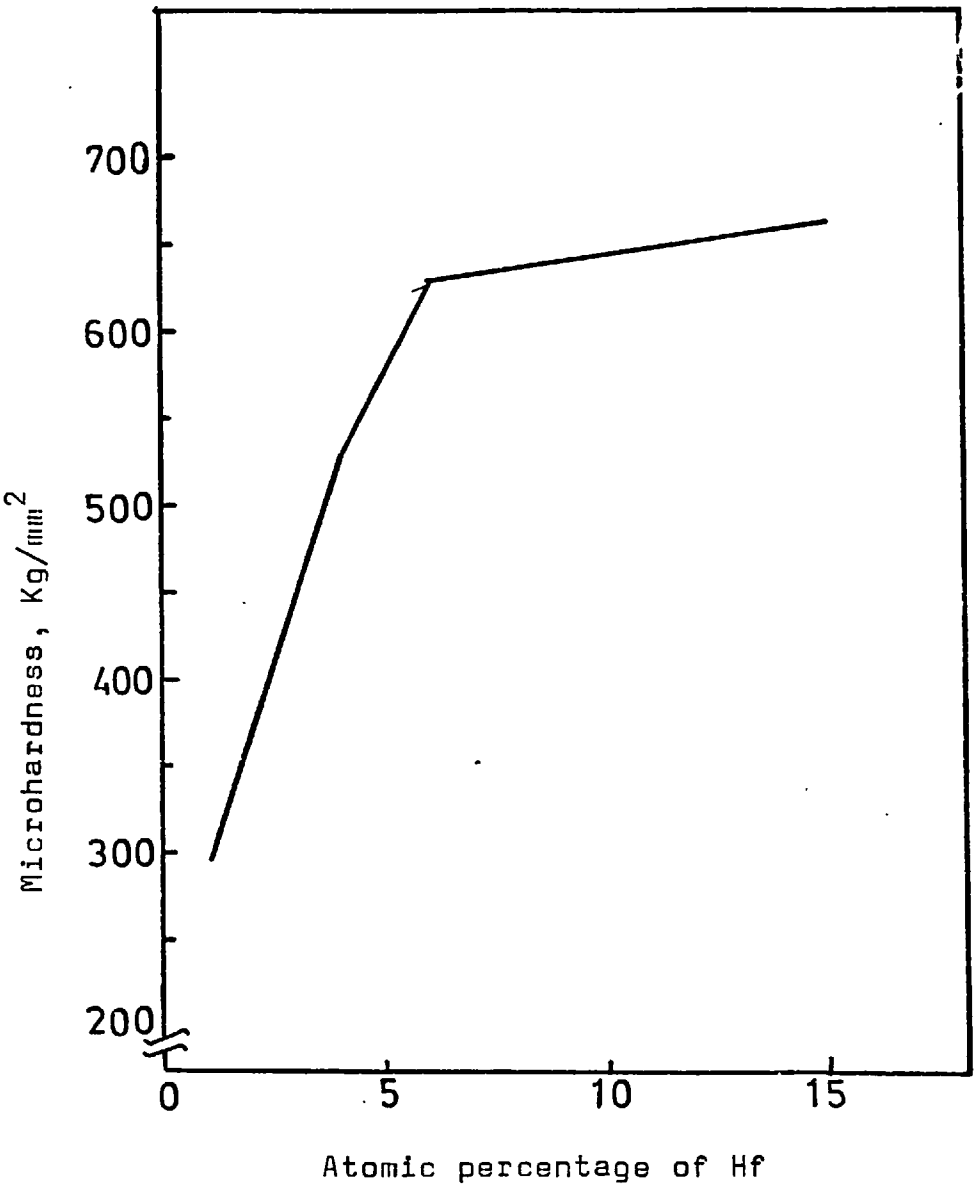

Fig. 2.11 Showing the microhardness versus Hf content in stoichiometric γ' (by Doherty et al, 1971)[38]

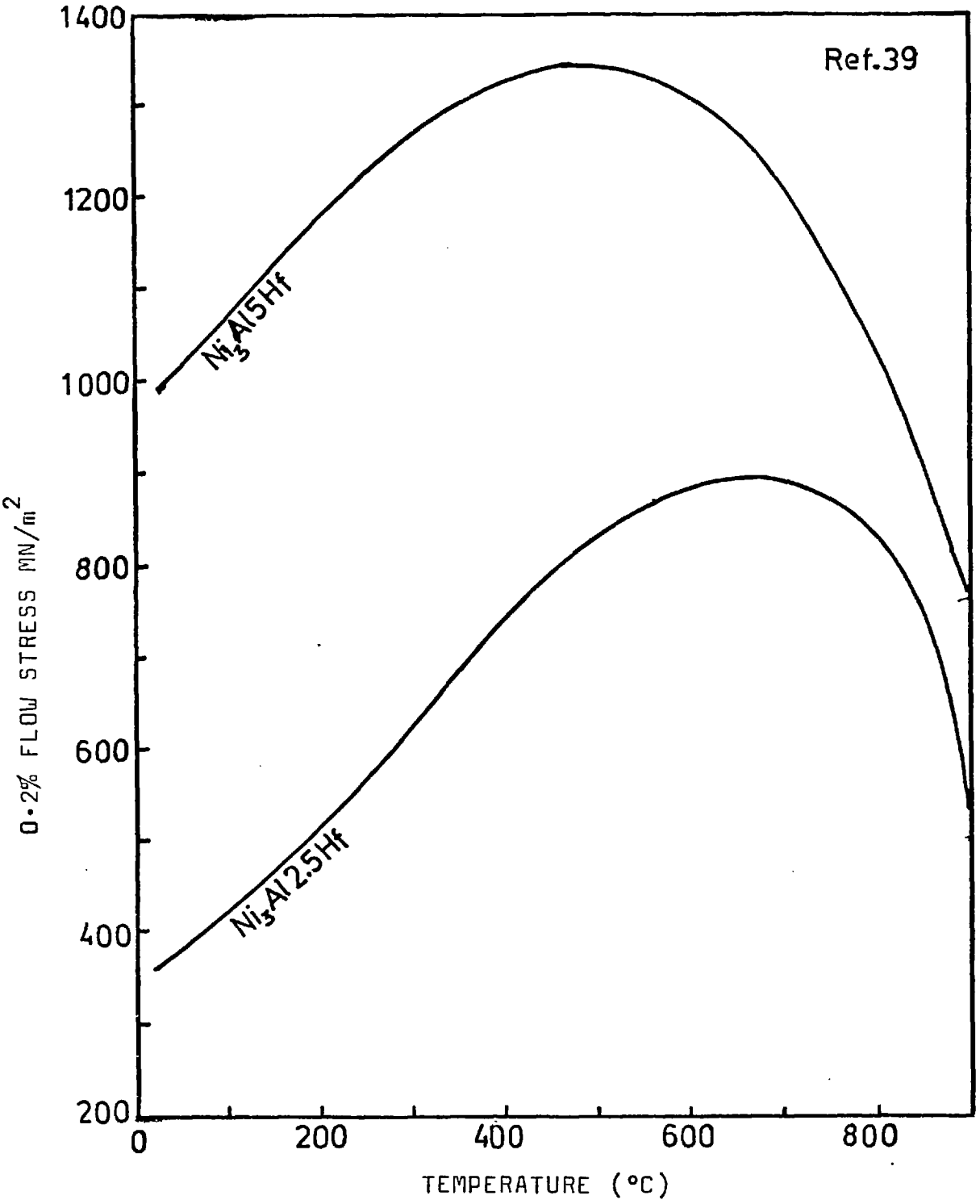

Fig. 2.12 The flow stress versus temperature curves of the stoichiometric Ni_3Al (2,5 at % Hf) and Ni_3Al (5 at % Hf)

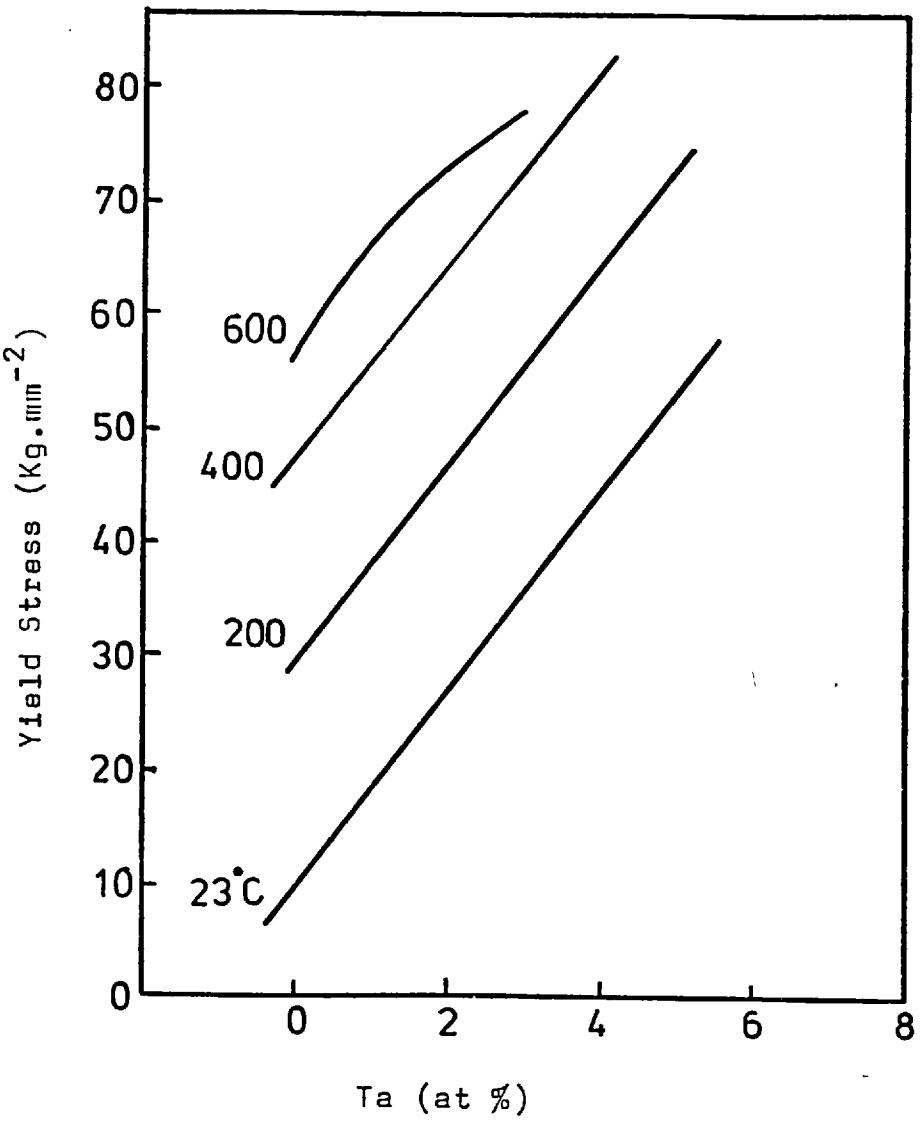

Fig. 2.13 Composition dependence of yield stress of $Ni_3(Al,Ta)$ (ref. 40).

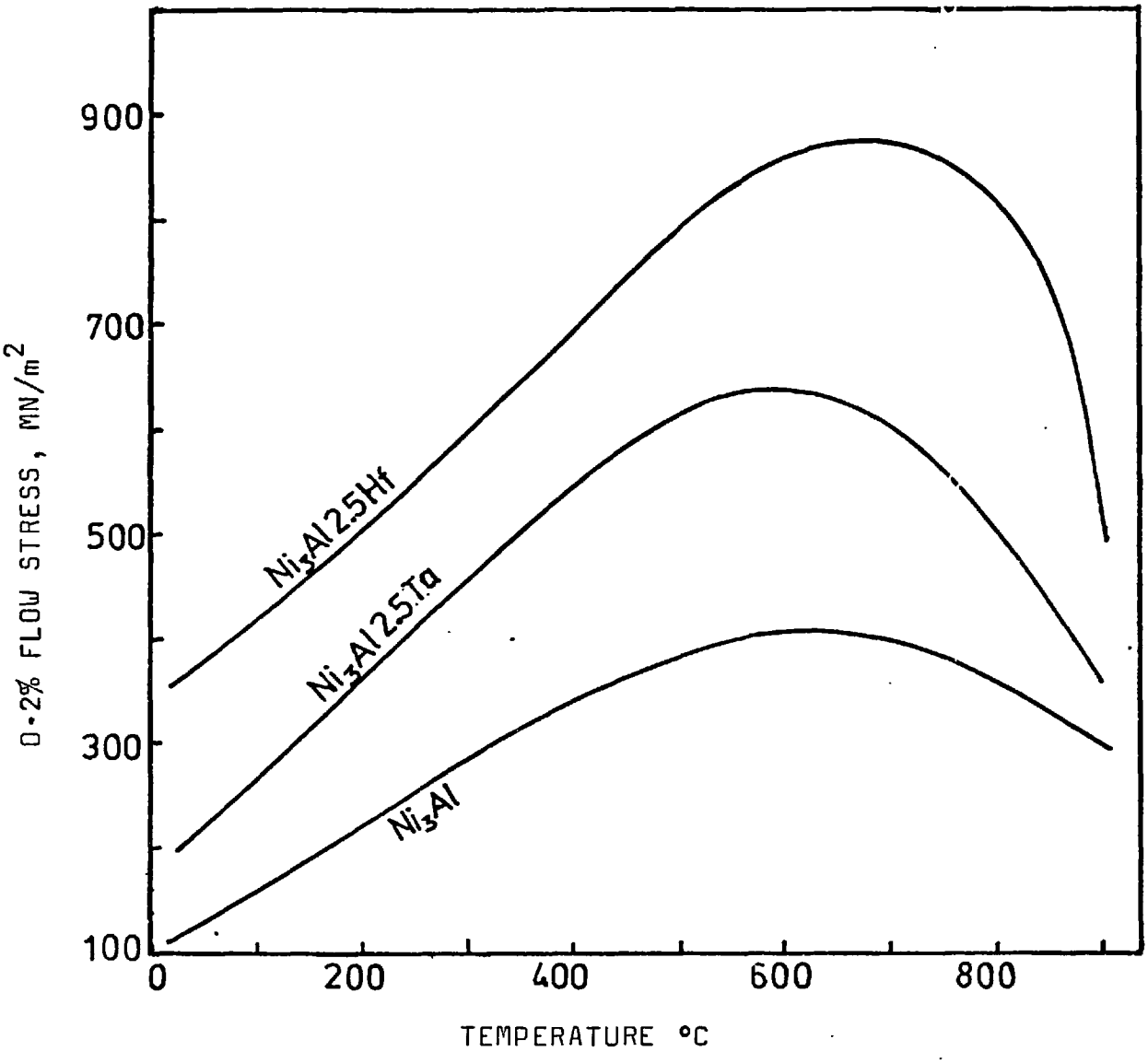

Fig. 2.14 Effect of additions of 2·5 at % Ta and 2·5 at % Hf on the strength of binary stoichiometric Ni_3Al (Ref. 39).

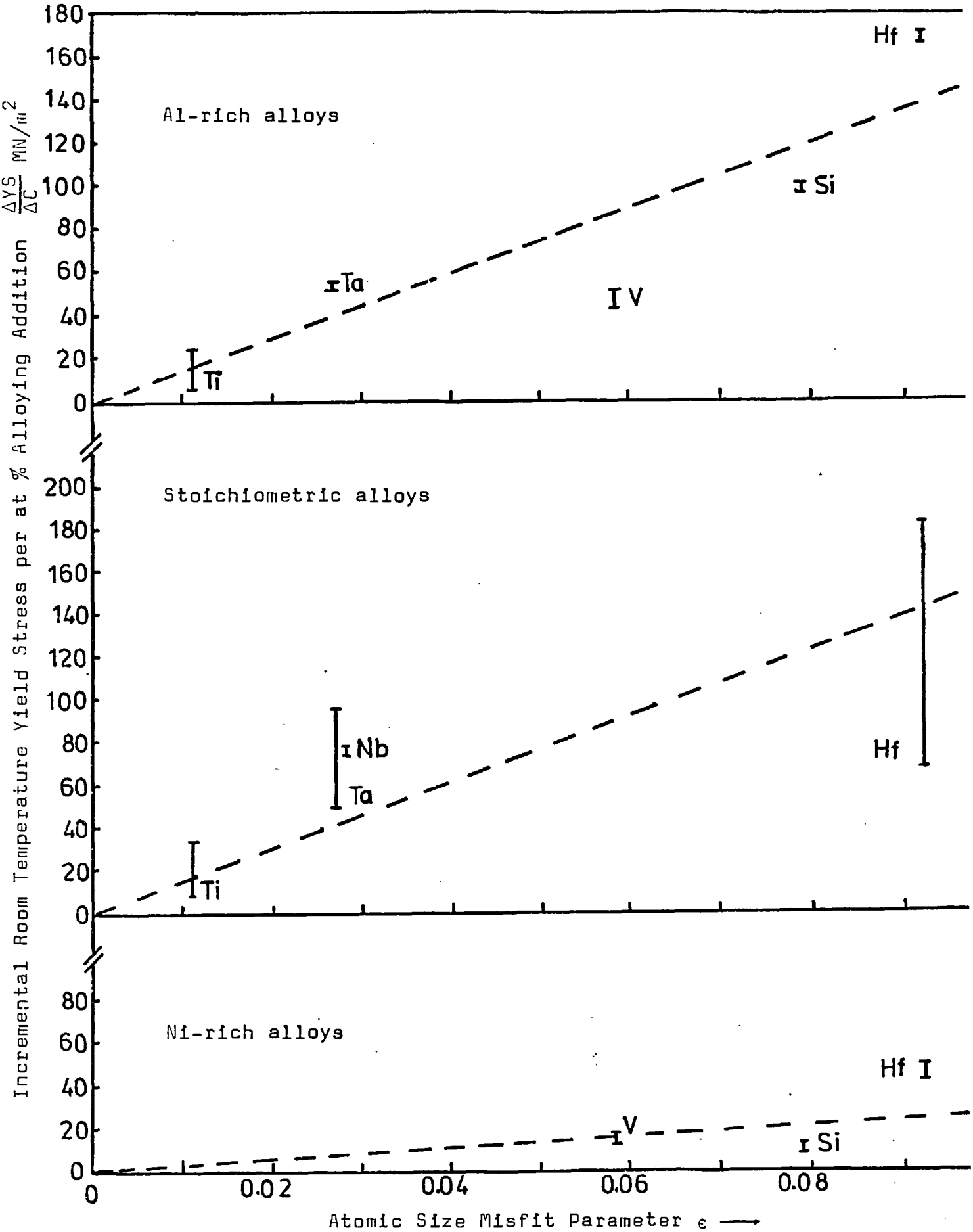

Fig. 2.15 The room temperature strengthening of γ′ phase associated with elements which substitute for aluminium (Rawlings and Staton-Bevan, 1975)[18]

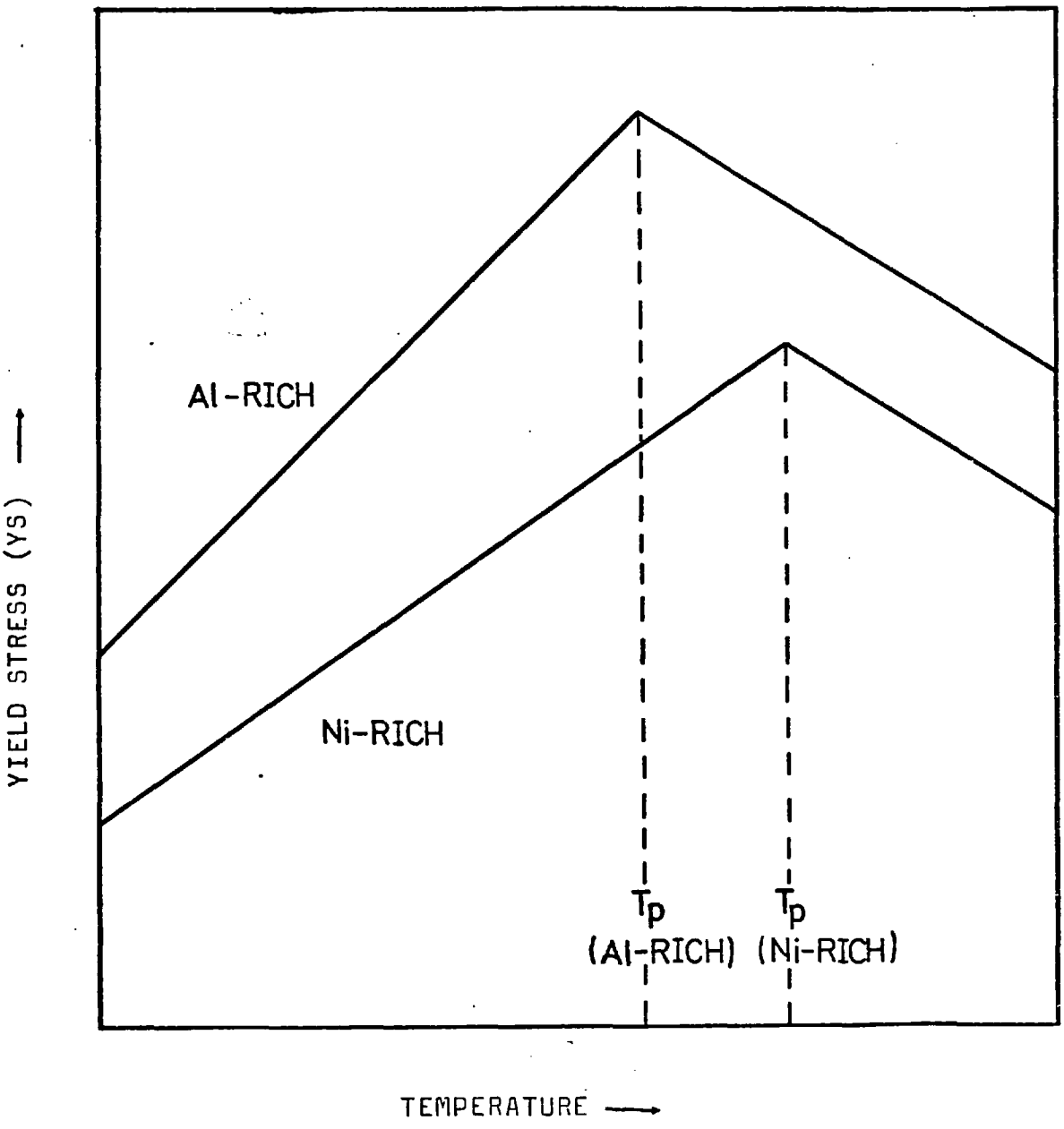

Fig. 2.16 Schematic yield stress versus temperature plots to illustrate the effects of deviations from stoichiometry (From Rawlings and Staton-Bevan (1975)) (ref.18)

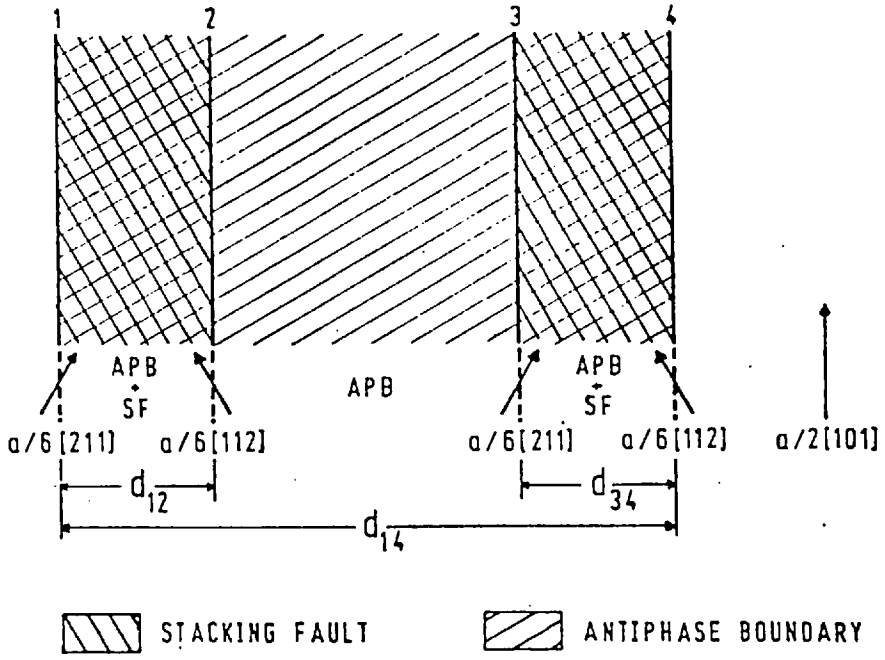

Fig. 2.17 A diagram of a screw superlattice dislocation in an A_3B superlattice.

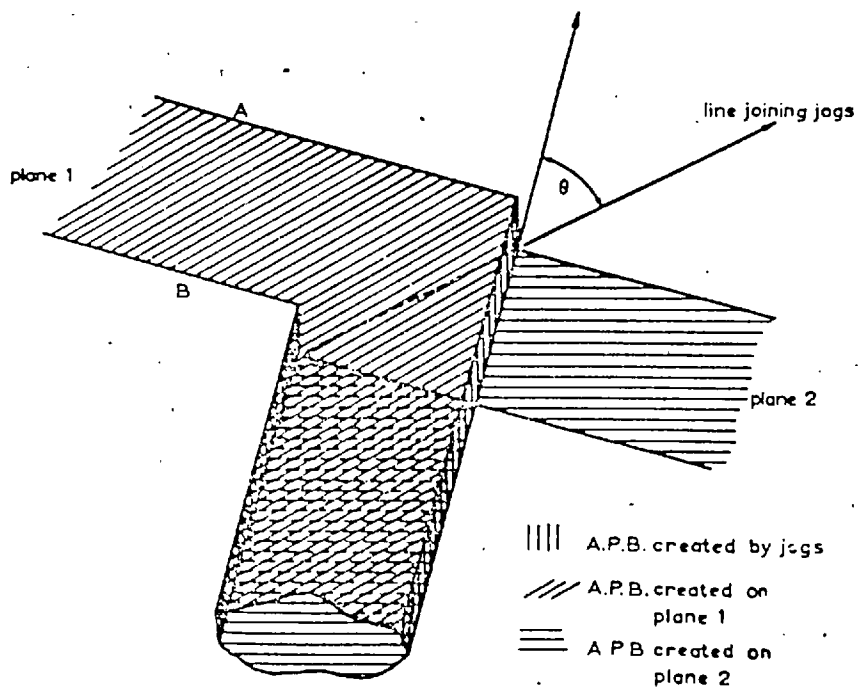

Fig. 2.18 Jogs on a superdislocation.

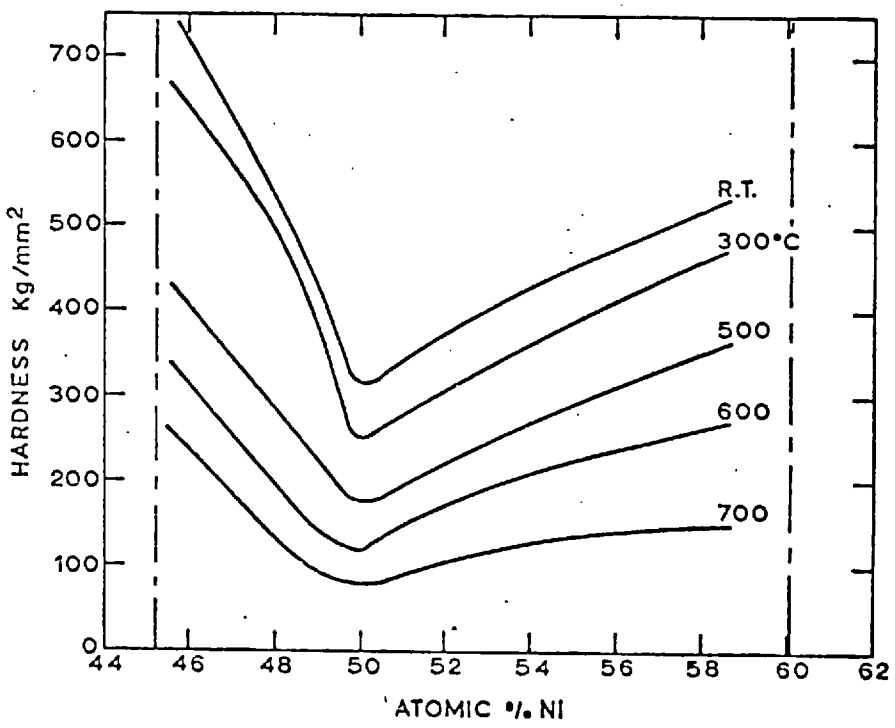

Fig. 2.19 Effects of Composition on hardness isoterms of NiAl (Westbrook, 1956)[33].

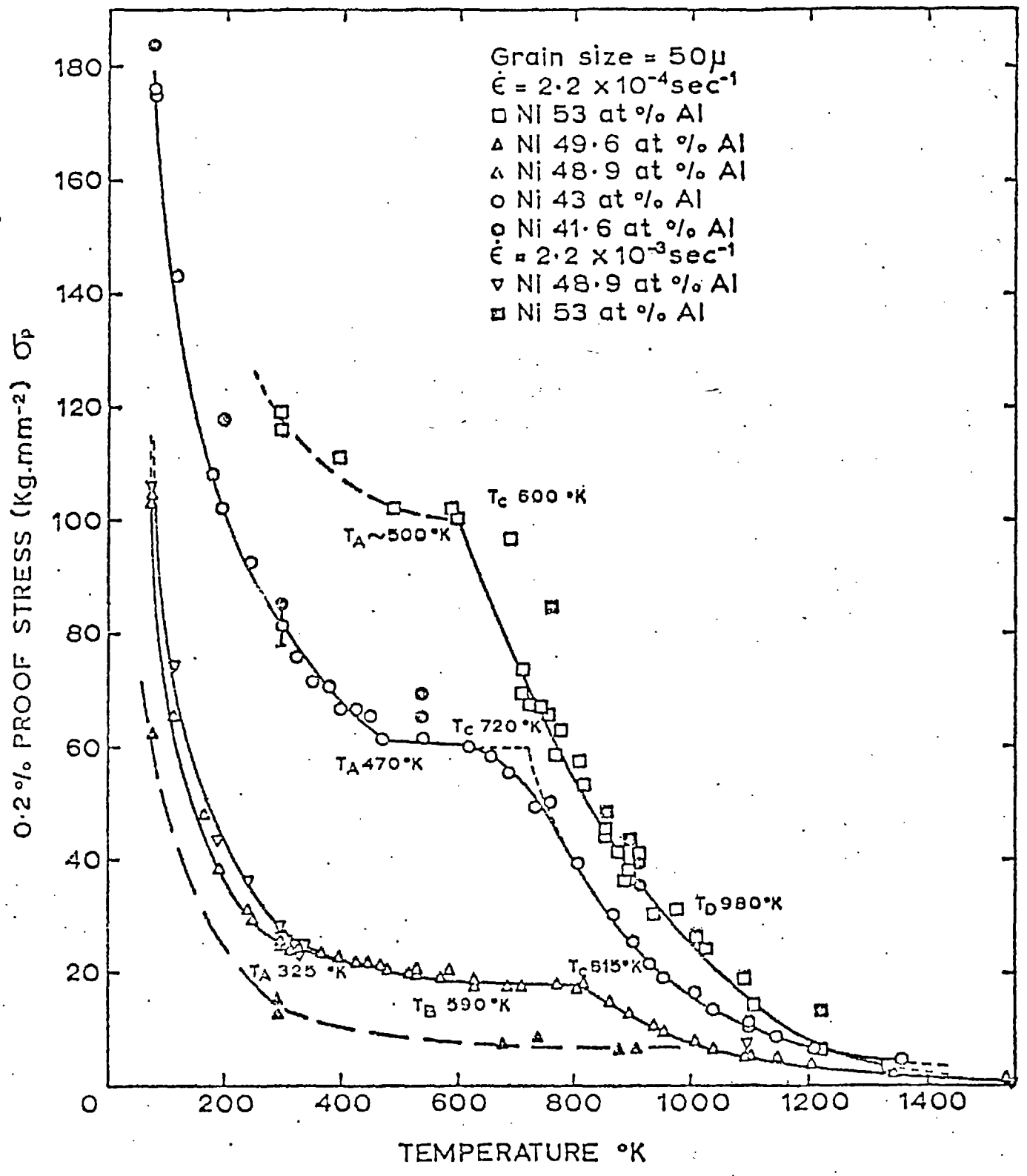

Fig. 2.20 Temperature dependence of flow stress of polycrystalline NiAl (Pascoe and Newey, 1968)[50]

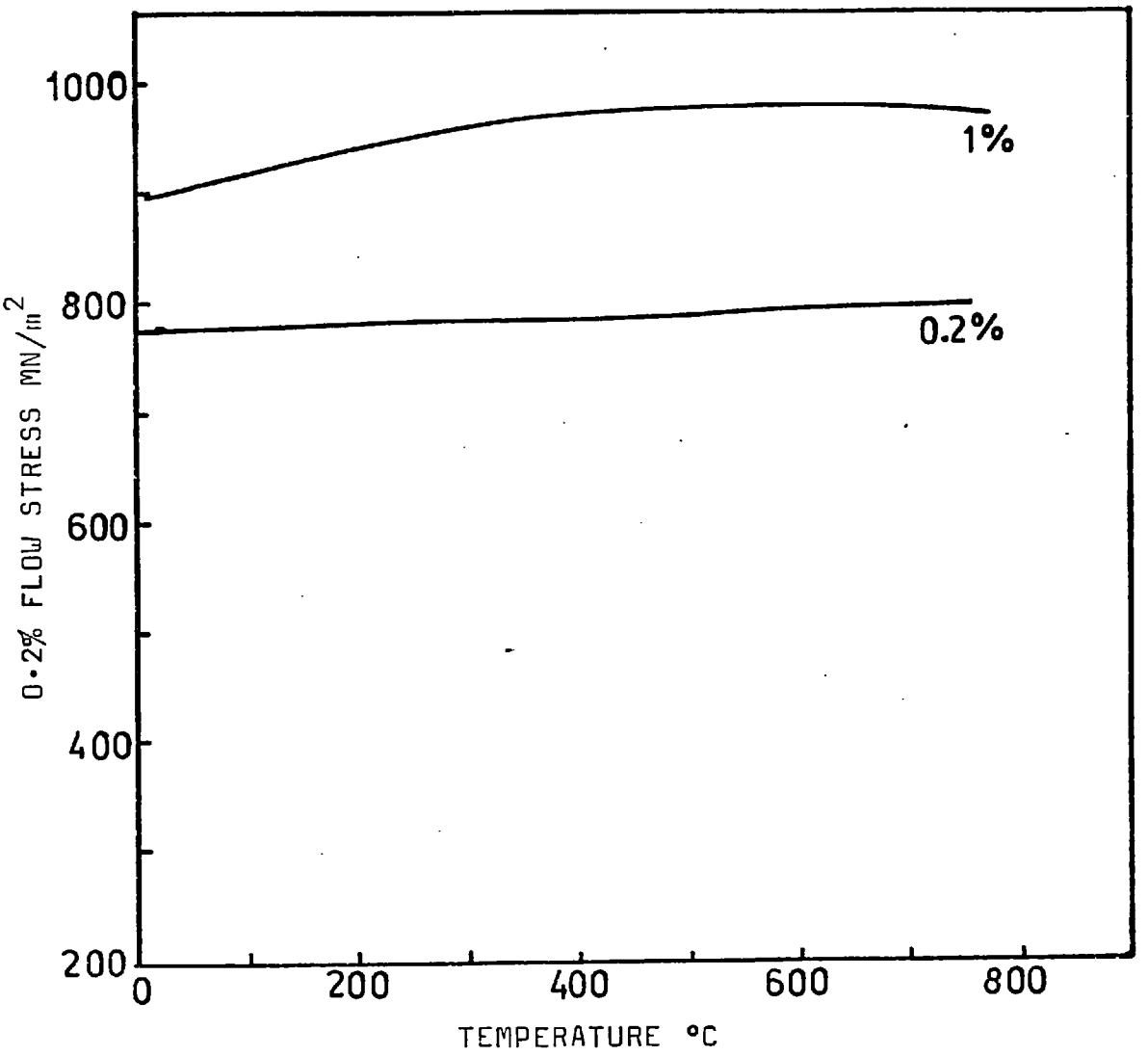

Fig. 2.21 The variation of 0·2% and 1% flow stress of a Ni - 36 at % Al alloy aged for 1 hour at 875°C. (Russell and Edington, 1972)[47].

Fig. 2.22 Tensile data for the Ni - 30·3 at % - 6·6 at % Cr alloy (Ref. 25).

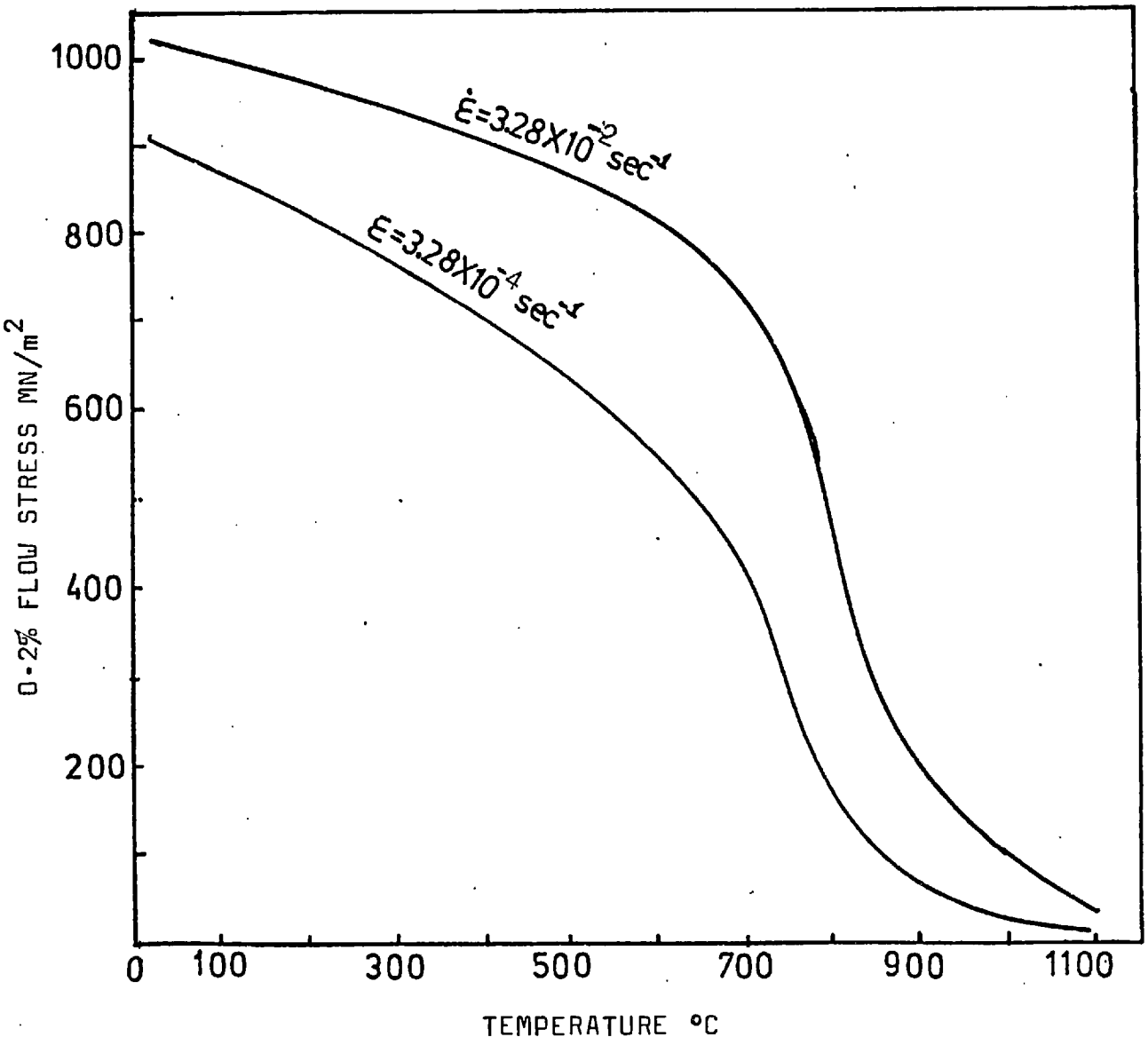

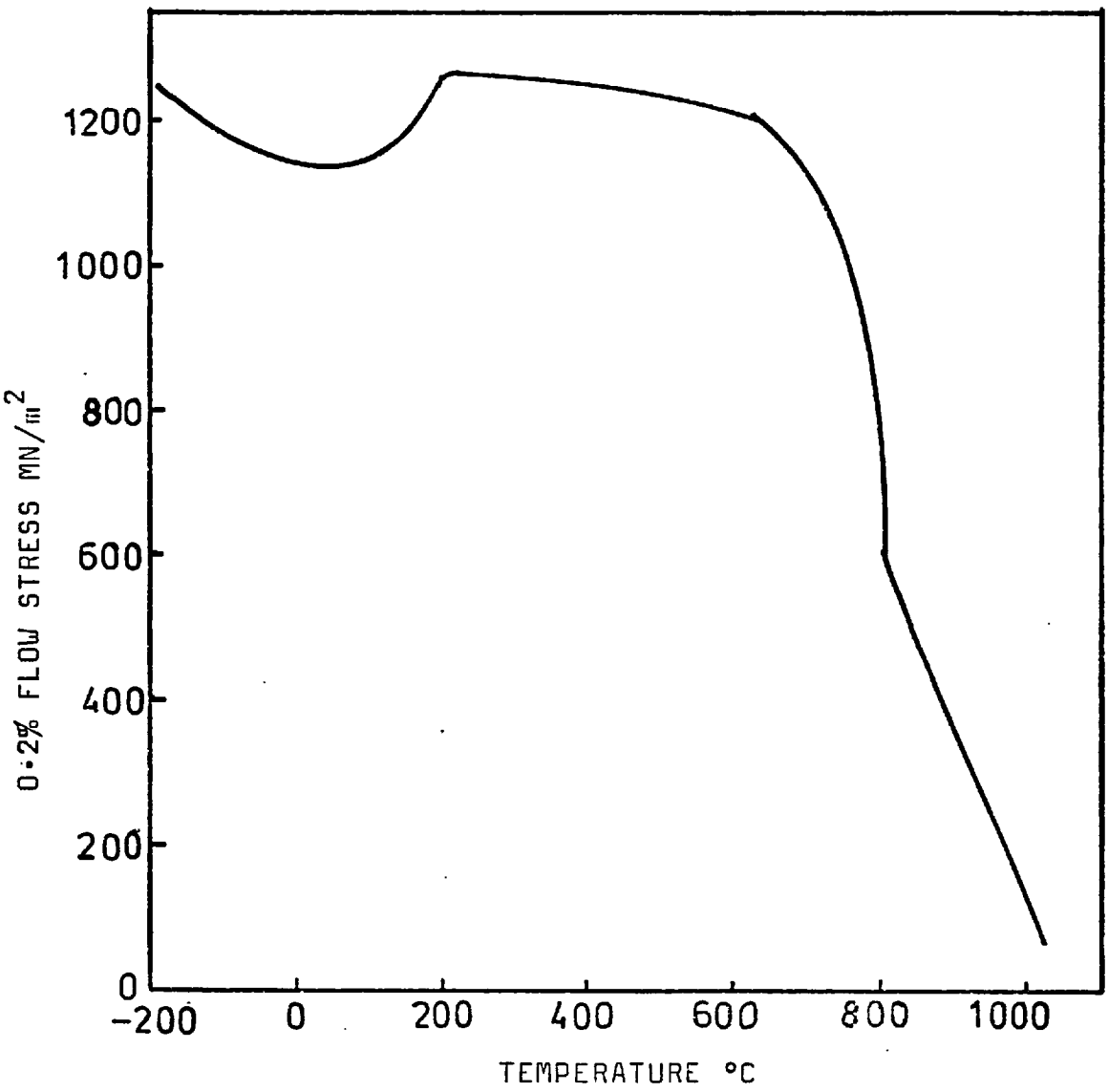

Fig. 2.23 The temperature dependence of the 0·2% flow stress of the Ni - 23·5 at % Al - 2·0 at % Hf - 2·0 at % Co (Ref. 48).

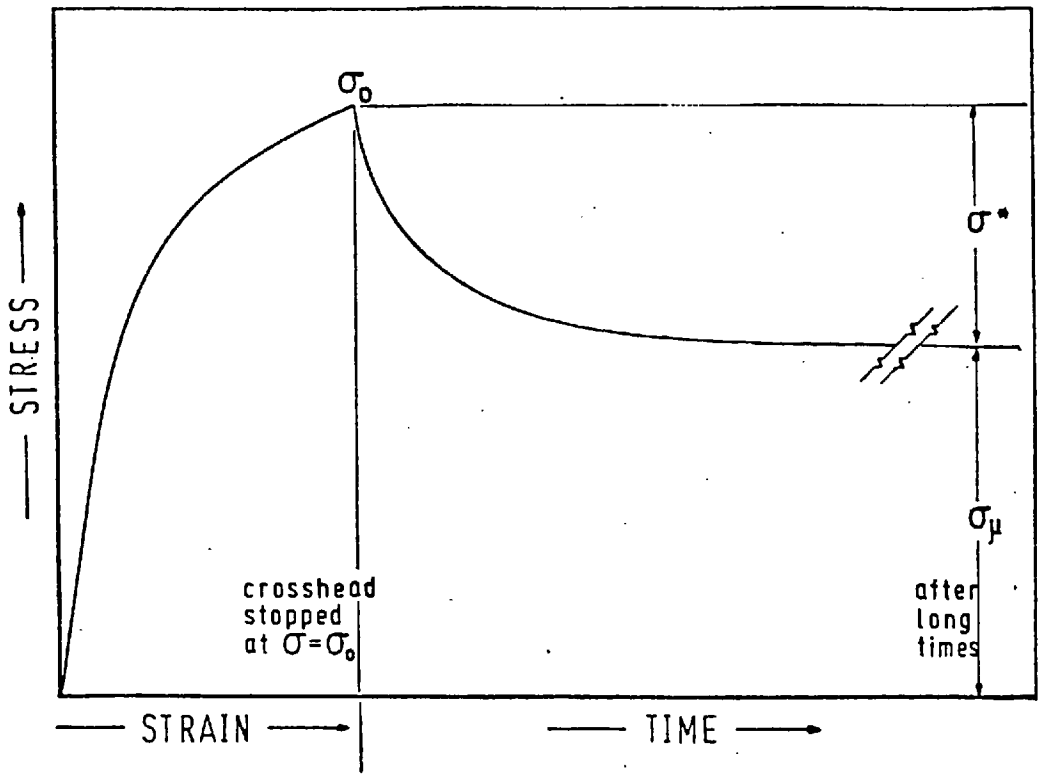

Fig. 2.24 The Schematic stress-relaxation test

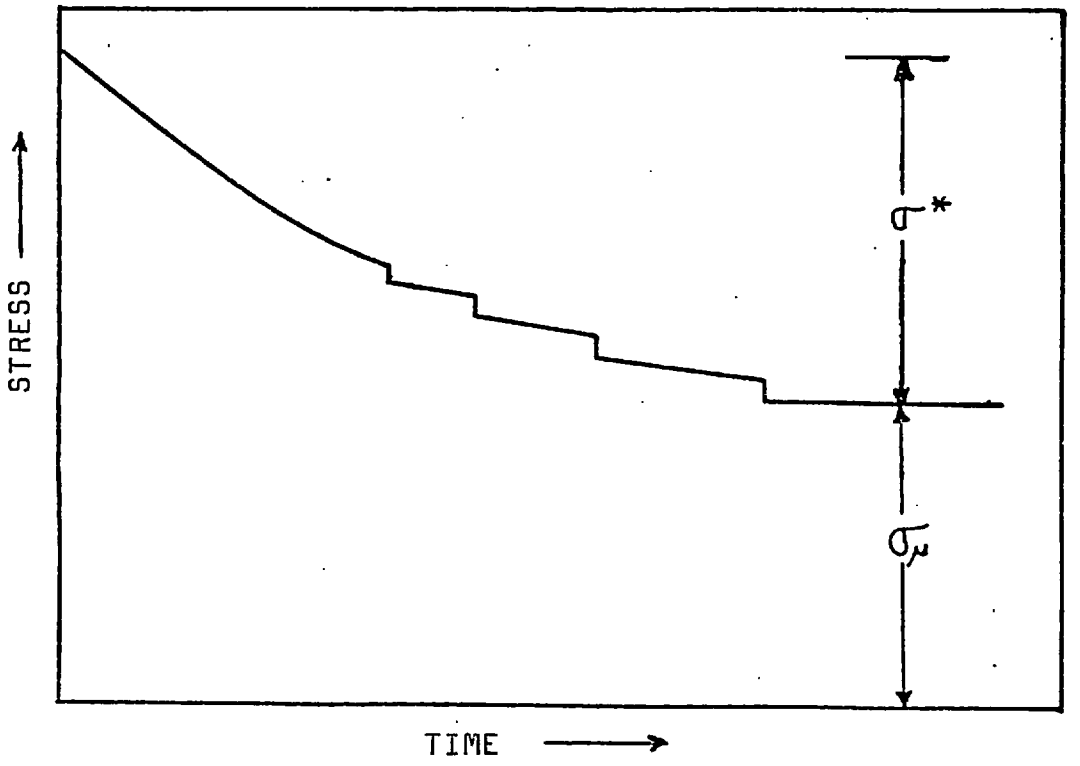

Fig. 2.25 Incremental unloading method.

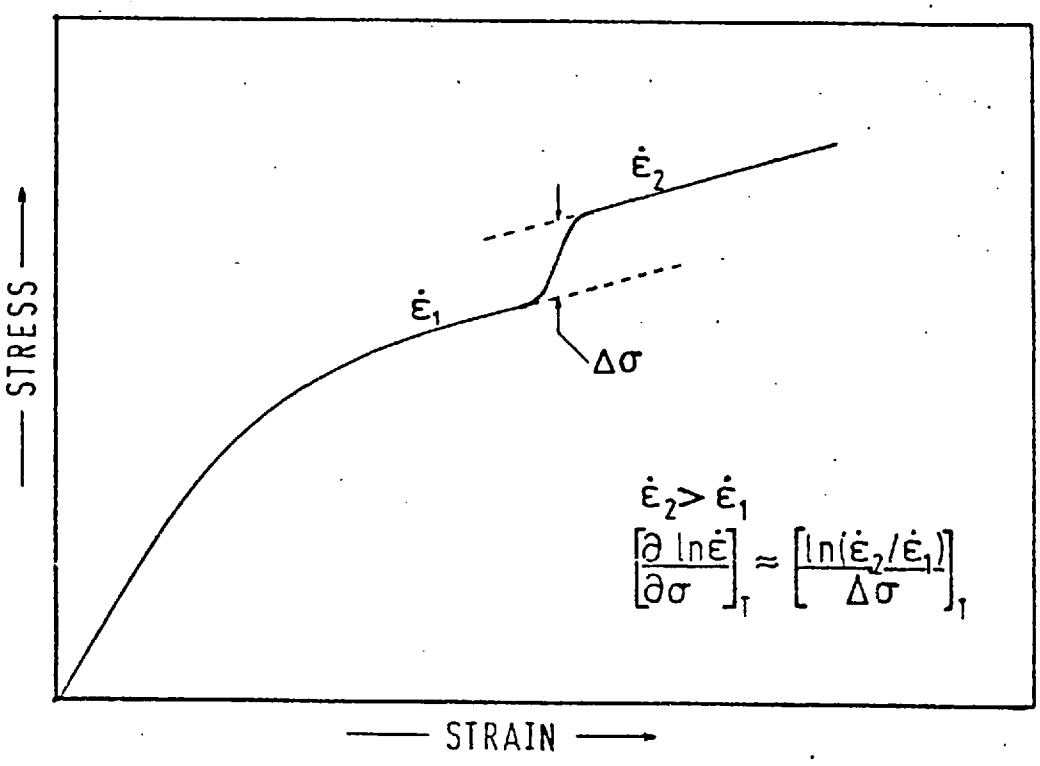

Fig. 2.26 The schematic strain-rate cycling test.

CHAPTER 3

3. EXPERIMENTAL TECHNIQUES

3.1. Alloy preparation

The alloys were prepared as 80 grams "ingots" using an argon arc furnace employing a water cooled copper hearth, tungsten electrode, titanium getter and protective atmosphere of high purity argon at 1/3 atmospheric pressure. The components required for the alloys were weighed separately to an accuracy of ± 0·0002 grams in quantities to give a total alloy weight of about 80 grams. The alloys were melted in a small round hearth in the furnace using an arc current of about 90 amps. Once the alloy had been fully melted the current was increased up to about 200 amps and the ingot was held in the molten state for about one and half minutes. The ingot was then allowed to solidify and was turned over using the furnace "button flipper". The alloy was then remelted: this procedure was repeated at least four times to ensure alloy homogeneity. The ingot was then cast into a rod shaped hearth to produce an ingot approximately (80 mm. x 10 mm. x 10 mm). The ingot was allowed to cool completely before the furnace was opened to air. The ingot was then weighed: weight changes were found to fall in the range $\leq \pm$ 1%. Since the weight changes were always small the composition of each ingot was taken to be that determined by the separate weights of the components.

3.2. Heat treatment

For homogenisation the tantalum-containing alloys were heated in a vertical furnace at 1260°C ± 5°C for 48 hours. The ingots were sealed in silica capsules under 1/3 atmosphere of argon during this heat treatment. After homogenisation treatment the alloys were quenched into water, the silica being broken on contact with the water to ensure a rapid quench. The tantalum-containing alloys after homogenisation were also given an additional heat

treatment of 3 days (72 hours) at 1000°C and then water quenched.

Treatments to homogenise the hafnium-containing Alloy 4 at 1260°C and 1180°C produced partial melting. It was therefore decided not to heat treat this alloy but to study it "as-cast". After the data of Kaufman and Nesor (1975)[8] (sec. 2.1.3) came to hand, a homogenisation temperature of 990°C was chosen for Alloy 5, lying below the relevant eutectics shown by Kaufman and Nesor (1975)[8]. Alloy 5 was also homogenised for 4 days at 990°C, then water quenched.

3.3. Compression Test Procedure

Compression testing was chosen since sufficient specimens for all the mechanical property tests could be made from a single ingot. Tensile testing would have required the use of several ingots.

The specimens of dimensions 6·0 x 2·5 x 2·5 mm. were cut using a macrotome 2 precision cutting machine. This machine consists of a rotating wheel on which SiC blades were placed and the work piece is fed into the wheel by a damped counter-balance. Great care had to be exercised in the preparation of the compression specimens to ensure that (a) the opposite sides of the specimens were parallel and (b) the ends of the specimens orthogonal to the other four faces. The slices were mounted in bakelite blocks during cutting operations. After each cut, a copper shim was put in the groove so that the specimen remained rigid. The top and bottom and vertical faces of the specimens were ground parallel using a 600 SiC paper.

3.4. Compression Tests

The compression tests were carried out using an Instron testing machine, converted for compression testing by means of rigs attached to the underside of the moving crosshead. All tests were done using a crosshead speed

of 5×10^{-3} cm/min. which resulted in a strain rate of $1{\cdot}3 \times 10^{-4}$ sec^{-1}. In the post-yield region the cross-head speed and chart speed were increased by a factor of ten and then returned to the original settings shortly afterwards, to measure the strain rate dependence of the flow stress, which is called the "strain-rate cycling" test (sec. 2.20.2). Stress relaxation tests were also carried out by stopping the crosshead. A relaxation period of twenty minutes was used. 100Kg full scale was used during the relaxation period. During the early relaxation period (up to one minute) the faster chart speed was selected for measuring time. These stress relaxation data were put into a programme made for Feltham's equation [eg. (1) in sec. 2.20.1] prepared by Nicholls and Rawlings[64]. From this computation the thermal and athermal stress components of flow stress were determined. Decremental unloading method was also applied for some cases (sec. 2.20.1) to determine the thermal and athermal stresses. At low temperatures both methods gave close results. Test temperatures were in the range of room temperature to 900°C. Tests were at least duplicated to achieve more correct data. However, at some points tests were repeated four or five times to make sure that particular data represent true values for the alloys. At low test temperatures (<400°C) the furnace temperature varied within ±5°C, whereas at high temperature (>400°C) testing, it varied within ±15°C.

3.5. Hardness measurements

Hardness measurements were made on a Vickers Hardness testing machine using a 10 Kg load to determine the ageing responses of the alloys. Microhardness tests were also done using a 100 gram load to compare the difference in hardness values between the γ' and β phases, and the effect of Ta and Hf on the mechanical properties of γ'. For each specimen, typically fifteen readings were made.

3.6. Metallography

3.6.1. Optical microscopy

Sections cut from as-cast, homogenised and homogenised plus aged specimens were studied using light microscopy.

The samples were successively ground through different grades of SiC papers. This was followed by polishing on horizontal wheels covered with "selvyt cloth" impregnated with 3μ and 1μ diamond paste. Finally they were etched using alcoholic ferric chloride (5g.$FeCl_3$,2cc. HCl and 95 cc. ethanol).

3.6.2. Electron microscopy

Specimens for transmission electron microscopy were prepared from underformed and deformed specimens.

Several methods have been used in attempts to produce thin foils for electron microscopic observations. Due to the presence of two phases, often as large particles, and rapid contamination of the materials during polishing, electropolishing methods attempted were not entirely successful. However, an ion beam thinning technique was successfully used to prepare thin foils. For this method specimens were prepared as discs. 3mm. diameter disc were spark machined out of the thin slices of crystal using cylindrical, hollow brass tube electrode. The specimen slices were glued onto a flat brass with a very thin layer of "Durofix" mixed with graphite powder and formed the second electrode. After spark-machining, the discs were removed from the brass, by dissolving the Durofix with acetone. 3mm. diameter discs of ≈ 0·4mm. thickness were ground to ≈ 70 μm, and were then placed in the ion beam thinner. The apparatus consists of two ionization chambers in which ions of energy 1-10 KV are formed and accelerated through holes in a disc-shaped cathode plate which also serves to focus on the specimen. The atoms are knocked out of the surface by impinging ions. The argon was used for bombarding ions. The 15° of incidence angle was used at 6 KV. When a hole appears on the disc, the ≈ 7° of incidence angle was used to obtain enough thin areas. After perforation the disc was washed in clean methanol.

Specimens were examined at 100 KV in a EM6 electron microscope. Standard electron microscopy imageing including

selected area diffraction, dark field microscopy and two beam analysis of structural defects were employed. Plane spacings (d) were determined from measurements of interspot distances in selected area diffraction patterns using the permanently calibrated camera constant $2\lambda L$.

3.7. Phase measurements

The amount of each phase present was measured by light microscopy using a "point counting" method. At least 2000 counts were made in the point counting. In measurements made on alloys, as-aged, the β phase as measured includes the precipitated γ' particles. Hence the actual volume percentage of β phase present is less than the value counted. The estimated accuracy of the data is typically $\pm$ 1·5-2%.

3.8. X-ray Diffraction

The x-ray work has been done using diffractometry from a flat specimen surface. The aim of this work was to identify the phases present in the alloys investigated and to determine the effect of ternary additions (Ta, Hf) on the lattice parameters of the phases. An anode voltage of 40 KV, a current of 40 mA, and CuKα radiation were used for this x-ray work.

The results were analysed using a "least squares best straight line" fitted to a plot of "a" vs the Nelson-Riley function; the values of "a", the intercept, were obtained.

Great care was exercised that the front face of the specimen be as flat as possible and its plane as nearly as possible perpendicular to its axis of rotation. This procedure increases the accuracy of the measurement[165].

CHAPTER 4

4. EXPERIMENTAL RESULTS

4.1. The Compositions of alloys

Table 4.1 gives the nominal compositions of the alloys prepared.

Table 4.1. The compositions of alloys

ALLOY	Ni at %	Al at %	Ta at %	Hf at %
Alloy 1	68,75	28,75	2,5	-
Alloy 2	70,75	26,75	2,5	-
Alloy 3	72,5	20·0	7·5	-
Alloy 4	72,5	20·0	-	7,5
Alloy 5	72,5	22·5	-	5·0

The position of each alloy is plotted on the ternary Ni-Al-Ta (fig. 4.1) and Ni-Al-Hf phase diagrams (fig. 4.2).

The tantalum-containing alloys (Alloys 1, 2 and 3) have been investigated in three different conditions:

i) As-cast condition
ii) Homogenised condition: heat treated at 1260°C for 48 hours and water quenched.
iii) Homogenised plus aged conditon: first heat treated at 1260°C for 48 hours, water quenched then aged at 1000°C for 3 days (72 hours) and water quenched.

In the hafnium-containing alloys, Alloy 4 has been investigated only in the as-cast state. Alloy 5 has been investigated in two different conditions:

i) As-cast condition
ii) Homogenised condition: heat treated at 990°C for 4 days (96 hours) and then water quenched.

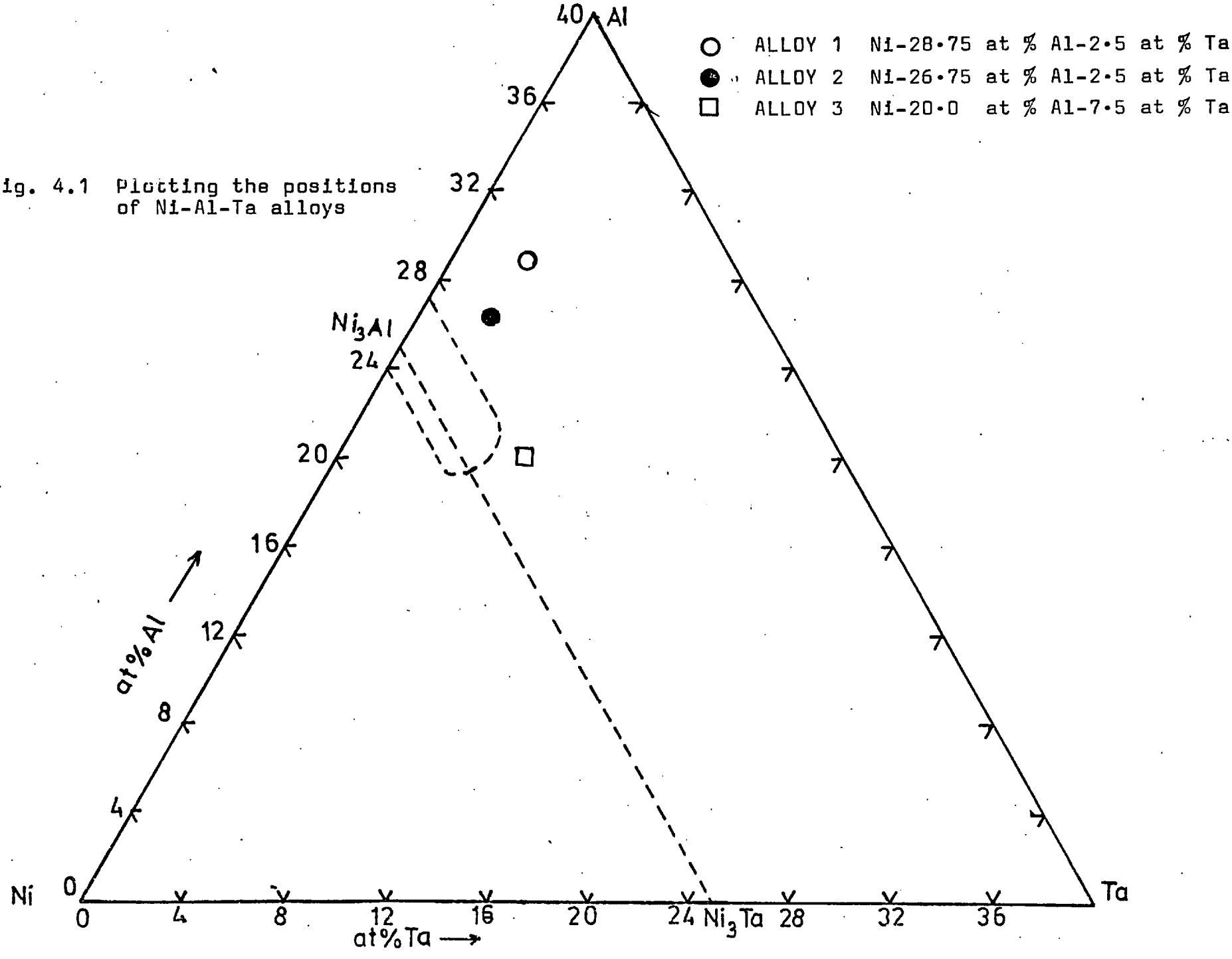

Fig. 4.1 Plotting the positions of Ni-Al-Ta alloys

Fig. 4.2 Plotting the positions of Ni-Al-Hf alloys

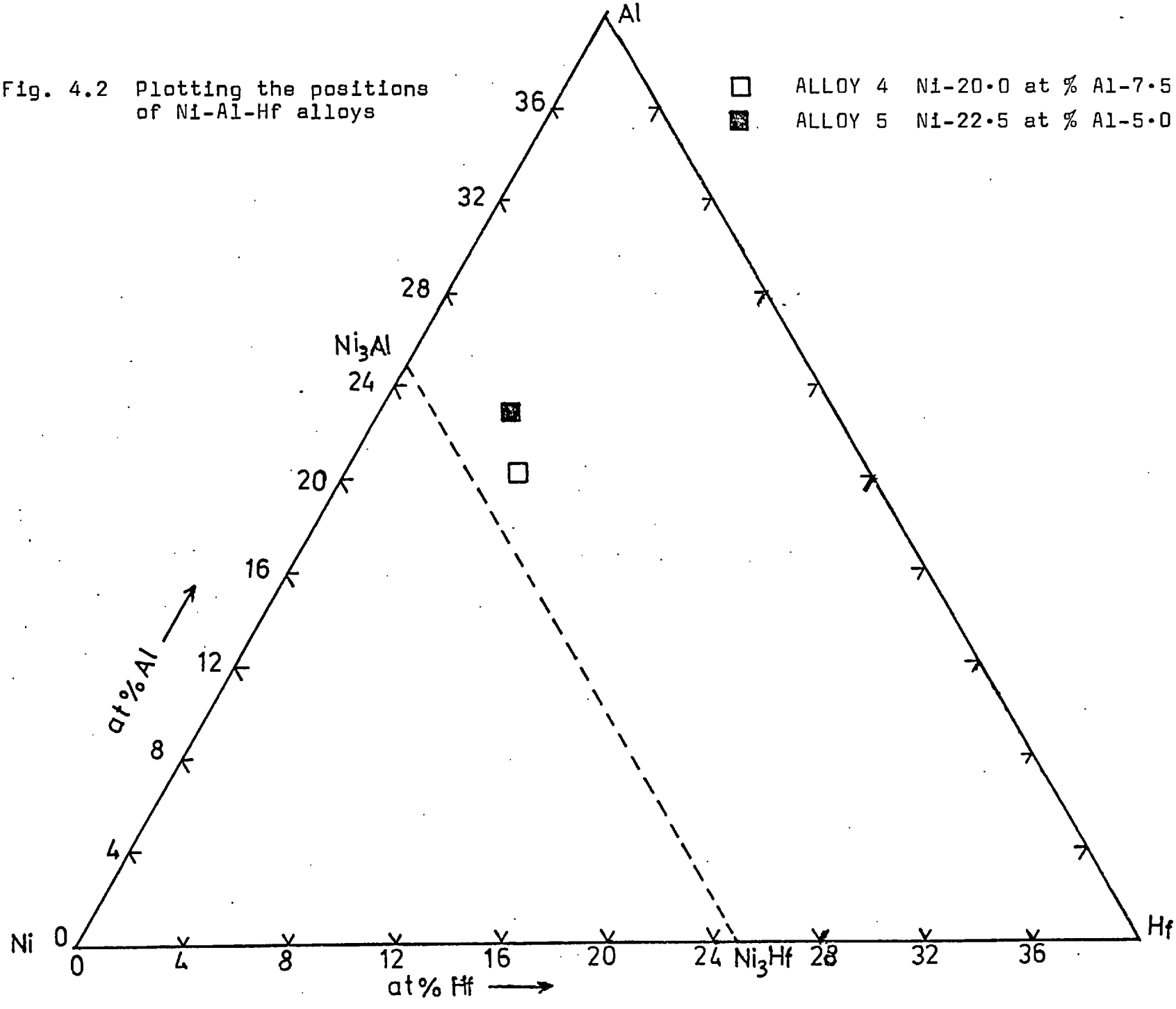

The object of the present research was to make a general survey of the structural and mechanical properties of these alloys. This was to be achieved by studying:

i) Structural and morphological properties;
ii) The influence of alloying additions (Ta, Hf) on the structural and mechanical properties,
iii) The effect of the individual phases, which constitute the alloy, on the mechanical properties.

Electron probe microanalysis (EPMP) was carried out to determine the content of each element in the phases which constitute the alloys investigated. Specimens of ≈10x10x2mm. size from each alloy were polished and etched as described in section 3.6.1. The raw data from the electron probe analyser was compared with that from pure metal standards and corrections were applied for Atomic Number effects, absorption and interelement fluorescence using the procedure described by Mason et al (1969)[66]. The experiments were done by the Analytical Services Laboratory in Imperial College and the National Gas Turbine Establishment (NGTE) in Farnborough respectively. The results from the EPMA are shown in Table 4.2. However, it was not possible to determine the compositions of the phases in the eutectic regions in Alloy 4 and Alloy 5, and of the β particles in Alloy 3, because the sizes of the phase particles were not big enough. The estimated accuracies are about ±1% relative.

As the Table 4.2 shows the tantalum content of the β phase in the alloys is $\leqslant$ 1 at %. The nickel composition of β phase in Alloy 1 has decreased by about 4 at % after homogenisation treatment compared to the as-cast state. In Alloy 2 the nickel content of the β phase has also decreased by about 5 at % after ageing treatment compared to that of the as-cast and homogenised states. The nickel content of the β phase in the as-cast state of Alloy 1 is the highest among the alloys investigated and lowest in that of the aged state of Alloy 2.

All the γ′ phases in the alloys investigated are

Table 4.2 The compositions of γ′ and β phases

ALLOY (Nominal composition)	Phase	Ni (at %)	Al (at %)	Ta (at %)	Hf (at %)
ALLOY 1 (as-cast) (Ni-28·75 at % Al-2·5 at % Ta)	γ′ β	- 66·7	- 32·3	- 1·0	-
ALLOY 1 (Homogenised)	γ′ β	72·6 62·3	23·0 37·1	4·4 0·6	- -
ALLOY 1 (Homogenised + Aged)	γ′ β	69·6 61·4	26·2 38·0	4·2 0·6	- -
ALLOY 2 (as-cast) (Ni-26·75 at % Al-2·5 at % Ta)	γ′ β	68·9 60·7	27·9 38·2	3·2 1.1	- -
ALLOY 2 (Homogenised)	γ′ β	68·1 60·2	28·1 39·4	3·7 0·4	- -
ALLOY 2 (Homogenised + Aged)	γ′ β	66·8 55·3	28·0 44·1	5·2 0·6	- -
ALLOY 3 (as-cast) (Ni-20·0 at % Al-7·5 at % Ta)	γ′ β	72·9	18·7	8·4	-
ALLOY 3 (Homogenised)	γ′ β	74·0	17·7	8·3	-
ALLOY 3 (Homogenised + Aged)	γ′ β	70·9	22·1	7·0	-
ALLOY 4 (as-cast) (Ni-20·0 at % Al-7·5 at % Hf)	γ′	74·0	19·3	-	6·7
ALLOY 5 (as-cast) (Ni-22·5 at % Al-5·0 at % Hf)	γ′	72·0	25·0	-	3·0
ALLOY 5 (Homogenised at 990°C for 4 days, wq)	γ′	71·0	24·4	-	4·6

aluminium-rich, i.e. the composition of the (Al + Ta) is more than 25 at % (Table 4.2). The tantalum composition of γ' phase in Alloy 1 and Alloy 2 is comparable, i.e. between about 3-5 at % Ta. However, the tantalum content of γ' phase in Alloy 3 is the highest among the alloys investigated, i.e. about 7-8 at %.

In the hafnium-containing alloys, the γ' phases are also aluminium-rich, i.e. the content of the (Al + Hf) is more than 25 at % (Table 4.2). The hafnium content of γ' phase in Alloy 4 is higher than that of Alloy 5. The hafnium content has increased (by about 1·6 at %) after homogenisation treatment compared to the as-cast condition, in Alloy 5.

4.2. The lattice parameters of γ' and β phases

The lattice parameters of γ' and β phases have been determined in the alloys investigated, using x-ray diffractometry. They are given in Table 4.3.

The lattice parameters of the γ' phases in all the alloys investigated are higher than that of the binary γ' phase (Table 2.1).

After quenching from 1260°C the β phase has undergone the martensitic transformation. The crystal structure of the martensitic β phase has been determined to be body-centred tetragonal (BCT) by x-ray diffractometry. The lattice parameters and the c/a ratios of the martensitic β phase in Alloy 1 and Alloy 2 have been determined and are given in Table 4.4.

Table 4.3 The lattice parameters of γ' and β phases

ALLOY	Lattice Parameters (°A)	
	γ' phase	β phase
ALLOY 1 (Homogenised)	3,585	-
ALLOY 1 (Homogenised + Aged)	3,586	$2,858_7$
ALLOY 2 (Homogenised)	3,587	-
ALLOY 2 (Homogenised + Aged)	$3,591_6$	2,852
ALLOY 3 (as-cast)	3,612	2,880
ALLOY 3 (Homogenised)	3,611	2,869
ALLOY 3 (Homogenised + Aged)	3,605	2,861
ALLOY 4 (as-cast)	3,625	2,864
ALLOY 5 (Homogenised at 990°C for 4 days, wq)	3,615	-

As Table 4.3 shows the β phase in Alloy 3 has not undergone martensitic transformation after homogenisation treatment.

Table 4.4 The lattice parameters of β martensite

ALLOY	Lattice parameters of martensitic β phase		$\frac{c}{a}$
	a (°A)	c (°A)	
ALLOY 1	2·65	3·245	1·22
ALLOY 2	2·68	3·25	1·21

In Alloy 4, as-cast, and in Alloy 5, both in the as-cast and homogenised conditions, an intermetallic compound has been found to exist. The structure of this phase (α) has been determined to be hexagonal by x-ray

diffractometry. The lattice parameters of this phase in Alloy 4, in the as-cast state, have been determined to be c = 6,042Å, a = 4·905Å, with c/a = 1·23. The d-values from this phase are given in Appendix 2. The crystal structure of this phase has also been confirmed by electron microscopy (sec. 4.5).

The lattice parameters of γ' phase in both the tantalum- and hafnium -containing alloys have been plotted as a function of tantalum and hafnium contents of γ' phase (fig. 4.3). As fig. 4.3 shows the lattice parameters of $(Ni_3(Al,Ta)$ and $Ni_3(Al,Hf)$ increase with increasing tantalum and hafnium contents in γ' phase, and hafnium has increased the lattice parameter of γ' phase more than the tantalum did.

4.3. The Volume fractions of phases

The volume fractions of the phases present in the alloys as determined by "point counting" are given in Table 4.5.

Table 4.5 The volume fractions of γ' and β phases

ALLOY	Treatment	Volume %	
		γ'	β
ALLOY 1	As-cast	42	58
	Homogenised	49	51
	Homogenised plus aged	51	49
ALLOY 2	As-cast		
	Homogenised	71	29
	Homogenised plus aged	75	25
ALLOY 3	As-cast	80	20
	Homogenised	80	20
	Homogenised plus aged	80	20
ALLOY 4	As-cast	76	
ALLOY 5	As-cast	92	
	Homogenised	96	

The estimated accuracy is typically ± 1·5 - 2%.

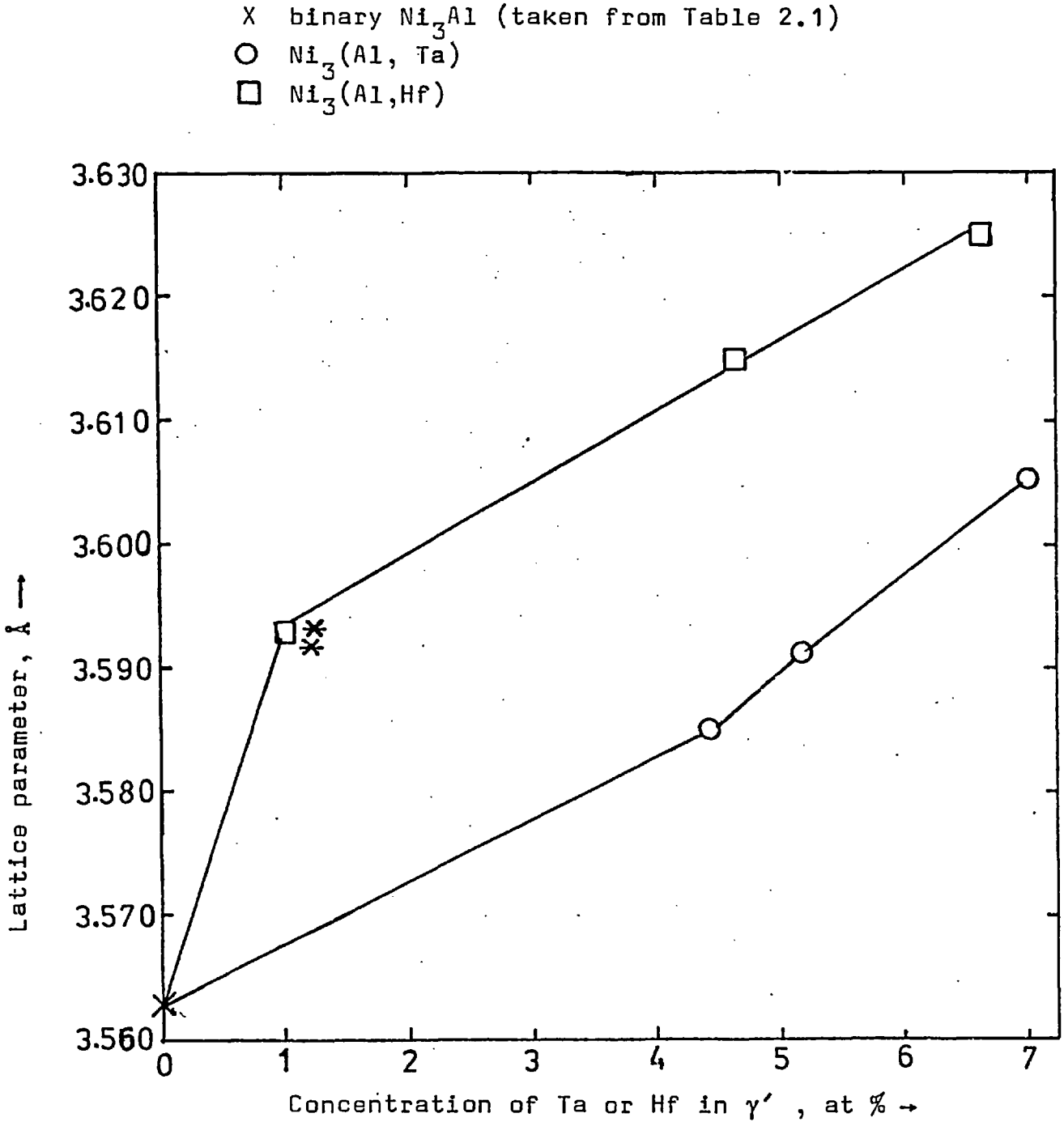

Fig. 4.3. The effects of tantalum and hafnium on the lattice parameters of γ' phase.

‡ This alloy was prepared by Dr S. Chakravorty. The lattice parameter of this γ' phase was determined by the author of this thesis.

In the tantalum-containing alloys observations made on the as-aged conditions, showed the β phases to contain precipitated γ′ particles (fig. 4.18(a)). Hence the actual volume fraction of β phase present is less than the values counted. If this is taken into account the volume fractions of γ′ and β phases have similar values in the aged condition of Alloy 2 and the homogenised conditions of Alloy 3 (Table 4.5).

As Table 4.5 shows there is a significant decrease of volume fraction of β phase from the as-cast condition to the homogenised in Alloy 1. If the γ′ precipitate particles in the β phase are also taken into account in the aged condition, there is a decrease of volume fraction of β phase from the homogenised state to the homogenised plus aged state.

Alloy 5 in the as-cast condition is predominantly γ′ (it contains 92 vol. pct γ′ plus 8 vol. pct of eutectic regions). The homogenisation treatment at 990°C has increased the volume fraction of γ′ in Alloy 5 to about 96% vol. fraction and 4% volume fraction coarse particles (the α phase).

As Table 4.5 shows Alloy 3 also contains about the same amount of γ′ and β phases in all three different conditions.

It was not possible to determine the volume fractions of β and α phases in the eutectic region in the as-cast condition of Alloy 4 and Alloy 5, because the particles were not big enough.

Table 4.5 also shows that the volume fraction of γ′ phase increases while the volume fraction of β decreases correspondingly from Alloy 1 to Alloy 3. In the hafnium-containing alloys the as-cast state of Alloy 5 contains a higher volume fraction of γ′ than the as-cast state of Alloy 4.

4.4. Hardness Measurements

The microhardness measurements have been made on the γ' and β phases at room temperature as an indication of the strength difference between the γ' and β phases and of the effects of tantalum and hafnium on the strength of γ' phase.

The microhardness results are shown in Table 4.6. Measurements on the β phase in Alloy 3 could not be made, because the sizes of the β phase particles were not large enough. It was also not possible to measure the microhardnesses of the β phase in Alloy 4 and Alloy 5, in the as-cast state, for the same reason.

As Table 4.6 shows the microhardness of the β phase in Alloy 1 has dropped sharply after homogenisation, compared to the as-cast state (about a decrease of 30%). In Alloy 2, there is no significant difference in the hardness of β phase in the as-cast and homogenised conditions, in contrast to the case of Alloy 1. There is also a decrease (about 13%) in microhardness of γ' in Alloy 1 after homogenisation compared to its as-cast state. However after ageing treatment the microhardness of γ' phase has increased about 8%, compared to the homogenised state, in Alloy 1. In Alloy 2 also, after ageing treatment, while the microhardness of γ' phase has increased (about 6%), the microhardness of β phase has decreased (about 5%).

The heat treatments did not change the microhardness of γ' phase in Alloy 3. The microhardness of γ' in Alloy 3 is higher than that of γ' and β phases in Alloy 1 and Alloy 2 (except the microhardness of β phase in the as-cast state of Alloy 1).

In the hafnium-containing alloys, the microhardness of γ' phase in Alloy 4 is higher than that of γ' phase in Alloy 5, in the as-cast state (about 15%) the γ' phase in Alloy 4 is also harder than that of Alloy 3 (about 20%). The microhardness of γ' has increased after homogenisation

treatment compared to the as-cast state, in Alloy 5.

Table 4.6. Microhardness data Load = 100 grames

ALLOY	Treatment	Hardness Value	
		γ' phase	β phase
ALLOY 1	As-cast	534	707
	Homogenised	463	494
	Homogenised + Aged	501	482
ALLOY 2	As-cast	499 (Eutectic region)	513
	Homogenised	476	501
	Homogenised + Aged	504	476
ALLOY 3	As-cast	582	-
	Homogenised	581	-
	Homogenised + Aged	575	-
ALLOY 4	As-cast	708	-
ALLOY 5	As-cast	612	-
	Homogenised at 990°C for 4 days, wq	642	-

The microhardness data of γ' phase in the tantalum- and hafnium-containing alloys are plotted as a function of the tantalum and hafnium contents of γ' phase (fig. 4.4). As fig. 4.4 shows hafnium has increased the microhardness of γ' phase more than tantalum did.

"Macrohardness" measurements as a function of ageing time have also been made on Alloy 2 and Alloy 3 in order to determine the effect of ageing on hardness and to relate this to the flow stress behaviour of each alloy. For this, each alloy has been homogenised in the two phase region ($\gamma' + \beta$) at 1260°C for 48 hours and water quenched. After

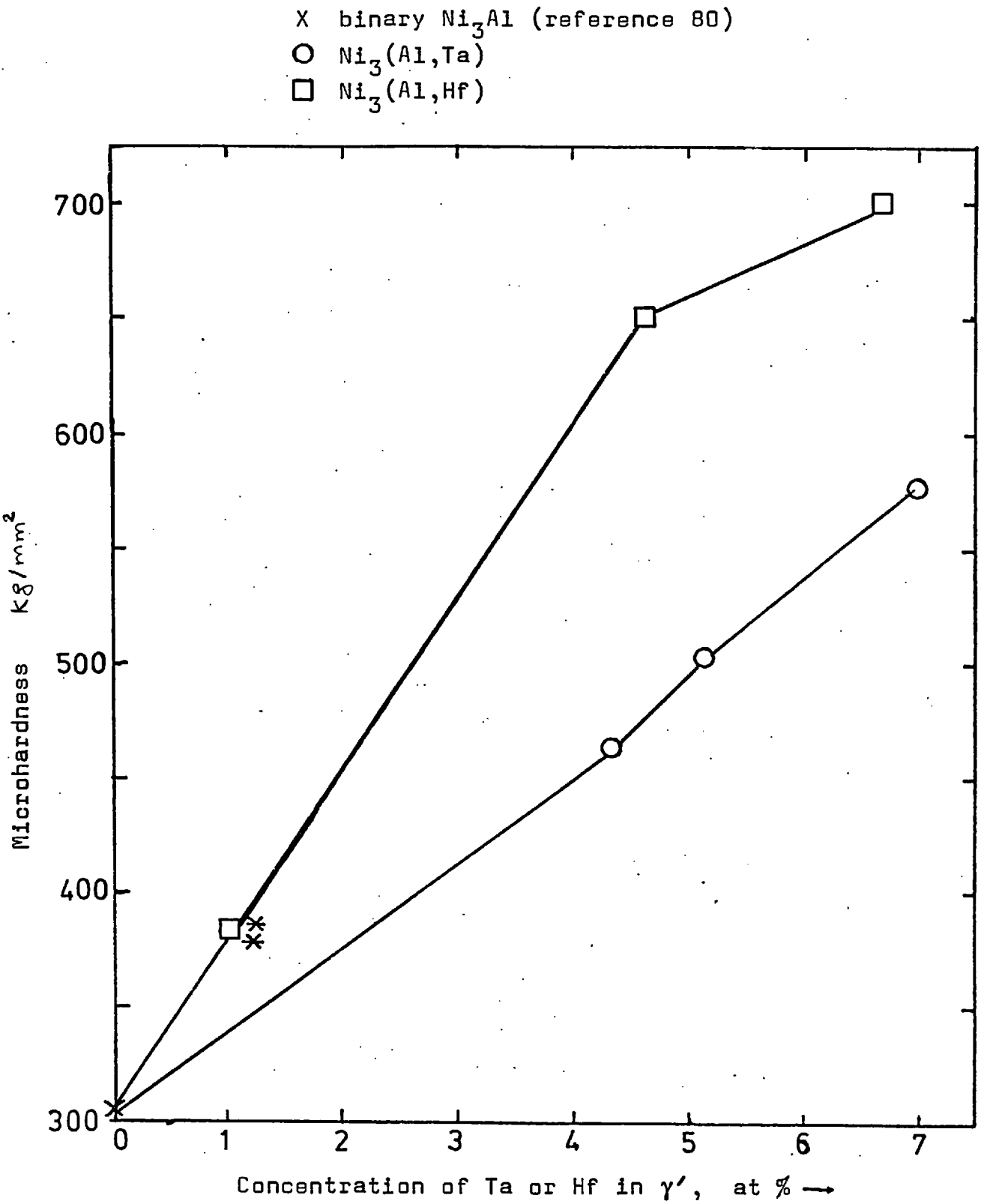

Fig. 4.4. The effects of tantalum and hafnium on the microhardnesses of γ' phases.

‡ This alloy was prepared by Dr S. Chakravorty.

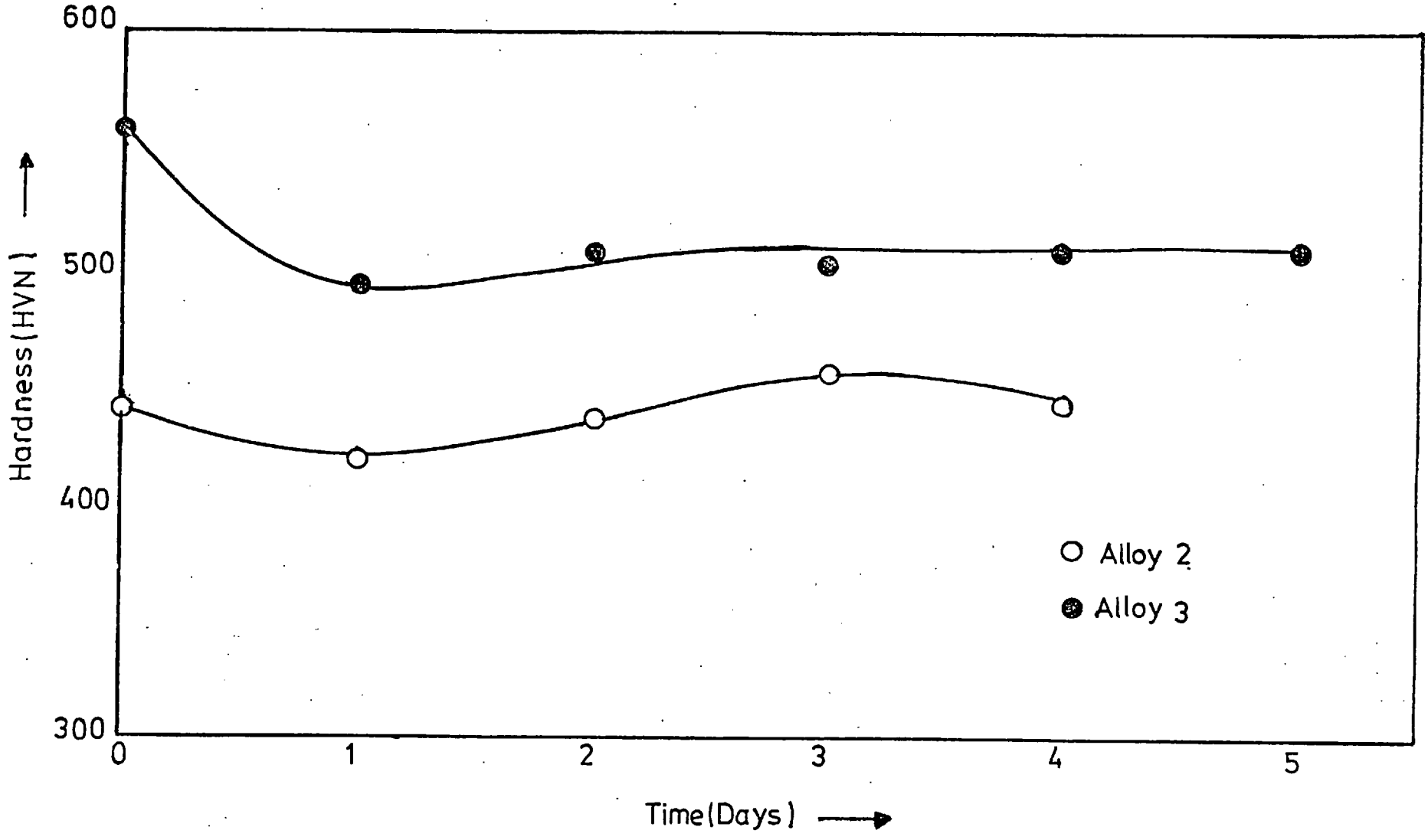

Fig. 4.5

homoganisation each alloy has been reheated at 1000°C for various times and water quenched. The results are shown in fig. 4.5. As this figure shows there is no significant change in hardnesses of Alloy 2 and Alloy 3 at different ageing times.

4.5. As-cast State of Alloys

Fig. 4.7 shows the overall morphological features of Alloy 4 and Alloy 5, in their as-cast states. This figure suggests that these alloys had undergone a eutectic reaction during solidification. Transmission electron microscopy has been applied to analyse and study the structure and morphology of the eutectic regions. It has been found that the eutectic regions in both alloys consist of two phases; i.e. β phase plus a phase designated α. The α phase has been determined to have a hexagonal structure. The lattice parameters of this phase has been determined by x-ray diffraction (sec. 4.2). Some examples of selected area electron diffraction patterns are shown in fig. 4.6. These confirm the x-ray results given in sec. 4.2. Fig. 4.11 shows that the β phase in the eutectic regions of Alloys 4 and 5, in their as-cast states, has the B2 structure.

Figs. 4.8 and 4.10 show two typical morphological features of eutectic regions from different parts of Alloys 4 and 5. Fig. 4.8(d) and 4.10(b) show low resolution dark-fields taken from the $(0001)_\alpha$ and $(\bar{1}011)_\alpha$ diffraction spots respectively. These show that the lamellar type structure (brighter) in fig. 4.8(a) and the rounded particles in fig. 4.10(b) are from the α phase. The remainder of the regions is β phase. Fig. 4.8(b) shows a diffraction pattern with the $[111]_\beta // [2\bar{1}\bar{1}0]_\alpha$ zone axis from fig. 4.8(b). This has been indexed in terms of β and α phases (fig. 4.8 (c)) and it shows that the $(0001)_\alpha$ plane is parallel to the $(1\bar{1}0)_\beta$ plane. From this, the orientation relationship of β and α phases was determined to be:

$$(1\bar{1}0)_\beta // (0001)_\alpha$$
$$[111]_\beta // [2\bar{1}\bar{1}0]_\alpha$$

This orientation relationship is sometimes called the Burgers relation.

The as-cast states of Alloys 1 and 2 also show a eutectic type structure (fig. 4.12; 4.14), which consists of γ' plus β phases. The γ' phase is continuous whereas the β phase exists as particles in the continuous γ' matrix in the eutectic region. In the as-cast state of Alloy 2 (fig. 4.14), eutectic regions predominate in the structure compared to the volume fraction of "primary" β phase, whereas in the as-cast state of Alloy 1 the situation is the reverse (fig. 4.12(a)). The as-cast state of Alloy 3, unlike those of Alloys 1 and 2, does not show a eutectic-type structure. Fig. 4.13 shows β particles in the γ' matrix in the as-cast state of Alloy 3. Fig. 4.15 shows a micrograph from the as-cast state of Alloy 3. If the corresponding selected area diffraction pattern (fig. 4.15(b)) is interpreted as the superposition of the $(1\bar{1}\bar{1})_{\beta}//(0\bar{1}\bar{1})_{\gamma'}$ zone axes (fig. 4.15(d)), then in the high-resolution dark field (fig. 4.15(c)) from a $(11\bar{1})_{\gamma'}//(110)_{\beta}$ spot, those needle-like particles could be γ' precipitate particles in the β matrix. The size of these particles is up to 500Å width. Such γ' precipitate particles have not been observed in β phase of Alloy 1 and Alloy 2, in their as-cast states during the investigation by transmission electron microscopy.

4.6. Characterisation of Microstructure of Tantalum- and Hafnium-containing Eutectics

Fig. 4.7 shows the general features of the eutectic structures at low magnification in Alloys 4 and 5, in their as-cast states. Electron microscopy work has been applied to study the morphological features of the eutectic phases. Two distinct microstructural features have been observed:

(i) Lamellar-type microstructure (fig. 4.8)
(ii) Discontinuous eutectic (fig. 4.10).

Fig. 4.8(a) is an electron micrograph illustrating

the degree of parallelism of the lamellar structure at high magnification. However, at low magnification the lamellae are not quite straight and parallel to each other and they appear to be smoothly curved (fig. 4.7). The lamellae are not always continuous (fig. 4.9(a) and 4.9(b) at A and B). In these figures (fig. 4.9(a) and (b)) it will be noted that the lamellae are broken. On further examination it is seen that the lamellae on either side of A-B line in fig. 4.9(b) are shifted slightly with respect to each other. Similar morphological features have been termed "lamellar terminations" (discontinuous lamellae) in the literature[67].

In discontinuous eutectic, the micromorphology consists of one phase (β phase) which is continuous throughout the eutectic region and in which is dispersed the second discontinuous phase (α phase) in Alloys 4 and 5 (fig. 4.10). In the case of the as-cast state of Alloys 1 and 2, the eutectic-type regions consists of γ′ phase which is continuous throughout the eutectic region and in which the β phase is dispersed (fig. 4.12 and 4.14).

4.7. The Structural features of Alloy 5 after heat treatment

The homogenisation treatment of Alloy 5 at 990°C for 4 days followed by water quenching led to the disappearence of the eutectic type structure (fig. 4.17). Using transmission electron microscopy no evidence of β phase was found, but there were coarse α particles existing in the γ′ phase matrix (fig. 4.16; fig. 4.17). Fig. 4.16(b) shows a selected area diffraction pattern from an α particle (fig. 4.16(a)) which corresponds to the hexagonal structure previously found in the as-cast structure of Alloy 5. Fig. 4.16(a) shows the microstructure characteristic of the interior of an α particle. Selected-area diffraction information has been obtained in order to determine the nature of the striations in the α particle (fig. 4.16(a)). A selected area electron diffraction pattern (fig. 4.16(b)) from this particle shows continuous streaking normal to the striations in the particle (fig. 4.16(a)). The

thinness of the faults which are represented by these striations apparently relaxes the Laue condition for the direction perpendicular to the plane of the faults. The streaking is along the $[0001]_\alpha$ direction in reciprocal space, suggesting that these striations, which represents the fine planar faults, lie on the (0001) basal plane which is the fault plane. The streaks are continuous from one spot to the next, suggesting that the alternating planar fault plates may be only one or two atoms thick and these planar faults are seen "on edge". These fine, planar faults which lie on the (0001) basal plane are interpreted as stacking faults.

4.8. Ageing Treatment

The tantalum-containing alloys (Alloys 1, 2 and 3) after ageing at 1000°C for 3 days and water quenching have shown large γ' precipitates in the β phase. Fig. 4.18(a) shows a light micrograph from Alloy 1 in the aged condition. Fig. 4.18(b) shows rod-like γ' precipitate particles 30-60 μm long and 10-20 μm in diameter, in β phase. The morphology of the precipitate particles may be deduced from an examination of fig. 4.18(a). They are mainly rod-like and equiaxed shapes.

As determined by x-ray diffraction (sec. 4.2) the γ' precipitates in β phase and the β phase, after ageing at 1000°C for 3 days and quenching, have $L1_2$ and B2 structures respectively.

4.9. Structure and Morphology of β Martensite

4.9.1. Homogenisation Treatment

The standard homogenisation treatment of 48 hours at 1260°C followed by water quenching was employed for the tantalum-containing alloys (Alloys 1, 2 and 3). The alloys were in the (γ' + β) region at 1260°C. This heat treatment produced a martensitic structure in the β phase in Alloys 1 and 2 (figs. 19 and 20; fig. 4·30) and a retained β structure in Alloy 3 (fig. 4.21(d)). Transmission electron microscopy showed that no untransformed β phase was present in Alloys 1 and 2, all selected area diffraction patterns being readily indexed in terms of a body centred tetragonal (BCT) structure. The diffraction patterns have been indexed in terms of the lattice parameters determined from the x-ray results (Table 4.4). Indexed examples of selected area diffraction patterns are shown in fig. 4.22.

Fig. 4.19 shows the morphology of β martensite in Alloy 1. This figure shows parallel martensite plates in three groups in various β particles (e.g. at A, B and C). A sample of Alloy 1 was homogenised at 1350°C for 5 hours to obtain a higher proportion of β phase and hence of β martensite (fig. 4.20). From a close examination of the martensite structure in fig. 4.20 it is found that the microstructure is composed of three different "groups". In fig. 4.20 these three groups are indicated by the capital letters B, D and E within an original β grain. However, in the smaller β grains apparently only one group of martensite plates exists (fig. 4.19 at D, fig. 4.31). This may suggest that the number of martensite plate groups increases with increasing size of β grains. Fig. 4.20 also indicates that the martensite plates in one group have straight and parallel-sided boundaries (the interfaces between the martensite plates are quite regular, straight), whereas in another group in the same grain the martensite plate boundaries are not as straight- and parallel-sided. This parallel-sided martensite plate morphology has also been observed in some non-ferrous martensites, i.e. in Cu-Zn, In-Tl. As may be seen in fig. 4.20 at B and C the martensite

plates are arranged in alternating fashion. As may be seen from the contrast in each martensite group the neighbouring martensite plates alternate in two variants. The ratio of the widths of these alternating neighbouring plates changes from group to group. This ratio remains approximately constant throughout each group.

Transmission electron microscopy has also been applied to study the substructure of the martensite. Analysis of electron micrographs has shown the following characteristic types of martensite subgrain structure:

(i) Parallel- and straight-sided plates or banded-like morphology (fig. 4.24(d), 4.24(e), 4.25, 4.27(d)).

(ii) Acicular-type martensite (fig. 4.28).

The acicular-type martensite morphology has been observed in Alloy 1 but not in Alloy 2, in their homogenised states. However, the predominant feature of β martensite in Alloy 1 is the type mentioned in (i). The type (ii) exists to a much less extent. In fig. 4.25, in a martensite plate group, the ratio of the widths of alternating neighbouring martensite plates is about 1:1, whereas in fig. 4.24(d) and 4.24(e) the ratio is about 1:2.

The diffraction data from fig. 4.25(a) has shown an essentially single crystal pattern, and in dark field a single reflection can be seen to be produced by a large number of neighbouring plates (fig. 4.25(b)). These results suggest that the misorientations across the martensite plates boundaries are of the low angle type.

A considerable difficulty is encountered in the interpretation of the diffraction data from β martensite because some of the diffraction maxima are extended (due to the relaxation of the Laue conditions) in certain directions from one reciprocal lattice reflection to another. This results in an apparent continuous range in d-spacings and angles between certain crystal planes

(fig. 4.29). In order to obtain unambiguous patterns the specimens had to be oriented such that the extension of reciprocal lattice points (streaks) lay in the plane of the diffraction pattern (fig. 24(f), fig. 4.24(g)). The positions of the intensity maxima in planes containing the streaks are then accurately determined. The diffraction streaks were found to be always perpendicular to the striations observed on the micrographs. This direction and the complete continuity of streaks indicates that the thicknesses of the faults which are represented by the striations are a few atoms thick.

Fig. 4.23(a) shows a bright field micrograph from β martensite in Alloy 1. This micrograph shows that a martensite plate is internally striated; the striations represent a stack of fine twins. The contrasts produced by these twins are due to the difference in orientation between the twinned and untwinned portions of the martensite plate. If the twins allow a considerable portions of the incident beam to pass through the objective aparture and the untwinned portions are in such an orientation to diffract the majority of the incident electrons away from the aparture, the twins should appear light against a dark background, while if the conditions are reversed the twins should appear dark against a light background as shown in fig. 4.23(a). The twinning plane was found by tilting the specimen until the plane was parallel to the electron beam. Indexing of the diffraction pattern of fig. 4.23(b) is shown in fig. 4.23(c). This indicates that the twinning plane is a $(101)_{BCT}$ plane. It may be noted here that, as in the case of martensites in copper-based alloys[144], the internal twinning of the martensite plates occurs throughout their section. This contrasts with the frequent occurrence of partially twinned martensite plates in ferrous alloy martensites. The detection of internal twinning with the aid of the electron microscope is very dependent upon the orientation of the martensite plates with respect to the electron beam. For a stack of fine twins arranged parallel to the electron beam, strong contrast will be observed.

The internal striations in the alternating neighbouring plates have been observed to exist in two orientations (fig. 4.27(a), fig. 4.24(a)). These striations in different orientations suggest that they either represent different variants of the (101) twinning which is already identified, or they are different faults existing in the alternating martensite plates. The internal striations in fig. 4.24(a) have been given special attention. The selected area diffraction pattern, fig. 4.24(f), from the martensite plate A shows streaks along the $(0\bar{1}1)$ plane normal which is perpendicular to the striations in Plate A. This suggests that these striations in martensite plate A represent the fine planar faults lying on the $(0\bar{1}1)_{BCT}$ plane. The selected area diffraction pattern (fig. 4.24(g)) from the martensite plate B also shows the streaks along the (101) plane normal. which is perpendicular to the faint striations in plate B in fig. 4.24(a). This observation also suggests that these faint striations in martensite plate B represent the fine planar faults lying on the (101) plane. As these observations indicate, the alternating martensite plates in fig. 4.24(a) are internally faulted on the two variants of the {101} type plane which is already identified as the twinning plane. Fig. 4.24(b) shows the selected area diffraction pattern from both sides of the A/B martensite plates in fig. 2.24(a). This diffraction pattern has been indexed in terms of the $[\bar{1}11]_{BCT}$ zone axis; but it also contains some extra spots which were interpreted in terms of the twin spots. There are two possibilities for these extra spots to occur:

i) The A/B martensite plates are twin-related to each other. Then the A/B interface should be "edge on". The twin plane is the (101) plane.

ii) The striations in the martensite plate B in fig. 4.24(a) are twinning faults and the twinning plane is the (101). This is possible since the faint striations in plate B have been observed to represent a fault lying on the (101) plane.

The possibility (ii) seems unlikely since the diffraction pattern from the martensite plate B did not show these extra spots (fig. 4.24(g)). Therefore the martensite plates A/B are twin-related to each other and the twinning plane is the $(101)_{BCT}$ plane; the boundary A/B lies on this plane.

The streaks in two directions in fig. 4.24(b) are probably a result of the thinness of the planar faults in the martensite plates A and B, as observed in the diffraction patterns from an individual martensite plate (fig. 4.24(f), fig. 4.24(g)).

Fig. 4.26(a) shows an interesting electron micrograph. An unusual feature of this micrograph is that each martensite plate is striated in two directions. The selected area diffraction pattern from fig. 4.26(a) has been indexed in terms of the $\approx[1\bar{1}1]_{BCT}$ zone axis (fig. 4.26(b), fig. 4.26(c)). The extra spots in the diffraction pattern may be indexed in terms of the twin spots (fig. 4.26 (c)) from the faults such as in A-A in fig. 4.26(a). Then the twinning plane is the $(\bar{1}01)$ which is consistent with the twinning plane found in fig. 4.23. But the stronger diffraction spots (fig. 4.26(b)) appear to be composed of a series of subsidiary satellite maxima. Similar diffraction patterns have been observed by Gevers et al (1966)[173] and Fitzgerald (1966)[174]. Gevers et al have claimed that the satellite spots are due to a dynamic interaction between electron beams (two beams or multiple beams) diffracted by a family of planar defects inclined to the incident electron beam. The satellite spots, termed "dynamical spots", are situated near the strongly diffracting reflections and their number is proportional to the number of strongly diffracting beams. Judging from the twin symmetry in the diffraction pattern in fig. 4.26(b), the twinning plane is very near to exact parallel orientation. However, as multiple satellite reflections are observed, the fault plane is evidently inclined to the beam. This evidence suggests that the faults in A-A and B-B lie very near to exact beam orientation. Therefore these faults are approximately

"edge on". If the $(\bar{1}01)$ plane is taken as the fault plane for A-A faults the angle between the traces of faults in A-A and B-B faults (as the faults are approximately "edge on" this angle represents the true angle between these two faults) suggests that the faults on B-B lie on the (011) plane. The selected area diffraction pattern (fig. 4.26(b)) from fig. 4.26(a) shows streaks in two directions. This suggests that the faults in A-A and B-B are fine, plate-like faults. Although these streaks are not continuous in reciprocal space they seem to lie approximately along the $(\bar{1}01)$ and (011) plane normal, which are approximately perpendicular to the striations on A-A and B-B respectively. From this observation it seems that the two variants of the {101} type faulting system exist within one martensite plate. Similar observations have been reported[144,147,149] to occur within one martensite plate in Cu-Sn and Cu-Al martensites.

Fig. 4.27(a) shows a bright field from β martensite in Alloy 2. In this micrograph the neighbouring martensite plates show the internal striations in two different directions as in fig. 4.24. The corresponding diffraction pattern (fig. 4.27(b)) may be indexed in terms of the zone axis $[121]_{BCT}$ (fig. 4.27(c)). The diffraction pattern shows streaks in two directions, which are probably due to the thinness of the faults lying on two planes in A and B martensite plates. Although the length of the streaks in a reciprocal space may be somewhat abridged due to the non-exact orientation of the crystal, their main shortening is unquestionably due to the thickening of the platelet. The streaks in fig. 4.27(b) are not continuous. As mentioned just now there are two possibilities for this,

- the foil is not exactly the [121] zone axis orientation, the non-symmetrical distribution of the intensity of the diffraction spots suggest this

- the thickness of the faults in A and B martensite plates.

Because of the lack of enough information it was not possible to determine positively the fault planes, an attempt was made to identify it in the following way. First of all it is assumed that these streaks are due to the thinness of the internal faults in the martensite plates. The striations in A and B are not quite perpendicular (few degrees) to the directions of the streaks. This and the intensity distribution in the reciprocal space (fig. 4.27(b)) suggest that the zone axis is not exactly the [121] and the faults are not "edge on". But the satellite spots may suggest that the fault planes are very near to exact "edge on" condition, as mentioned above. Therefore it seems from the directions of the streaks in the reciprocal space and the angle between the traces of faults in A and B martensite plates that the internal faults in the neighbouring A and B martensite plates lie on the $(01\bar{2})_{BCT}$ and $(\bar{2}10)_{BCT}$ planes. Streaks parallel to <210> in the diffraction pattern of an Al-62·5 at % Ni β martensite have been reported recently by Raynaud (1977)[68]. He called these streaks an "anomaly" of martensite. By taking into account also the above discussion these streaks parallel to <210> are probably due to the fine, planar faults in the martensite.

Fig. 4.21(a) shows a bright field from a specimen of the homogenised Alloy 3. The selected area diffraction pattern from the region A indicates that this region consists of γ′ phase (fig. 4.21(c)), whereas the selected area diffraction pattern (fig. 4.21(d)) from the region B indicates that this region is β phase and did not undergo martensitic transformation. The diffraction pattern (fig. 4.21(b)) from the both sides of A/B shows two superimposed diffraction patterns with the $[\bar{1}11]_{\gamma'}$ and $[\bar{1}11]_{\beta}$ zone axes.

4.9.2. Fine precipitate in β phase

A fine precipitate has been observed in the retained β and in the β martensite in the aged at 1000°C and in the solution treated condition of Alloy 1 and Alloy 2 respectively. Fig. 4.32(a) shows a dark field using the (110)

spot. This foil reveals a substructure having a striated or "tweed" appearance. The corresponding selected area diffraction pattern (fig. 4.32(b)) shows streaks parallel to the (110) plane normal. This "tweed" substructure and streaking is evidence of the existence of fine precipitates which are plate-like on {110} planes. The precipitates are located between the "weave" of the "tweed" substructure. Evidence for a fine dispersion of plates on {110} planes in the retained β and in the martensitic phase of binary Ni-Al and Ni-Cr-Al alloys has also been observed by Russell and Edington (1972[47], Moskovic (1974)[25] and Muir (1975)[21].

4.9.3. Morphology of β martensite in as-cast states of Alloy 1 and Alloy 2

The β phase had undergone martensitic transformation in Alloys 1 and 2 during cooling of the ingots after solidification (fig. 4.12, fig. 4.33).

The morphology and fine structure of β martensite in the as-cast structure of Alloy 1 has been given particular attention. Figs. 4.12 and 4.33 show the characteristic feature of β martensite in Alloy 1 and Alloy 2. These micrographs show an acicular-type morphology. Fig. 4.33(b) is the selected area diffraction pattern from fig. 4.33(a) with the indexing in fig. 4.33(c). Fig. 4.33(e) is a low-resolution dark field taken by using the $(110)_{BCT}$ diffraction spot, which indicates that the acicular structure is contributed from the $(110)_{BCT}$ spot, whereas the regions between the acicular structure are contributed from the $(101)_{BCT}$ diffraction spot (fig. 4.33(d)). The diffraction pattern (fig. 4.33(b)) from fig. 4.33(a) shows streaks along the $(110)_{BCT}$ and $(0\bar{1}1)_{BCT}$ plane normals which are perpendicular to the striations at A and B in fig. 4.33(a). These streaks indicate that the striations represent thin, planar faults and lie on $(110)_{BCT}$ and $(0\bar{1}1)_{BCT}$ type planes. In the previous section the $(0\bar{1}1)_{BCT}$ planar faults have been interpreted as twinning faults.

In summarising the above observations and observations made in sec. 4.9.1. it appears that the different fault systems and two variants of the {101} fault system exist in the β martensite.

4.10. Dislocation Structure in γ' Phase

The dislocation structure of γ' phase has been mainly investigated in Alloys 1, 3, 4 and 5. Examination of thin foils of the deformed specimens by transmission electron microscopy revelaed distinct differences in the dislocation structures in the γ' phase for the "low" and "high temperature" deformation respectively. For the purpose of description of the dislocation structure it is convenient to divide the range of testing temperatures into two regions:

i) Low temperature; refers to temperatures below the "peak" temperature of the γ' phase.

ii) High temperature; refers to temperatures above the "peak" temperature of the γ' phase.

As the composition of γ' phase differs from one alloy to another (Table 4.2) it is expected that the peak temperature will be different in each alloy and changes with the degree of non-stoichiometry (sec. 2.12).

4.10.1. Low temperature dislocations

Investigation of deformed γ' phases, at different testing temperatures, has been made to determine the behaviour of dislocations and possible effects on the mechanical properties of the γ' phase.

In this study two distinct types of dislocations have been observed:

i) Dislocations aligned closely along the <110> direction.

ii) Dislocations aligned closely along the <111> direction.

Fig. 4.38(a) refers to a (011) foil from Alloy 3, deformed at room temperature. In this foil the long and straight dislocations must lie in the foil plane, because of their considerable projected length, as compared with

the foil thickness (approximately 1000Å). By comparing with the corresponding diffraction pattern (fig. 4.38(b)) it was found that these long dislocations lie close to <111>. Dislocations closely aligned along <111> directions have also been observed for higher deformation temperatures. Figs. 4.39 and 4.40 show dislocations lying close to <111> directions in Alloy 3 and Alloy 1, deformed at 600°C. Dislocations along the <111> direction also exist in γ' phase of Alloy 4 and Alloy 5, deformed at similar temperatures.

Fig. 4.42(a) shows dislocations lying in the $(\bar{1}12)$ foil plane in Alloy 3 deformed at 600°C. The corresponding diffraction pattern (fig. 4.42(b)) shows that the relatively long and straight dislocations are very closely aligned to the <110> direction. The <110> type dislocations exist also at lower deformation temperatures. Fig. 4.41 shows dislocations in an ≈(001) foil in Alloy 3, deformed at 400°C. In this foil there are two sets of relatively long and straight dislocations which align along the [110] and $[1\bar{1}0]$ directions. In each set, dislocations are parallel to each other and nearly perpendicular to those of the other set. It is possible that these dislocations are from the $(\bar{1}11)$ and (111) type slip planes, assuming the Burgers vector is the b = a<110> type.

A few experimental observations have been made to determine the possible Burgers vector, by using the "invisibility criterion method". As shown in figures 4.43 and 4.44 the dislocations are invisible or nearly invisible with the $22\bar{4}$ and 220 operating reflections which are consistent with the b = a<110> type Burgers vector.

As may be seen in fig. 4.43 the dislocations are aligned along the [110] direction, and the Burgers vector consistent with the b = a[110] type. This suggests that the direction of dislocation line and the Burgers vector are the same [110] direction. This is consistent with screw type dislocations.

The main feature of the dislocations in the alloys investigated for "low temperature" deformation is that they are relatively straight and parallel to each other. For "high temperature" deformation the dislocations lose their straightness and become tangled. These two types of behaviour of the dislocations suggest that different deformation mechanisms operate at "low" and "high temperatures". In Alloys 1 and 5, up to about 600°C, and in Alloys 3 and 4, up to about 700°C, the dislocations keep their straightness and parallelism (fig. 4.40, fig. 4.45). However, in Alloys 1 and 5 above 600°C, and in Alloys 3 and 4 above 700°C, the dislocations have lost their straightness and parallelism (fig. 4.46, fig. 4.47, fig 4.48).

4.10.2. Evidence for Dipoles

Dipoles are dislocations of opposite sign on nearby parallel slip planes. It is rather difficult to distinguish between superpartials (superdislocations) and dipoles. Bell et al (1964)[69] has given methods by which dipoles can be identified. Dislocation pairs which show dotted contrast arising from primary extinction can be determined to have either like or unlike Burgers vectors by comparing the direction in which the maximum to minimum contrast changes occur about the true position of the dislocation. The images of pairs of like sign will both bow out in the same direction while those pairs of unlike sign will bow out in the opposite directions. Fig. 4.34(a) shows this effect. Another method of identifying the dipoles involves the specimen in exciting two diffracted beams so as to observe double diffraction contrast. The secondary images from a dipole will lie either both to the inside or both to the outside of the primary dislocation images (fig. 4.34 (b)).

Figs. 4.49(a) and 4.49(b) show dislocations in γ' in Alloy 3, deformed at room temperature and 600°C. In these micrographs dislocations at A, B and C bow out in the opposite direction. These suggest that these pairs are dislocation dipoles, rather than superpartials.

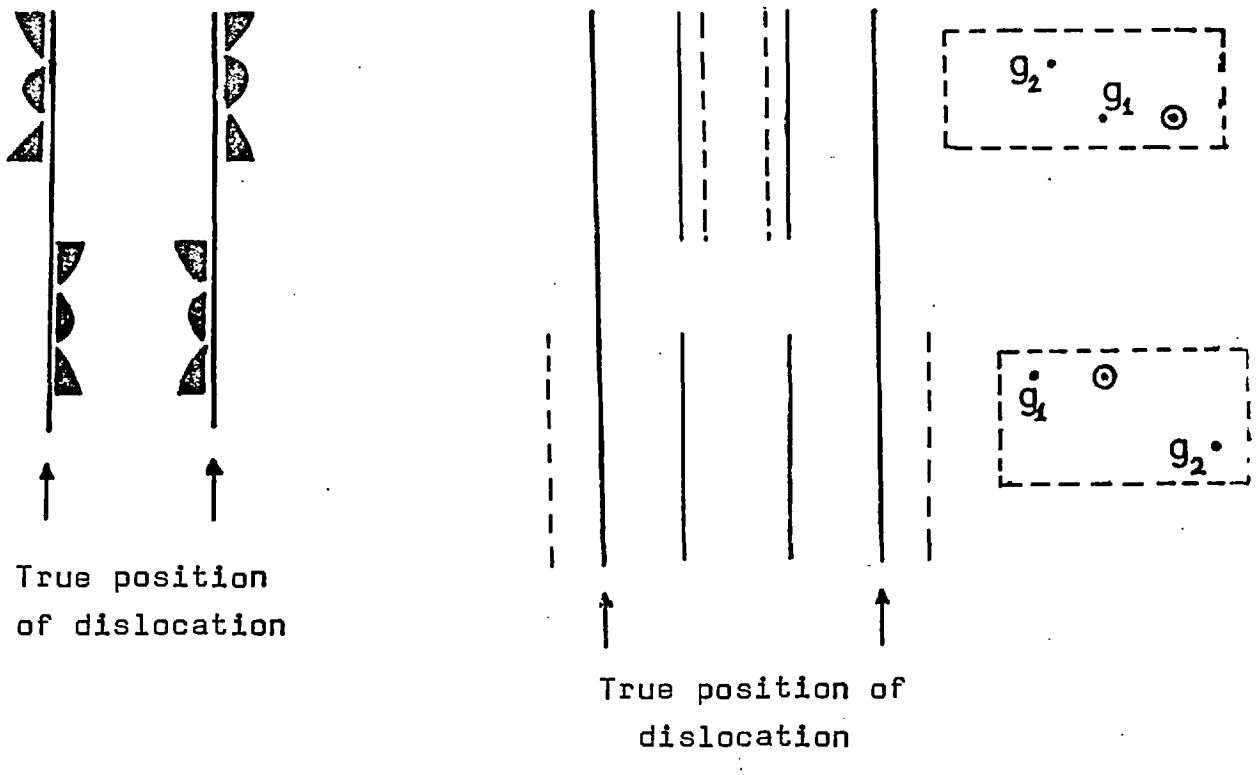

Dotted Contrast (primary extinction)

Double diffraction

(a)

(b)

[After Bell et al (1964)][64]

Fig. 4.34 Identification of dislocation dipoles

In Fig. 4.50 with reference to the dislocations at A, B and C the fact that the contrast changes from light to darker on going from the inside to the outside of the dislocations is clear evidence that these pairs are also dipoles, aligned close to <111> direction.

Fig. 4.45(b) shows dislocations in γ' of Alloy 4, deformed at 700°C, in double beam diffraction conditions, aligned close to <110> direction. As may be seen at A and B, the secondary images from those pairs lie both to the outside of the primary dislocation images, suggesting that those pairs are dipoles.

Fig. 4.51 and fig. 4.42 show dislocations along the <110> direction in Alloy 3, deformed at room temperature and 600°C respectively. From the change of contrast, as mentioned earlier, from inside to the outside dislocation pairs, at A and B they appear that the dislocations are tending to make up dipoles.

The evidence from the observations suggests that two distinct dipoles are present at "low temperatures", i.e. namely the <111> and the <110> oriented dipoles.

4.10.3. Dislocation substructure at "Low" and "High" Temperatures

Fig. 4.51 shows a $[\bar{1}12]$ foil from Alloy 3 deformed at room temperature. The long dislocations lying along [110] could be of the screw type, assuming the Burgers vector to be of the b = a[110] type. A dislocation in the centre of the foil is jogged. There are a number of possibilities for these dislocations to be jogged:

i) Localised cross-slip of part of these dislocations to neighbouring {111} type planes, assuming that a possible slip plane of these dislocations is the {111} type.

ii) The intersection of gliding dislocations with already existing "forest dislocations".

Kear (1966)[70] has suggested that jogs could be created in screw dislocations by a mechanism of localised cross-slip, in a manner shown in fig. 4.35. The movement of such screw dislocations with jogs creates point defects or near edge dipoles depending on the height of the jog[46] (Fig. 4.36).

The other interesting feature of these long dislocations is their tendency to form screw dipoles (at A and B in fig. 4.51). A single dipole of screw dislocations is not stable since the two screw dislocations can be annihilated by slipping in a cross-slip plane[71]. The evidence of the existence of the screw dipoles suggests that it is difficult for screw components of dipoles to cross-slip. Staton-Bevan (1973)[45] also has found evidence of screw dipoles in nickel-rich γ' phase.

An alternative model has been put forward on the formation of dipoles[72]. Tetelman (1962)[72] has objected to the Gilman and Johnston (1962)[46] model on the ground that the trails behind a moving screw dislocation will always be pure edge dislocations and sudden cross-slip of dislocations out of their slip plane are needed. The formation of dipoles proposed by Tetelman (1962)[72] is summarised below:

Two non-parallel dislocations MM' and NN' (fig. 4.37(a)) are slipping in parallel slip planes separated by a distance y. If the Burgers vectors of the dislocations are equal but of opposite sign, the dislocations can lower their energy by reorienting part of their lengths in the slip plane so that PP' is parallel to RR' (fig. 4.37(b)). Both PP' and RR' are mixed. If either the dislocation P'M' or R'N (fig. 4.37(b)) is close to pure screw orientation part of this dislocation (say P'M') might then cross-slip down and join the dislocation R'N at R'. Since P'M' and R'N have opposite Burgers vectors the cross-slip segment will be annihilated leaving a dislocation dipole MPP'R'RN' (fig. 4.37(c)). The dislocation NTT'M' will have a jog TT'. This jogged NTT'M' will move according to the mechanism described in fig. 4.36, or it will form a closed loop as

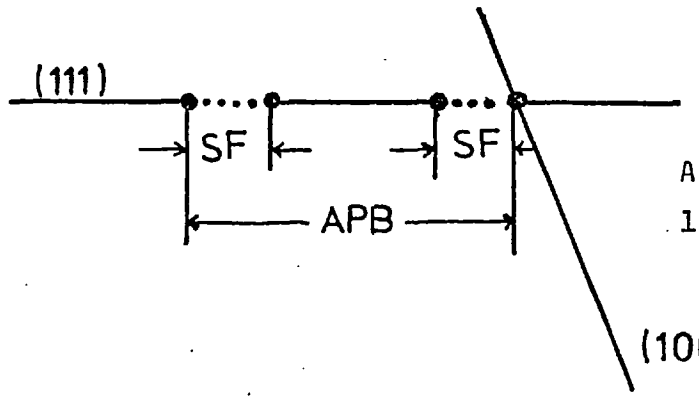

An Extended Super-lattice Dislocation

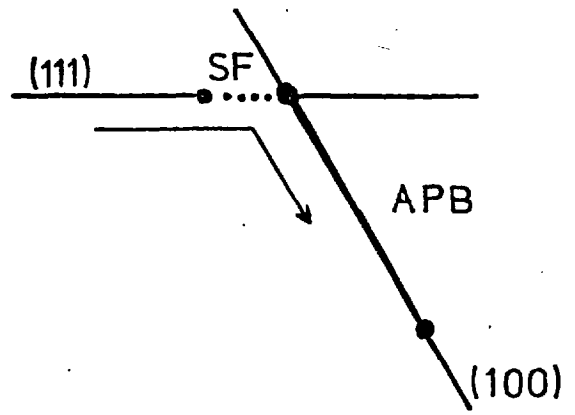

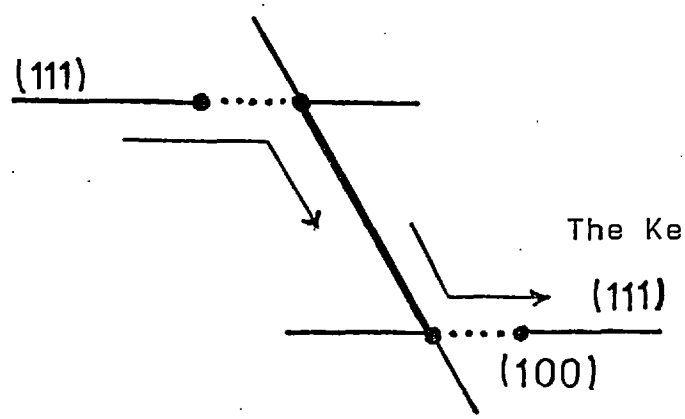

The Kear-Wilsdorf Lock

(After Kear; 1966)[70]

Fig. 4.35

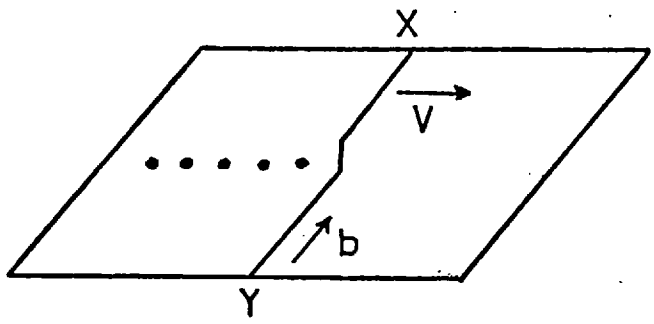

(a) A small jog creates point defects as it moves.

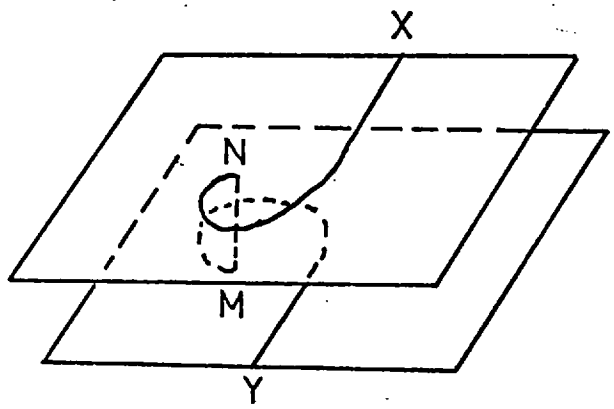

(b) Very large jog. Dislocations XN and MY move independently.

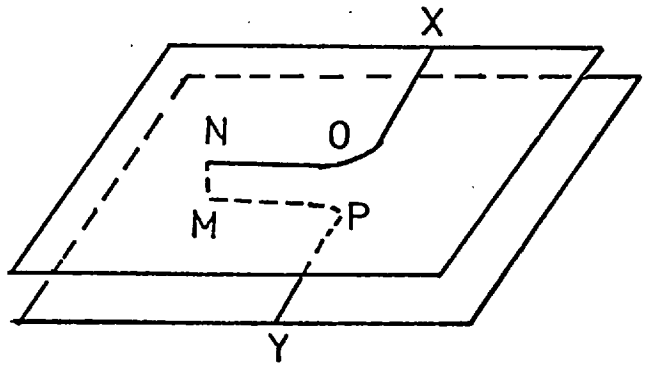

(c) An intermediate jog. The dislocations NO and MP interact and can not pass by one another except at high stresses.

(After Gilman and Johnston;1962)[46]

Fig. 4.36

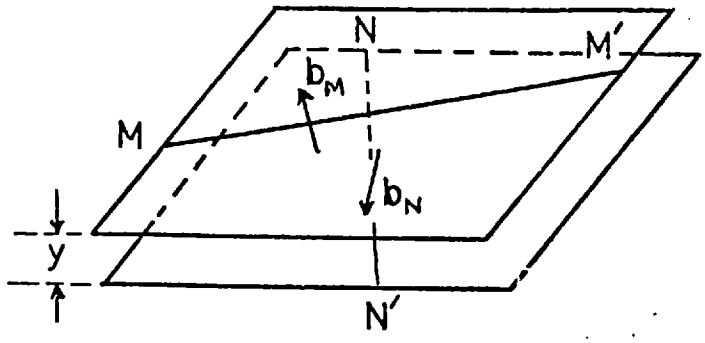

(a) Non-parallel dislocations with opposite Burgers vectors lying in parallel slip planes.

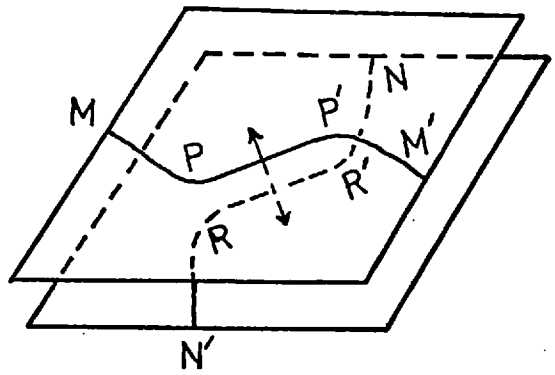

(b) Equilibrium shape of the dislocations MM' and NN'.

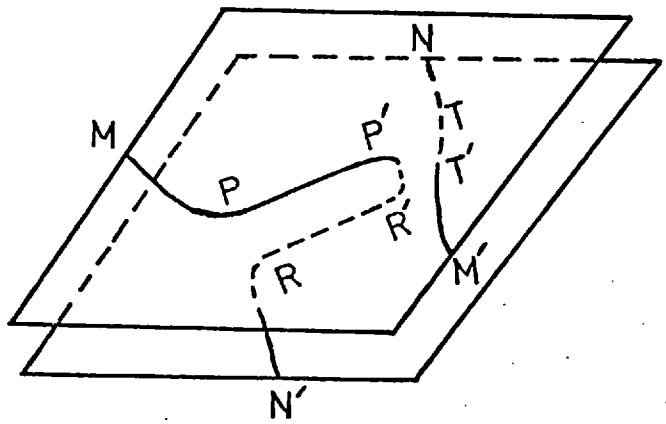

(c) Dislocation M'P' cross-slips down and forms a segment P'R' connecting PP' to RR', producing a dislocation MN' containing a cus p, and a dislocation NM' containing a jog TT' at the point of cross-slip

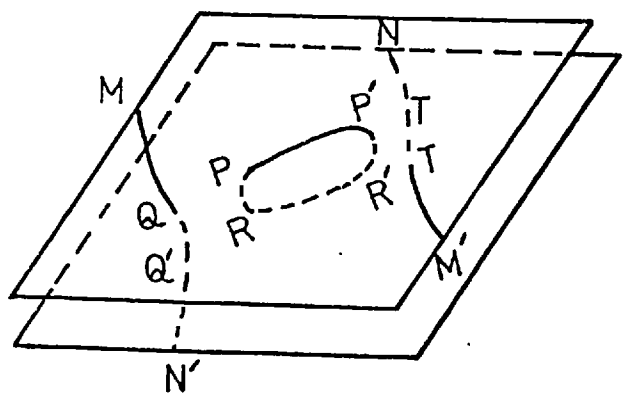

(d) Dislocation segment MP cross-slips down and forms a segment PR connecting PP to RR', producing a close loop PP'R'R and a dislocation MN' that is jogged at the point of cross-slip.

(After Tetelman (1962)[72])

Fig. 4.37

shown in fig. 4.37(d). This model may account for the evidence of mixed dislocations in fig. 4.52 at A, B and C, since the dipoles in this model do not have to be pure edge dislocations, as in the model of Gilman and Johnston (1962)[20]. The long dislocations in fig. 4.52 lie close to the [111] direction. It will be noted that these dislocations exhibit cusps (at C in fig. 4.52). The cusps in these dislocations are frequently associated with resolvable "trails" of roughly mixed dislocations. In some cases these double trails are connected to the cusps (fig. 4.52 at C); in others, the trails appear to have "pinched off" (at A) to form narrow, elongated loops (at B). The jogs and resulting drag on the <111> oriented dislocations, as evidenced by the numerous cusps in these dislocations will make the movement of these dislocations more difficult.

Fig. 4.53 shows a (011) foil from Alloy 3 deformed at 300°C. This foil shows loops elongated along the $[01\bar{1}]$ direction. As mentioned earlier the existence of these loops may be accounted for by the Tetelman model; that is the dipole can break up and lower its overall energy by forming a loop.

At higher temperatures the jogged dislocations have also been observed. Fig. 4.40 and fig. 4.45 show jogged dislocations aligned close to <111> and <110>, in Alloy 1 and Alloy 4, deformed at 600°C and 700°C.

Fig. 4.48 shows a foil from Alloy 3 deformed at 900°C. In this foil the long dislocations lie approximately along [100], suggesting that they are edge type dislocations, assuming that the Burgers vector is the b = a[011] type. In this foil the edge dipoles apparently have collapsed (such as at A), and may have formed loops. The probable mechanism for this dipole to collapse at this temperature (900°C) is that of the climb of one of the edge components into the slip plane of the other, which lowers its overall elastic energy.

In fig. 4.46 the relatively long dislocations lie in the $(\bar{1}12)$ plane about 10° away from the $[\bar{1}11]$ direction. At A dislocations are interacting. In a further stage at B an elongated loop has been formed, probably as a result of dislocation interaction, such as at A, leaving a cusped (or jogged) dislocation at C. This process may be accounted for by Tetelman model, as mentioned earlier.

Fig. 4.6 Selected area diffraction patterns from the hexagonal intermetallic compound (α). Zone axes (a) $[2\bar{1}\bar{1}0]_\alpha$, (b) $[0001]_\alpha$, (c) $[1\bar{2}1\bar{3}]_\alpha$.

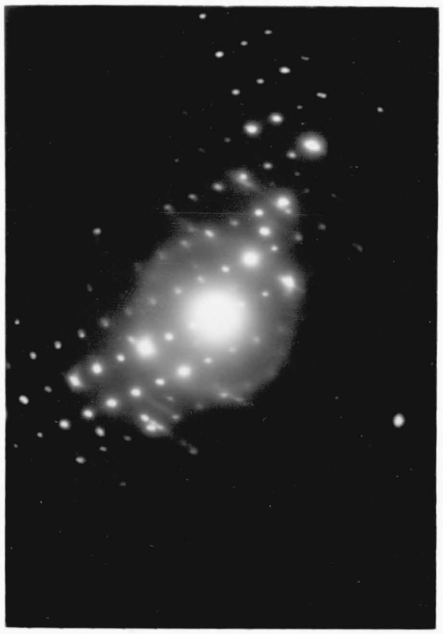

zone axis=$[2\bar{1}\bar{1}0]$

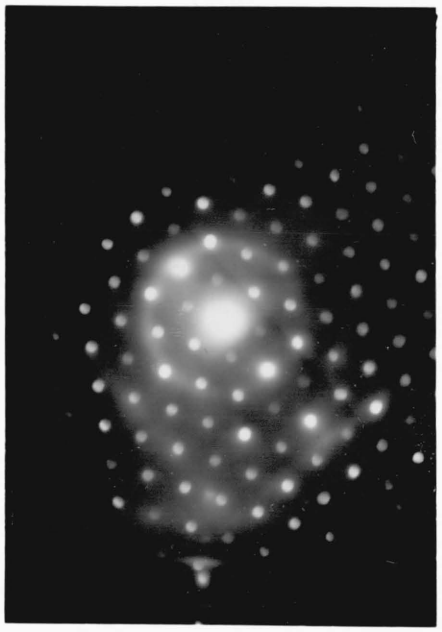

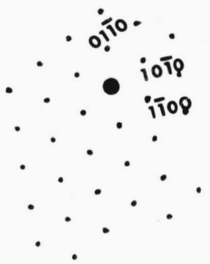

zone axis=$[0001]$

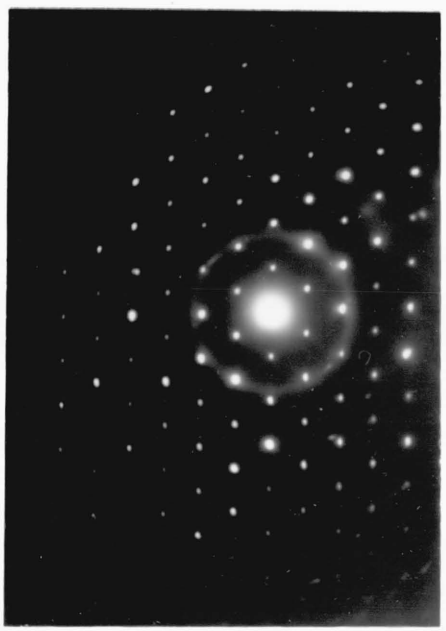

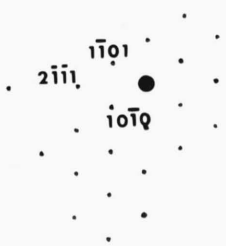

zone axis = $[1\bar{2}13]$

Fig. 4.7. Showing continuous γ' phase (white) and eutectic-type regions which consist of $(\alpha + \beta)$ phases.

a) As-cast condition of Alloy 4
b) As-cast condition of Alloy 5

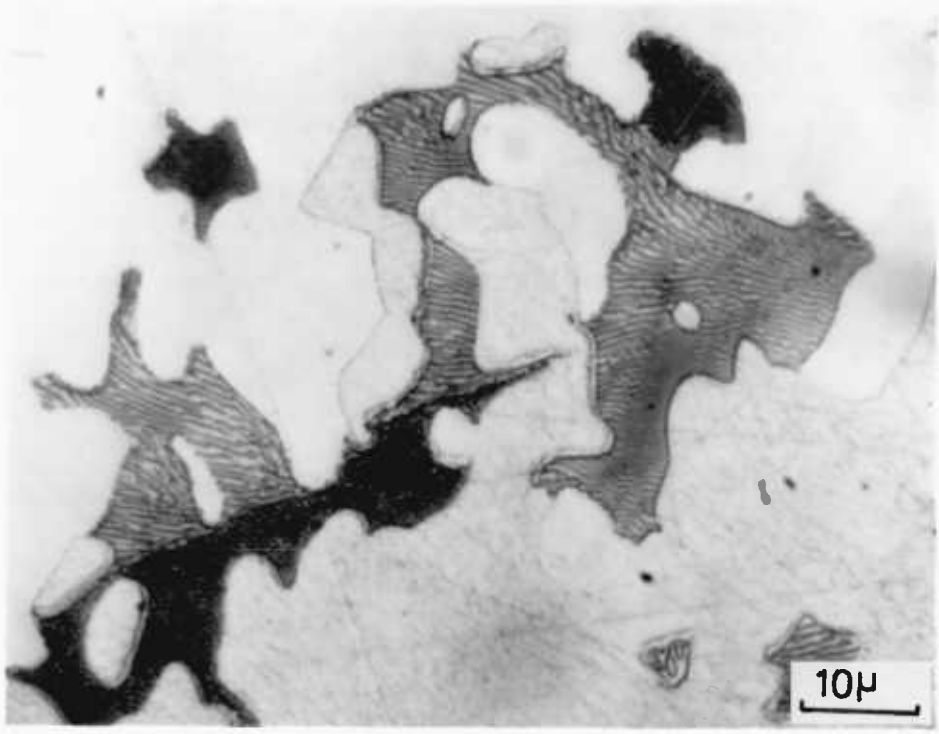

(a)

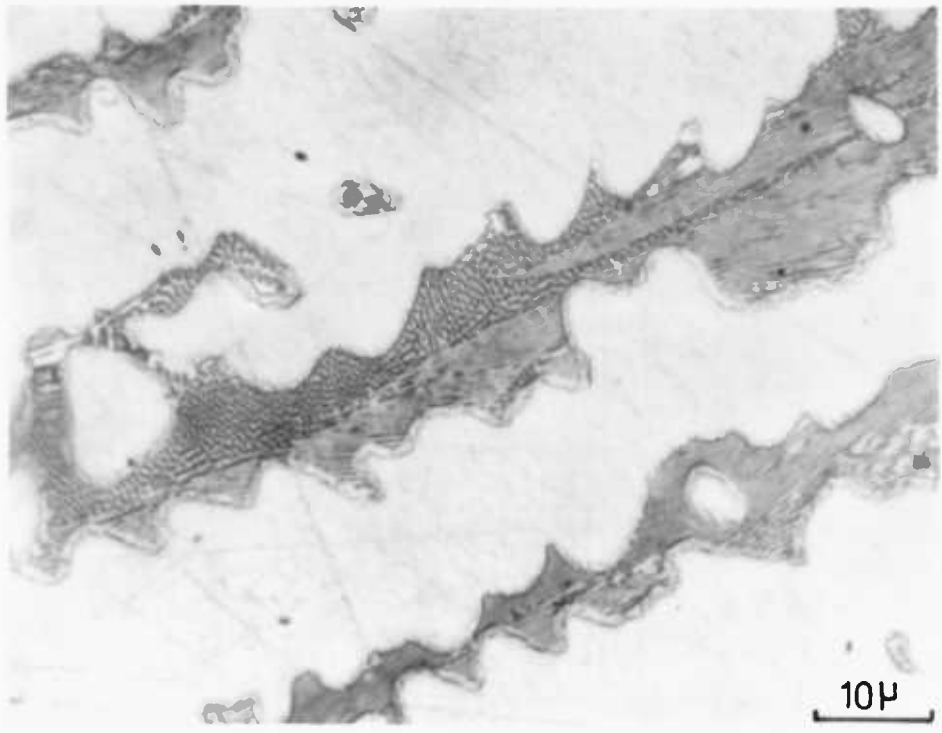

(b)

Fig. 4.8 Showing eutectic structure of as-cast Alloy 4.

a) BF., lamellar structure of eutectic
b) selected area diffraction pattern of (a)
c) indexing of SADP (b)
d) low resolution dark field from $(0001)_\alpha$ spot, showing lamellar α phase (white) and β phase (dark area) between α lamellae.

(a)

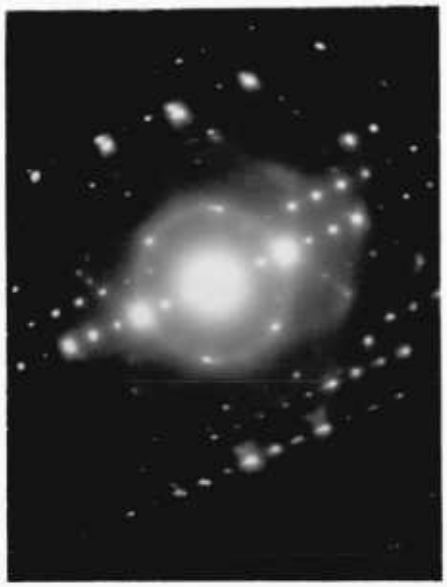

(b)

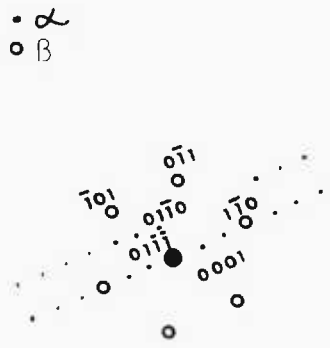

zone axis = $[111]_{\beta} \,//\, [2\bar{1}\bar{1}0]_{\alpha}$

(c)

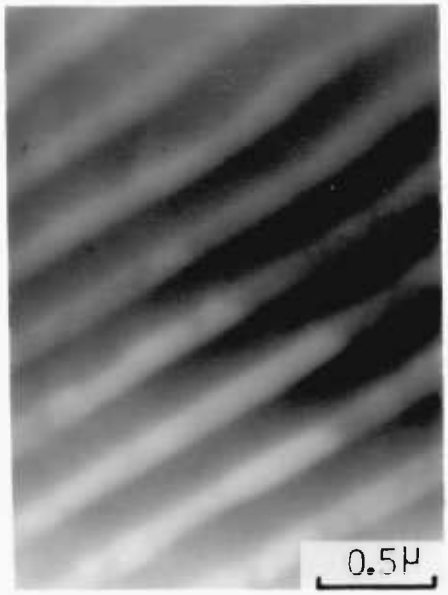

(d)

Fig. 4.9 Eutectic morphology in as-cast state of Alloy 4

a) Bright field, showing extra lamellae and termination of lamellae (at A)
b) Bright field, showing the terminations of lamellae (at A-B)
c) Bright field, showing distorted lamellar morphology.

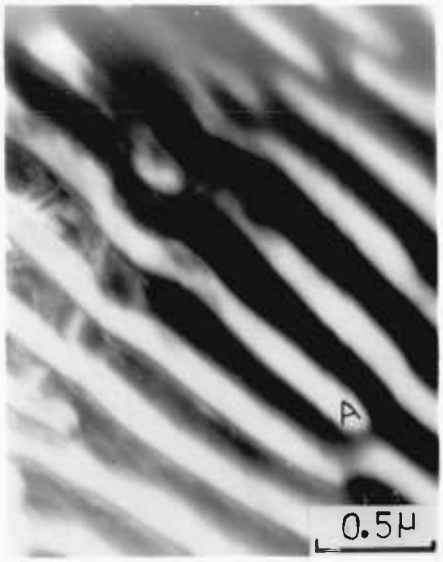

(a)

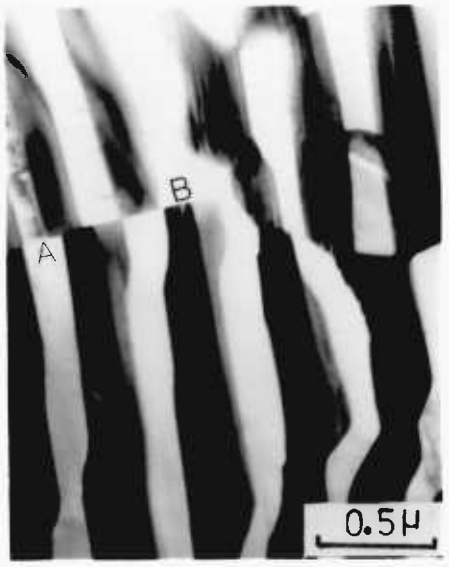

(b)

(c)

Fig. 4.10 Showing discontinuous eutectic morphology from different regions of Alloy 4 and Alloy 5. The particles (white) are from α phase; continuous regions (dark) are from β phase.

(a) and (c) are Bright fields,
(b) is the dark field.

Fig. 4.11 Showing selected area diffraction pattern of β phase in eutectic region of as-cast state of Alloy 4. The as-cast state of Alloy 5 also shows the same structure.

Zone axis = $[111]_{B2}$

(a)

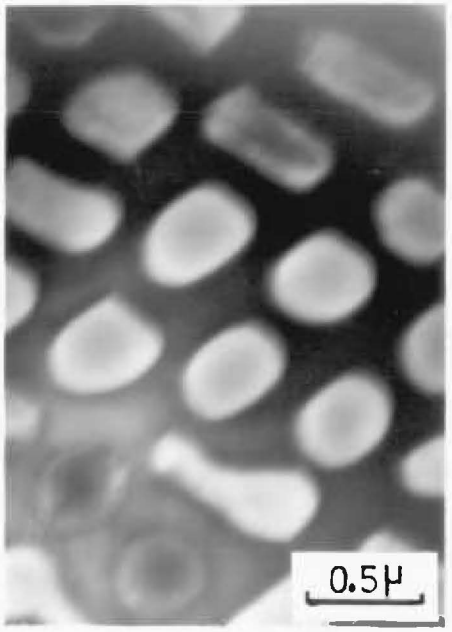

(b)

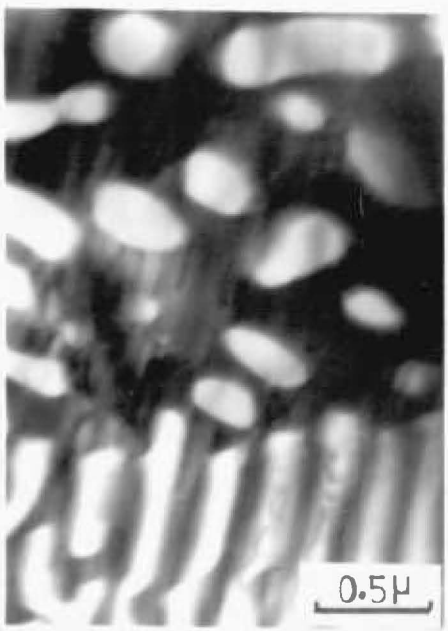

(c)

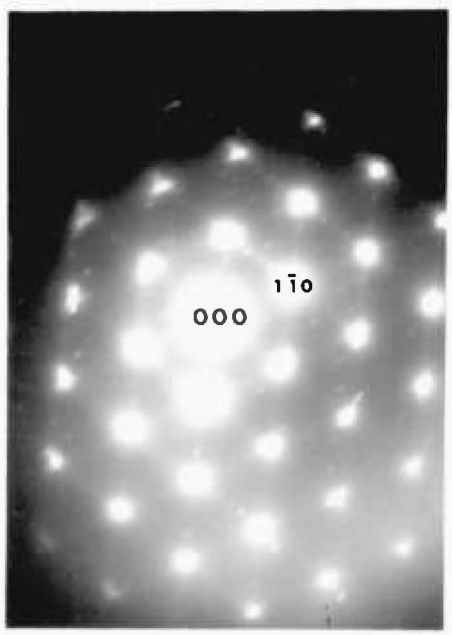

fig. 4.11

Fig. 4.12 Showing "primary" β phase particles (large rounded shape) and eutectic-type regions between these "primary" β particles

a) As-cast state of Alloy 1
b) As-cast state of Alloy 2

Note in the eutectic region the γ' phase is continuous and the β phase is dispersed as particles. The β phase shows acicular-type morphology.

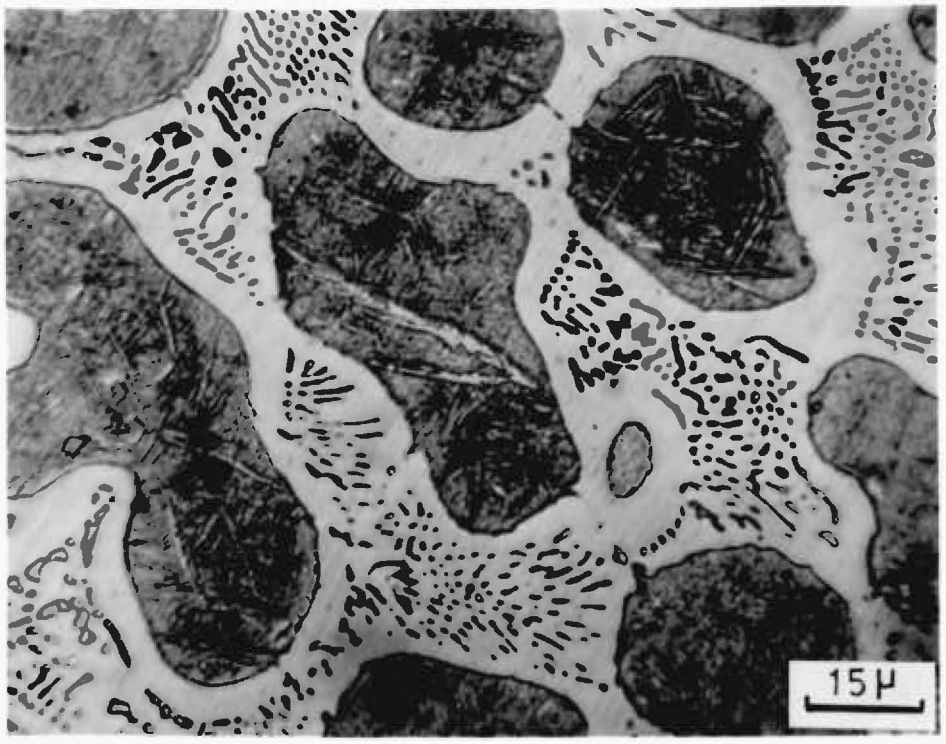

(a)

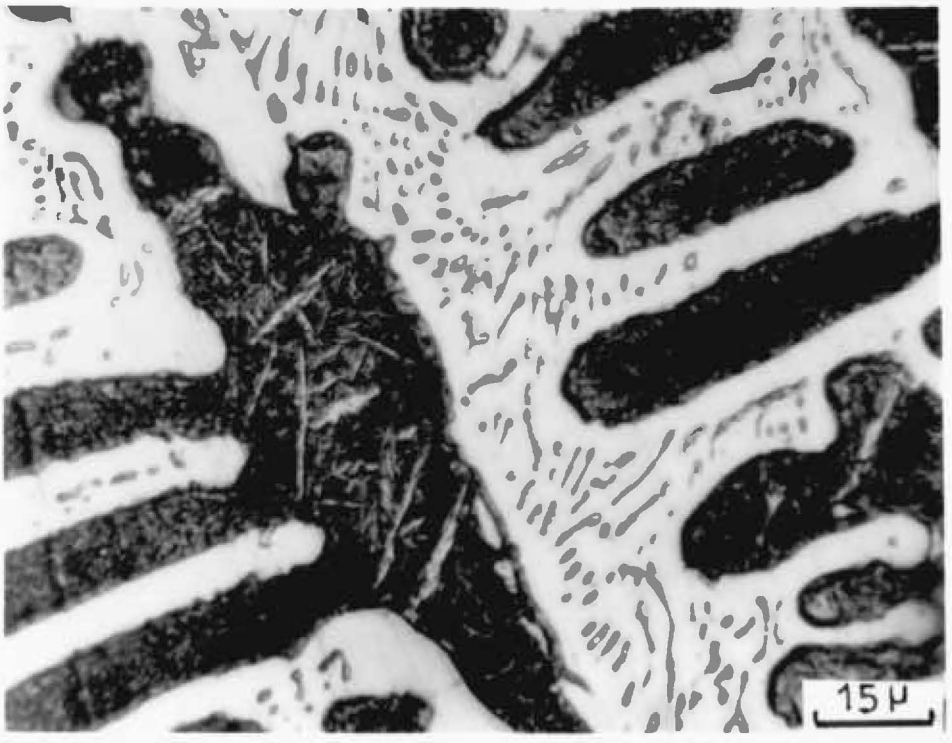

(b)

Fig. 4.13 Showing β particles in the continous γ′ matrix phase in Alloy 3, as-cast state.

Fig. 4.14 Showing eutectic-type structure which consists of (γ′ + β) with "primary" β particles (large dark particles) in as-cast state of Alloy 2.

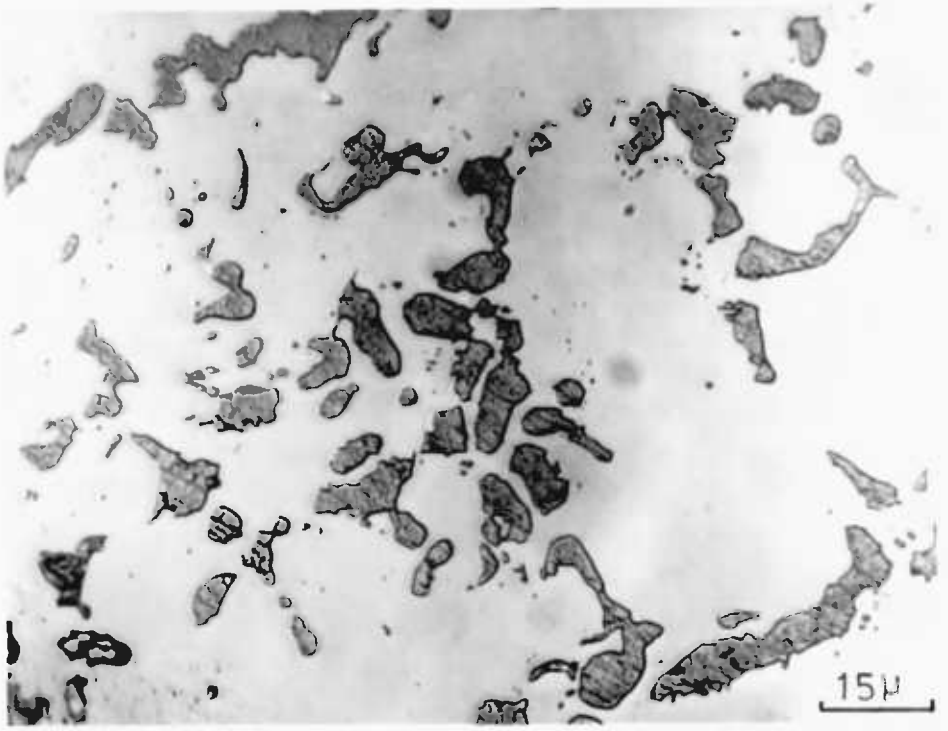
15μ

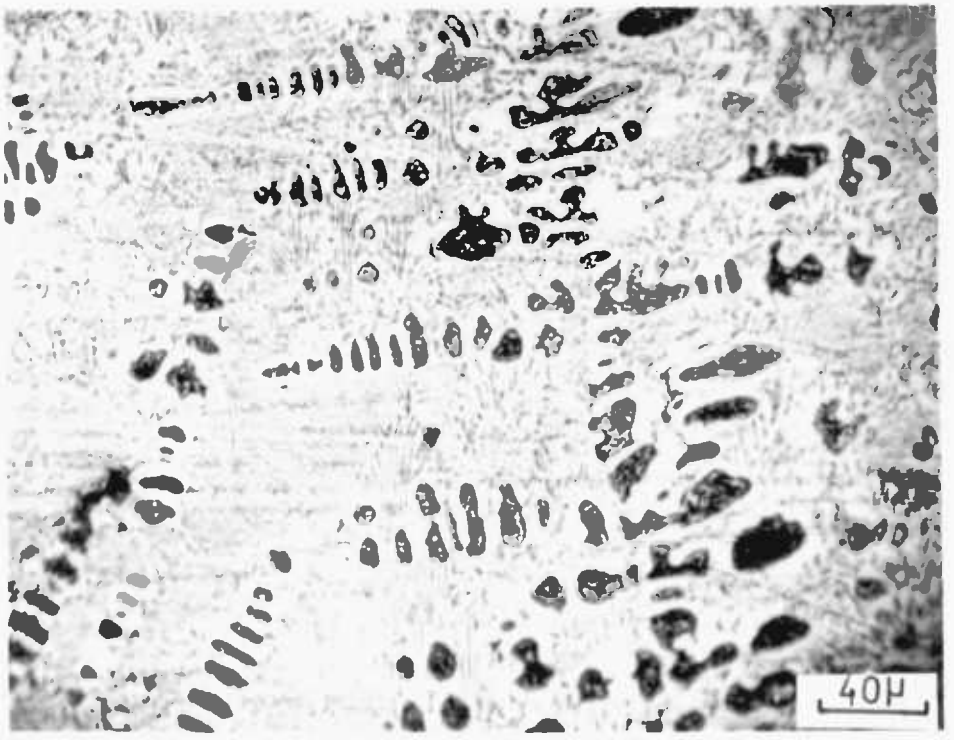
40μ

Fig. 4.15 Showing needle-like γ' precipitate particles in β matrix.

a) bright field
b) selected area diffraction pattern
c) high resolution dark-field from $a(11\bar{1})_{\gamma'}//(110)_{\beta}$ spot.
d) indexing of (b).

(a)

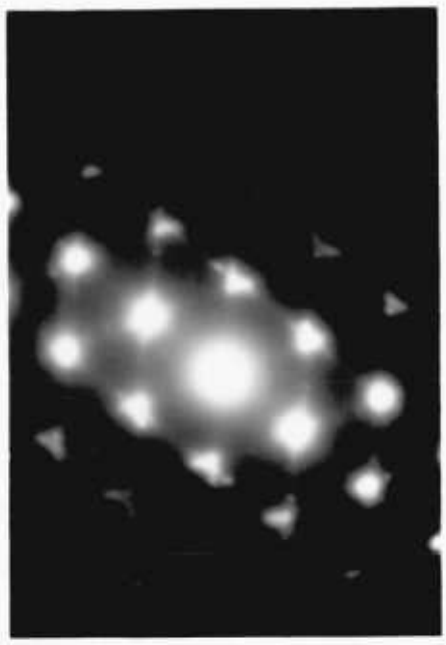

(b)

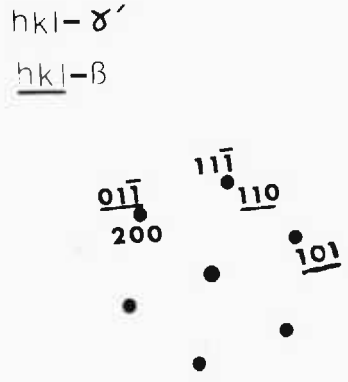

(d)

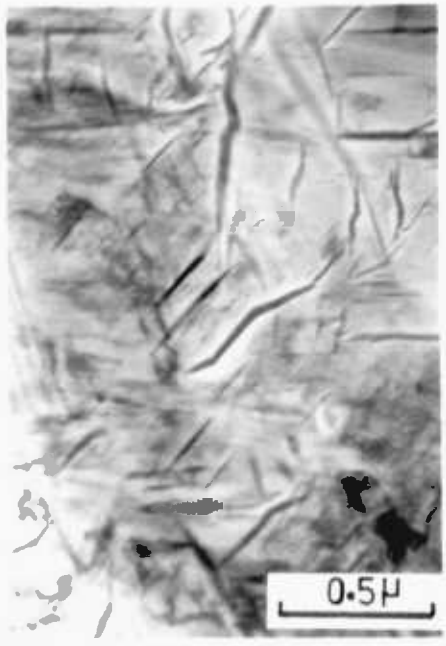

(c)

Fig. 4.16 Showing the fine planar fault plates on the $(0001)_\alpha$ basal plane in an α particle

(a) bright field
(b) selected area diffraction of (a)
(c) indexing of (b)

Fig. 4.17 Homogenised at 990°C for 4 days and water quenched. Showing the coarse particles in Alloy 5.

(a)

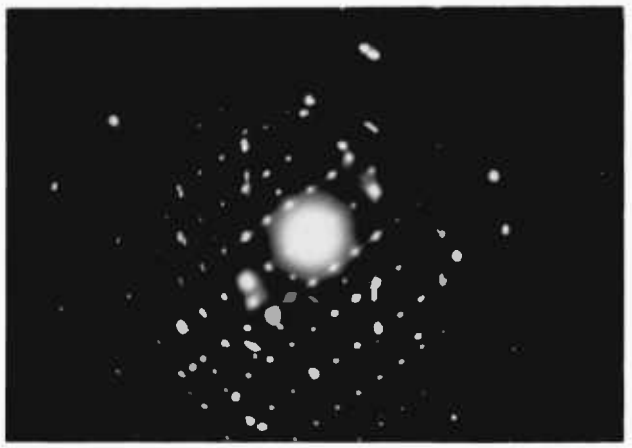

(b)

zone axis = [2 1̄ 1̄ 0]

(c)

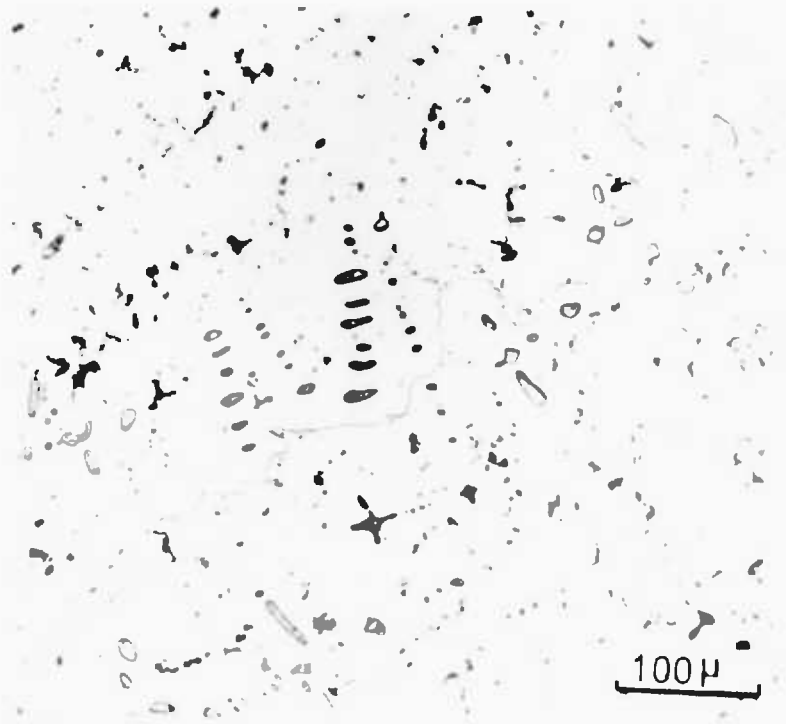

fig. 4·17

Fig. 4.18 Showing coarse γ' precipitates aged at 1000°C for 3 days and water quenched. Note the alloys are in the (γ' + β) phase region at 1000°C.

(a) Showing general features of γ' precipitate particles in the β phase in Alloy 1.

(b) Showing rod-like γ' precipitate particles in β phase in Alloy 3.

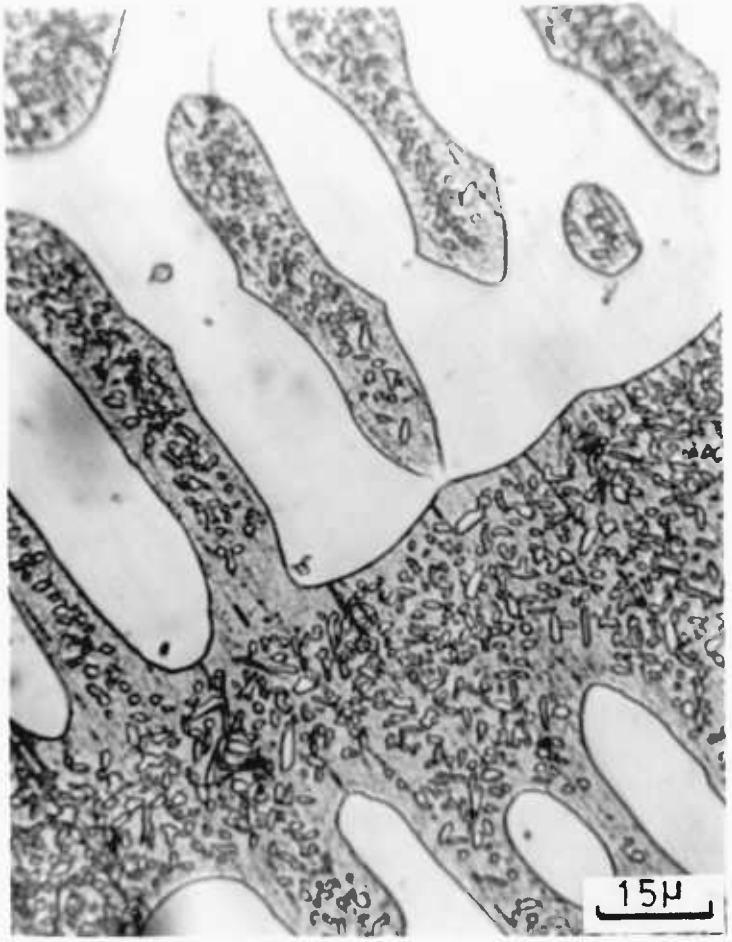

(a)

(b)

Fig. 4.19 Homogenised at 1260°C for 48 hours and water quenched. Light micrograph showing β martensite plates in Alloy 1. Three different martensite plate groups can be found (denoted by the letter A, B, C) in a β particle. In a smaller β particle (such as D) there is only one group of martensite plates.

Fig. 4.20 Showing general features of Alloy 1, homogenised at 1350°C for 5 hours and water quenched.
γ' phase at A
β martensite: straight and parallel-sided plate-like martensite at B.
The martensite plates in three groups (at B, D and E) in a β grain.

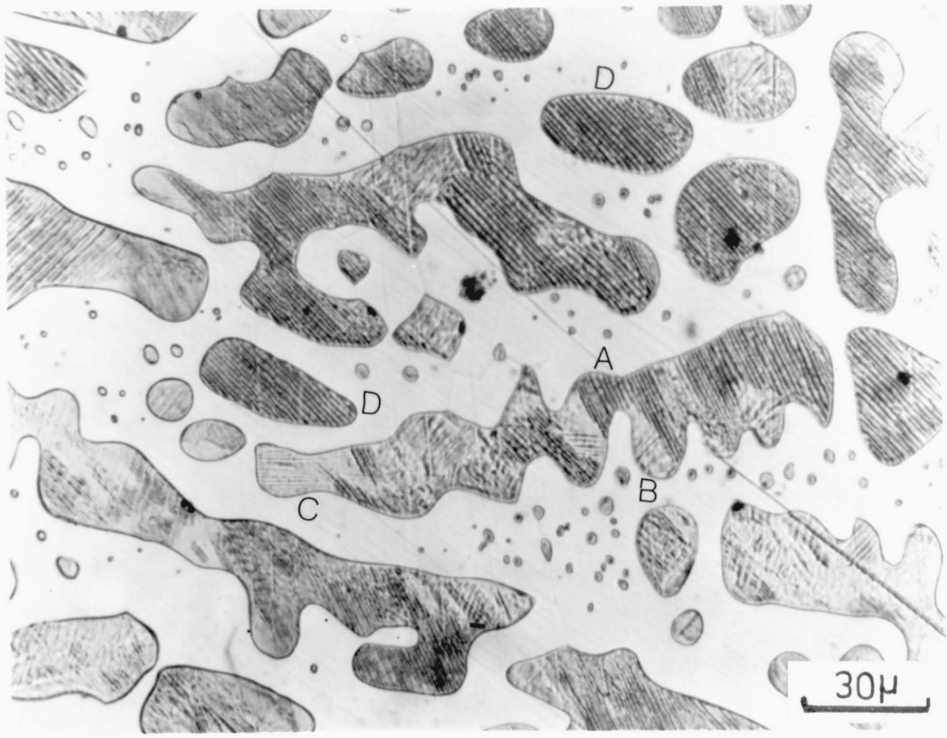
D
A
D
B
C
30μ

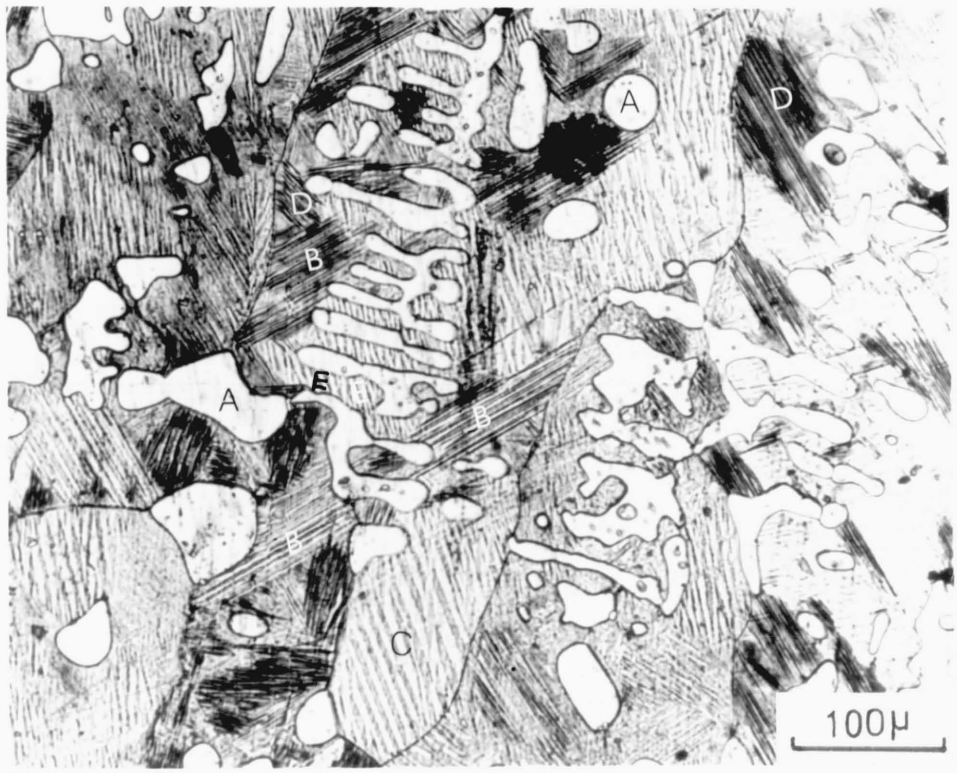
A
D
D
B
A
C
100μ

Fig. 4.21 Showing homogenised condition of Alloy 3

(a) γ' phase in region A and β phase in region B.

(b) Diffraction pattern from both sides of γ' plus β interface

(c) $[\bar{1}11]_{\gamma'}$ zone axis from γ' phase

(d) $[\bar{1}11]_{\beta}$ zone axis from β phase

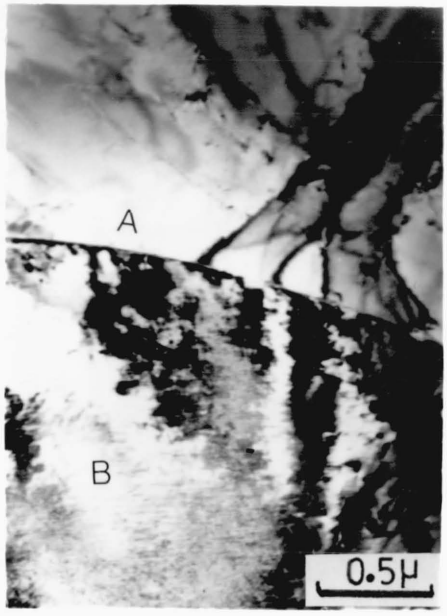

(a)

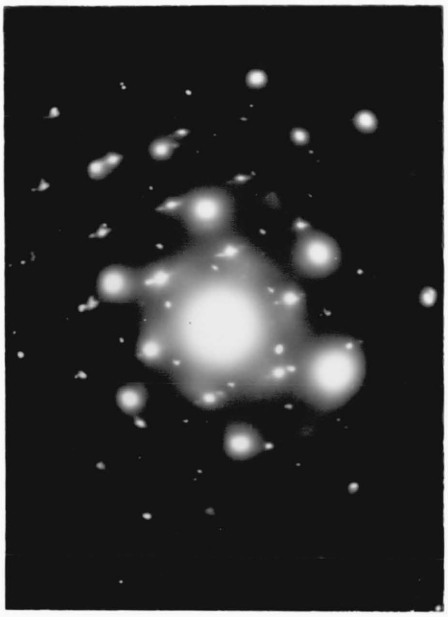

(b)

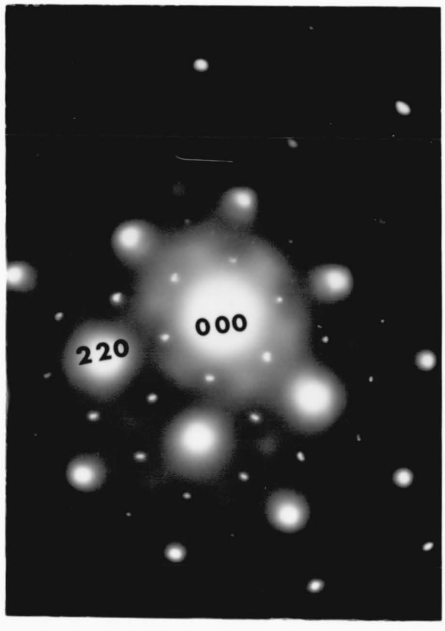

(c)

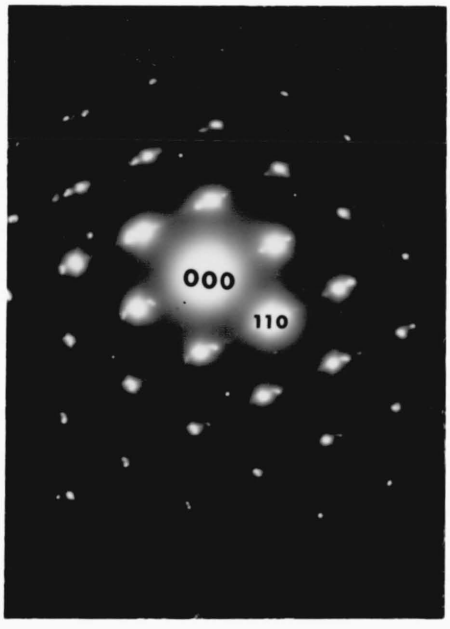

(d)

Fig. 4.22 Examples of selected area diffraction patterns from body-centred tetragonal β martensite.

a) [111] zone axis
b) [011] zone axis

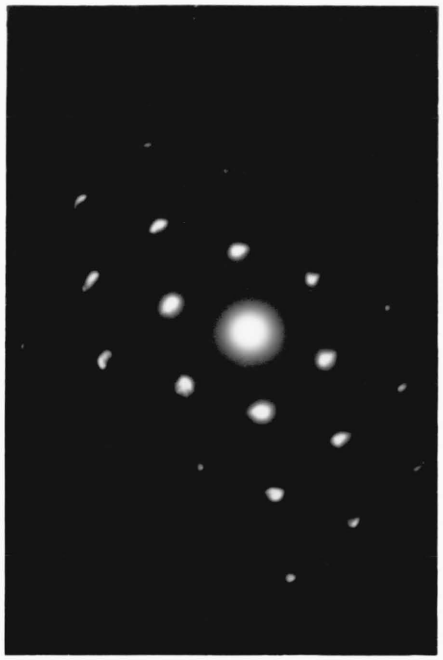

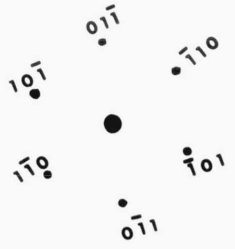

zone axis = [111]

(a)

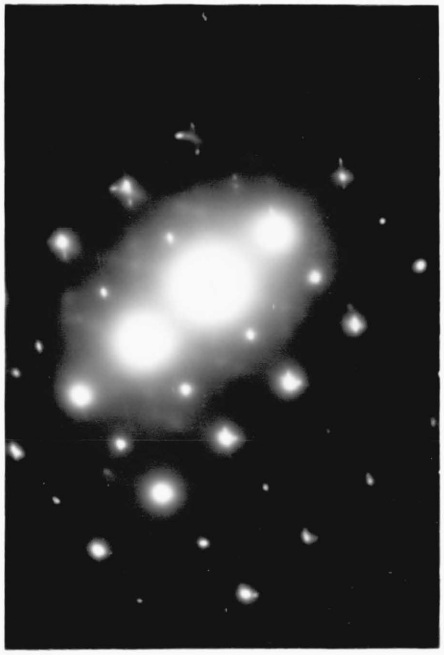

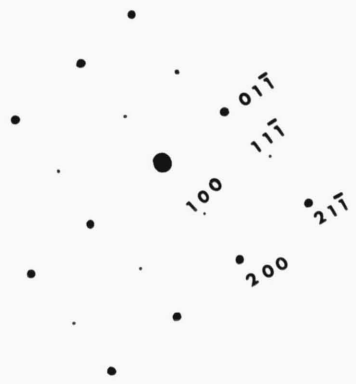

zone axis = [011]

(b)

Fig. 4.23 Showing internal twinning of the β martensite plate

a) Bright field
b) Selected area diffraction pattern of (a)
c) indexing of (b)

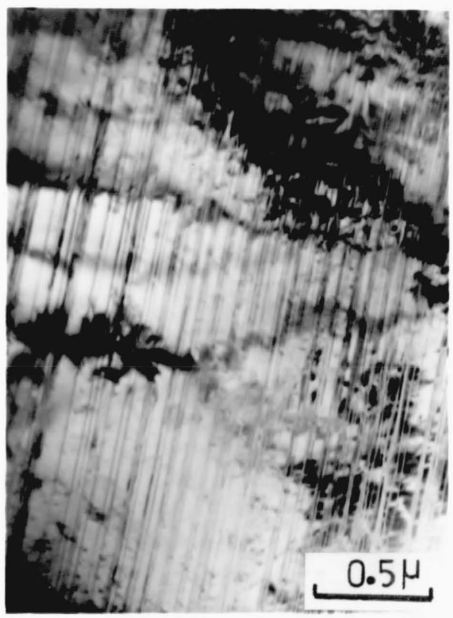
0.5μ

(a)

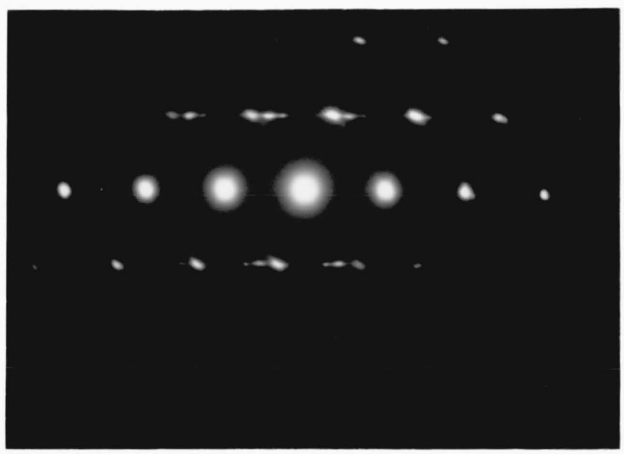

(b)

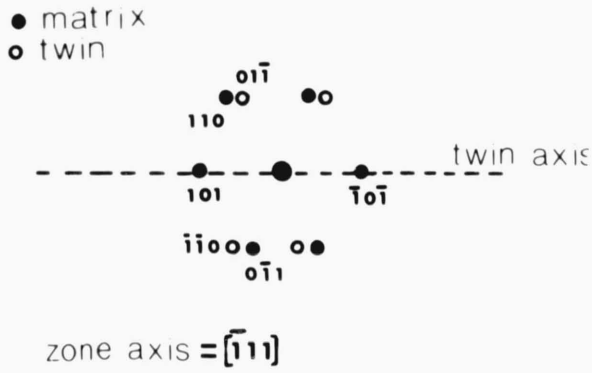
● matrix
o twin
0 1 1̄
1 1 0
twin axis
1 0 1
1̄ 0 1̄
1 1̄ 0 0
0 1̄ 1
zone axis = [1̄ 1 1]

(c)

Fig. 4.24 Showing internal faults in two variants of the same faulting system in alternating neighbouring martensite plates.

a) Bright field micrograph
b) Selected area diffraction pattern of (a) from A/B
Zone axis $\cong [\bar{1}11]_M$
c) indexing of (b)
d) low resolution dark field, taken using (101) diffraction spot.
e) low resolution dark field taken using $(0\bar{1}1)$ diffraction spot.
f) Selected area diffraction pattern from martensite plate A, showing continuous streak along the $(0\bar{1}1)$ plane normal.
g) Selected area diffraction pattern from martensite plate B, showing continuous streak along the (101) plane normal.

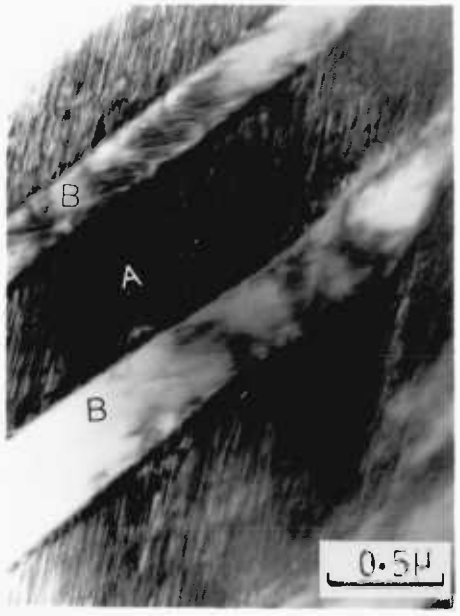

(a)

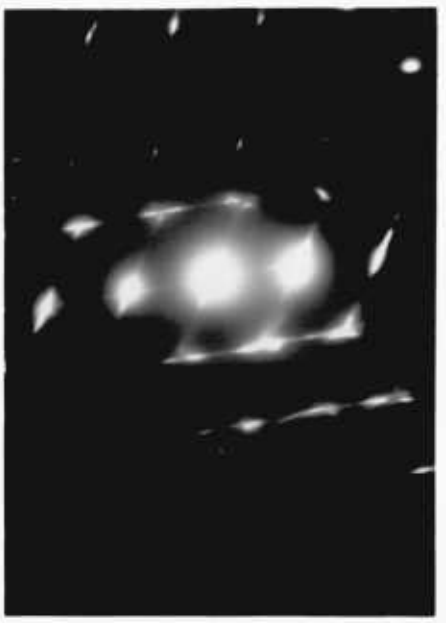

(b)

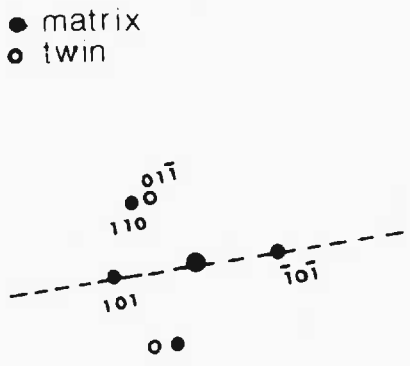

(c)

(d)

(e)

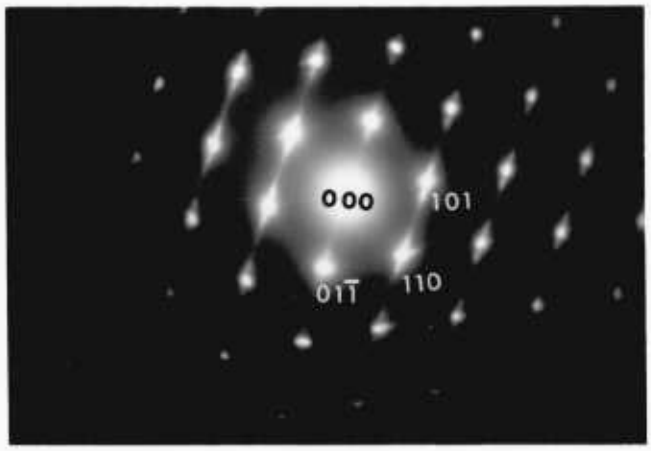

(f)

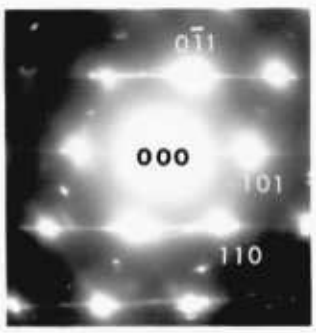

(g)

Fig. 4.25 Showing alternating neighbouring martensite plates in a group. The ratio of the widths of the neighbouring martensite plates is ≈ 1:1

a) Bright field
b) low resolution dark field of (a), taken from $(011)_{BCT}$ diffraction spot.
Foil plane = $(\bar{1}11)_{BCT}$

Fig. 4.26 Showing internal striations in two directions within one martensite plate

a) Bright field
b) selected area diffraction pattern of (a)
c) indexing of (b)


0.5μ

(a)


0.5μ

(b)

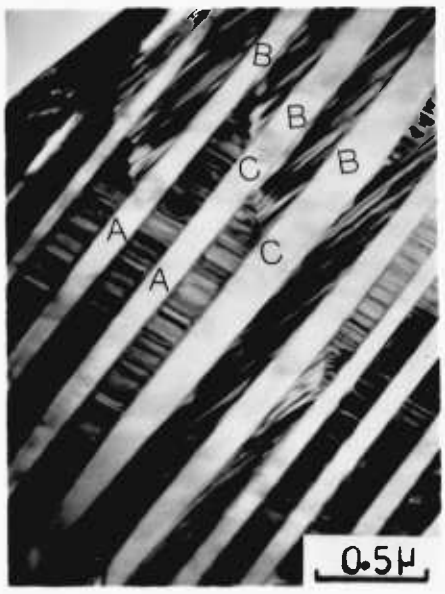
B
B
B
C
C
A
A
0.5μ

(a)

(b)

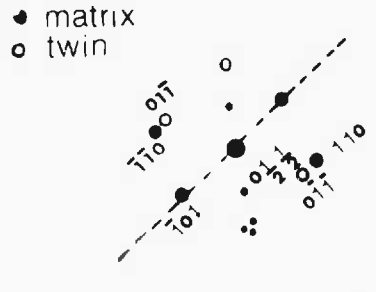
matrix
twin
o
011
$\bar{1}10$
$\bar{1}01$
$01\bar{1}$
$\bar{1}10$
$01\bar{1}$

(c)

Fig. 4.27 Showing fine, planar faults lying on different planes in the neighbouring martensite plates, i.e. at A and B, in Alloy 2

a) Bright field

b) Selected area diffraction pattern of (a), showing streaks in two directions Zone axis $\simeq [121]_{BCT}$

c) indexing of (b).

d) Low resolution dark field taken using $(\bar{1}01)$ diffraction spot.

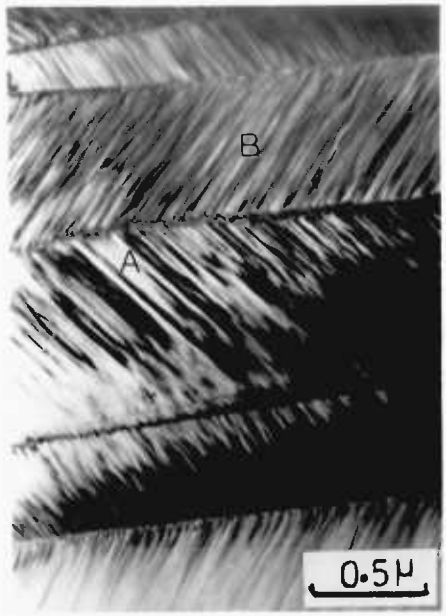

(a)

(b)

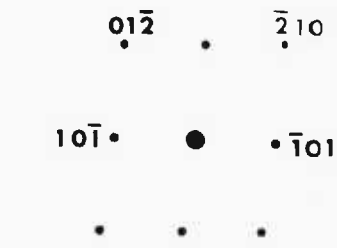

zone axis = [12 1]

(c)

(d)

Fig. 4.28 Showing acicular-type β martensite morphology in homogenised condition of Alloy 1

a) Bright field

b) Bright field, showing fine, stack of internal striations.

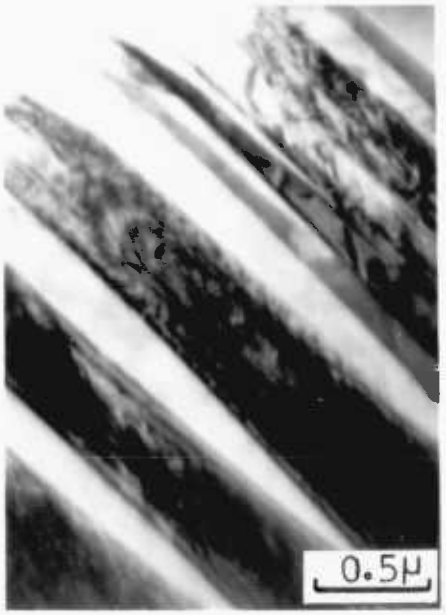

(a)

(b)

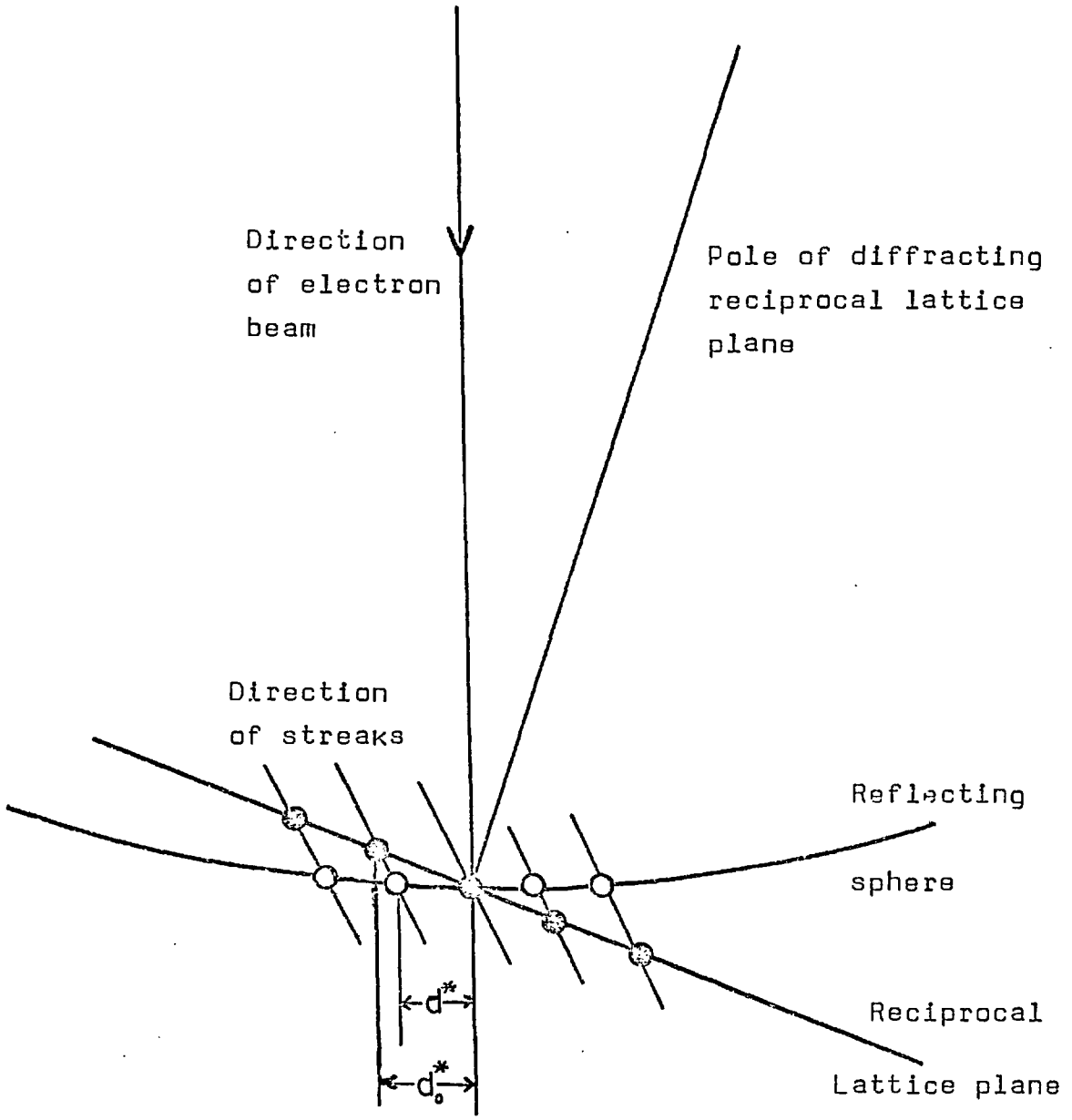

Fig. 4.29 A two-dimensional illustration showing the origin of displaced diffraction maxima due to relaxation of a Laue condition. Crystals having a true d^*_o spacing may appear to have a spacing d^*_1.

⊛- true reciprocal lattice points

○- apparent diffraction maxima

Fig. 4.30 Homogenised at 1260°C for 48 hours and water quenched. Light micrograph of Alloy 2, showing β martensite morphology.


A
15μ

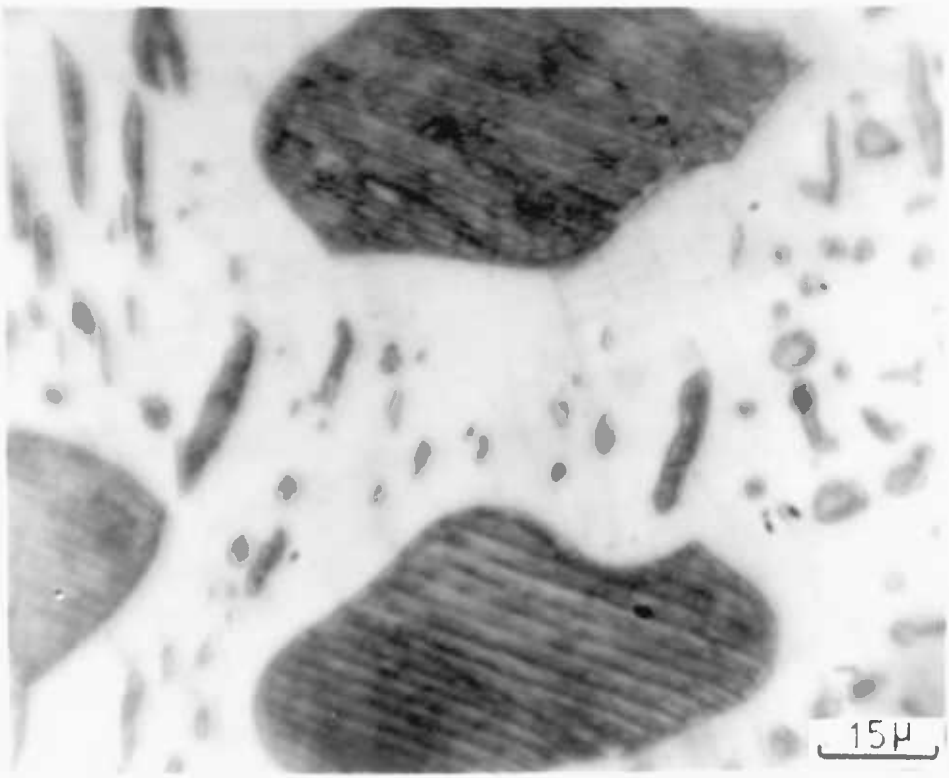
15μ

Fig. 4.31 Showing β martensite plate morphology in a β particle (such as at A in fig. 4.30) in Alloy 2.

Fig. 4.32 Showing electron micrograph of the "tweed" substructure in β phase

a) Dark-field image of (110) spot
b) Electron diffraction pattern showing an elongation along the [110] direction
Zone axis = $[\bar{1}11]_{\beta}$

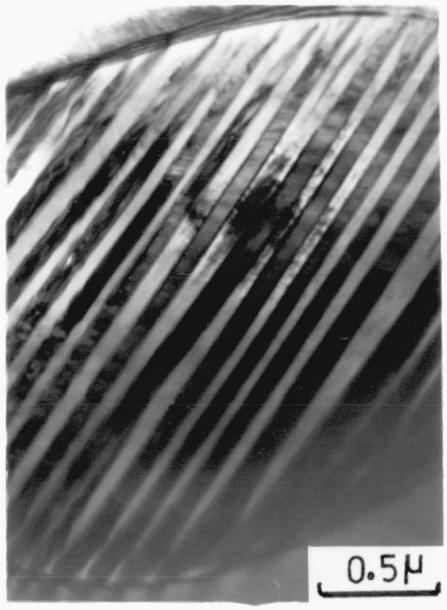

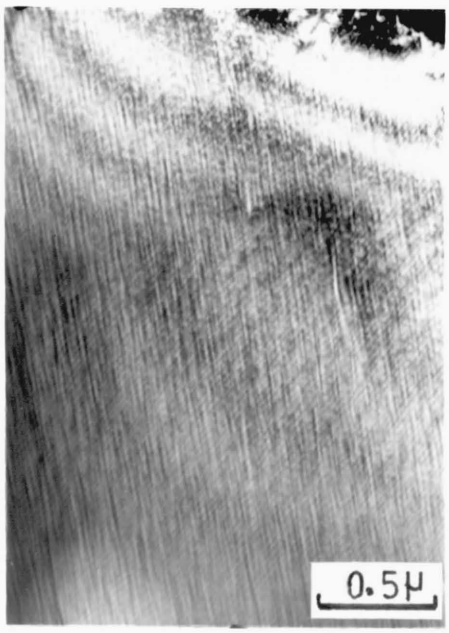

(a)

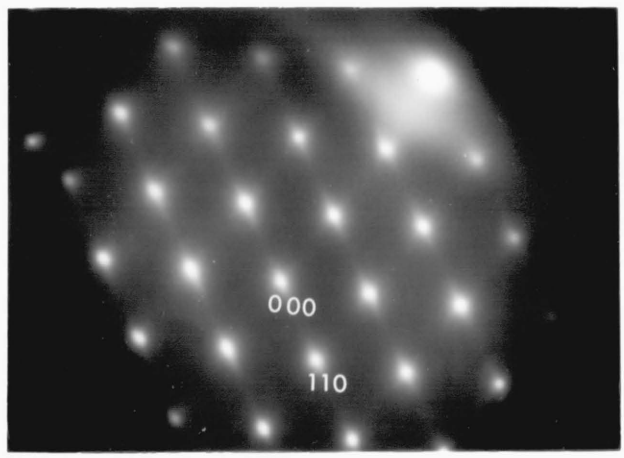

(b)

Fig. 4.33 Showing β martensite morphology in the as-cast condition of Alloy 1.

a) Acicular-type or needle-like β martensite which contains thin plate-like striations lying on the $(0\bar{1}1)$ and (110) planes (such as at A and B needles).
b) selected area diffraction pattern, foil plane = $(\bar{1}11)_{BCT}$
c) indexing of (b)
d) low resolution dark field from the $(0\bar{1}1)_{BCT}$ diffraction spot.
e) Low resolution dark field from the $(110)_{BCT}$ diffraction spot.

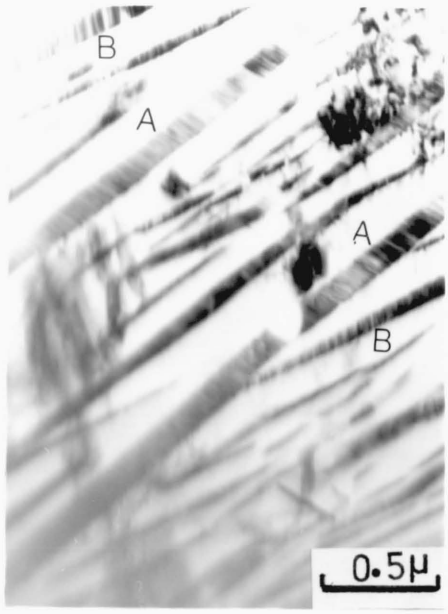

(a)

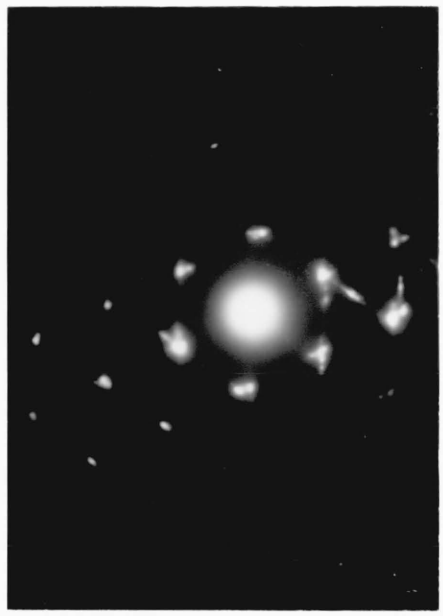

(b)

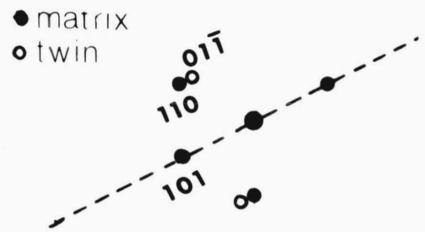

(c)

(d)

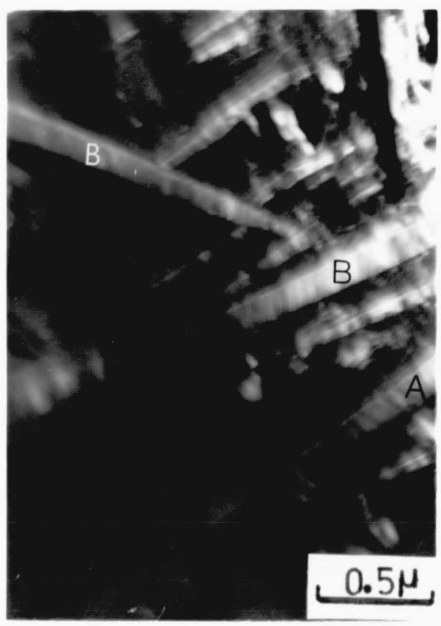

(e)

Fig. 4.38 Showing dislocations aligned along the $[11\bar{1}]$ in Alloy 3 deformed at room temperature.

a) Bright field micrograph.
b) Selected area diffraction pattern of (a). Foil plane = (011).

Fig. 4.39 Showing dislocations closely aligned along the $[11\bar{1}]$ in Alloy 3, deformed at 600°C.

a) Bright field micrograph.
b) Selected area diffraction pattern of (a). Foil plane = (011).

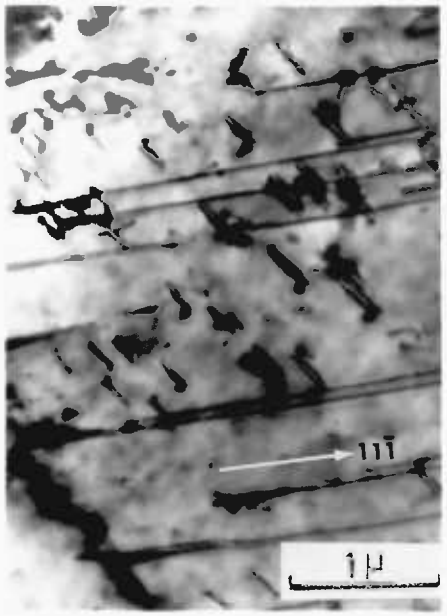

(a)

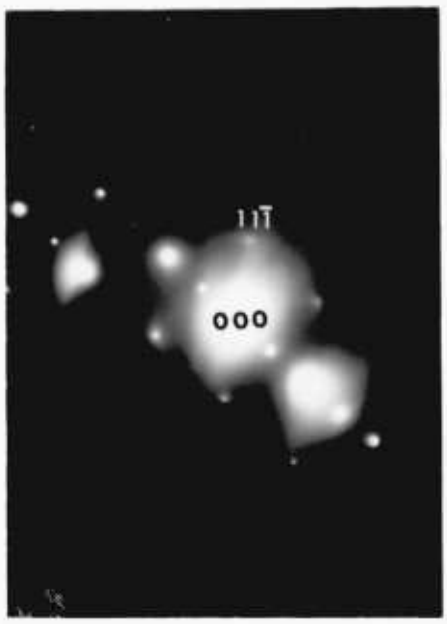

(b)

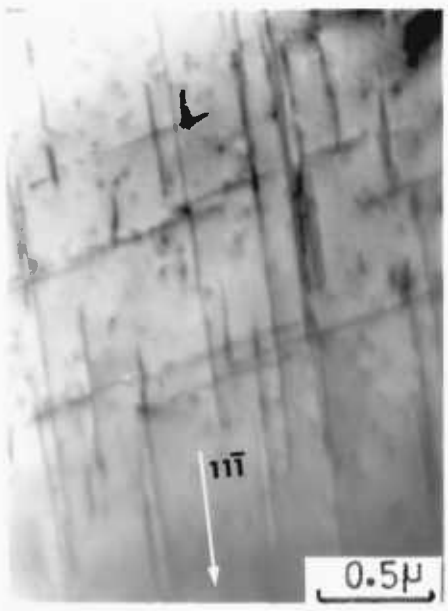

(a)

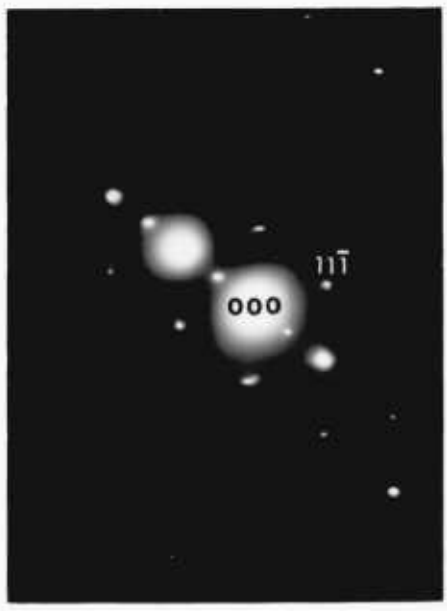

(b)

Fig. 4.40 Showing jogged dislocations aligned close to the $[1\bar{1}1]$ direction in Alloy 1, deformed at 600°C.

a) Bright field micrograph.
b) Selected area diffraction pattern of (a). Foil plane $\cong$ $(\bar{1}12)$.

Fig. 4.41 Showing relatively long, straight and parallel dislocations in two sets in the (001) foil plane, from Alloy 3 deformed at 400°C.

a) Bright field micrograph.
b) Selected area diffraction pattern foil plane $\cong$ (001)

Note: Dislocations in two sets lie along the [110] and $[1\bar{1}0]$ directions.

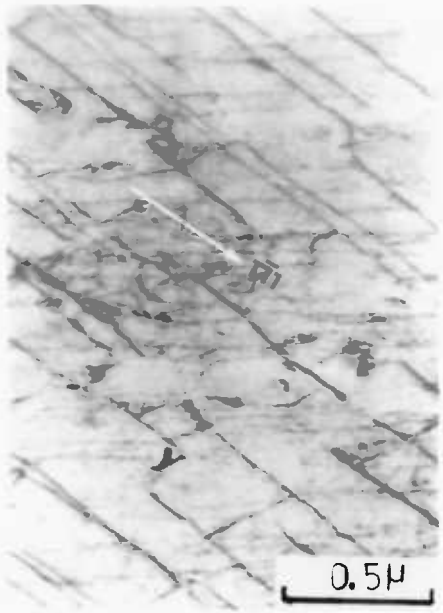

(a)

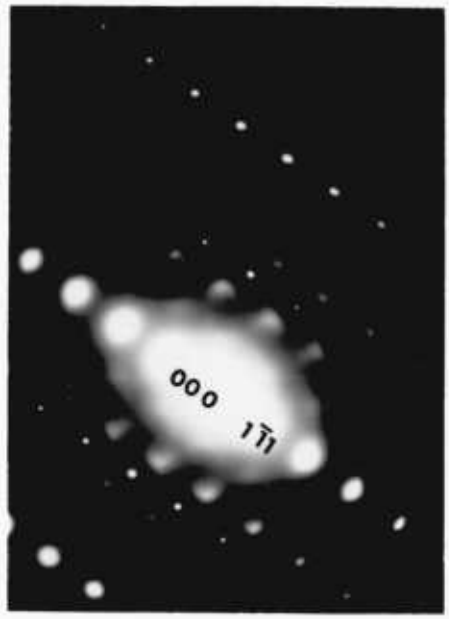

(b)

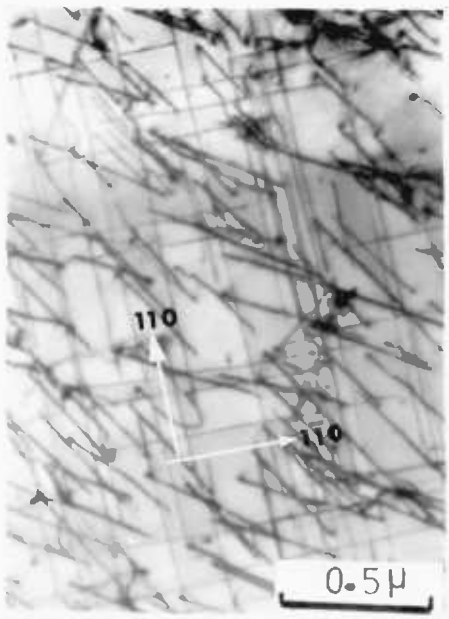

(a)

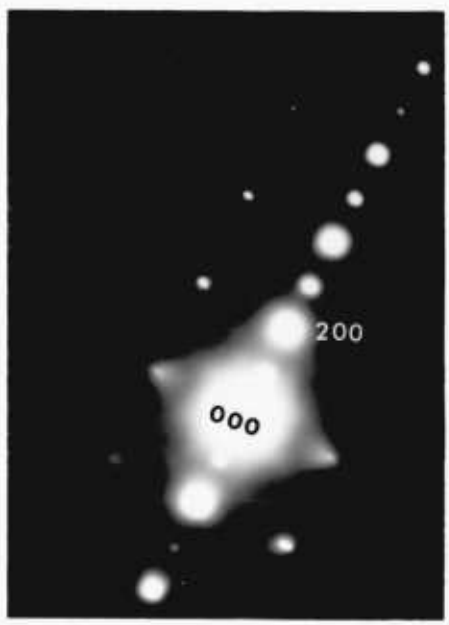

(b)

Fig. 4.42 Showing dislocations in Alloy 3 deformed at 600°C.

a) Showing long and straight dislocations along the [110] direction.

b) Selected area diffraction pattern of (a).
Foil plane = $(\bar{1}12)$, g = 220
Note: long and straight dislocations are tending to form dipoles.

Fig. 4.43 Dislocations in Alloy 3 deformed at room temperature.

a) Bright field micrograph.

b) Selected area diffraction pattern of (a), g = 220

c) Selected area diffraction pattern, taken when dislocations in (a) disappeared, g = $22\bar{4}$

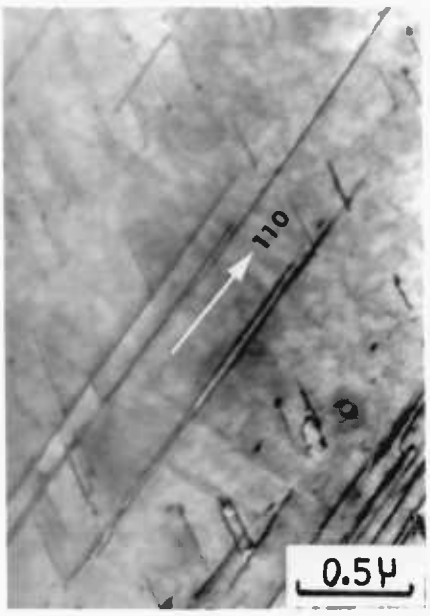

(a)

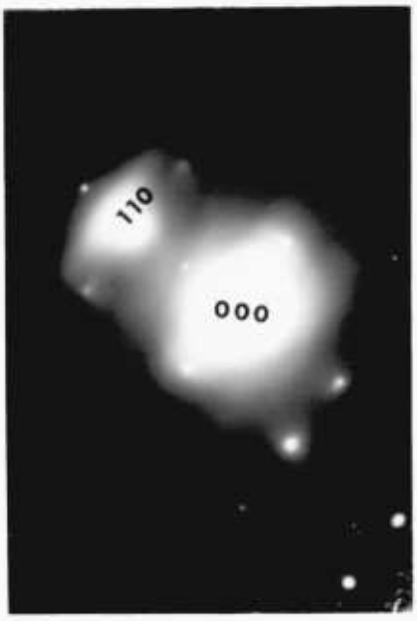

(b)

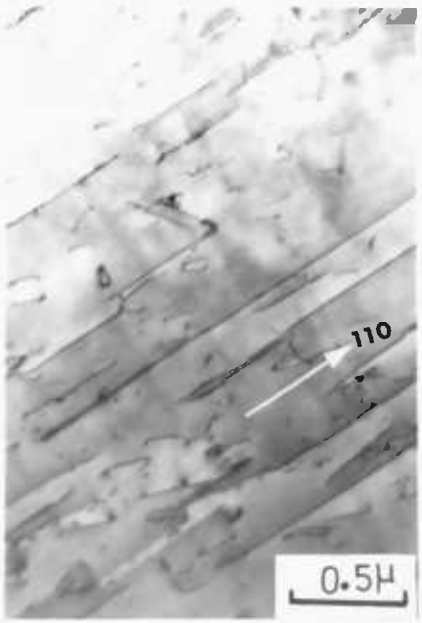

(a)

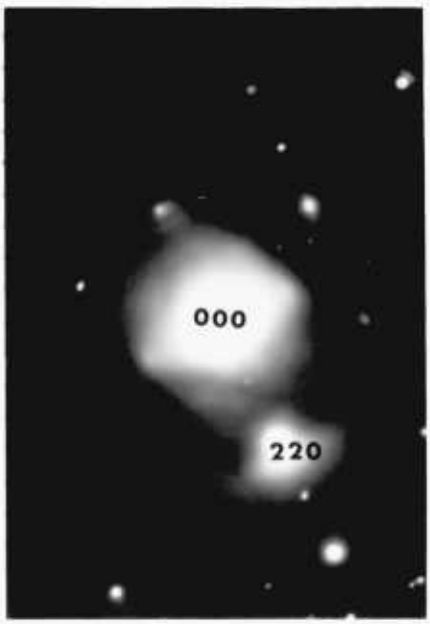

(b)

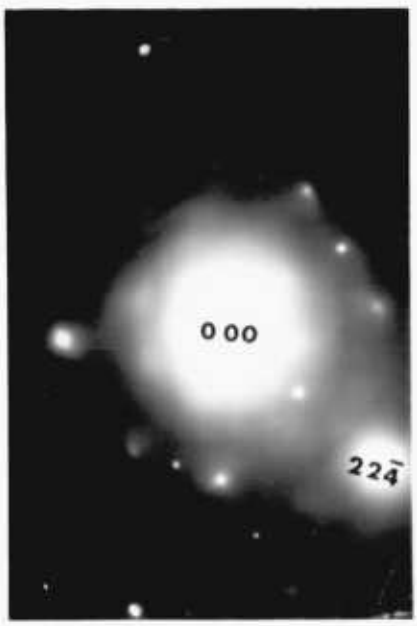

(c)

Fig. 4.44 Dislocations in Alloy 4 deformed at room temperature.

a) Bright field micrograph. Dislocations are close to the $[1\bar{1}1]$, $g = 1\bar{1}1$

b) Disappearance of dislocations in (a), $g = 220$

c) Selected area diffraction pattern of (b), $g = 220$

Fig. 4.45 Dislocations in Alloy 4 deformed at 700°C

a) relatively straight and parallel dislocations along the [110] directions; foil plane = (001), $g = 200$

b) Dislocations align close to the [110] direction. Double beam condition. Dipoles at A and B

Fig. 4.46 Dislocations in Alloy 1 deformed at 900°C. Foil plane = $(\bar{1}12)$, $g = 1\bar{1}1$

(a)

(b)

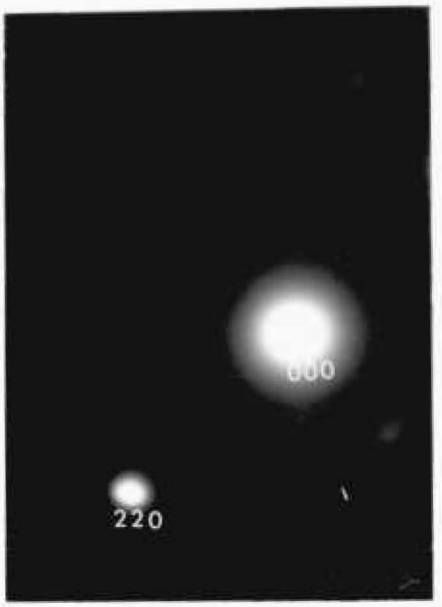

(c)

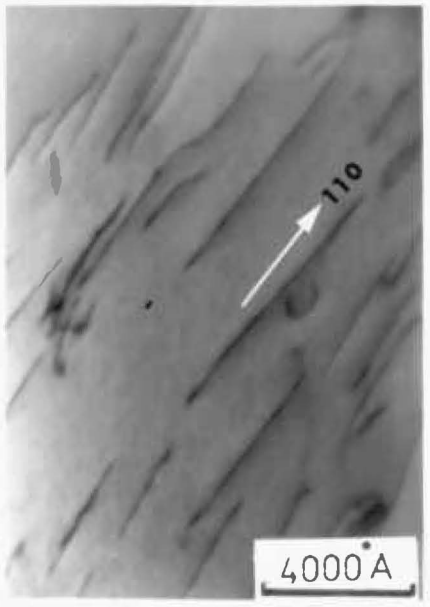

(a)

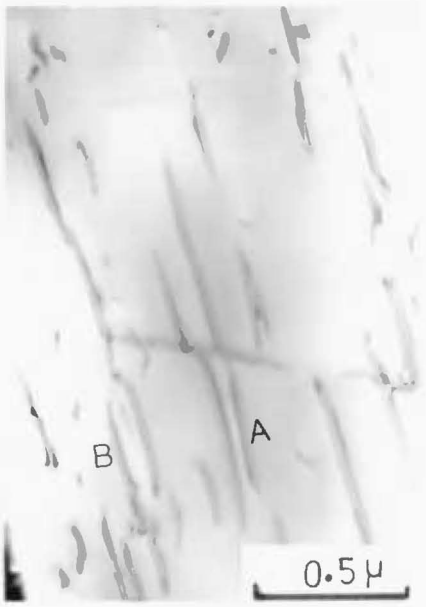

(b)

fig. 4.46

Fig. 4.47 An (001) foil of Alloy 5 deformed at 700°C, showing curved and tangled dislocations.
Foil plane = (001); g = $0\bar{2}0$

Fig. 4.48 An (011) foil of Alloy 3 deformed at 900°C, showing dislocations
foil plane = (011); g = $1\bar{1}1$

Fig. 4.49 Dislocation dipoles in Alloy 3

a) Deformed at room temperature;
foil plane = (011), g = $11\bar{1}$

b) Deformed at 600°C
foil plane = (011), g = 200

Fig. 4.50 Dislocations in Alloy 1 deformed at room temperature;
foil plane = (011); g = 200

Fig. 4.51 Jogged dislocation along the [110], in Alloy 3 deformed at room temperature.
Foil plane = $(\bar{1}12)$, g = 220
Note: Dislocations at A and B are tending to form dipoles.

fig. 4.47

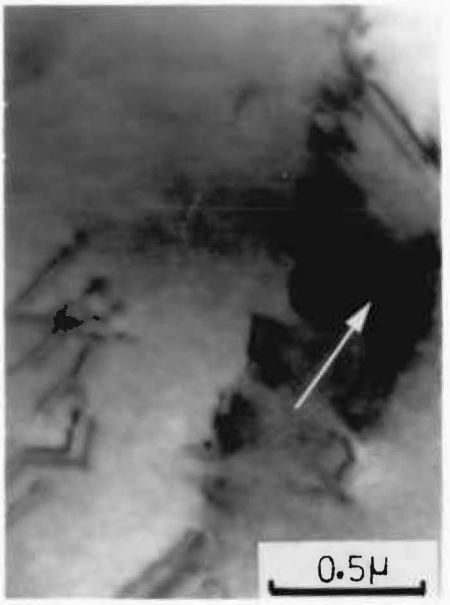

fig. 4.48

fig. 4.49(a)

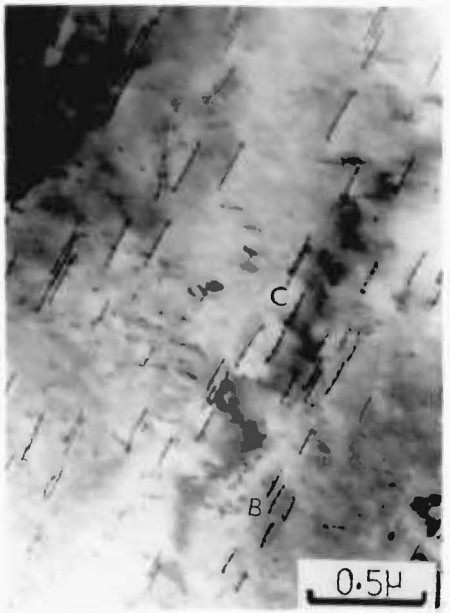

fig. 4.49(b)

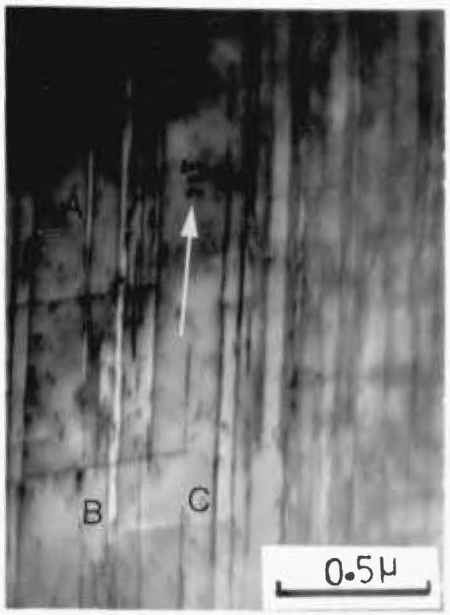

fig.4.50

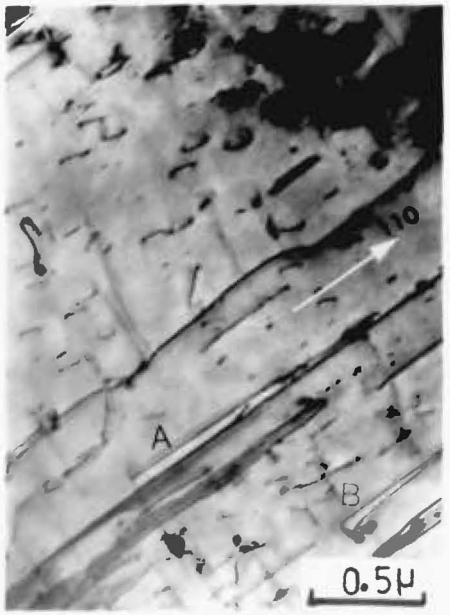

fig. 4.51

Fig. 4.52 Dislocations in Alloy 3 deformed at room temperature

a) Bright field micrograph pinching off of trails at A. Dislocation loop debris at B. Dipole trails or dislocation cusps at C. x 40·000

b) Selected area diffraction pattern of (a) foil plane = $(\bar{1}12)$, g = $1\bar{1}1$

Fig. 4.53 Dislocations in Alloy 3 deformed at 300°C. Showing elongated loops along the $[01\bar{1}]$ direction. Foil plane = (011), g = $11\bar{1}$

x 30·000

Fig. 4.54 Showing pile-up in γ' phase of Alloy 5 deformed at 600°C. An analysis of the slip plane in γ'. x 30·000
Note: ends of dislocations in the pile-up lie along the $[01\bar{1}]$ direction which is considered to be the trace of the slip plane. Foil plane = (011)

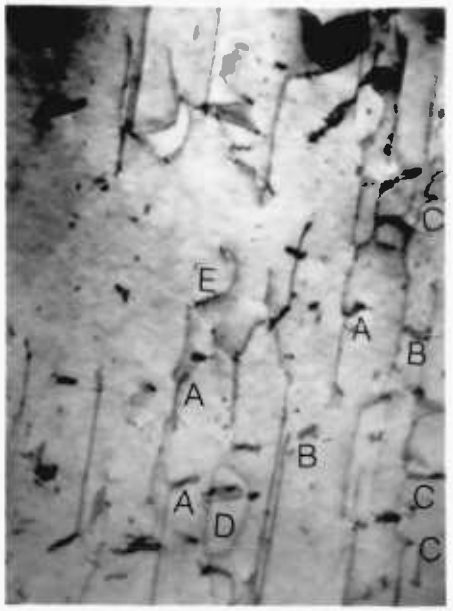

(a)

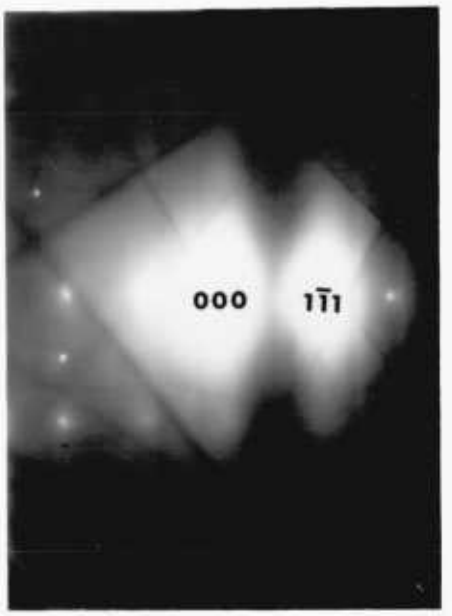

(b)

fig.4.53

fig.4.54

4.11. Temperature Dependence of Flow Stress

4.11.1. Tantalum-containing Alloys

The three alloys (Alloy 1, Alloy 2 and Alloy 3) were chosen for this study by changing the volume fraction of β phase and the tantalum content. The 0·2% flow stress of these alloys as a function of temperature from room temperature to 900°C was measured in three different conditions:

i) As-cast condition; the flow stress was measured in this condition, because in recent years many nickel-based superalloys are being used in the as-cast condition.

ii) Homogenised condition; heat treated at 1260°C in the (γ' + β) region for 48 hours, then water quenched.

iii) Aged condition; first the alloys were heat treated as for the homogenised condition, then further aged at 1000°C for 3 days followed by water quenching. The objective of this heat treatment was to explore possible precipitation effects.

The flow stresses of the tantalum-containing alloys, for different conditions, are shown in figures 4·55 - 4·57.

i) As-cast Condition

In Alloy 1 and Alloy 2, the flow stress versus temperature curves show a peak at approximately 300°C and 400°C respectively (fig. 4.55 - 4.56). Therefore the flow stress behaviour of these alloys with temperature in this condition is similar to that of single phase γ' . The room temperature and the peak flow stresses of Alloy 1 are considerably higher than those of Alloy 2. However, in Alloy 1 the flow stress above the peak temperature falls faster than that of Alloy 2 with increasing test temperature. Eventually they reach similar flow stresses at 900°C despite the fact that Alloy 1 has an appreciably higher flow stress

than that of Alloy 2 at low temperatures.

In contrast, Alloy 3 shows constant flow stress behaviour with increasing temperature up to about 700°C. Alloy 3 with a higher tantalum content (Table 4.1) and lower volume fraction of β phase, compared to Alloy 1 and Alloy 2 (Table 4.5) has a room temperature flow stress between Alloy 1 and Alloy 2. There is a tendency for the flow stress to increase with increasing tantalum content and to decrease with increasing volume fraction of β phase at high temperatures; this may be seen by comparing the flow stresses of Alloy 3 and Alloy 1, at 900°C, by taking into account their tantalum content and volume fraction of β phases (Table 4.1 and 4.5). Above 700°C the flow stress of Alloy 3 starts to decrease rapidly.

ii) Homogenised Condition

After homogenisation the room temperature flow stress of Alloy 1 has dropped sharply (by about 30%), compared to that of its as-cast condition (fig. 4.55). The peak flow stress has also dropped by about 20% and the peak temperature is shifted to higher temperature (≈ 400°C), compared to that of the as-cast condition. The flow stresses at 900°C, in both the as-homogenised and as-cast conditions are almost the same, indicating that the homogenisation treatment did not affect it despite the fact that the volume fraction of β phase has decreased considerably (Table 4.5).

The homogenisation treatment has not changed significantly the level and behaviour of the flow stress of Alloy 2 with temperature, compared to that of its as-cast condition (fig. 4.56).

After homogenisation treatment Alloy 3 has retained the flow stress, compared to its as-cast condition, up to about 700°C (fig. 4.57). However, the flow stress at 900°C has decreased by about 20%, compared to its as-cast state; it is still much higher than that of Alloy 1 and Alloy 2

at 900°C.

iii) Aged Condition

The room temperature flow stress of Alloy 1 has increased after ageing treatment (fig. 4.55), compared to its homogenised condition. Below approximately 600°C there is a small decrease in the flow stress of Alloy 1 with increasing temperature. Above 600°C, the flow stress falls relatively steeply with increasing temperature. However the flow stress is about the same in the aged, and the homogenised conditions.

The ageing treatment has not produced a significant change in the flow stress of Alloy 2 at low temperatures (fig. 4.56), compared to its homogenised state. However the ageing treatment has increased the flow stress by a factor of about 20% at 900°C, compared to that of the homogenised condition at 900°C.

The ageing of Alloy 3 has not changed the behaviour of its flow stress with temperature, compared to its as-cast and homogenised conditions, which means that the flow stress has kept constant up to about 700°C. However, there is an increase of flow stress at 900°C by a factor of about 20% compared to that of the homogenised condition of Alloy 3 at 900°C.

4.11.2. Hafnium-Containing Alloys

Two alloys have been prepared (Alloy 4 and Alloy 5) by changing the content of hafnium. At the beginning of the work it was hoped that the same heat treatments could be applied to these alloys as to the tantalum-containing alloys for an investigation of the structural and mechanical behaviour. However, homogenisation treatments at 1260°C and 1180°C were found to produce partial melting of Alloy 4. After Kaufman's data[8] had become available (sec. 2.1.3.) a homogenisation temperature of 990°C was then chosen in the light of the data published by Kaufman. It was thought

that hafnium produces a low-melting eutectic. Alloy 4 was investigated in the as-cast condition. Another hafnium-containing alloy (Alloy 5) was prepared of lower hafnium content in the hope of avoiding the low-melting point eutectic.

Alloy 4 has the highest flow stress between room temperature and 900°C of all the alloys investigated (fig. 4.58). This alloy shows similar flow stress behaviour as a function of temperature to that of Alloy 3. As Alloy 3, Alloy 4 has a constant flow stress up to about 700°C. Above 700°C the flow stress decreases sharply with increasing temperature.

In the as-cast state Alloy 5, consisting predominantly of γ' (Table 4.5), unlike Alloy 4, shows a rather broad peak (fig. 4.59). The room temperature flow stress of Alloy 5 is about 30% less than that of Alloy 4. This difference decreases by a factor of 15% at the peak temperature of Alloy 5 (at 600°C) and at 900°C this difference is about 20%. Although both Alloy 3 and Alloy 4 contain the similar volume fraction of γ' phase (Table 4.5) the flow stress of Alloy 4 is much higher (by a factor of about 25%) than that of Alloy 3 up to about 700°C, at 900°C this difference decreases to 10% in their as-cast states.

As mentioned above Alloy 5 was homogenised at 990°C for 4 days and water quenched. This homogenisation treatment produced a predominantly γ' phase with 4 vol. pct an intermetallic compound. The structure of these particles has been given in sec. 4.5. and 4.7. This heat treatment has increased the flow stress of Alloy 5 as compared to that of its as-cast state. This increase is about 8% at room temperature and the peak temperature (at 600°C), whereas at 900°C it is about 27%. However, the position of the peak did not change after homogenisation as was the case in Alloy 1 and Alloy 2.

4.12. Athermal stress, Thermal stress and Strain-rate sensitivity as a function of temperature

The relaxation tests have been carried out to determine the athermal and thermal component of the flow stress. The relaxation tests have been done by stopping the cross-head of the Instron machine for about twenty minutes. The method of the relaxation test has been described in sec. 2.20. The data from the relaxation tests have been put into a computer programme, which was made, for the Feltham equation[73,74] (equation 1 in sec. 2.20.1), by Nichols and Rawlings (1974)[64], to determine the athermal and thermal stresses.

Figures 4.60 - 4.62 show the athermal stress versus temperature curves of Alloys 1-3 and Alloy 5.

The change in flow stress produced by increasing the strain rate (strain-rate cycling) by a factor of ten was also measured over the entire range of strain at each test temperature. The strain rate cycling test is described in sec. 2.20.2. In all the tests the stress increment rose with the total imposed strain. The strain-rate sensitivity, determined from the strain-rate cycling data, of the alloys, is presented, as a function of temperature, in fig. 4.64.

Fig. 4.63 shows the thermal stresses of alloys as a function of temperature.

As fig. 4.63 and fig. 4.64 show, the thermal stresses and the strain-rate sensitivity of alloys are very low at low temperatures, whereas at high temperatures the thermal stresses and the strain-rate sensitivity of the alloys are very high.

The athermal stresses of Alloys 1, 2, Alloy 3 and Alloy 5 show similar temperature dependence to those of the flow stresses (figs. 4.55 - 4.57, 4.59).

The activation volume for deformation was calculated for each specimen from the strain-rate sensitivity data, using equation (6) of sec. 2.20.2. The activation volume was calculated in dimensionless units obtained by dividing it by b^3, where b is the Burgers vector of the γ' phase. The results will be given in sec. 5.8.

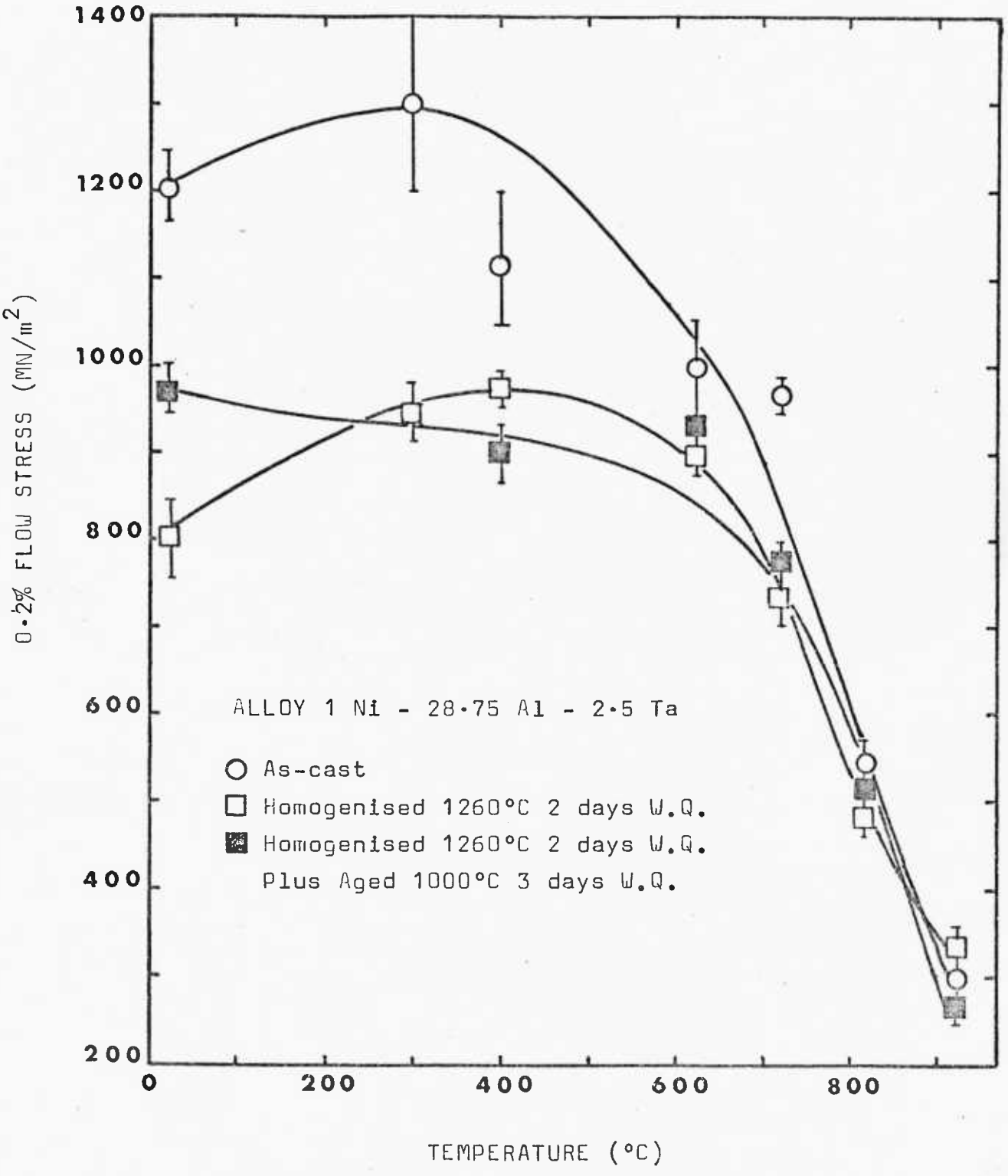

Fig. 4.55 Temperature dependence of 0·2% flow stress of Alloy 1 for different conditions.

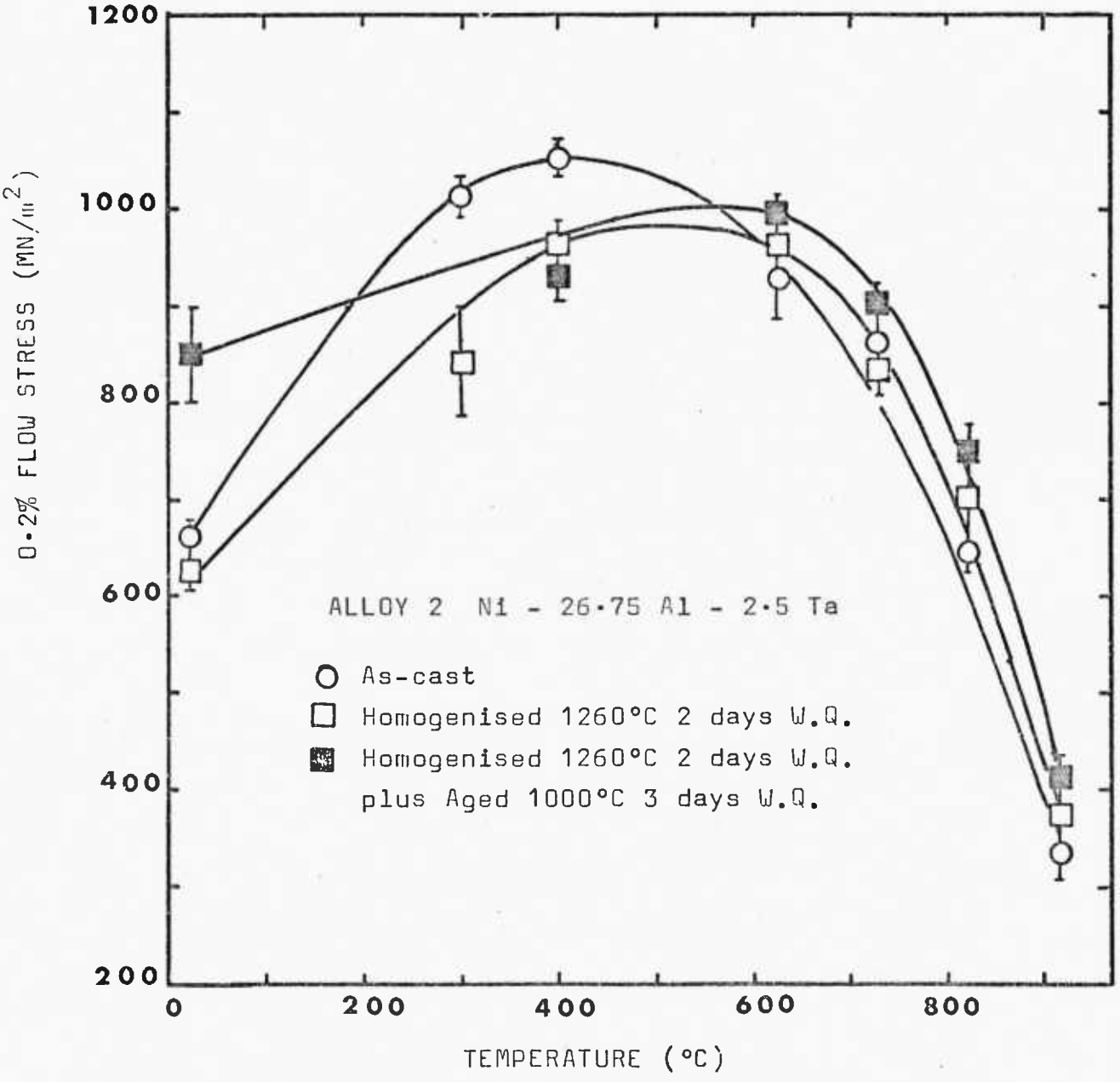

Fig. 4.56 Temperature dependence of 0·2% flow stresses of Alloy 2 for different conditions.

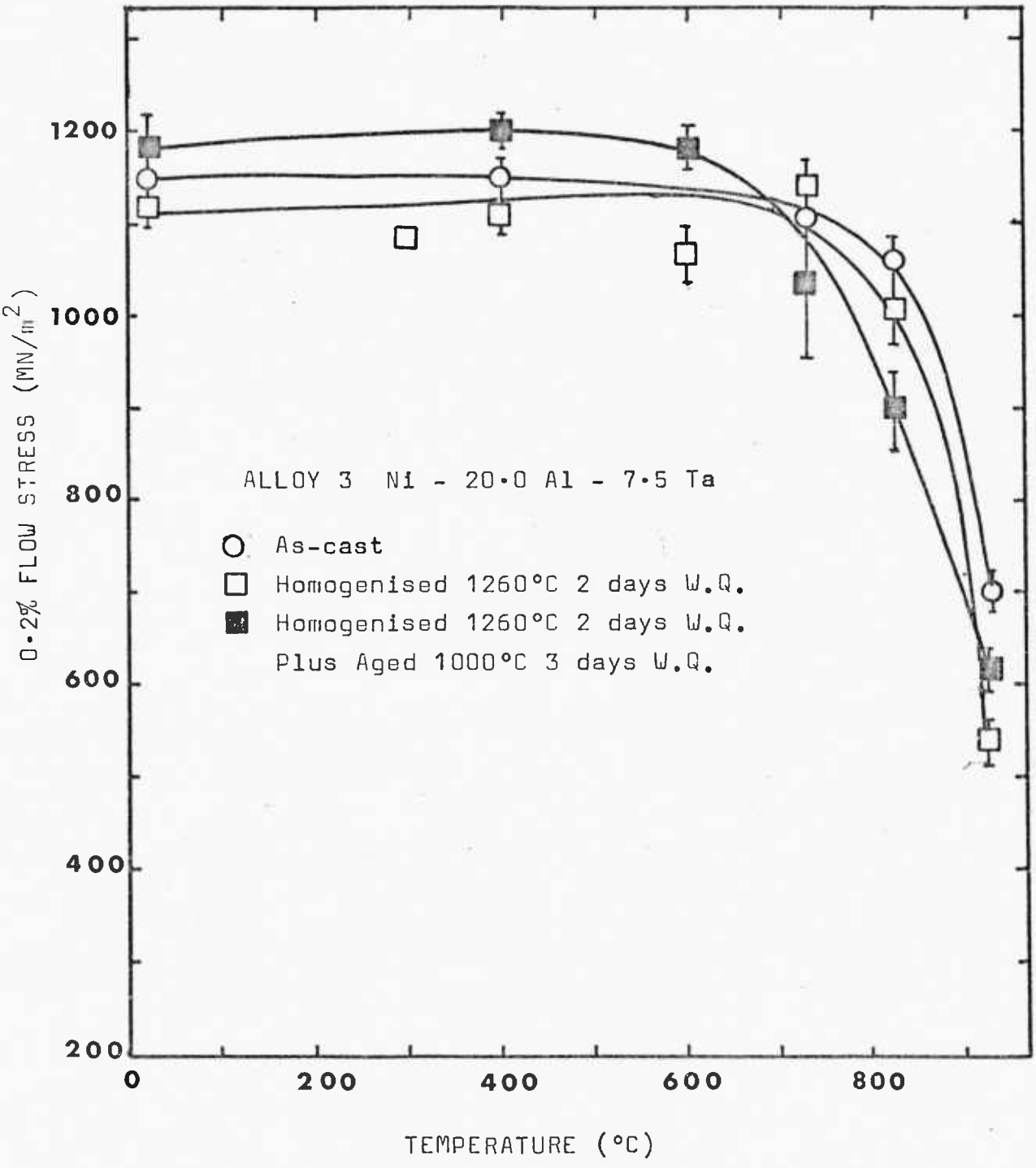

Fig. 4.57 Temperature dependence of 0·2% flow stresses of Alloy 3 for different conditions.

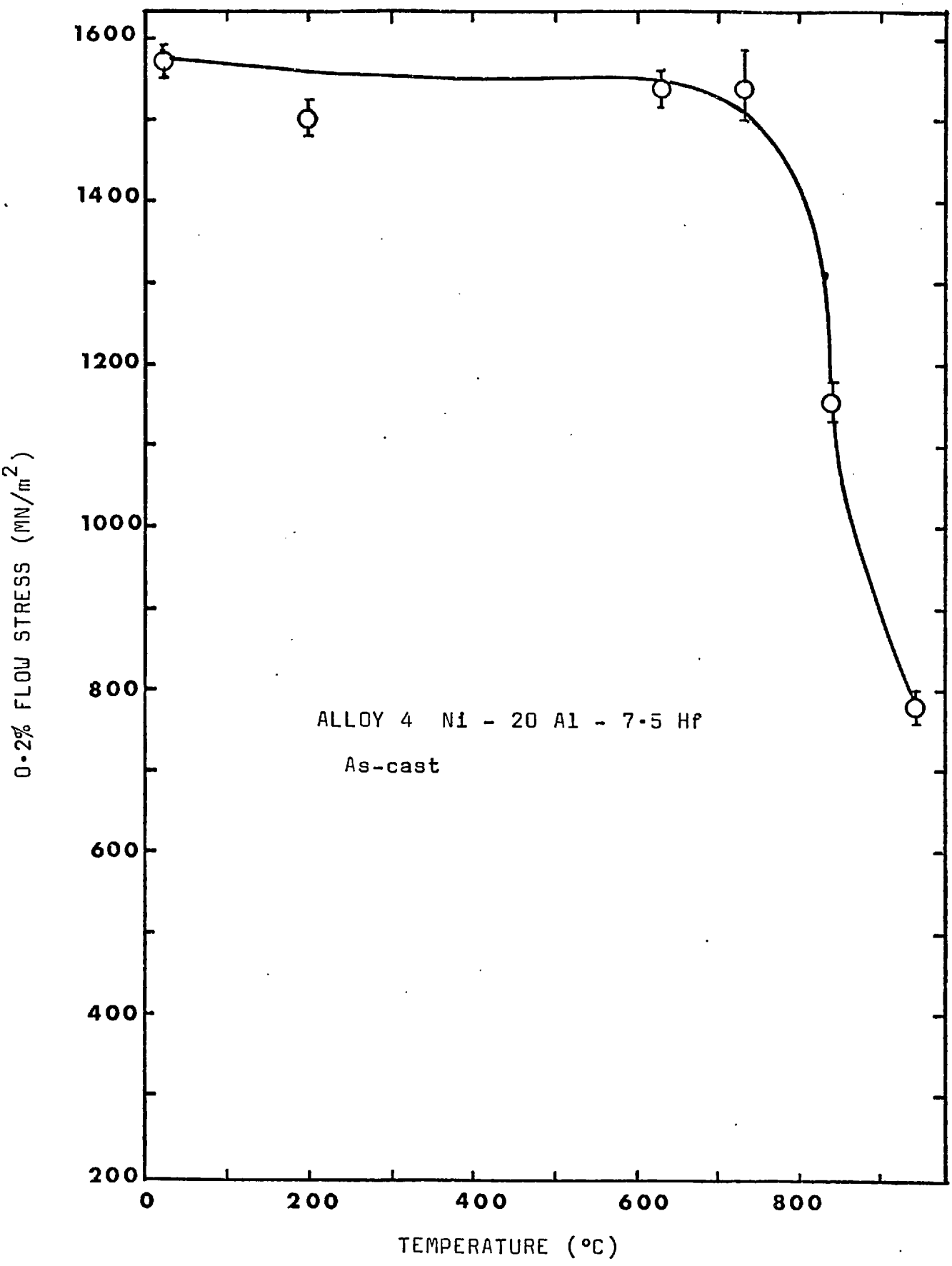

Fig. 4.58 Temperature dependence of 0·2% flow stress of Alloy 4.

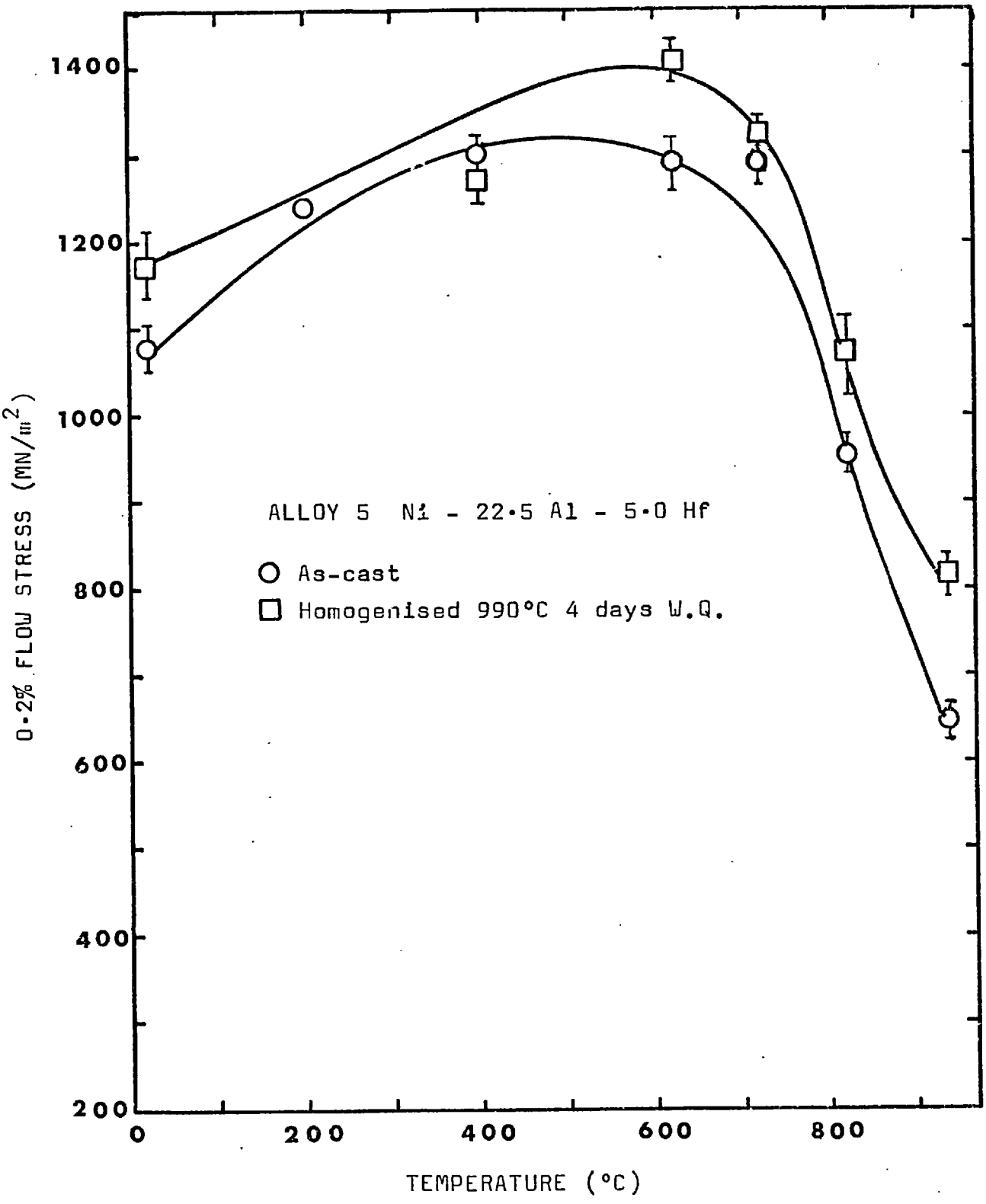

Fig. 4.59 Temperature dependence of 0·2% flow stress of Alloy 5 for different conditions.

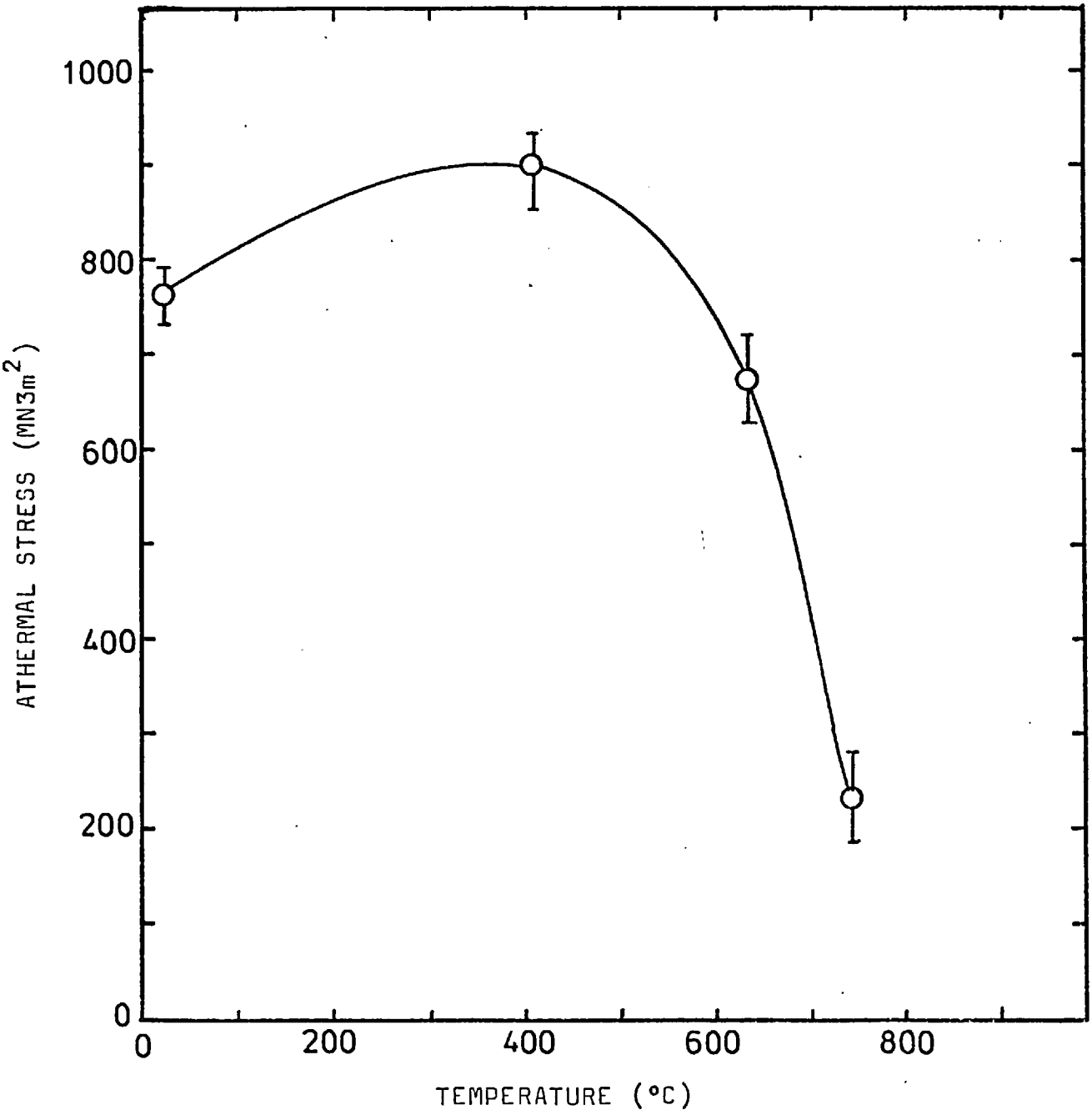

Fig. 4.60 Temperature dependence of Athermal stress of homogenised Alloy 1 and Aged Alloy 2.

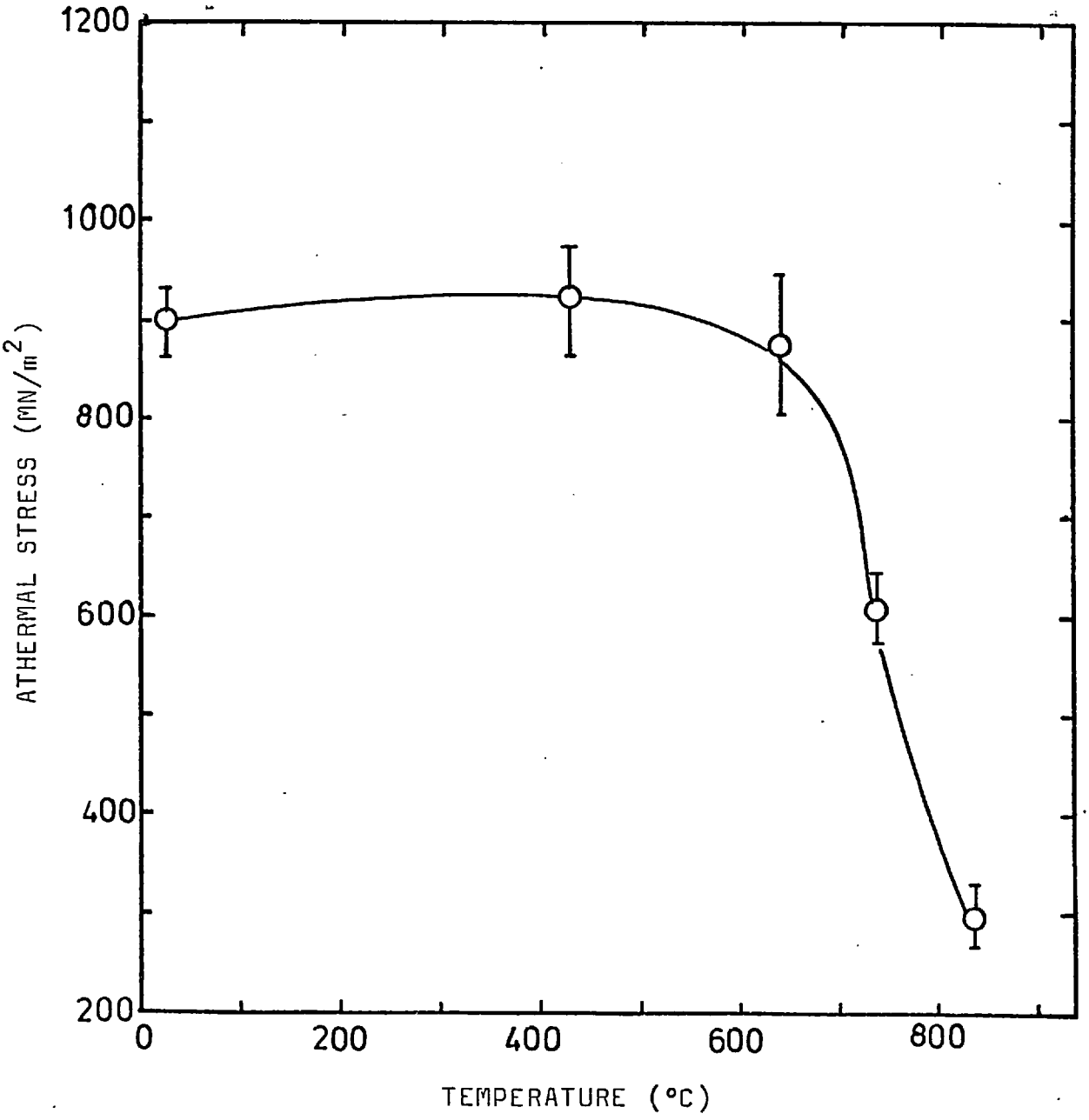

Fig. 4.61 Athermal stress of Alloy 3 as a function of temperature in as-cast, homogenised, and homogenised plus aged conditions.

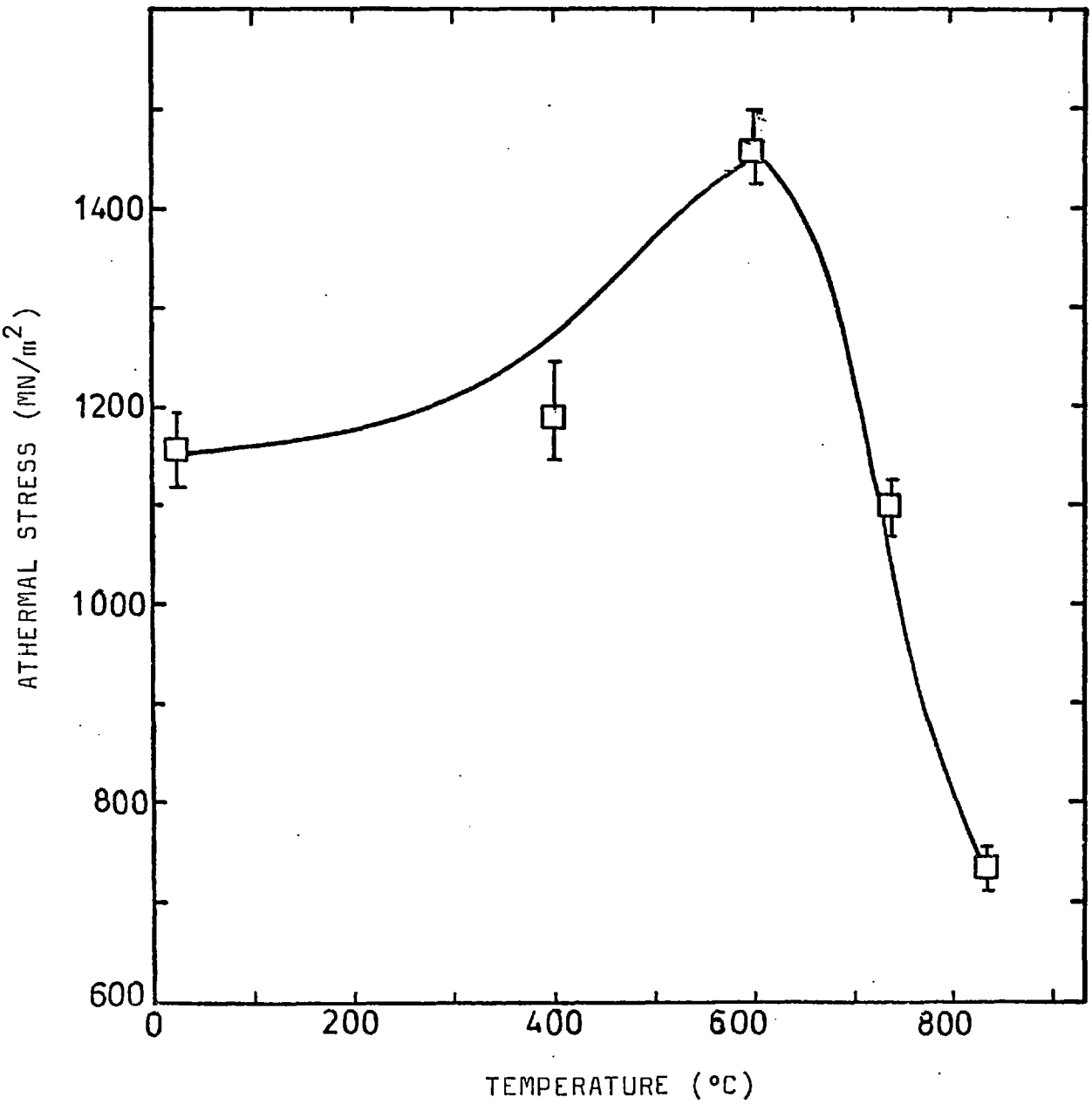

Fig. 4.62 Athermal stress versus temperature curve of Alloy 5 in homogenised condition.

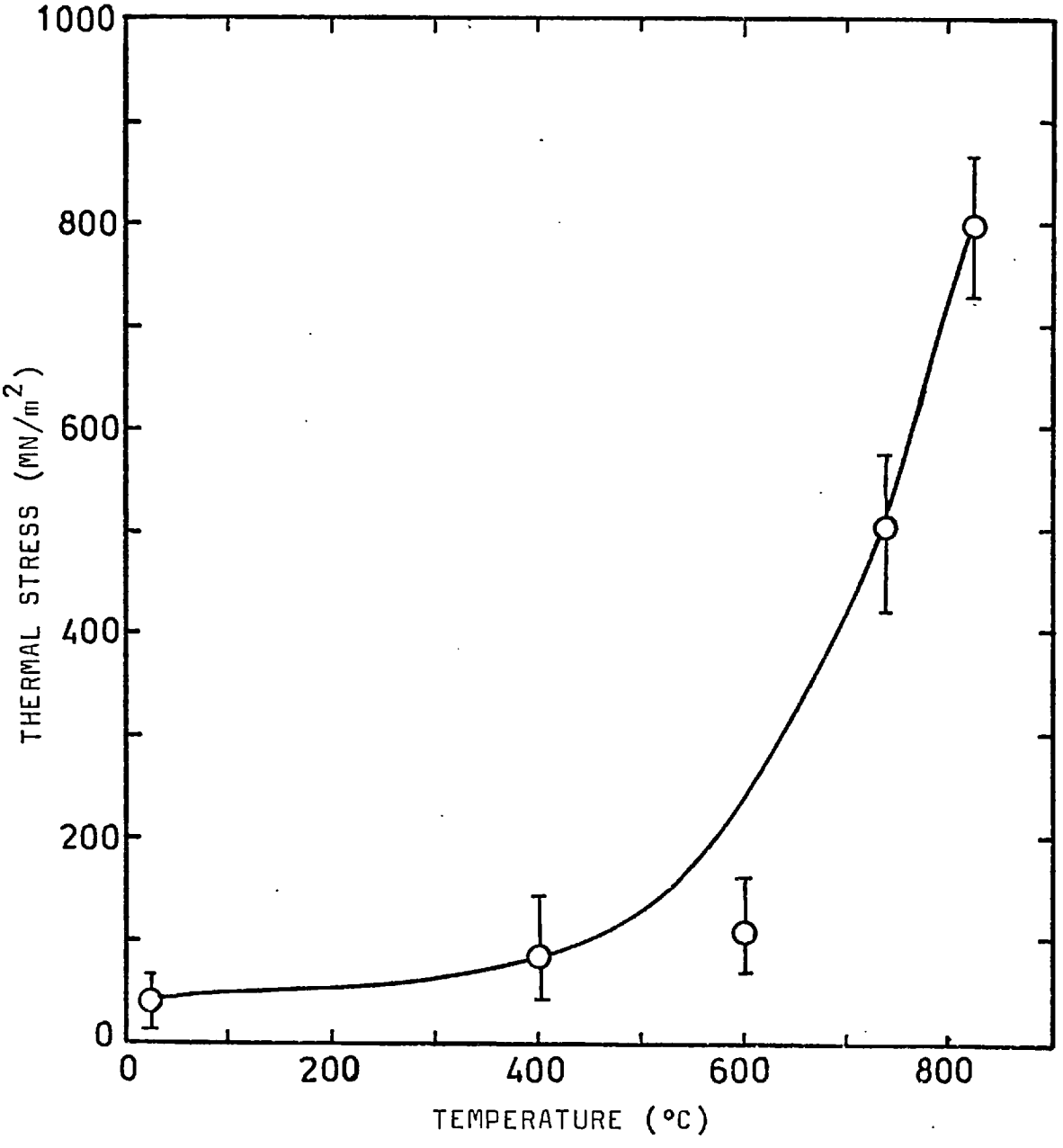

Fig. 4.63 Thermal stress versus temperature curve in Alloy 1, Alloy 2, Alloy 3, Alloy 4 and Alloy 5.

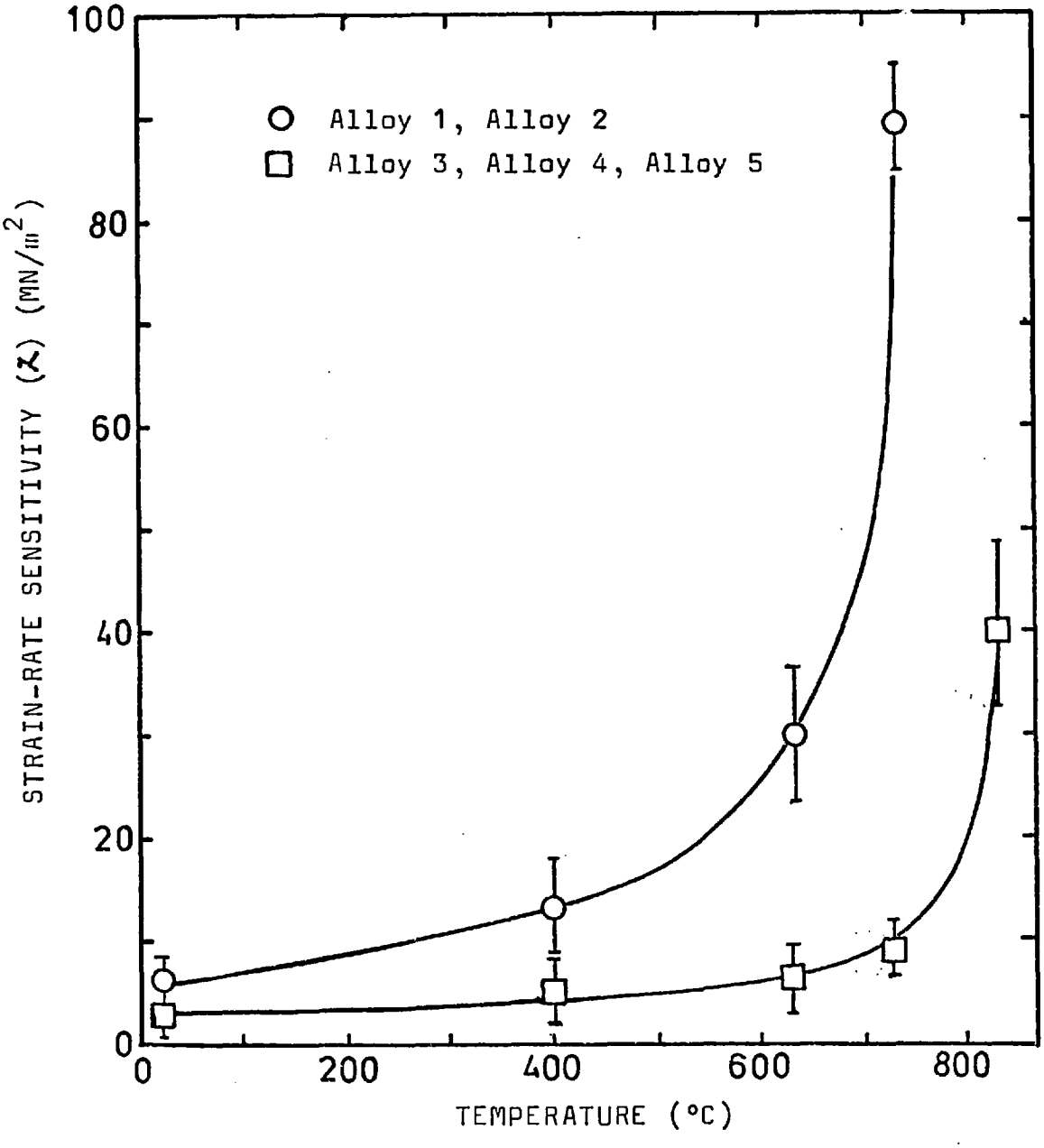

Fig. 4.64 Strain-rate sensitivity(λ) versus temperature curves for Alloys 1-5.

CHAPTER 5

5. DISCUSSION OF RESULTS

The discussion of results obtained in this work is presented in six sections. The discussion mainly deals with:

- The solid solution hardening of γ' phase by Ta and Hf,
- Eutectic type structure in the hafnium-containing alloys,
- The crystallography, nucleation, morphology and strength of β martensite,
- Dislocations in γ' on the Al-rich side of ternary $Ni_3(Al,Ta)$ and $Ni_3(Al,Hf)$ phases.
- Mechanical properties of the alloys investigated.

5.1. The effect of tantalum and hafnium on the Lattice parameter of γ' phase

It is known that tantalum and hafnium substitute for aluminium in the γ' phase (75,76,9). Since the atomic sizes of tantalum and hafnium are larger than that of aluminium (Table 5.1), for which they substitute in the γ'

Table 5.1 Atomic size of elements

Alloying Element	Goldschimdt diameter (Å)	Atomic size difference, compared to Al in %
Al	2,864	0
Ta	2,941	2,7
Hf	3,127	9,2

phase, it is expected that tantalum and hafnium will expand the lattice of the γ' phase. The observations that the lattice parameters of the $Ni_3(Al,Ta)$ and $Ni_3(Al,Hf)$ are considerably larger than that of binary Ni_3AL (Table 2.1,

fig. 4.3), show this expansion of the γ' lattice. Hafnium expanded the lattice parameter of γ' more than tantalum did (fig. 4.3). This is to be expected since there is a bigger difference between the atomic sizes of hafnium and aluminium than between those of tantalum and aluminium (Table 5.1).

5.2. Solid Solution Hardening of γ' Phase by tantalum and hafnium

Hardening will result whenever a dislocation encounters an irregularity within a crystal lattice. In this case, a dislocation is repelled by particles or atoms, so that it must do work to reach them, or it is attracted to them and thus becomes difficult to pull them away. There are various types of dislocation-solute interactions:

- Elastic
- Electrical
- Chemical

In elastic interaction if the total elastic energy of the system changes with the relative positions of the dislocation and the atom, they interact elastically and exert forces on one another. In trying to analyse such an elastic interaction it is usual to represent the atom in a crystal by an elastic sphere embedded in an elastic continuum[175,176]. Such a defect will interact with a dislocation, provided it either distorts the material around it or it is composed of elastically different material from its surroundings. The strains around substitutional solute atoms may be represented by a misfitting-sphere-in-hole model[177]. If the crystal is expanded by solute, it is supposed that the foreign atoms are larger than the ones they replace; hence they distort the lattice spherically just as an elastic sphere would, which had been forced into a spherical hole of smaller diameter in an elastic continuum[175].

As also mentioned above, alloying elements in solid solution can act as atomic-sized obstacles to dislocation movement. The biggest contribution to the flow stress of solid solutions arises from resistance to dislocation movement, the magnitude of which is sensitive both to[77]:

- atomic size differences,
- and differences in elastic properties between solute and solvent (modulus difference).

The presence of a dislocation in a crystal requires that extra work be done to insert a foreign atom into a crystal[177]. This extra work, the energy of interaction, is merely the work that must be done against the stress field of the dislocation in inserting the atom. For instance, in edge dislocations, the compressed region lies above the slip plane and the dilated region is below. Oversized atoms, since they expand the lattice, will be attracted to the position below the slip plane and close to the dislocation, undersized ones are repelled from that region and crowd into their low-energy positions above the slip plane; there they tend to contract the lattice, just as does the dislocation. In modulus interaction, if a solute atom is represented by a small region not of different size but of different elastic properties from the matric material, a second interaction is of at least equal importance[178,179]. In this case there is no pre-existing lattice distortion; the effect of solute arises only when the stress field of a dislocation is introduced. The interaction comes from the extra work which a dislocation must do as it approaches an elastically hard spot in the crystal (or extra work the dislocation must supply while being pulled away from a soft spot).

Fleischer (1963)[77] has investigated the strengthening of copper-base alloys, taking into account both the size factor effect and the effect of difference in shear modulus between solvent and solute atoms. Fleischer has concluded that both effects are substantial, but they will contribute a varying proportion to the increased

strength dependent on the solute metal. Fleischer has considered solid solution hardening effects in terms of the mismatch parameter $(\varepsilon_G' - 3\varepsilon_a)$

$$\text{where} \quad \varepsilon_a = \frac{1}{a_o} \cdot \frac{da}{dc}$$

$$\varepsilon_G' = \frac{1}{G_o} \cdot \frac{dG}{dc} \left(1 + \frac{1}{2G} \left| \frac{dG}{dc} \right| \right)^{-1}$$

where a is the lattice parameter, c the atomic concentration of solute atoms, and G the shear modulus. Fleischer has found a fairly close linear relationship between the solid solution hardening $(d\tau/dc)$ and the $(\varepsilon_G' - 3\varepsilon_a)$ mismatch parameter in certain copper base alloys. In an investigation of the effects of ternary elements on the solid solution hardening of the γ' phase Aoki and Izumi (1976)[41] have claimed a good linear relationship between the solid solution hardening $(d\tau/dc)$ and $(\varepsilon_G - 3\varepsilon_a)^2$.

In the present work these parameters have been calculated for $Ni_3(Al,Ta)$ phase:

a_o = 3,558 Å (Table 1.1)
a = 3,585 Å for γ' in homogenised Alloy 1 (Table 4.3)
dc = 4,4 at % Ta for γ' in homogenised Alloy 1 (Table 4.2)
$G_o = 7{,}55 \times 10^4$ MN/m^2 (ref. 27)
$G = 8{,}27 \times 10^4$ MN/m^2 for γ' phase (Ni - 20·5 at % - 4·5 at % Ta) (Ref. 27)
$\frac{d\tau}{dc}$ = 90 MN/m^2 per atomic Ta pct (ref. 18)

Results of calculations:

ε_a = 0·17
ε_G' = 2·11
$(\varepsilon_G' - 3\varepsilon_a)$ = 1,60
$(\varepsilon_G' - 3\varepsilon_a)^2$ = 2,56

These values are shown in fig. 5.1 with those of Aoki and Izumi. As this figure shows the better linear relationship is obeyed for the Fleischer parameter (fig. 5.1(a)). It appears that the Aoki and Izumi's parameter does not give

Figure 5.1

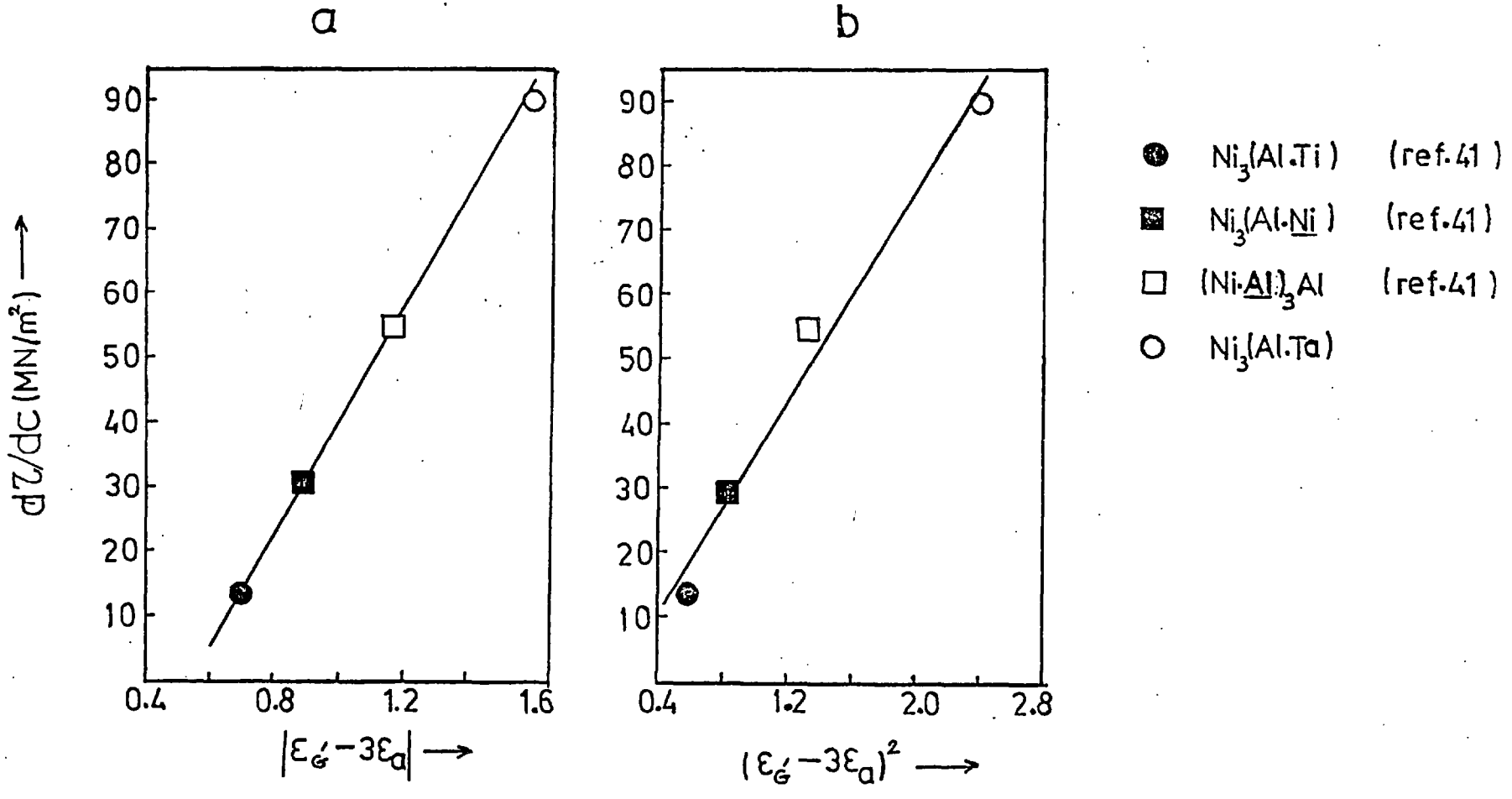

The relationship between $d\gamma/dc$ and Fleischer s parameter

The relationship between $d\gamma/dc$ and $(\varepsilon_{G'}-3\varepsilon_a)^2$

a good linear relationship (fig. 5.1(b)). According to the Fleischer relationship the contributions of the atomic size effect and the effect of the difference in shear modulus between solvent and solute to the solid solution hardening are 30% and 70% respectively. As this calculation shows the modulus effect is the dominant factor in the solid solution hardening of the γ' phase.

The correlation of the hardnesses of the $Ni_3(Al,Ta)$ and $Ni_3(Al,Hf)$ in the alloys investigated with the tantalum and hafnium concentration has shown that the hafnium has hardened the γ' phase more than tantalum did. This is to be expected since hafnium has expanded the lattice of γ' phase more than tantalum did. Unfortunately it was not possible to make a similar calculation for hafnium, because the change of the shear modulus of the γ' lattice with hafnium is not known.

The higher the concentration of tantalum and hafnium in the γ' the higher is the hardness (fig. 4.4). By means of microhardness measurements on the effect of hafnium on the γ' phase Doherty et al (1971)[38] have also found a similar result (fig. 2.11).

The more important significance of fig. 5.1(a) is that it confirms that both atomic size and shear modulus are important in determining the hardening of Ni_3Al phase by Ti, Ni, Al and Ta.

The deviations from stoichiometry generally lead to an increase or a decrease of the flow stress depending on both the temperature and the type of the defect structure. This increase of the flow stress resulting from the deviations of composition is sometimes termed defect hardening[169]. In an investigation of the composition dependence of the lattice parameter, the density and the long-range order parameter in Ni_3Al Aoki and Izumi (1975)[10] have concluded that at the Al-rich side all excess Al atoms occupy vacant face centre sites and at the Ni-rich side all excess Ni atoms occupy vacant cube corner sites; consequently the

compositions may be expressed as $(Ni.\underline{Al})_3Al$ and $Ni_3(Al.\underline{Ni})$, respectively, where underlined letters indicate excess atoms. As mentioned in the previous section, some elements substitute exclusively for Al atoms or Ni atoms, and the compositions are expressed as $Ni_3(Al.Ti)$ and $(Ni.Cu)_3Al$. Ti and Cu atoms occupy cube corner sites and face centre sites, respectively. Consequently, the deviations of composition are of the same kind as the exclusive substitution in the Ni_3Al phase[10]. From this it was suggested[10] that both the defect hardening and the substitutional solution hardening are controlled by the same mechanism, which is the elastic interaction between dislocations and the substitutional solute atoms. They have also suggested that the noticeable strengthening at the Al-rich side of Ni_3Al at room temperature is caused by this elastic interaction between dislocations and substitutional solute atoms. However, as observed in the present work (sec. 4.10.1) and discussed in sec. 5.6., 5.6.1. and 5.6.2., the dislocations along <111> have been observed and the {110} and/or {112} type slip planes have been suggested for these dislocations in the Al-rich γ' phases. It was suggested (sec. 5.6.2.) that the noticeable strengthening at the Al-rich side of Ni_3Al (fig. 2.16) is due to the existence of the dislocations along <111>, in addition to the dislocations along <110>. As tantalum and hafnium substitute for aluminium it would be expected that they will increase the strength as Al does at the Al-rich side of Ni_3Al; if also the shear modulus misfit parameter and the atomic size misfit parameter are taken into consideration, the strengthening effects of these elements will be higher than that of aluminium at Al-rich side. Rawlings and Staton-Bevan (1975)[18] have related the size misfit parameter to the solution hardening in Ni_3Al ternary alloys (fig. 2.15). They used the difference of atomic radius between solute and solvent as the size misfit prameter instead of the lattice parameter variations as used in this work, and found that the hardening rate increased with the size misfit parameter; the solid solution hardening by hafnium is higher than that of tantalum, due to the higher misfit parameter of hafnium (fig. 2.15).

Considering the difference of composition of γ' phase in the homogenised, and homogenised plus aged conditions of Alloy 1 the increase of the microhardness of γ' phase after ageing compared to the homogenised state (Table 4.6) is probably due to the higher aluminium content in the aged state of Alloy 1 (Table 4.2). Similarly the higher microhardness of γ' phase in the aged condition of Alloy 2, compared to its homogenised state (Table 4.6) could be due to the higher tantalum content of γ' phase in the aged condition of Alloy 2 compared to its homogenised state (Table 4.2). From comparison of the composition of γ' phase in Alloy 1, Alloy 2 and Alloy 3 (Table 4.2) it is expected that the γ' phase in Alloy 3 should have a higher microhardness than that of Alloy 1 and Alloy 2 since γ' phase in Alloy 3 contains considerably higher tantalum than that of Alloy 1 and Alloy 2 (Table 4.2). The observations confirm this (Table 4.6).

In the hafnium-containing alloys the higher microhardness of γ' phase in the as-cast state of Alloy 4, and the homogenised condition of Alloy 5 (Table 4.6) could be due to the higher hafnium contents in γ' phase in the as-cast state of Alloy 4 and the homogenised condition of Alloy 5 (Table 4.2).

5.3. Hafnium-containing alloys

5.3.1. Lamellar-type microstructure in the eutectic structure of Alloy 4 and Alloy 5

The lamellar-type structures are not perfectly parallel throughout an entire colony. In fact, the parallel structure is partially destroyed by extra lamellae at some places (fig. 4.9(a,b,c)). There is a line between extra lamellae (such as A-B in fig. 4.9(b)). This line is called a mismatched region in the lamellar structure[78,67]. The cause of these mismatched faults is simply the presence of an extra lamella. It is commonly believed that, as in all solidification processes, the eutectic reaction occurs by a nucleation and growth process. There is little doubt

that the initial stages of the reaction are controlled by heterogeneous nucleation on foreign particles in the liquid or of one eutectic phase on another[78-79, 185-189]. For the nucleation of lamellar type eutectic structure the different theories have been put forward. In the early theories, it was assumed that when the eutectic liquid was undercooled slightly below the equilibrium eutectic temperature, a nucleation centre promoted the growth of one of the phases in the form of a plate (fig. 5.2). As this plate grew, the liquid adjacent to it became enriched in the second component and the second phase then nucleated sympathetically on one side of the plate of the first phase, in its "equilibrium" orientation. The two plates could then grow simultaneously in an edgewise manner, and more lamellae of the two phases were supposed to continue to nucleate onto the sides of the growing eutectic composite and always in their equilibrium orientations. A slight modification of this growth model was given[190] in which the nucleation and growth of the first two plates of the eutectic structure occurred in exactly the same way as described above (fig. 5.2), but then further plates of both phases grew by the mutual overlapping of one phase over the edge of the other phase, thus avoiding the problem of repeated nucleation inherent in the early theories. However, an alternative, realistic model founded upon experimental observations, to replace this simple model mentioned above, has been developed as follows.

Impurity particles will undoubtedly be present in the bulk eutectic liquid and some of these will act as heterogeneous nucleation centres when the eutectic liquid is undercooled. In the eutectic region for the sake of discussion let the first phase to nucleate be the α phase (fig. 5.3) and consider the situation where it does in fact nucleate the β phase. The bulk liquid will supercool slightly before the α phase is nucleated by the impurity particle nucleus, but once nucleated it will grow very rapidly in the supercooled liquid and attain a finite spherical shape before the β phase is nucleated upon it

(fig. 5.3). Then the β phase will nucleate and grow both along the surface of the α phase and normal to it (fig. 5.3). As the β lamella grows out from the nucleation centre it overlaps the α lamellae that border it on both sides, giving rise to more β lamellae of the same crystallographic orientation as the first. The first β lamellae can be thought of as propagating circumferentially around the α nucleus in a discontinuous fashion (fig. 5.3). It is possible for the original α nucleus to nucleate two or more independent β lamellae each of which grow and multiply in the manner discussed. However, the growing nodule of eutectic will not now be a single eutectic crystal, but will consist of as many crystals as there were independent β nuclei. In general the lamellae of different grains will not be in parallel (fig. 5.3).

The nucleation and growth of an extra lamella has been considered by Kraft and Albright (1961)[78]. They proposed that if an extra lamella of one phase is nucleated and begins to grow, automatically an extra lamella of the other phase also occurs. The nucleation and growth of an extra lamella of one phase is shown shematically in the three portions of fig. 5.4(a). It can be seen that each extra plate (top sketch, fig. 5.4(a)) causes the formation of two faults - one at each end of the plate. However they showed that the extra lamellae usually did not nucleate at random as shown in fig. 5.4(a), but at a previously existing mismatch surface as shown in fig. 5.4(b); the nucleation of the extra lamellae at a previously existing mismatch surface is favourable since the surface energy in the vicinity of a mismatch surface is higher[67].

The micrographs have shown that the parallelism is partially destroyed by the presence of discontinuous lamellae, or terminations (fig. 4.9(a, b, c)), which force some minor adjustments in the positions of neighbouring lamellae (fig. 4.9(c)).

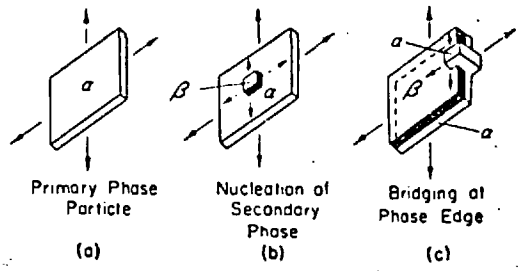

Fig. 5.2 Diagram showing the simplified nucleation and growth mechanism of lamellar eutectic alloys (From Tiller Liquid Metals and Solidification 1958, American Society for Metals, Metals Park, Ohio)[190]

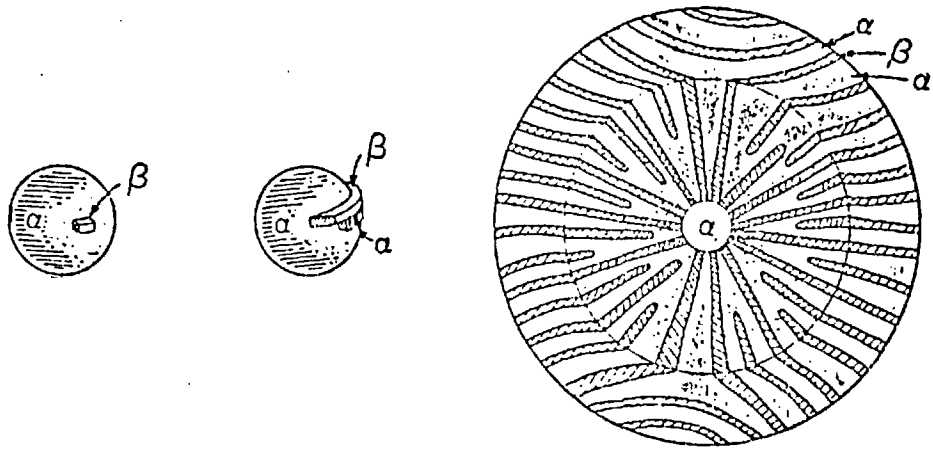

Fig. 5.3 Mechanism of nucleation and growth in lamellar eutectic alloys. (Ref. 67)

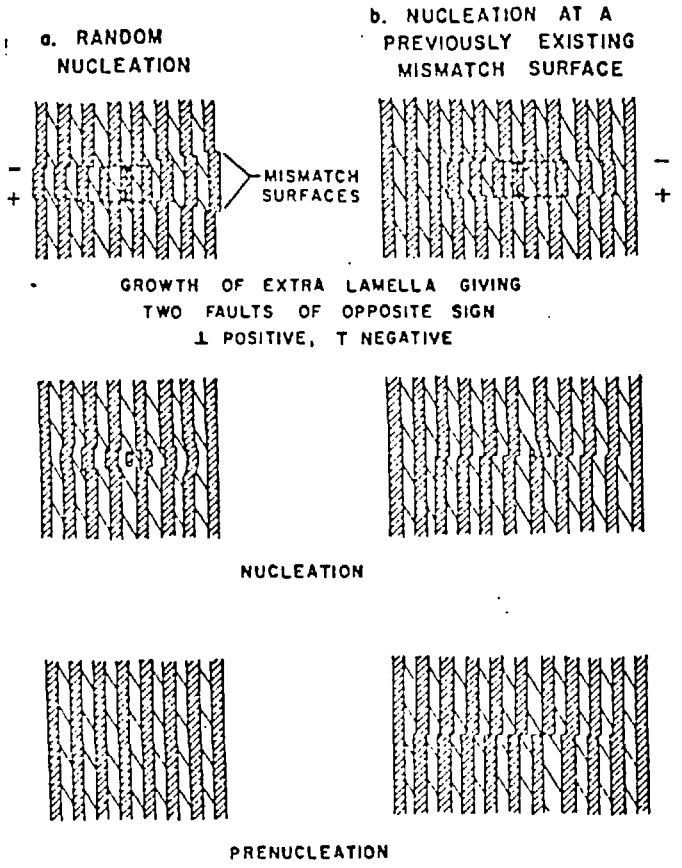

Fig. 5.4 Schematic representation of nucleation and growth of an extra lamella. Transverse sections. Growth direction from bottom to top.
(a) random nucleation,
(b) nucleation at previously existing mismatch surface
(from Kraft and Albright, 1961)[78]

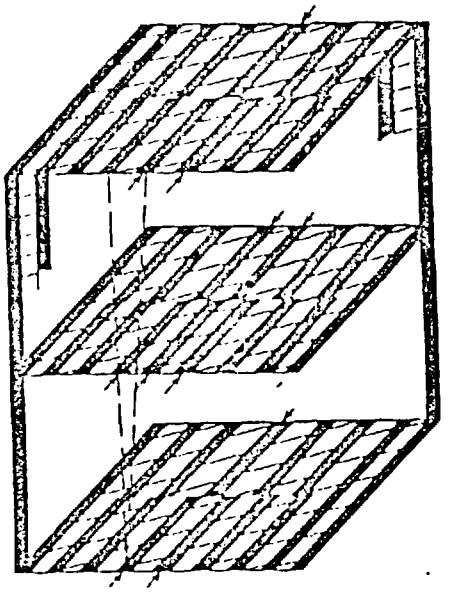

Fig. 5.5 Illustration showing shifting of lamellar fault during growth. Solidification direction was from bottom to top (Kraft and Albright)[78]

Fig. 5.5 shows shifting of lamellar faults during growth. It has been customary in previous works[191-194] to subdivide the whole field into several different structural groupings:

i) Normal eutectics, typified by the simultaneous growth of the two phases which produces structures with the two phases intimately intermixed. The lamellar structures, which have been observed in the hafnium-containing alloys, is classified in this group.

ii) Anomalous eutectics show much less coupled growth. The two phases are intermixed, but without a uniform crystallization front. This group is also called discontinuous microstructure, in which one of the phases of the alloy is dispersed in the second phase as discrete particles, and there is no continuity of the phase in any direction. The eutectic structure in the tantalum-containing alloys (in Alloys 1 and 2) could be classified into this group.

iii) Degenerate eutectics show no coupling. In fact the two phases attempt to minimize their area of contact and form separate crystals.

Scheil (1954)[193] qualitatively related the type of eutectic with the ratio of the two phases present; normal eutectics are formed when the amount of the two phases is approximately equal, anomalous or degenerate ones when one of the two phases predominates. However, Chadwick (1963)[195] found that, for example, the Zn-Sn eutectic with a ratio of the two phases 12/1 freezes as a normal eutectic at all growth rates. By investigating the structure of eutectics as related to undercooling for nucleation and the progress of solidification[196], it was found that normal eutectics were formed when one of the phases acted as nucleating agent for the other one, anomalous eutectics when both phases were nucleated independently by impurities. Thus

by classifying eutectic structures into one of these three classes not only the distribution of the phases can be defined, but also the solidification conditions that have produced them. It is apparent that this classification partly on morphology or mode of formation, applies only to the actual structure of any given sample. The presence or absence of some impurity decides the type of structure formed[187], and occasionally different types can be formed within the same alloy as observed in the hafnium-containing eutectics (fig. 4.8, fig. 4.10).

5.3.2. Orientation Relationship

There are a number of factors which might influence the orientation relationship of the phases in eutectic alloys[79]:

i) The disregistry or lattice misfit, between particular directions in two types of crystals.

ii) The atomic density or interplanar spacing of planes in two types of crystals.

iii) The degree of undercooling of the eutectic alloy during solidification.

As Table 5.2 shows the atomic density or interplanar spacing is highest in the (0001) plane in α phase. The surface energy increases as the surface is rotated from its low-index (high atomic density) orientation; in other words, the energy of the interface will vary inversely with the density of atoms from each structure which coincide in the boundary planes[80]. Then it is expected that the $(0001)_\alpha$ plane has a lower surface energy than that of the other planes. Since the {110} planes are the densest planes in BCC structures, these planes would have lower energy than any other plane in the structure. Therefore this argument suggests that the $(0001)_\alpha // (110)_\beta$ orientation relationship is the lower-energy form in the eutectic.

Table 5.2. Relative density of atoms, and interplanar spacings in $\{10\bar{1}0\}$ and (0001) planes

Phase	c/a ratio	Ratio of atom density, $\frac{(10\bar{1}0)}{(0001)} = \frac{2/ac}{2/a^2\sqrt{3}}$ or Ratio of interplanar spacing
α	1,23	0,703

Kraft (1963)[81] has shown that the parallel lamellae tend to assume a unique crystallographic relationship during unidirectional growth of Al-$CuAl_2$ eutectic. The hypothesis was proposed in that the phase particles tend to become aligned in a particular way during the course of solidification because the interfacial energy between them is thereby minimized. Other workers have also confirmed that lamellar structures have low-energy forms of eutectic (78,82,67).

5.3.3. Comparison of the phases existing in the hafnium-containing alloys with the literature

In the present work three phases have been found to exist in the as-cast condition of the hafnium-containing alloys (e.g. Alloy 4, Alloy 5), by x-ray diffraction and transmission electron microscopy. These phases are γ′, β and α phases. The α phase, which has an hexagonal structure, has been determined[167] to be the Ni_3Hf type intermetallic compound. It appears therefore that the present experimental results agree with the ternary Ni-Al-Hf isothermal diagram which was determined experimentally by Markiv and Burnashova (1969)[9] (sec. 2.13; see fig. 2.3(a)). According to Kaufman and Nesor's[8] predicted isothermal of the Ni-Al-Hf ternary diagram (sec. 2.13; fig. 2.3(b)) at 800°C the present alloys should consist of γ′ + β + μ ($Ni_{64}Al_{20}Hf_{16}$) or γ′ + μ + y (Ni_7Hf_2) which does not agree with the present result.

The $Ni_3Hf(\alpha)$ phase has been reported as having the $TiNi_3$ (DO_{24}) type structure[170].

5.4. The β martensite

5.4.1. Crystallography of β martensite

Experimental observations have shown that the high-temperature ordered bcc ($L1_o$) β phase decomposes during quenching to form martensite which was found to be body-centred tetragonal (bct) in structure by x-ray and transmission electron microscopy. The β phase also decomposes to martensite at slower cooling rates, as occurred in the as-cast states of Alloys 1 and 2, which suggests that for the martensitic transformation of the β phase, sudden quenching is not a necessary condition for these alloys. Zelenin et al (1971)[27] have also observed the same result for the binary β phase with 64 at % Ni. The bct structure of β martensite has also been observed[21,25] in the past and, Enami et al (1973)[23] and Moskovic (1974)[25] have described it as an inverse Bain correspondence as shown in fig. 5.6(a).

As fig. 4.26(b) shows sometimes $0\frac{1}{2}\frac{1}{2}$ superlattice reflections arise in diffraction patterns. Such extra reflections has also been observed[25] in the β martensite. A crystal structure has been proposed[25] to account for the presence of $0\frac{1}{2}\frac{1}{2}$ superlattice reflections (fig. 5.6(b)); it is proposed that this structure is characterized by alternate stacking of Ni atoms and Ni or Al atoms on (011) planes and called as "Super-ordered".

In the β martensite the following faults have been observed:

i) The $\{101\}_{bct}[101]_{bct}$ twinning system has been observed to exist in the β martensite plates. Two variants of the {101} have also been observed in the neighbouring martensite plates. Within one martensite plate evidence of these variants have

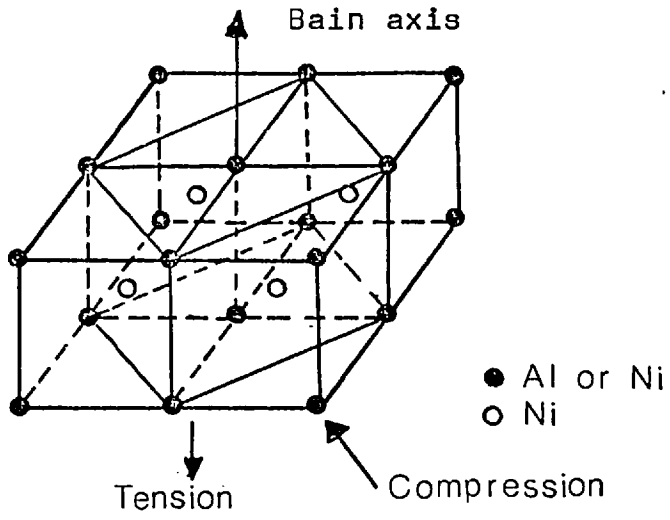

Fig. 5.6(a) Inverse Bain distortion for a body centred cubic lattice transforming to a body centred tetragonal lattice (BCT). The BCT lattice is equivalent to the CuAu I structure, which is outlined inside the four BCT cells (ref. 25).

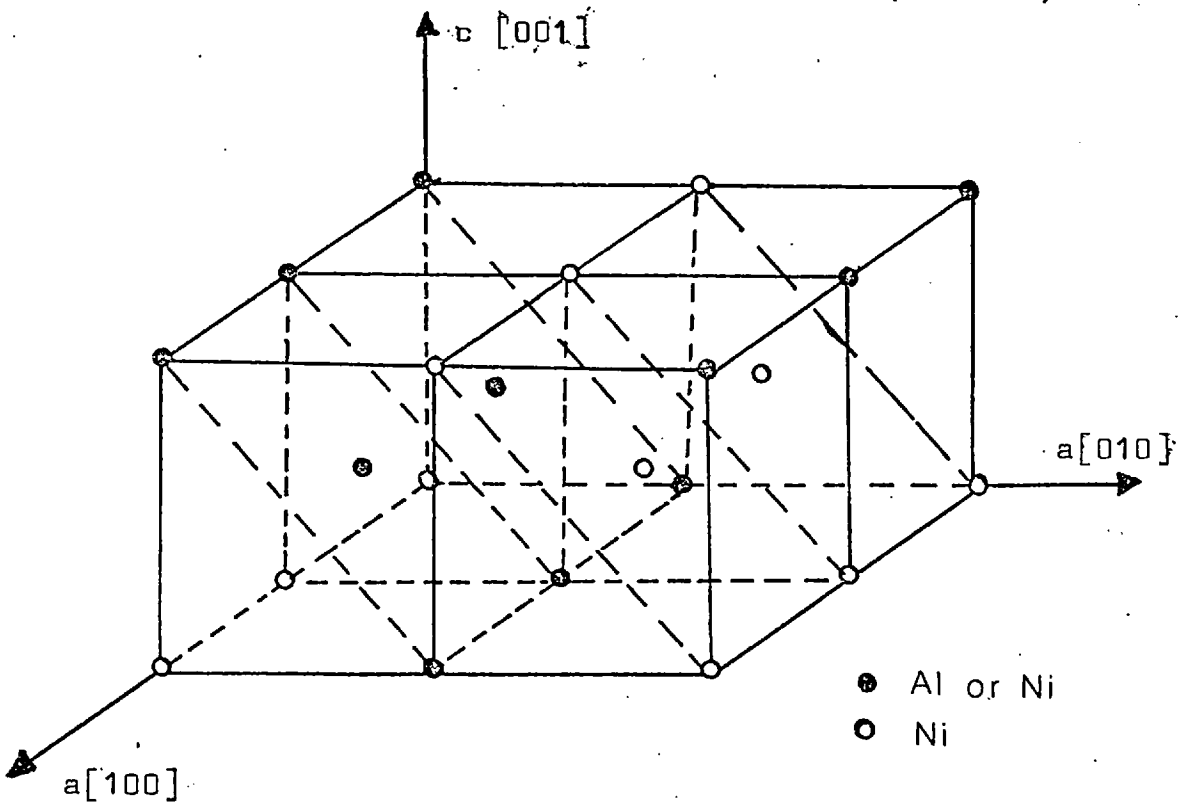

Fig. 5.6(b) The crystal structure of NiAl martensite showing further ordering brought about by coordinated lattice shear. Four unit cells are shown (ref. 25).

been inconclusively observed to exist.

ii) The {110} planar faults have been observed from the striations and the streaks in the reciprocal space.

iii) In the neighbouring martensite plates the evidence of the {210} and {012} planar faults has been found inconclusively.

Evidence of the <210> streaks has been recently found in β martensite with the Al - 62·25 at % Ni composition by Raynaud (1977)[68]; the origin of these effects was not explained, but it is probable that they are due to the existence of the {210} type fine planar faults.

The {110} type planar faults, which are observed in this work, has been interpreted as the twinning fault by Muir (1975)[21]. However, the {110}[110] twinning system is not a possible twinning system[171,172] in the bct structure.

The twinning systems in the {101}<101> and the {111}<112> are possible twinning systems in the bct[171] and observed in the β martensite in the past. Although the {101}<101> twinning system has been commonly observed in the β martensite the {111}<112> twinning system has not been observed in the present work. Assuming the {111}<112> twinning system exists in the β martensite the lack of the observation of the {111}<112> twinning system may be due to the twinning shear in the system {101}<101> (b = 0·38Å) being much less than in {111}<112> (b = 0·70Å), which may be taken as the factor responsible for predominant twinning in the {101}<101> system.

From the combined examination of the striations in the image and diffraction patterns it appears that several fine, planar fault systems exist in the β martensite. If the faults are taken into consideration as necessary for

martensite transformation then it appears that multishear mechanisms must be taken into account to predict the crystallographic features of β martensite. The classical phenomenological theory of martensite is based on the assumption that the shape deformation associated with the phase transformation is an invariant plane strain so that one plane is left undistorted and unrotated by the shape deformation. This implies that the lattice deformation which together with any necessary atomic shuffling converts one structure into other, is accompanied by a second deformation which leaves the lattice in which it occurs unchanged and by a lattice rotation. This lattice invariant deformation is usually assumed to be either slip or twinning, but faulted product structures, as observed in the present work, are also possible[85]. However, the effects on the macroscopic crystallographic features arising from the simultaneous occurrence of the independent lattice invariant shears cannot be predicted correctly by using the classical phenomenological theory[86,87]. More general approaches to the martensite crystallography have been made in terms of double or multiple shears[86-88]. On the basis of the calculation of the total energy, which consists of surface, strain and chemical driving force, for the transformation from a matrix to martensite, it was shown by Easterling and Thölén (1976)[89] that twinned nuclei of martensite have a lower energy than untwinned nuclei and also further strain energy reduction can be obtained if twins form on two or more systems instead of only one; therefore the existence of the different variants of the twinning faults in the β martensite occurs in order to reduce the energy of the martensite formation.

As shown in fig. 4.26 within one martensite plate the striations in two directions exist. These striations have been interpreted as the twinning faults lying on the two variants of the {101} plane (sec. 4.91). Different faults or the different variants of the same fault in one martensite plate have also been reported in the past by a number of workers[98,109,144,147,149]. Warlimont (1965)[98] has suggested that this effect is due to interactions of

different martensite plates during growth; in other words, impingement of martensite plates. Evidence of such an impingement in the present case is shown in fig. 4.26 (at C-C). However, as mentioned above two variants of this fault in one martensite plate exist in order to reduce the strain energy[89], which seems more likely.

The occurrence of self-accommodating groups, which are observed in the present work, in addition to individual martensites are thought[108,107,106] to be the reason why the twinning on several systems occurs.

Combined examination of micrographs and diffraction patterns has suggested that the martensite plates are in twin orientation with one another on the {101} planes.

5.4.2. The Fine Precipitate in the β phase

The heat treatment of Alloy 1 and Alloy 2 in the two phase region (β + γ′) has produced streaking along the <110> directions in electron diffraction patterns. The corresponding micrographs have shown a tweed-like structure. This pronounced streaking along the <110> directions is interpreted as indicating the existence of small, coherent, disc-shaped particles on {110} planes (Hirsch et al, 1965)[90].

Any difference in atomic spacing between the precipitate and matrix phases results in coherency strain fields around the clusters. The strain field of each precipitate has an associated strain energy (self strain energy) and, in addition, the interactions of the strain fields of nearby clusters involve interaction strain energies. In general, the strain energy as well as any additional energy associated with the precipitate-matrix interface depend on the configuration (shape and orientation) of the precipitate whereas the bulk free energy change is configuration independent. The precipitates are thus expected to form preferentially in configurations, which minimize a combination of strain and interfacial energies, thereby minimizing the free energy of the precipitates. The self

strain energy of an inclusion has been shown to depend on the shape of the inclusion[91,181-183].

Nabarro (1940)[91] has shown that when there is an appreciable difference in atomic size, as in the present case: Ni-2·492Å, Al-2·864Å, a plate or disc is likely to have the lowest strain energy. Furthermore, such discs tend to nucleate parallel to {100} planes since cubic crystals are elastically anisotropic to some degree and thus possess a minimum Young's modulus along <100> directions[92]. However, in the present case, the discs lie parallel to {110} planes. The question now arises as to why this happens. Typkin (1964)[93] has suggested that the answer lies in the relative degree of elastic anisotropy of the solvent (matrix). This may be seen by examining the elastic anisotropy factor, $A = 2C_{44}/(C_{11} - C_{12}) = G_{<100>}/G_{<110>}$. Enami et al (1976)[94] have obtained a value of A = 8·95 for β phase for Al-63·2 at % Ni, which composition is similar to the β phases investigated in the present work. This shows that the β phase is highly anisotropic. As the A, anisotropy factor, is much greater than unity $G_{<110>}$ becomes a minimum, where $G_{<110>}$ is the shear modulus along the <110> direction. This argument supports the idea that the β phase will have relatively low resistance to shear on {110}<110> (Christian, 1965)[85].

The precipitation has probably occurred during quenching since the shear resistance on the {110}<110> system decreases with decreasing temperature (see fig. 5.7 (c)).

However, the dependence of the self strain energy of nonspherical coherent precipitates on their orientation in an elastically anisotropic matrix has been examined by Schwellinger et al (1971)[184] in the special case of two-dimensionally infinite misfitting precipitate sheets. Their results indicate that plates will lie on {100} or {111} planes when the A is greater or less than one; respectively.

5.4.3. Nucleation of β martensite

Any phase transformation requires a re-arrangement of the atomic structure of the assembly. The atoms take up new relative positions under the influence of the different factors, such as the strain energy, surface energy, or external force etc.

The driving force for martensitic transformation is the difference in free energy (usually Gibbs free energy) of the initial and final states. By definition, martensitic transformations involve no concentration changes. In the absence of surface and strain energy contributions the free energy change upon transformation from β parent phase (P) to the β martensite (M) may be written

$$\Delta G_i^{P\rightarrow M} = G_i^P - G_i^M$$

However, beyond the formation of an interface the very nature of martensitic transformations causes transformation-induced defects (interstructural interfaces, twin boundaries, stacking faults etc.) and elastic strains such that the effective free energy change is modified by these "non-chemical" contributions:

$$\Delta G_{eff}^{P\rightarrow M} = \Delta G_i^{P\rightarrow M} + (\Delta G_d + \Delta G_\epsilon)$$

where ΔG_d = the interfacial free energy and the free energy due to the transformation induced defects, ΔG_ϵ = the strain free-energy due to elastic strains (volume and shear strains) arising from the transformation.

The amount of supercooling (that is the difference $T_o - M_s$; To is the temperature at which parent and martensite have the same free energy) is a measure of the driving force needed to begin the transformation. When there is a small shape change associated with the formation of martensite, the driving force, $T_o - M_s$, the temperature range of transformation, $M_s - M_f$, and the hysteresis, $A_f - M_f$, are usually small[113]; especially when these can be self-accommodating

as observed in the present work, the transformation begins at small driving forces and is completed in small temperature intervals[113]. For a binary β NiAl alloy of similar nickel content to homogenised Alloy 1, the small M_s-M_f and A_f-M_f (hysteresis) have been observed[101]. These suggest that the temperature at which the transformation begins is influenced by non-chemical terms in the overall energy change of β martensite.

In addition to the factors mentioned above which influence the nucleation of martensite, other factors might influence also the nucleation of martensite have been suggested in the past, one of which is the elastic anisotropy consideration:

The two primary moduli parameters characterizing resistance to shear in a cubic crystal are C_{44} and $C' = 1/2\ (C_{11} - C_{12})$[80]. The concept of lattice instability has been introduced to explain martensitic transformation[95]. Warlimont and Dealey (1974)[96] have considered martensite transformations in their review article and have drawn the following conclusions on the transformation of the bcc phases:

1) The elastic anisotropy factor, $A = 2C_{44}/(C_{11} - C_{12})$ increases with decreasing temperature as Ms is reached.

2) A increases with changes in composition as the concentration range of instability to martensitic transformations is approached.

3) Superlattice formation and other coherent precipitation reactions upon cooling of bcc alloys raise C'.

The transformation of β phase to the martensitic structure has been considered here in terms of elastic moduli. Enami et al (1976)[94] have determined elastic constants of a nickel-rich β phase with the Al-63·2 at % Ni

composition, which is similar to the compositions of the β phases in the present work. Fig. 5.7(b) shows the temperature dependence of the shear constant $C' = 1/2 (C_{11} - C_{12})$, i.e. for the shear along the $[01\bar{1}]$ direction in the (011) plane, and fig. 5.7(c) the anisotropy factor $A = C_{44}/C'$. The shear stress on the (011) plane along the $[01\bar{1}]$ direction has been given by Mercier and Melton (1976)[97]:

$$\sigma_c = \frac{2\alpha}{l} \cdot b\left[\frac{(C_{11} - C_{12})}{2} \cdot C_{44}\right]^{\frac{1}{2}}$$

σ_c is the critical stress for dislocation multiplication by the Frank-Read mechanism, where l is the length of a dislocation and α is a constant. Mercier and Melton (1976)[97] have used the influence of an anisotropic elastic medium on the motion of dislocations on the nucleation of the martensite phase. They have suggested that for a material showing the elastic anisotropy factor $A = 2C_{44}/(C_{11} - C_{12})$ increasing with decreasing temperature towards Ms will lead to the transformation of a material according to the above formula.

As fig. 5.7 shows, $C' = 1/2(C_{11} - C_{12})$ decreases with falling temperature towards Ms while A increases. These results suggest that elastic softening (the critical shear stress σ_c decreases), i.e. lattice instability along $[0\bar{1}1]$ on (011), exists in the NiAl phase. Hence, these anomalies suggest that the martensitic transformation may be nucleated by $(011)[0\bar{1}1]$ shears of the β phase lattice [80,97]. The hypothesis that the lattice instability is a trigger of the martensitic transformation has been applied to several martensitic transformations in the past[98,99].

Moskovic (1974)[25] has proposed that nucleation of martensitic β employs supercritical precipitate regions which are formed during cooling.

The temperature dependence of the shear modulus of nearly stoichiometric NiAl (50·6 at % Al) between - 150°C

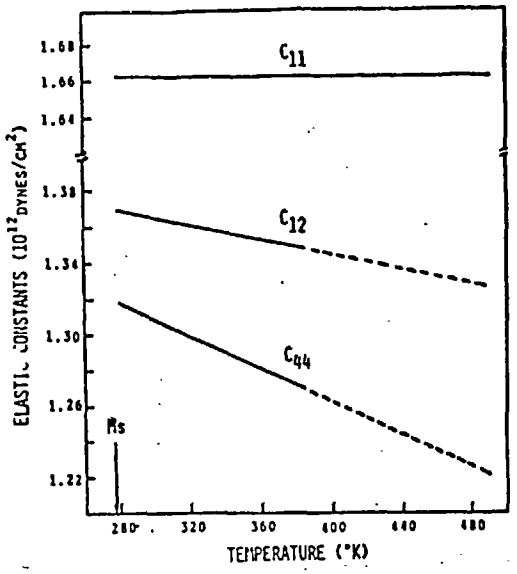

(a)

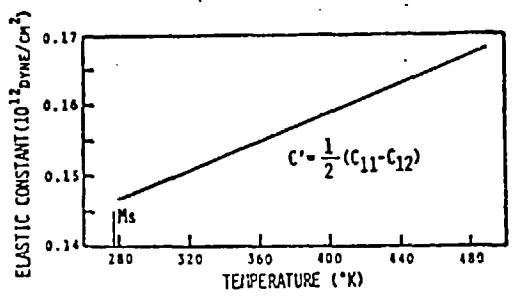

(b)

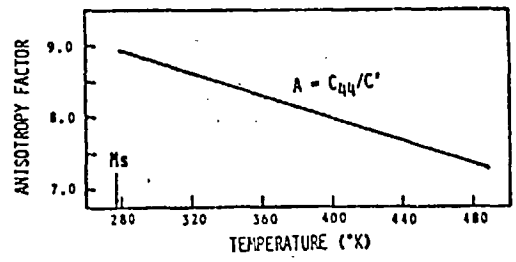

(c)

Fig. 5.7 Temperature dependence of the shear constants in the Al - 63·2 at % Ni alloy.

a) elastic constants C_{11}, C_{12} and C_{44}
b) the shear constant C'
c) the anisotropy factor A

and 800°C, which was determined by Wasilewski (1966)[100], exhibits no such lattice instability such as those reported[139] for the nickel-rich Al-63·2 at % Ni alloy; this supports the suggestions given above on the nucleation of β martensite, because it is known[101] that the β phase with the Ni-50·6 at % Al composition does not undergo martensitic transformation during cooling from the β phase.

5.4.4. Morphology of Martensite

A detailed transmission electron microscopy investigation of β martensite in the homogenised and as-cast states of Alloy 1 and Alloy 2 has shown two distinct morphologies; the banded and acicular respectively. Up to three groups of martensite plates (or bands) have been observed. In each group the martensite plates are parallel-sided.

One type of banded martensite consists of alternating lamellar martensite plates. This arrangement of lamellae is shown schematically in fig. 5.8. It is a concept of the phenomenological approach that the interface between the parent and the growing martensite must be a plane of zero average macroscopic distortion. In the lamellar martensite these strains in the (M) and (T) neighbouring plates (fig. 5.8) are opposite in sense[102]. These strains are not generally of equal magnitude. Therefore a fixed ratio of the width of the lamellae, which was observed in each group of martensite plates, is necessary to ensure an overall zero distortion. Under these conditions the microscopic strains introduced by the alternating individual lamellae compensate each other at the plane of the interface. The magnitude of strain due to the shear increases with increasing size of the martensite plates such that a group of plates with a shear component in the opposite direction if favoured to form[96] at the plane of the interface. The production of parallel-sided rather than lenticular plates seems to be possible because the crystallography is degenerate in the sense that opposite shape deformations may possess a common invariant (habit) plane. Martensite

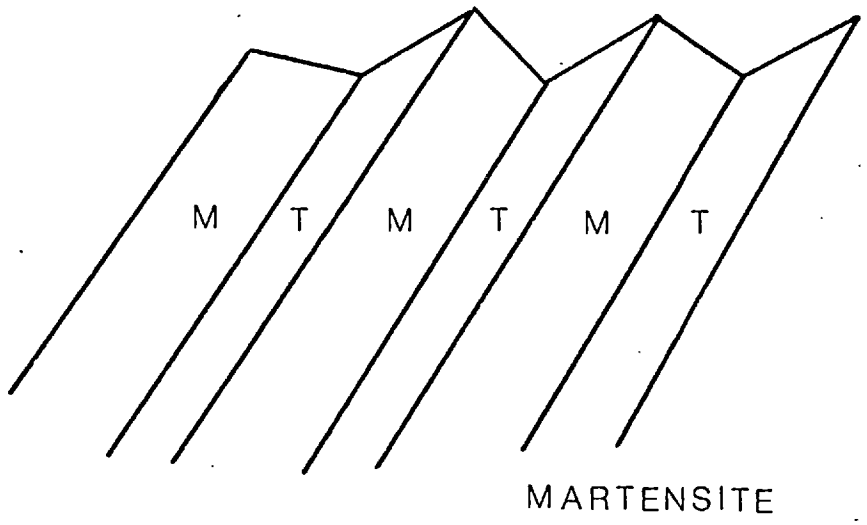

Fig. 5.8. Schematic representation of the interface. The microscopic strains in the lamellae (M) and (T) are in opposite in senses, and for appropriate width ratio of the lamellae are self-accommodating to zero average macroscopic strain.
(from Wasilewski, 1975)[102]

plates can thus accommodate one another, so that accumulating long-range stresses in the matrix are avoided[85]. This mechanism leads to a quasi-autocatalytic process of formation of neighbouring individual or groups of martensite plates with opposite shear components[85].

The growth of a self-accommodating system is favoured over that of individual martensite plates because it is associated with a lower rate of increase in strain energy during growth[103-105]. The occurrence of multi-shears has been attributed to the presence of self-accommodating groups of martensite plates[106-108]. In the similar morphological structure found in Cu-Al martensite by Tas and Deruyttere (1973)[103] it has been suggested that the high degree of mechanical coupling between the martensite plate combinations is responsible for the self-accommodating mechanism.

It has been suggested by Wasilewski (1975)[102] that an essential feature of the martensite formation is its self-accommodating nature, and for that reason the martensite crystallography, in general, cannot be predicted correctly by an invariant plane strain approach. Since martensite formation in bulk material is a three-dimensional phenomenon it is expected that there is no reason why the strain should be minimized in only two dimensions; however, the classical phenomenological martensite theory proposes an inhomogeneous (two dimensional) shear strain minimization of the invariant plane strain condition associated with the formation of a habit plane. Tas et al (1973)[105] have shown that for the twinned γ_1' martensite (hcp structure), which occurs in the Cu-Al and Cu-Sn systems, the three-dimensional strain minimization rather than the two-dimensional invariant plane strain condition determines the "fine structure" of the martensite plates. It has been further shown[105] that since the simultaneous growth of three or more different martensite plate variants is, in general, spatially impossible, the third and further variants will be present as fine internal plates in the first two variants, and the presence of fine internal

twins is energetically the most favourable situation; this may account for the presence of fine internal twinning and fine planar faults observed in the present study.

There is a tendency for the morphology to change from mainly plate-like to acicular type martensite morphology with increasing nickel content in β martensite. This may be seen by comparing the general features of Alloy 2 in the homogenised condition and with the homogenised and the as-cast states of Alloy 1 (fig. 4.25, fig. 4.26, fig. 4.28, fig. 4.33). It has been reported[113,114,111] that the fundamental factors that determine the morphology of martensite are:

i) The relative yield strengths of the parent and product phases.

ii) The magnitude of the shape strain.

iii) The multiplicity of the habit plane adopted.

iv) The stacking fault energy.

Kelly and Nutting (1961)[111] have suggested, and Marder and Marder (1969)[112] have shown that the transition in morphology from low-carbon to high-carbon martensite in iron-carbon alloys is a function of the Ms temperature. In the present study, such a tendency has been found. The Ms temperature of binary β martensite increases with increasing nickel content (fig. 2.9), whereas the morphology changes from completely plate-like in β phase with 60 at % Ni in the homogenised state of Alloy 2 to mostly acicular type in β martensite with 66·7 at % Ni in the as-cast state of Alloy 1. This suggests that the tendency for the transition from plate-like to acicular-type morphology increases with increasing transformation temperature (Ms).

The existence of the acicular type morphology in martensite has been mainly attributed to the constraints imposed on the growth of a plate by the surrounding matrix[85].

As the formation of the acicular-type morphology increases with the increasing nickel content or Ms temperature of β phase according to the above discussion, the strength of the β phase is expected to increase with the increasing nickel content in the same way. This suggests that the tendency to form the acicular type morphology increases with increasing strength of the β matrix; according to reference (85) the constraints imposed on the growth of a plate by the matrix β phase will increase; therefore the tendency to form the acicular type will increase.

Kelly and Nutting (1961)[111] have also suggested that, in addition to the Ms temperature, the stacking fault energy is the other important factor that affects the morphology of martensite. According to them, lowering the Ms temperature or raising the stacking fault energy in ferrous martensite should favour the formation of martensite plates.

The x-ray studies and the transmission electron microscopy have shown that the β phase in Alloy 3 did not undergo martensitic transformation. As is known[26] no thermally induced martensite should be expected for β NiAl alloys, containing less than ≈ 60 at pct Ni. Therefore the retention of β phase in Alloy 3 may indicate that the β may contain less than 60 at % Ni.

5.4.5. The possible factors affecting the strength of martensitic β phase

It has been recognised that no single mechanism is responsible for the strength of martensites (111-117). The following factors which have been suggested as contributing to the strength of martensites (115,96,113):

5.4.5.1. Solid Solution hardening
5.4.5.2. Size of martensite plates
5.4.5.3. "Substructure", e.g. dislocations and internal twinning within the martensite crystals

5.4.5.1. Solid Solution Hardening

A significant increase of the low temperature strength of β phase results from departure from the stoichiometric composition (fig. 2.19). As the β phases investigated contain much more than 50 at % Ni (Table 4.2), the β phases potentially could have considerably higher strengths than the stoichiometric alloy. The hardness of the β phase with 66·7 at % Ni in the as-cast state of Alloy 1 (707; in Table 4.6) is much higher than that of stoichiometric alloy (≈350 HV in the binary stoichiometric composition; ref. 33), indicating the importance of off-stoichiometric composition. In bulk, although the as-cast and homogenised states of Alloy 1 do not show the same morphology, it is suggested that the considerable softening of the β phase after homogenisation (Table 4,6) in this alloy is mostly due to the decrease of nickel content after homogenisation (Table 4.2). The effects of morphology on the strength of β phase will be discussed later. As is known from Fleischer's work (1963)[77] the size of the misfit parameter ($\varepsilon_a = 1/a_o \cdot da/dc$), (where a_o and c are lattice parameter of β phase and concentration of tantalum content respectively), is one of two factors which influence strengthening of solid solutions, not forgetting that the shear modulus is one of the major contributing factors. As the lattice parameters of the ternary β phases (NiAlTa) did not change significantly compared to the binary β phase (NiAl)[118] it appears that the tantalum content (⩽1 at %) did not markedly increase the strength of the ternary β phases. Therefore it may be suggested that the tantalum content in martensitic β phases also does not affect significantly the strength.

Arkhangel'skaya et al (1972)[53] have investigated the effects of cobalt and iron on the nickel-rich β martensite. They have found that addition of 6 at % cobalt or iron did not affect the microhardness significantly, but when the nickel concentration was raised the microhardness increased.

5.4.5.2. Size of martensite plates

Evaluation of product grain size effects in martensitic alloys is difficult since plates or needle dimensions vary.

Based on the hypothesis that a grain boundary constitutes a barrier to dislocation movement, a quantitative relationship between strength and grain size has been proposed by Hall (1951)[116] and Petch (1953)[117]. It has been shown by many workers (118-121) that a Hall-Petch type relationship, $\sigma = \sigma_o + \kappa_y \cdot d^{-\frac{1}{2}}$, holds for the yield stress as a function of martensite plate thickness. Where σ is the yield stress, σ_o a lattice friction stress, κ_y a locking parameter, and d the grain diameter (in this case, thickness of martensite plate). The effect of grain size on the yield stress is thus dependent upon the locking term in the Hall-Petch relationship. In the present work the κ_y value for the β martensite is not known. However, Speidel and Warlimont (1968)[119] have used κ_y values obtained for α solid solutions in copper-based alloys to estimate the possible contribution of the martensite plate thickness to the yield stress. Similarly the κ_y value for untransformed β phase has been used in this case. The κ_y value has been calculated from the data for 48·9 at % Ni binary β phase at room temperature, given by Pascoe (1966)[57]. It was found that the contribution of martensite plate thickness to the overall strength of β martensite in Alloy 1 is about 20%, compared to the overall strength of β martensite. However, this estimate is highly speculative, because the data used for calculating the κ_y value were taken from β phase with a considerable difference of composition, and assuming that the κ_y value for untransformed β phase holds also for the martensitic β phase.

In the microhardness measurements made on the 60 at % Ni binary NiAl phase by Litvinov et al (1971)[27] the microhardness of β martensite has increased about 10% compared to the untransformed β phase, which must account for both the contributions of the martensite plates and the substructure or internal twinning and faults. It was

also found[57] in the untransformed β phase that the grain size had little influence on the room temperature flow stress.

Therefore it appears that the martensite plates play no major role in the strength of β martensite.

5.4.5.3. Strengthening by Substructure

There has been controversy over the effect of substructure on the strength of martensite. In twinned martensites, the twin boundaries are barriers against the dislocation movement during the plastic deformation of martensite. Richman (1963)[122] has made a statistical study of internal twins in steels. He has correlated the twin thickness and spacing between the twins as a function of carbon content. In that study, since neither of these twin dimensions is sensitive to the carbon content, these twin structures per se cannot account for the strengthening of martensite due to carbon. Winchell and Cohen (1962)[123,124], and Speich and Swann (1965)[125] have suggested that internal twins or substructure play only a minor role in the strength of Fe-Ni-C and Fe-Ni alloys. However, Kelly and Nutting (1960, 1961, 1965)[126,111, 115] have concluded that the transformation substructure, espeically the fine internal twinning in ferrous martensites may play a major role in determining the overall strength.

There has not been systematic work on the effect of structure ot the strength of β NiAl martensite. However, by using the microhardness data from a 60 at % Ni binary alloy Litvinov et al (1971)[27] have found an increase of 10% in the hardness of β martensite as compared to the untransformed β phase. They have attributed this increase to the presence of defects in martensite such as twins. If the effect of grain size or size of martensite plates is taken into account then it is possible that the contribution of substructure will decrease under 10%, which suggests that it plays only a minor role. In the present work, unfortunately it was not possible to separate the contribu-

tion of substructure to the overall strength of β martensite.

In the light of the above discussion, it may be suggested that the substructure of β martensite plays only a minor role in determining the strength of β martensite.

5.5. Coarse γ′ precipitate in β phase

Ageing treatment of the tantalum-containing alloys at 1000°C for 3 days has produced equilibrium, coarse γ′ precipitate particles in β phase. This observation suggests that the nickel content of the β phase in equilibrium with γ′ decreases with decreasing temperature in the Ni-Al-Ta system as in the Ni-Al system (fig. 2.1). The coarse γ′ precipitate particles in β phase have also been observed [47,25,21] in binary NiAl and Ni-Al-Cr alloys. In an investigation of a ternary Ni-30·3 at % Al-6·6 at % Cr alloy, Moskovic (1974)[25] has observed that the ageing treatment at 850°C for 10 minutes produced a precipitate in β phase, which has a face-centred tetragonal structure with c/a = 0·976. However, longer ageing at 850°C for 2 hours produced equilibrium Ni_3Al precipitates, i.e. the tetragonality diminished with increasing ageing time.

The contribution of the γ′ precipitate particles to the observed 0·2% flow stress has been estimated, using the Orowan equation[127]. The Orowan equation may be written

$$\tau = \frac{Gb}{d}$$

where τ is the shear stress component produced by precipitates, G is the shear modulus of the matrix, b the Burgers vector of the glide dislocations and d the average interparticle spacing in the active slip plane. As the matrix is the β phase with B2 crystal structure, the Burgers vector has been taken as $b = a\langle 001\rangle$[49,128].

$G = 11{\cdot}17 \times 10^4$ MN/m^2 for binary β phase (ref. 100)
a = 2,855Å
b = 2,855Å
d = 20000Å in Alloy 1

Hence $\tau \cong 15$ MN/m^2

The compression stress component, σ will be twice this value for polycrystalline material, i.e. 30 MN/m^2, which is if the alloy contained 100 vol. pct β phase. However the volume fraction of β phase in Alloy 1 is about 50 vol. pct, which is the highest in the alloys investigated; even for this alloy the contribution of the γ′ precipitate particles to the 0·2% flow stress of the alloy will be about 15 MN/m^2, which is not significant.

As shown in fig. 4.5 there is no change in the hardness of Alloy 3 during ageing for different times. Alloy 2 also shows similar behaviour (fig. 4.5). In addition to the precipitation hardening, which is the difference between the increase in hardness due to the presence of the γ′ precipitate in the β phase and the decrease in solid solution strengthening due to the removal of solute atoms from the β phase to the γ′ precipitate, the γ′ phase outside the β phase might also contribute to the strengthening of the alloys. As shown in Table 4.6 there is no appreciable change in the microhardness of the γ′ phase in the homogenised, and aged conditions in Alloy 2 and Alloy 3. This suggests that any change in hardness of these alloys during ageing for various times is contributed by the precipitation hardening. As the hardnesses of Alloy 2 and Alloy 3 at various times show the precipitation hardening is not significant in these alloys. In an investigation of the Ni-24 at % Al-6 at % Cr alloy, Moskovic (1974)[25] has also found a similar ageing response in the hardness versus time curve, at 950°C.

As will be discussed in sec. 5.7 the effects of coarse γ′ precipitate particles on the strength of the alloys will be considered in terms of the "mixture rule".

5.6. Dislocations in Al-rich γ' phase

Evidence has been observed of the coexistence of two types of dislocations in the Al-rich γ' phase, at "low temperatures", oriented close to <111> and <110> respectively. It is commonly known that the {111} type plane is the expected slip plane in fcc or ordered fcc ($L1_2$) structures. However, this plane cannot be a possible slip plane for the <111> type dislocations. The {110} and/or {112} type planes are the possible slip planes, assuming that the Burgers vector is the b = a<110> type. There were no slip traces or pile-ups to determine possible slip planes for these dislocations. However, in Alloy 5, deformed at 600°C, a little evidence of pile-ups of dislocations has been observed. Fig. 4.54 shows one of the pile-ups observed in Alloy 5 deformed at 600°C. As this figure shows, the ends of dislocations in the pile-up lie along the $[01\bar{1}]$, which is the trace of slip plane of these piled-up dislocations. This is consistent with the {110} type slip plane suggested above. The few other pile-ups observed at the same deformation temperature support this. However these observations are not sufficient to state that the {110} type plane is the slip plane for these dislocations. Existence of the dislocations aligned close to <111> is surprising since Young's modulus is a maximum compared to that of <110> and <100> in cubic structures[129]. These dislocations will be discussed in terms of elastic anisotropy theory in sec. 5.4.1.

It is probable that those dislocations aligned along <110>, glide on the {111} type plane, supposing they have the b = a<110> type Burgers vector.

The "invisibility criteria" method to determine the Burgers vectors of dislocations is based on the two-beam theory of image contrast developed by Howie and Whelan (1961, 1962)[130,131]. According to this, a perfect screw dislocation will show no contrast under two-beam conditions, in an elastically isotropic material, if the condition g.b = 0 is satisfied, where g is the diffracting vector

and b is the Burgers vector of the dislocation. Similarly, an edge dislocation will be invisible if g.b = 0, and if g.b U = 0, where U is a unit vector along the dislocation line. For mixed dislocations some contrast is expected under all two-beam conditions. However, this criterion for invisibility of dislocation images no longer hold for materials of large anisotropy (132,133). For this reason it is not possible to apply "invisibility criteria" to γ' phase which is a relatively anisotropic material (Anisotropy factor, A = 3,58, Table 5.5). Because of the insufficiency of the "invisibility criterion" method, Muir (1975)[21] has used a computer programme to determine the Burgers vector of the Al-rich binary γ' phase. He has found the b = a<110> type Burgers vector in γ' phase at low temperatures, for dislocations in the <111> direction, as well as in the <110> direction.

Although "the invisibility criterion" has been applied for some cases, the results of which are consistent with the b = a<110> type Burgers vector, these could be erroneous results, in view of the fact mentioned above. Invisibility or "near-invisibility" does occur with large diffracting vectors under two-beam conditions when $g.b \neq 0$, which leads to erroneous results (134). It was shown (135) that in Ni_3Al, when g.b = 2 and g.b = 4, images may be invisible under certain conditions. This also suggests the unreliability of the "invisibility criterion".

As the γ' phase investigated is Al-rich in composition as was that of Muir's (21), it is expected that γ' phase in the present work also has the b = a<110> type Burgers vector, which was also confirmed to be the same in Ni-rich γ' phase (45) by the "invisibility criterion method".

It appears from the present work on the ternary Al-rich $Ni_3(Al,Ta)$ and $Ni_3(Al,Hf)$ phase, and from the work done on the binary Al-rich γ' phase by Muir (1975)[21] that the main difference between the dislocation behaviour of γ' phase is that the fully Al-rich γ' phase has the <111>

oriented dislocations in addition to the <110> oriented dislocations found in the Ni-rich γ' phase, at low deformation temperatures.

5.6.1. Prediction of the Operative Slip Systems in γ' Phase using Anisotropic Elasticity Theory at "Low temperatures"

It is commonly supposed that the shortest lattice translation vector and the most widely spaced plane containing this vector comprise the slip system[136,137]; this may be rationalized in terms of the ideal shear strength of a perfect crystal[138]:

$$\tau = \frac{G}{2\pi} \cdot \frac{b}{d}$$

where G, b and d are the shear modulus, lattice translation vector and interplanar spacing of the particular slip system of interest. If elastic anisotropy is ignored, it is usually assumed that the easiest slip system will be that which has the smallest value of b/d. The shortest lattice translation vectors in $L1_2$ structure (ordered face-centred cubic) are 1/2<110> and <100>; 1/2<110> is shorter by a factor of $\sqrt{2}$ than <100>, and all of the criteria will predict that 1/2<110> will be observed Burgers vector. However in ordered $L1_2$ structures such as Ni_3Al, as the dislocation consists of two 1/2<110> dislocations the Burgers vector will be <110>. The expected slip planes would be {111}, {110} and {100}. The spacings of these planes are in the ratio 1:0·82:0·58, and since {111} has the largest interplanar spacing this would indicate that the observed slip system should be {111} <110>, in agreement with the usual experimental result.

However, the observation of the existence of dislocations along the <111> directions, in addition to the dislocations along the <110> directions, in the present work, leads us to a consideration of the stability of the observed dislocations in terms of anisotropic elasticity theory.

In interpreting the modes of deformation of a metal crystal in terms of the theory of dislocations it is usually assumed that the factors affecting the determination of operative slip systems[139,140] are:

a) The energy of the dislocations
b) The mobility of the dislocations

Therefore to predict the possible slip system in a crystal, the following treatments should be made,

i) Comparison of the elastic energies of possible dislocations,
ii) Comparison of the relative mobilities of the lower energy dislocation configurations.

The elastic energy per unit length of a dislocation in an anisotropic medium is given[87] by

$$E = \frac{Kb^2}{4\pi} \cdot \ln\left(\frac{R}{r_o}\right)$$

where K is the "energy factor" which depends on the elastic constants, C_{11}, C_{12} and C_{44} and of the directional cosines (α, β, γ) of the dislocation line with respect to the cube axis, and R and r_o are the outer and inner cut off radii. Values of K for various dislocation configurations may be calculated using formulae available in the literature [141,142a,142b].

Energy considerations alone are often not sufficient to determine the operative slip system. If one type of dislocation possesses a great deal less energy than the other possible types, it may be expected to be more common in the as-grown crystal. Also, early in the deformation process such low energy dislocations may be favoured for generation by sources. However, if these dislocations are not able to move out into the crystal, the back stress causes the sources to cease generation. The more mobile dislocations then dominate the slip process.

An estimation of the relative mobility S is provided by the following expression of the equation proposed by Eshelby (1949)[143].

$$S = 4\pi \frac{\delta}{b} \cdot \exp[-2\pi \frac{\delta}{b}]$$

where δ is the width of the dislocation core. The particular value of δ/b can be calculated from the equation[143].

$$\frac{\delta}{b} = \frac{1}{2} \cdot \frac{K}{G} \cdot \frac{d}{b}$$

for an anisotropic substance. Where G is the shear modulus in the slip direction on the slip plane and d is the spacing between the slip planes. Note that small values of the mobility parameter (S) correspond to dislocations which are easily moved. The dislocations with the lowest mobility parameters are expected to dominate the slip process.

The elastic constants used are those for a Ni-24·3 at % Al-0·9 at % Ta γ' phase determined by Curwick (1972)[11]:

$C_{11} = 21{\cdot}1 \times 10^{10}$ N/m^2
$C_{12} = 14{\cdot}2 \times 10^{10}$ N/m^2
$C_{44} = 12{,}4 \times 10^{10}$ N/m^2
$A = 3{,}58$

These values have been used for calculating the energies and mobilities of dislocations.

The energies and the mobilities of dislocations are given in Table 5.3 for various possible slip systems, i.e., {111}<110>, {110}<110> and {112}<110>. Examination of the energies and mobility parameters for γ' phase calculated in Table 5.3 shows those slip systems considered are equally likely to operate (within ± 8%) in the γ' phase.

Table 5.3. Showing energies and the mobility parameters of the dislocations of the γ' phase with the Ni-24·3 at % Al-0·9 at % Ta in various possible slip systems, i.e. {111}<110>, {110}<110>, {112}<110>.

b	Slip Plane	Direction	Screw Mixed Edge	d/b	$Kx10^{10}$ (N/m^2)	$Gx10^{10}$ (N/m^2)	E (Joule/m)	δ/b	S
$\bar{1}01$	111	$\bar{1}01$	Screw	$1/\sqrt{6}$	6·54	12·40	133	0·11	0·69
110	$1\bar{1}0$	111	mixed (35·26°)	1/2	6·13	9·42	125	0·14	0·73
$\bar{1}10$	112	$\bar{1}\bar{1}1$	Edge	$1/2\sqrt{3}$	6·54	9·42	133	0·19	0·67

Nabarro (1952)[144], and Foreman and Lomer (1955)[139] have suggested that in face-centred cubic (fcc) crystals the core effects and dissociation on a close-packed plane (octahedral plane) may be the more important factors in affecting the operative slip system. It was suggested[144] that when a dislocation becomes extended there is a decrease in elastic energy accompanied by an increase in mobility, so that dislocations would be expected to glide more easily on the {111} planes of a fcc crystal; but dislocations cannot extend and reduce their energy in the {011} plane[144]. It was suggested that an undissociated dislocation on the {111} plane would be unfavourable energetically compared to that of the {011} in fcc[139]. Although the dissociation of any kind has not been observed in the γ' phase in the present work some workers have claimed to observe it in the past. In γ' phase the extended dislocations of the a/3<121> and a/3<21$\bar{1}$> partials bounded by the stacking fault have been claimed[145,146] to be observed. Therefore the a<110> superdislocation may dissociate:

$$a\langle 110\rangle \longrightarrow \frac{a}{3}\langle 121\rangle + \frac{a}{3}\langle 21\bar{1}\rangle$$

This dissociation creates a stacking fault between two a/3<211> partials. To determine whether this dissociation is energetically possible, it has been the practice to assume that the energy of a dislocation is proportional to the square of its Burgers vector. As the γ' phase is considerably elastically anisotropic, this was considered in terms of anisotropy elasticity theory.

The energy and mobility of the dissociated dislocations have been recalculated. The energy of this extended dislocation is

$$E_\gamma = E_1 + E_2 + E_{12} + \gamma w$$

where E_1 and E_2 are the self-energies of the partials. E_{12} is the interaction energy between the partials, and γw the energy of the stacking fault ribbon having width w and energy γ per unit area.

where

$$E_{12} = \frac{Kb_1b_2}{2\pi} \cdot \ln\left(\frac{R}{w}\right)$$

where b_1 and b_2 are the Burgers vectors of the partials. The value of the width, w of the stacking fault was calculated from the expression $\gamma = Kb_1b_2/2\pi w$ using the value of the stacking fault energy (γ) estimated from the expression $\gamma = \sqrt{2}\ \kappa Tc/2a^2$. Where κ is the Boltzman's constant, Tc the melting point (1688°K) of the γ' phase and a the lattice parameter of the γ' phase; the resulting value can only be regarded as an estimate. From this calculation the energy and mobility parameter of dissociated dislocations have been found to be the E_γ = 152 Joule/m and S = 0·68 respectively. The energy of a dissociated dislocation is about 10% higher than that of an undissociated one. This suggests that the dissociation of dislocations on the {111} plane is not energetically favourable. But the mobilities in both cases are almost equal. If these calculations of energy and the mobility parameter are taken to be correct then it is suggested that the dissociation of the 1/3<211> type dislocations on the {111} plane in γ' phase in this composition of the γ' phase is not possible.

However, another type of dissociation of the dislocations on the {111} plane has also been suggested in γ' phase by Kear et al (1970)[147]. This dissociation has also been considered in terms of the energy and the mobility parameter. This dissociation is:

$$a\langle 110\rangle \longrightarrow \frac{a}{2}\langle 110\rangle + \frac{a}{2}\langle 110\rangle$$

separated by antiphase boundary (APB). The calculation has shown that the dislocations in this dissociated condition on the {111} plane have the energy E_γ = 115 Joule/m and the mobility parameter S = 0·70. According to this calculation this dissociation leads to 4% energy reduction compared to the undissociated one. However, there is no appreciable change in the mobility parameter

(within ± 2%). Whether this small decrease in energy would lead to the dissociation of the a/2<110> type dislocation is doubtful. In addition there is no increase at all in mobility of dislocations. In terms of the mobility parameter it seems this dissociation is not favourable.

Therefore reconsidering Table 5.3 the energies and the mobility parameters of the dislocations considered are equal within ± 6% and ± ≈ 8% respectively, by taking into account the uncertainties involved in calculations of the energy and the mobility parameter of dislocations. From these calculations it seems to appear that the dislocations considered, namely screw in the $\{111\}\langle 10\bar{1}\rangle$, mixed in the $\{110\}\langle 1\bar{1}0\rangle$ and edge in the $\{112\}\langle\bar{1}10\rangle$ slip systems, are equally likely to exist in the γ' phase.

It is interesting to consider the dislocations in γ' phase in terms of the elastic anisotropy factor, $A = 2C_{44}/(C_{11} - C_{12})$. The anisotropy factors of the γ' phase for various compositions have been calculated and are shown in Table 5.4. As this table shows the elastic anisotropy factor is significantly greater than unity. The shear modulus $1/2\ (C_{11} - C_{12})$ is therefore small, and since this is the modulus for the $\{110\}\langle 110\rangle$ system, it might be possible that the shear becomes easier in this system. Increasing the aluminium content from 22·6 at % to 25·2 at % in γ' phase increases the elastic anisotropy factor by ≈ 20% (Table 5.4). This suggests that the shearing in the {110} plane becomes easier with increase in aluminium content of γ' phase. This may be the reason why only the {111} <110> slip system[8] has been observed below the peak temperatures of nickel-rich γ' phase; it may be suggested that in the Al-rich side of γ' phase the resistance to shear in the $\{110\}\langle 110\rangle$ slip system is small enough to be propagated.

The existence of the <111> oriented dislocations in the binary Al-rich γ' phase has also been observed in the past[21]. Slip on the non-octahedral slip plane, i.e. $\{110\}\langle 110\rangle$ has also been observed recently in fcc

Table 5.4 Shows anisotropy (A) of γ' phase in different composition

Composition (at %)	C_{11} ($\times 10^{10}$ N/m^2)	C_{12} ($\times 10^{10}$ N/m^2)	C_{44} ($\times 10^{10}$ N/m^2)	A
Ni-22,6 Al (ref. 148)	16,88	8,86	12,12	3,02
Ni-23,7 Al (ref. 11)	22,4	14,8	12,3	3,25
Ni-24 Al (ref. 149)	19,80	12,66	11,79	3,30
Ni-24,3 Al-0,9 Ta (ref. 11)	21,1	14,2	12,4	3,58

crystals, namely in Al, Ag, Cu, Ni and Au[106,107]. It was suggested by Hazif and Poirier (1972)[150] that in fcc metals this unusual {110}<110> slip mode only appears after rather large deformations have taken place. In the present work the <111> oriented dislocations has been observed at deformations as low as 2%, which is contrary to Hazif and Poirier's suggestion. It was also suggested[151] that this slip occurs during shock-loading. The {112}<$\bar{1}$10> type slip system has also been suggested to operate in aluminium under creep conditions[168]. From the above discussion and the previous work on both fcc and γ' phase non-octahedral slip planes, {110} and/or {112}, appears to operate in γ' phase at "low temperatures". From Table 5.4 it seems that the occurrence of these non-octahedral slip system(s) is related with the composition change. The nickel-rich γ' phase has been investigated in detail by Staton-Bevan (1973)[45]. She did not observe such dislocations. This also supports the suggestion given above that the existence of dislocations on non-octahedral slip system(s) might be due to the Al-richness of γ' phase, although as Table 5.4 indicates there is a trend in favour of the {110} slip plane to occur from the nickel-rich side to the aluminium-rich side of the γ' phase. In order to show if there is such a trend in energy and mobility of dislocations, the energy and mobility of dislocations for {111}<110> screw and {110}<110> mixed have been calculated for different compositions of γ' phase.

As Table 5.5 shows there is not much difference in the energies of the {111}<110> and {110}<110> slip systems for different compositions of γ' phase. But despite that the difference of the energies in these two systems reduces from 13% to 6% from Ni-22·6 Al to the Ni-24·3 Al-0·9 Ta γ' phase. This trend may suggest also that these two slip systems becomes equally possible slip system energetically as the composition of γ' phase changes from Ni-rich side to the Al-rich side. In mobility parameters however there is no appreciable change (Table 5.5).

Table 5.5

Composition of γ' phase	E(energy) (Joule/m)		S(mobility)		A
	{111}<110> screw	{110}<110> mixed (35,26°)	{111}<110> screw	{110}<110> mixed (35,26°)	
Ni-22·6 Al	149	130	0,70	0,73	3,02
Ni-24 Al	138	125	0,70	0,72	3,30
Ni-24·3 Al-0·9 Ta	133	125	0·69	0·71	3,58

5.6.2. The Possible effect of the <111> oriented dislocations on the strength of γ' phase

Since plastic deformation occurs by the movement of dislocations the critical stress for the onset of plastic deformation is the stress required to move dislocations through other dislocations and obstacles in the material. There are different types of barriers which might provide resistance to motion. These barriers are elastic interaction with stress fields of individual dislocations; interaction with dislocations parallel to the moving dislocations and interaction with dislocations which intersect the slip plane, i.e. forest dislocations.

As plastic deformation proceeds slip occurs on other slip systems and the slip plane of the one system intersects slip planes of the other systems, thus increasing the number of forest dislocations. This mutual interference of dislocations gliding on intersecting slip planes increases the work hardening. It is not essential that there should be equal amounts of slip on two or more families of slip planes; what is important is that some dislocations on intersecting slip planes should be forced into activity.

Even when the orientation is suitable for double slip there is a tendency for the slip in localized regions to take place mainly on one family of planes. This chequered pattern of clustered slip bands is to be expected since, once a high density of dislocations in one slip family happens to build up in one region of the crystal, these dislocations will protect this region from penetration by dislocations in other families, so that even though the orientation is favourable for multiple slip there is a tendency for single slip to predominate in small regions. This may account for why the <111> and <110> oriented dislocations have not been observed together in the same small region.

Strengthening mechanisms of the $L1_2$ type superlattice have been investigated theoretically[166,153,152]. It was found[166] that the resistance due to reacting forest dislocations makes up a part of the flow stress:

$$\tau \cong 0{\cdot}35\ Gb\sqrt{\rho}$$

where τ = flow stress, G = shear modulus, b = Burgers vector, ρ = dislocation density. As <111> oriented dislocations have been observed, in addition to the <110> oriented dislocations, at low temperatures, undoubtedly the <111> oriented dislocations will contribute to the strength of the Al-rich γ' phase present in the alloys investigated. As discussed in sections 5.6 and 5.6.1. there are two possible types of slip planes for the <111> oriented dislocations, namely the {110} and/or {112} planes. The <111> oriented dislocations on the {110} and/or {112} possible slip planes will provide forest dislocations, additional to the <110> oriented dislocations on the {111} octahedral slip planes. Therefore according to the above formula, the <111> oriented dislocations will contribute to the strength of the Al-rich γ' phase.

Popov et al (1972)[153] have estimated the stresses needed to break through the different kinds of barriers in ordered alloys with the $L1_2$ superstructure. In addition to the other barriers they have proposed a barrier which is related to the present work:

$$\tau = \frac{\gamma_{\frac{a}{2}<110>\{110\}}}{b}$$

where τ is the stress needed to overcome the barriers on the {110} slip plane. $\gamma_{a/2<110>\{110\}}$ is the antiphase boundary energy on the {110} slip planes, b = Burgers vector. According to the above formula, they have calculated that a stress of τ = 110 MN/m^2 is needed to overcome these barriers for binary Ni_3Al phase.

With regard to any given active slip plane, there will be a certain number of dislocations that lie in this plane and are capable of producing slip along it. At the same time, there will be many other dislocations, lying on other slip planes mentioned above, that intersect it at various angles. Consequently, when a dislocation moves it must pass through those dislocations that intersect its slip plane. This requires work to make the intersections. These intersections could also produce jog segments on the dislocations. The formation of a jog in a dislocation increases the length of the dislocation and therefore its energy. This energy must be supplied by the external force that moves the dislocation. The creation of the jog has been considered by Gilman and Johnston (1962)[46], and Tetelman (1962)[72] (see sec. 4.10.3). The jog height determines the movement of the dislocation and the resulting dislocation multiplication. For the Gilman and Johnston process[46] fig. 4.36, summarizes the movement of screw dislocations as a function of jog height N-M. As shown in fig. 4.36(a), dislocations with small jog heights move non conservatively because of the edge character of the jog and thus produce point defects (vacancies or interstitials). Intermediate jog heights, fig. 4.36(b), result in the production of dipoles, while at large jog heights (over 300Å) the dislocations can act as single-ended sources, fig. 4.36(c). Dislocations with jogs normal to their slip planes require an additional force in order to move them because of the drag offered by their jogs that must be pulled along with the rest of the dislocation. Such jogs on the <111> oriented dislocations have been observed (fig. 4.52, fig. 4.40) and their possible effects on the work hardening of the γ' phase discussed in sec. 4.10.3.

From the above and previous discussions it appears that the higher strength observed in the Al-rich side of the γ' phase compared to the nickel-rich side (fig. 2.16) is due to the existence of the <111> oriented dislocations, becuase in the nickel-rich side of the γ' phase no such dislocations have been observed[45].

The unusual temperature dependence of the flow stress of γ' phase has already been considered[32,45,37,180]. It has been suggested[32] that this unusual behaviour is the consequence of a change in the mechanism that controls the flow stress as the temperature is increased: at low temperatures where slip is confined essentially to the {111} system, super dislocations of screw character cross slip onto {100} planes where they remain largely immobile; edge dislocations remain mobile since they do not interact with the screw dislocation debris, and thus the mean free path for edge dislocation motion at small strains is high. At higher temperatures, e.g., when the flow stress is increasing most rapidly, the key feature is the emergence of {100} slip. In almost all reports the positive temperature coefficient is attributed to the superlattice dislocations being blocked as a result of common slip planes; this is the Kear and Wilsdorf locking. As the energy of an antiphase boundary $\gamma_{(111)}$ is high in the octahedral plane. The dislocation therefore tries to lower the energy by transforming to the cubic plane, where $\gamma_{(100)} < \gamma_{(111)}$[31]. This produces a resistant, blocked configuration of screw segments of dislocation. The transition to the cube plane may be achieved by cross slip. Since this is a thermally activated process on screw dislocations, the probability of cross slip increases with the temperature. Thus, as the temperature rises, an ever-increasing number of screw segments of superlattice dislocation segments goes over to the cube planes. These dislocations become blocked. This is reflected by the increasing flow stress with increasing temperature.

5.7. Deformation of alloys containing two phases

There are different types and distributions of two phases which occur in practice. Unkel (1937)[154] has carried out the first systematic experiments on a number of two phase alloys. He has found that the softer phase will always plastically deform first and the relative rates of work hardening will determine the relative deformation of the phases. However, more detailed

investigation has been made later by Clarebrough (1950)[155], using mainly Ag-Mg alloys containing two phases. He has found that the relative deformation of two phases is influenced both by the total deformation of the alloy and by the volume fractions of the phases. When very little of the hard phase was present most of the deformation occurred in the soft phase. If the proportion of the hard phase was not greater than 30 per cent by volume the soft phase deforms more than the hard phase for deformations of up to 60 percent. When both phases were present in about equal proportions they deformed to the same extent. Fishmeister and Karlsson (1977)[156] have also investigated coarse two-phase materials which consists of hard and soft phases, by using steels and aluminium bronzes. The presence of a hard component was found to affect mainly the rate of strain hardening at small strains. They have shown that the deformation process can be described by an empirical "mixture rule" which distributes both stresses and strains in the ratio of the volume fractions of the phases.

In the mixture rule it is assumed that each phase in the alloy behaves independently from the other one and the strain is equal in each phase. Then the average stress σ can be given as

$$\sigma = f_1\sigma_1 + f_2\sigma_2$$

where f_1 and f_2 are the volume fractions of the two phases, and σ_1 and σ_2 the flow stresses of the two phases.

5.7.1. Correlation between strength and structure of alloys

5.7.1.1. Room temperature flow stress

The possible factors which might contribute to the overall strength of the alloys are:

a) the individual strength of each phase;
b) the volume fraction of each phase;

c) solid solution strengthening by tantalum and hafnium;
d) off-stoichiometric compositions of γ' and β phases;
e) precipitation hardening in the β phase;
f) the effect of the substructure of the β martensite.

The factors (c), (d), (e) and (f) have been discussed in previous sections. Only the factors (a) and (b) will be considered in this section.

As discussed in the result section, the tantalum-containing alloys consist of γ' and β phase. On the other hand, the hafnium-containing alloys, in the as-cast state, contain γ', β and Ni_3Hf (α) phases.

Since the phases in the alloys exist as coarse particles it is assumed that they obey the mixture rule.

The large differences of the room temperature flow stresses of Alloy 1 and Alloy 2, in their as-cast state, may be mainly due to the much higher strength associated with the higher volume fraction of β phase in Alloy 1 compared to Alloy 2, since γ' phase has a similar microhardness in the two alloys (Table 4.5 and 4.6). The strength of the single phase β increases away from either side of its stoichiometric composition (fig. 2.19). As the composition of β phase changes from 66.7 at % Ni to 62.3 at % Ni in Alloy 1', in the homogenised condition compared to the as-cast state, it can be expected that the β phase in the homogenised state softens. A decrease in hardness of $\approx$ 30% of the β phase in the homogenised state compared to its as-cast state confirms this (Table 4.6). It is suggested that the softening of Alloy 1 after homogenisation compared to the as-cast state is mainly due to the softening of β phase. After ageing treatment the increase of flow stress compared to that of homogenised state in Alloy1and Alloy 2 may be due to the increasing strength of γ' phase associated with increase in volume fraction of γ' (Table 4.6; Table 4.5, sec. 4.3).

If the coarse γ' precipitate particles in the β phase are taken into account then the volume fraction of the γ' phase in the aged Alloy 2 should be more than the value shown in Table 4.5 and accordingly the volume fraction of the β phase should be less. Then the relative volume fractions of the γ' and the β phases are similar in the aged Alloy 2 and the homogenised Alloy 3. The large difference in the room temperature flow stress of these alloys could be suggested to be mainly due to the fact that the γ' phase has relatively a much higher strength in Alloy 3 than that of the aged Alloy 2 (Table 4.6); because the γ' phase in Alloy 3 contains a higher tantalum content than that of the aged Alloy 2 (Table 4.2).

The room temperature strength of the eutectic constituent in Alloy 4 was estimated to find its contribution to the overall strength of Alloy 4. It was assumed that the γ' and eutectic regions behave independently of each other and hence the "mixture rule" has been applied:

$\sigma_{\gamma'}$ = 1200 MN/m^2 at room temperature (ref. 39)
$f_{\gamma'}$ = 76% (Table 4.5)
f_E = 24% (Table 4.5)
σ = 1575 MN/m^2 at room temperature (fig. 4.58)

$$\sigma = \sigma_{\gamma'} \times f_{\gamma'} + \sigma_E \times f_E$$
$$1575 = 1200 \times 0{\cdot}76 + 0{\cdot}24 \times \sigma_E$$
$$\sigma_E = 2762 \ MN/m^2$$

The estimated strength (σ_E) of the eutectic is surprisingly high. This suggests that the strength of the single Ni_3Hf (α), which is one of the phase in the eutectic, should be very high (>2762 MN/m^2) which is doubtful. If this is the true strength of the eutectic regions, then about 50% of the room temperature flow stress of Alloy 4 is contributed by the eutectic regions.

However, the flow stresses of eutectic alloys are commonly displayed as Hall-Petch plots, the microstructural variable being the interlamellar spacing. The results by Shaw (1967)[197] on the Cd-Zn eutectic and by Cline and Stein (1969)[198] on the Ag-Cu eutectic have shown that the strengths of these lamellar systems are describable in terms of a Hall[116] - Petch[117] equation, i.e.

$$\sigma = \sigma_o + K_y \lambda^{-\frac{1}{2}}$$

By reducing the interlamellar spacing, λ, very high strengths have been produced in the intermetallic $Ni_3Al(\gamma')$ - $Ni_3Nb(\delta)$ lamellar eutectic system[199]; the strength of the Ni_3Al - Ni_3Nb lamellar eutectic has increased about 100% by reducing the intermetallic spacing (λ) from 4 microns to 1 micron. A similar increase of strength has been found for the Al-$CuAl_2$ eutectic alloy[200].

The lamellar spacing of the present eutectic is about 1-2 microns. If the $NiAl(\beta)$ - $Ni_3Hf(\alpha)$ eutectic in the present work behaves as the lamellar eutectic alloys mentioned above then it may be possible that about half of the flow stress ($\approx$ 1400 MN/m^2) of the eutectic derives from a Hall-Petch effect.

The higher room temperature flow stress of Alloy 4, compared to that of Alloy 5, in the as-cast state, could be attributed to the higher volume fraction of the eutectic constituent and the higher strength of γ' phase in Alloy 4, compared to those in Alloy 5, in the as-cast condition (Table 4.6; Table 4.5).

5.7.1.2. The Flow Stress as a function of temperature

The flow stresses of the alloys investigated show two types of behaviour at low deformation temperatures:

i) Insensitivity of flow stress with increasing temperature up to a certain temperature. For example Alloy 3 and Alloy 4

ii) Increasing flow stress with increasing temperature up to a certain temperature, similar to that observed for single γ' phase.

At high deformation temperatures in all the alloys investigated the flow stress decreases with increasing temperature.

If, as assumed in the previous section (sec. 5.7.1.1.) each phase behaves independently from other in the alloy during deformation. Then the "mixture rule" may be used to explain the temperature dependence of the flow stress behaviour of the alloys.

The temperature dependence of the flow stress of the single phase γ' and β phases are shown schematically in fig. 5.9. In the tantalum-containing alloys, which consist only of γ' and β phases, the flow stress will be determined by the relative volume fractions and the individual strengths of these phases.

In alloys showing the temperature insensitivity of the flow stress it is possible that a balancing between the softening of the β phase and an increase in strength of γ' phase with increasing temperature occurs. Similarly, the temperature independent flow stress behaviour has also been observed in nickel-based alloys which consist of γ' and β phases (sec. 2.18). Moskovic (1974)[25] has also explained the temperature dependence of the flow stress of a ternary Ni-Al-Cr alloy which consist of 50/50 volume fraction β/γ' phase, in terms of the "mixture rule".

In alloys showing increasing flow stress with increasing temperature, one may expect that the increase of the flow stress of γ' phase is higher than that of softening of β phase (fig. 5.9).

The peak temperature or the beginning of the fall in stress is different in each alloy. The possible factors determining the position of the peak temperature

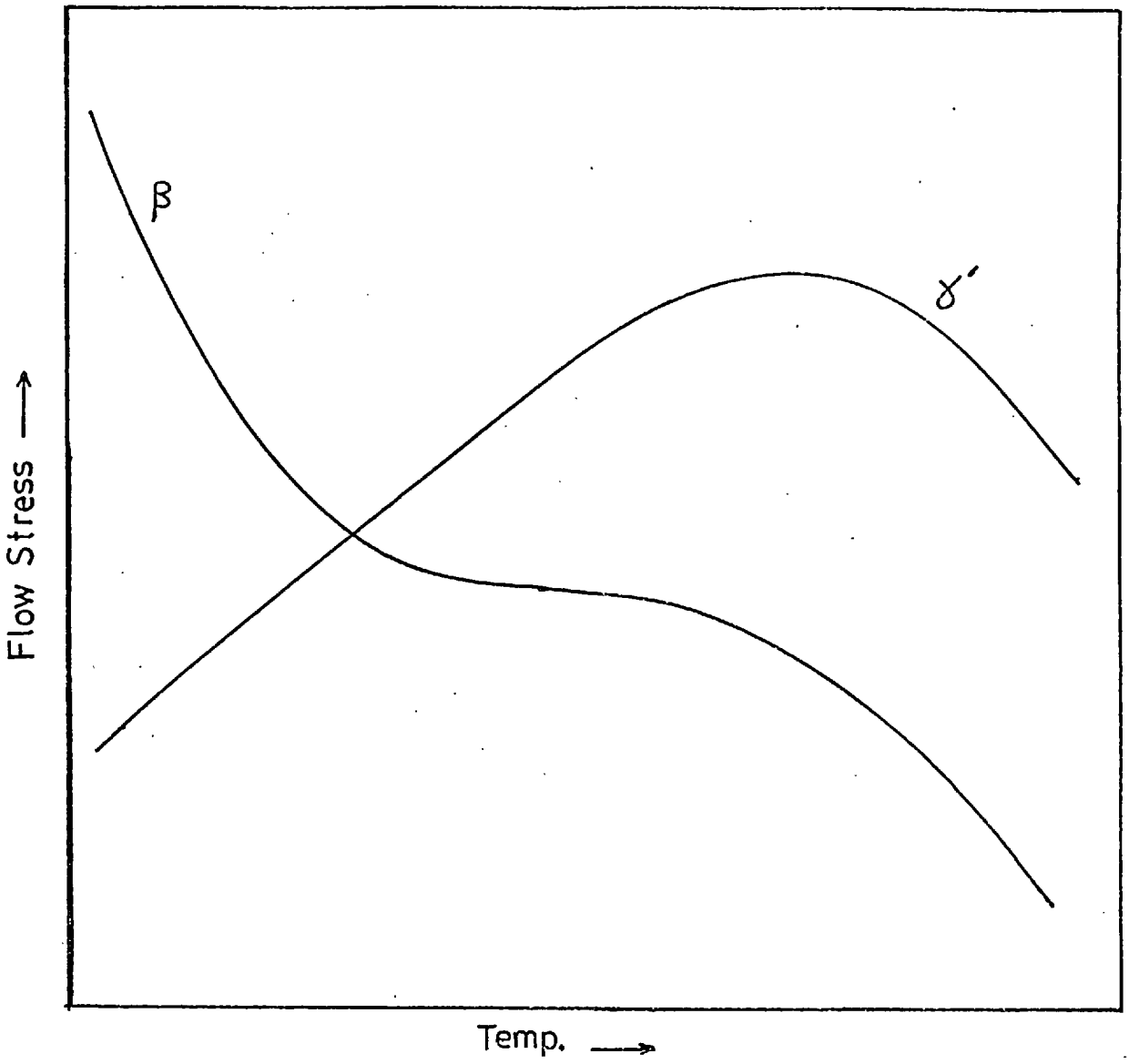

Fig. 5.9 Schematic representation of the flow stresses of γ' and β phases as a function of temperature.

or the temperature at which the flow stress starts to fall are:

i) the volume fraction and the flow stress of each phase;
ii) the "peak" temperature of single phase γ' in the alloy.

In alloys with the higher volume fraction and the stronger γ' phase, the γ' phase will dominate at higher temperatures and the position of the temperature at which the flow stress of the alloy starts to fall will come closer to the peak temperature of γ' phase in the alloy. Investigation of dislocations of γ' in Alloy 3 has shown that the dislocations were mainly straight and parallel to each other below 700°C, whereas above 700°C they have lost this characteristic; it was suggested that different deformation mechanisms operate below and above 700°C (sec. 4.10.1) is approximately where the flow stress of Alloy 3 starts to fall. It was suggested (sec. 4.10.1) that this temperature is the peak temperature of γ' phase in Alloy 3. The evidence indicates therefore that the onset of the fall of the flow stress of Alloy 3 coincides with that of single γ' phase in Alloy 3. Alloy 4 also shows similar behaviour. The coincidence of the temperature at which the flow stress of the alloy starts to fall with that of single γ' phase in the alloy is suggested to be due to:

i) the much higher proportion of γ' (80 vol. pct) compared to that of β phase (20 vol. pct) in Alloy 3,
ii) the higher strength of γ' phase compared to that of the β phase.

Although the strength of the β phase is not known (sec. 4.4) to compare it with that of the γ' phase, in Alloy 3 it was evaluated in the following way. The electron microscope and x-ray results have shown (fig. 4.21(d), sec. 4.2) that the β phase in Alloy 3 did not undergo martensitic transformation after homogenisation treatment. This suggests that the β phase in this alloy contains less than 60 at % Ni, since it is known from previous work[26] that the β phase with less than 60 at % Ni

content does not undergo martensitic transformation. As the β phase with ≈ 60 at % Ni content in the homogenised state of Alloy 2 has a hardness value of 501 (Table 4.6) the β phase in the homogenised state of Alloy 3 should have a hardness value less than 501; since the room temperature microhardness of γ′ in Alloy 3 is ≈ 580 (Table 4.6) the difference in microhardness between the γ′ and β phases in the homogenised state of Alloy 3 is more than 15%. This difference will increase even much further up in favour of the γ′ phase at higher temperatures, up to the peak temperature of the single phase γ′ in Alloy 3. Therefore the higher strength with the much higher volume fraction of γ′ compared to the β phase in Alloy 3 will dominate at higher temperatures of the 0·2% flow stress versus temperature curve (fig. 4.57).

From the characteristic features of the dislocations in Alloy 1 (sec. 4.10.1) it was suggested that the peak temperature of γ′ phase in Alloy 1 is ≈ 600°C; at about this temperature the flow stress of aged Alloy 1 starts to fall at a faster rate. From this similarity it is suggested that the steep fall of the flow stress of Alloy 1 in the aged state above 600°C is due to the onset of the softening of γ′ phase. However, the peak temperature for the as-cast state of Alloy 1 is about 300°C which does not coincide with the peak temperature (≈600°C) of γ′ phase. Considering the higher strength and the higher volume fraction of β phase (Table 4.6; Table 4.5), in the as-cast state of Alloy 1, it is likely that the β phase has lowered the peak temperature of the alloy, compared to that of single phase γ′ ; according to the "mixture rule", above 300°C in the as-cast condition of Alloy 1, probably the fall in the strength of β phase is more than the increase in the strength of γ′ phase, according to their volume fractions in the alloy, assuming the peak temperature of γ′ phase is about 600°C, as suggested earlier. The decrease in strength of β phase (that is due to the decrease in nickel content; Table 4.2) and the decrease in volume fraction of β phase, after homogenisation of Alloy 1 (Table 4.5), has decreased

the contribution to the overall strength of the alloy and so increased that of γ' phase; therefore it is suggested that the shift of the peak temperature of the alloy closer to the peak temperature of single γ' phase, after homogenisation treatment, is due to the increased contribution of γ' phase to the overall strength of the alloy. The acceleration of the fall of the flow stress above 600°C, compared to that between 300°C and 600°C, in the cast state of Alloy 1, also supports the conclusion that the peak temperature of γ' is ≈600°C; between 300°C and 600°C, the softening of the alloy due to β phase is slowed down by the increased flow stress of γ' phase.

In Alloy 5, with predominantly γ' phase, homogenisation treatment has increased the flow stress, compared to that of the as-cast state. This increase of the flow stress is attributable to the increase of hafnium content of γ' phase after homogenisation (Table 4.2). Alloy 5, in the as-cast and homogenised conditions, shows similar flow stress behaviour to that of a single phase γ' alloy as a function of temperature. This is expected since in the homogenised condition Alloy 5 predominantly consists of single phase γ', with a small amount (approximately 4%) of coarse Ni_3Hf particles, and in the as-cast state the alloy consists of predominantly γ' phase (92% by volume) and the eutectic-type structure (8% by volume).

In Alloy 1 it appears that at low temperatures the flow stress is increased by the increasing volume fraction and the strength of β phase (the increase in nickel content increases the strength of β phase at low temperature, see fig. 2.19); at high temperatures, although there are considerable differences of volume fraction and nickel content of β phase in the as-cast and homogenised states, the high temperature flow stresses in these two conditions do not show big differences, indicating that the β phase is not the major contributor to the overall high temperature strength of the alloy.

As mentioned in sec. 5.7.1.1, in the aged condition of Alloy 2 and homogenised condition of Alloy 3, where the γ' and β phases have closely similar volume fractions, the higher temperature dependence of the flow stress of Alloy 3, compared to that of Alloy 2, could be due to the higher strength of γ' phase in Alloy 3, compared to that of Alloy 2, assuming the flow stress of β phase in these two alloys has similar values.

Considering the compositions of β and the strength of γ' and β phases (Table 4.2, Table 4.6) the large drop of the flow stress of Alloy 1 after homogenisation compared to the as-cast condition, up to about 600°C could be due to the softening of the β and γ' phases.

The increase of the flow stress of Alloy 5, after homogenisation, compared to its as-cast condition (fig. 4.59) at room temperature, 600°C and 900°C could be due to the increase of hafnium content in γ' phase (Table 4.2), considering that the increase of hafnium content increases the flow stress of γ' phase between room temperature and 900°C (fig. 2.12).

To keep the flow stress of Alloy 4 constant up to about 700°C (fig. 4.58) the strength of the eutectic constituent should decrease with increasing temperature while the strength of γ' phase increases in temperature. Therefore it is expected that the eutectic constituent becomes weakened at 900°C. However the flow stresses of as-cast Alloy 4 and the homogenised Alloy 5 are the same ($\approx$ 800 MN/m^2) at about 900°C despite the fact that the γ' phase contains more hafnium in Alloy 4 than does γ' in the homogenised Alloy 5 (Table 4.2). This is explained by the fact that Alloy 4 contains a higher proportion of eutectic (β + Ni_3Hf) than Alloy 5, and the strengthening contribution of the eutectic at high temperatures is relatively small.

From the above discussion a number of points seem to become clear: High strength at low temperature

may be achieved by:

i) increasing the strength (that is the increase of nickel content) and the volume fraction of the β phase in the alloy,
ii) increasing the aluminium content of the γ′ phase,
iii) adding alloying elements, such as tantalum and Hf, to the γ′ phase.

High strength at high temperature may be achieved by:

i) adding alloying elements to γ′ phase, i.e. tantalum and hafnium,
ii) increasing the volume fraction of γ′ phase,
iii) optimizing the Al-richness of γ′ phase with respect to the Ni_3Al (fig. 2.16, sec. 2.12).

5.7.2. The Effects of Tantalum and Hafnium on the Strength of Alloys

In the tantalum-containing alloys (Alloys 1, 2 and 3) the tantalum is mostly in solid solution in the γ′ phase, and the β phase contains very little tantalum (⩽1 at %). Therefore, the main effect of tantalum on the strength of the alloys will be by solid solution hardening of γ′ phase. Increase of tantalum content will increase the flow stress of the γ′ phase (fig. 2.13), so the flow stress of alloys will increase according to the volume fraction of γ′ phase, assuming the "mixture rule" is obeyed (see sec. 5.5).

The homogenised condition of Alloy 3 and the aged condition of Alloy 2 have similar volume fractions of γ′ and β phases (sec. 4.3), if the γ′ precipitate particles in the β phase of the aged Alloy 2 are also taken into account. The large differences in their flow stresses between room temperature and 900°C (figs. 4.56 and 4.57) are mainly due to the difference in the tantalum contents of the γ′ phases in Alloy 2 and Alloy 3 (Table 4.2),

assuming that there is no large difference in the strength of the β phases in these alloys. Considering the highest flow stress (550-700 MN/m^2) of Alloy 3 at about 900°C in the tantalum-containing alloys it appears that the tantalum (≈7-8 at %) in the γ′ phase (Table 4.2) has increased the flow stress of the alloy considerably at 900°C.

In the hafnium-containing alloys the hafnium in solid solution has also considerably increased the strength of the γ′ phase and hence the flow stress of the alloy in which it exists, according to the volume fraction of γ′. Although the hafnium content of β phase in the as-cast state of Alloy 4 and Alloy 5 is not known it is suggested that the β phase does not contain high hafnium (sec. 4.2). These alloys also contain an intermetallic compound which is interpreted as binary Ni_3Hf (sec. 5.3.3). From the previous discussions this phase may contribute significantly to the flow stress of the as-cast states of Alloy 4 and Alloy 5 at low temperatures. However, as argued in sec. 5.7.1.1, this phase should also soften as does the β phase at higher temperatures. Therefore, the contribution will decrease with increasing temperature, although there is a lack of the information on the temperature dependence of the flow stress of this compound. From the above discussions it seems that the hafnium mainly affects the strength of the hafnium-containing alloys through the γ′ phase and Ni_3Hf phase, according to their volume fraction; assuming the "mixture rule" is obeyed.

5.8. Deformation mechanisms

It is now generally recognised that the plastic deformation of metals is dynamic, i.e. it is time, temperature and strain-rate dependent. The basic problem of understanding plastic deformation is the determination of the nature of the dislocation motion produced by an external stress. From an investigation of the activation parameters of plastic deformation a more comprehensive understanding can be obtained of the barriers which prevent

the motion of dislocations, and the means by which dislocations overcome these barriers. The activation parameters (activation volume and activation energy) depend on the nature of the barrier. These two quantities may be used to identify rate-controlling mechanisms from experimental observations if appropriate techniques are employed (157).

A dislocation may encounter two types of obstacles, in addition to the inherent resistance of the crystal lattice to the motion of the crystal lattice to the motion of a dislocation; i.e. the Peierls-Nabarro Stress (60, 62, 157):

1) Those that possess long-range stress fields, i.e. of the order of 10 atomic diameters or greater. These are called athermal obstacles.
2) Those that possess short-range stress field, i.e. of less than about 10 atomic diameters. The Peierls-Nabarro Stress may also be considered as this type of obstacles. These are called thermal obstacles.

The energy required to overcome the athermal type of obstacle may be so large that thermal fluctuations cannot assist the applied stress in the temperature range under consideration. Thermal activation thus plays no role in overcoming these long-range obstacles. The possible athermal obstacles are the forces due to dislocations on parallel slip planes, large precipitate or second-phase particles and grain boundaries.

Thermal fluctuations can assist the applied stress in overcoming short-range obstacles, i.e. thermal obstacles. It is these thermal obstacles that are responsible for the dynamic aspects of plastic deformation. These obstacles are forest dislocations, the motion of jogs in screw dislocations, cross-slip of screw dislocations, and climb of edge dislocations. The Peierls-Nabarro stress, forest dislocations, and jogs represent resistance to the motion of dislocations in the slip plane, while cross-slip

and climb represent resistance to motion out of the slip plane.

In principle, the rate-controlling deformation mechanism may be identified by comparing the magnitude of the experimentally determined activation volume (V^*) and activation energy (H), and their variation with thermal stress, with theoretical values predicted by specific hardening models, which are given elsewhere (60, 62, 157).

The comparison of the flow stresses of the alloys with the corresponding athermal stresses, suggests that the flow stress behaviour of these alloys results from the behaviour of the athermal stress as a function of test temperature. In other words, in these alloys the athermal stresses show similar behaviour to that of corresponding flow stresses.

Alloy 3 and Alloy 4, in the low temperature range (below 700°C) in which the flow stresses were insensitive to temperature change, have shown a very small strain-rate sensitivity and thermal stress. It may be possible that the athermal stress, in Alloy 3 and Alloy 4, below 700°C, is determined by a long-range interaction between dislocations and the second phase particles, i.e. β particles in Alloy 3, and eutectic particles in Alloy 4. In Alloy 3 and Alloy 4 the strain-rate sensitivity, above 700°C, and thermal stress above 600°C, rose rapidly with increasing temperature, suggesting that the deformation is strongly thermally activated in this temperature range. In this temperature it is possible that more than one process is rate-controlling. Li (1965)[158] has shown that if more than one process occurs the measured activation volume and energy will be a mean value weighed in the ratios of the number and type of dislocations involved in each process. A consideration of the effective values of activation parameters can therefore give an indication of which processes do not influence a significant number of mobile dislocations. The activation volume is about

$10b^3$ - $50b^3$ above 700°C, which decreases with increasing temperature. Mechanisms that are likely to be rate-controlling in this temperature range, on the basis of activation volume and the present study of the dislocation structure of γ' phase:

i) Cross-slip
ii) Climb

In sec. 4.10.1 the evidence has been reported about the difference in dislocation structures in γ' phase below and above 700°C in Alloy 3 and Alloy 4. It was suggested that this difference is due to the change of slip system from the octahedral to the cube system; assuming that 700°C is about the peak temperature of γ' phase, then it is expected that cross-slip occurs at around 700°C[45]. Evidence of cross-slip of dislocations has been found for deformation at 700°C (sec. 4.10.3). But at higher temperatures, the possibility of climb processes also becomes important, and evidence was found of climb in γ' phase at 900°C (fig. 4.48). The activation volume ($10b^3$ - $50b^3$) in this temperature range is higher than expected on the basis of dislocation climb, which requires that V^* be $\approx 1b^3$. However, above 750°C recovery takes place which makes the accurate measurement of activation volume impossible.

In all the alloys investigated only Alloy 5, in the homogenised condition, is almost single phase γ' with only about 4 vol. pct of coarse Ni_3Hf particles. It may therefore be expected that in this alloy the deformation mechanisms are the same as that of the single phase γ'. The activation volume has been determined to be between $40b^3$ and $85b^3$ below 600°C and increases with increasing temperature. The likely rate-controlling mechanism is the movement of jogged screw dislocations. Evidence of jogs on the screw and mixed type dislocations has been found in the low temperature range in the present work (sec. 4.10.3). Nicholls (1974)[64], in his activation analysis, has found that overcoming Peierls barriers,

cross-slip between octahedral and cube planes, and intersection of dislocation dipoles, in addition to the motion of jogged screw dislocations are the rate-controlling mechanisms in γ' phase below the peak temperature. Dislocation dipoles have been observed at various deformation temperatures at the "low temperatures" (sec. 4.10.2, fig. 4.49, fig. 4.50, fig. 4.51), which might suggest the operation of the intersection of dislocation dipoles as the rate-controlling mechanism. However, the observed activation volume ($40b^3$ - $85b^3$) does not agree with this mechanism, for which an activation volume of 10^3b^3 - 10^4b^3 is needed. Therefore on the basis of the activation volume it seems that the intersection of dislocation dipoles is not likely to be the rate-controlling mechanism. At higher temperatures near 600°C, cross-slip cannot be ruled out since close to the peak temperature (i.e. ≈600°C) the change from octahedral to cube slip transition occurs[45]. The temperature dependence of the homogenised Alloy 5 shows a peak at about ≈600°C (fig. 4.59). As discussed in sec. 4.10.1, the dislocations in Alloy 5 change their characteristics below and above 600°C which is close to the "peak" temperature of the alloy, this was suggested to be the indication of the occurrence of cross-slip. From this discussion it is therefore suggested that cross-slip occurs at around 600°C in the homogenised Alloy 5. Above 600°C the observed activation volume ($<70b^3$) decreases which suggests that cross-slip becomes less favourable above 600°C.

At higher temperatures (above 600°C), from evidence found in dislocations in the γ' phase in sec. 4.10.3, the climb of dislocations might become the dominating factor with increasing temperature.

As the flow stress of Alloy 5 in the as-cast state (which consists of γ' plus eutectic type regions), shows similar behaviour as a function of temperature, to that of the homogenised state of Alloy 5, therefore it is suggested that similar deformation mechanisms take place as in both states.

The as-cast and homogenised states of Alloy 1 and Alloy 2 show a comparatively small strain-rate sensitivity and thermal stress below 400°C, indicating that thermally activated processes are not prominent in this temperature range; however, above 400°C thermal stress and strain-rate sensitivity increase rapidly with increasing temperature, indicating that the deformation is strongly thermally activated, as in the case in Alloy 3 and Alloy 4 above 700°C, and Alloy 5 above 600°C. Because of the similarity between the flow stress, thermal stress and strain-rate sensitivity of these alloys and Alloy 5 it is suggested that a similar rate-controlling process(s) occurs, as mentioned above for Alloy 5 below 600°C. This suggestion assumes that the effective deformation mechanism is controlled by the γ' phase in these alloys. On the basis of this assumption the activation volumes of Alloy 1 and Alloy 2 have been determined by using strain-rate cycling data. Below 400°C the activation volume has been found to be between $10b^3$ - $45b^3$, and increases with temperature, which is similar to that found for homogenised Alloy 5 below 600°C; this is not contradictory with the rate-controlling process(s) in the homogenised Alloy 5 below 600°C. Above 400°C the activation volume is typically $<5b^3$ and decreases with temperature, which is not inconsistent with the climb process, taking into account also the evidence of dislocation climb (sec. 4.10.3), although the predicted activation volume is about $1b^3$ for climb. Although in γ' and β phases different deformation processes operate[64,65], and the β phase is strongly thermally activated compared to that of γ' phase at low temperatures; however, as pointed out by Schoeck (1961)[159], when more than one mechanism is operative the overall or effective rate will be controlled by the easier one for parallel (independent) processes.

CHAPTER 6

6. SUMMARY AND CONCLUSIONS

The following alloys have been studied in the present work: Alloy 1 (Ni - 28·75 at % Al - 2·5 at % Ta), Alloy 2 (Ni - 26·75 at % Al - 2·5 at % Ta), Alloy 3 (Ni - 20·0 at % Al - 7·5 at % Ta), Alloy 4 (Ni - 20·0 at % Al - 7·5 at % Hf) and Alloy 5 (Ni - 22·5 at % Al - 5·0 at % Hf).

The tantalum-containing alloys consist of (γ' + β) phases; the γ' phases are aluminium-rich with respect to stoichiometric Ni_3Al and contain significant amounts of tantalum. Whereas the β phases are nickel-rich with respect to stoichiometric NiAl and contain very little tantalum ($\approx \lesssim 1$ at %).

The hafnium-containing alloys (Alloy 4 and Alloy 5) consist of (γ' + β + an intermetallic compound, Ni_3Hf).

6.1. Lattice Parameter and Hardness

The correlation of lattice parameter and tantalum and hafnium contents in γ' phase has shown that hafnium expanded the lattice of γ' phase more than tantalum did. This difference of the expansion has been attributed to the atomic sizes of these alloying elements.

From the correlation of the microhardness with the tantalum and hafnium contents of γ' phases, it was found that hafnium was a more potent solid solution strengthener of γ' phase than tantalum. By applying Fleischer's work it was estimated that the shear modulus is the major contributor to the solid solution hardening of the ternary γ' phase, while the size misfit effect contributes to lesser extent.

6.2. The Eutectic-type structure in Alloy 4 and Alloy 5

The hafnium-containing alloys (Alloys 4 and 5) have shown a eutectic-type structure which consists of (β + an intermetallic compound, Ni_3Hf, designated α. This intermetallic compound (α) has a hexagonal structure, with a = 4,905Å, c = 6,042Å, c/a = 1·23. The following Burgers orientation relationship has been observed between the β phase and this intermetallic compound in the eutectic region

$$(1\bar{1}0)_\beta // (0001)_\alpha$$
$$[111]_\beta // [2\bar{1}\bar{1}1]_\alpha$$

The eutectic microstructure has shown mainly a lamellar type morphology. The lamellar structure contained "faulted regions".

The α intermetallic compound, Ni_3Hf, has shown fine, planar faults lying on the (0001) basal plane, which are interpreted as stacking faults.

6.3. The β Martensite

Solution treatment of the tantalum-containing alloys (Alloy 1 and Alloy 2) at 1260°C followed by water quenching, has produced the martensitic β phase with the body-centred tetragonal structure. In the as-cast condition of Alloy 1 and Alloy 2 the β phase has also undergone a martensitic type transofrmation; it was suggested that the rapid cooling is not a necessary condition for β phase to undergo martensitic transformations in these alloys. Several types of planar faults have been observed in the β martensite, i.e. {101}[101] twinning, {110} fault and {210} and {012} faults perhaps. Two variants of the {101} twinning faults have been observed in the neighbouring martensite plates. From these observations it was suggested that a multishear mechanism operates in the formation of β martensite.

Fine, disc-shaped precipitate particles on {110} planes have been observed to exist in the untransformed

and transformed β phase.

The nucleation of the β martensite has been considered in terms of elastic moduli. It was suggested that, the fact that the shear elastic coefficient $C' = (C_{11} - C_{12})/2$ decreases with decreasing temperature, (i.e. the resistance to a $(011)[01\bar{1}]$ shear decreases with decreasing temperature), favours the martensitic transformation being nucleated by $(011)[01\bar{1}]$ shears in the ordered bcc (B2) β phase.

It seems also likely, in addition to the softening of the resistance to a $(011)[01\bar{1}]$ shear, that the twinning on different variants and the formation of the parallel-sided martensite plates promotes the nucleation of the martensite.

The main morphological feature of the β martensite in the solution treated condition has been the presence of "self-accommodating" martensite plates have been observed to exist in a β grain. Each group consists of two alternating martensite plates. Correlation has been considered between the morphology and Ms temperature (or nickel content). It was suggested that the effect of increasing nickel content is to increase the tendency for the acicular-type morphology to occur.

Considering the likely factors affecting the strength of martensitic β phase, i.e. solid solution hardening, size of martensite plates, substructure and precipitates, it appears that solid solution hardening by nickel content in the β phase is the main strengthening factor; the effect of increasing nickel content is to increase the strength of β martensite.

6.4. Dislocations in the Al-rich γ′ phase

Investigation of dislocations in γ′ phase has shown the presence of dislocations close to the <111> direction, in addition to the dislocations along the <110> directions. The {111} plane cannot be the possible slip

plane for the <111> type dislocations. The {110} and/or {112} planes are the possible slip planes, assuming that the dislocations have the b = a<110> type Burgers vector. The {111}<110>, {110}<110> and {112}<110> possible slip systems have been considered in terms of elastic anisotropy. From the energies and the mobility parameters of dislocations in these systems it is likely that these dislocations are equally easy to move.

The likely effects of the <111> oriented dislocations on the strength of the γ' phase have been discussed and the higher strength of the Al-rich side of the γ' phase compared to that of the Ni-rich side has been attributed to the existence of these dislocations.

6.5. The Temperature Dependence of the Flow Stress

The temperature dependence of the flow stress of the alloys investigated has been qualitatively analysed in terms of the "mixture rule". Two main characteristics have been observed at "low temperature":

i) The insensitivity of the flow stress to temperature, i.e. in Alloy 3 and Alloy 4.

ii) The increasing of the flow stress with increasing temperature, similar to that found in single phase γ'.

At high temperatures the flow stresses of the alloys decreased with increasing temperature.

There is no decrease in flow stress on increasing the temperature from the room temperature up to about 700°C in Alloy 3 and Alloy 4; it was suggested that the softening of the β phase in Alloy 3 and of the eutectic in Alloy 4 is balanced by the hardening of the γ' phase.

Increasing the nickel content of the β phase (which increases low temperature strength) and the volume fraction of the β phase increased the low temperature

strength of the alloys. However, it seems that at high temperatures the β phase has decreased the strength of the alloy.

Increasing the tantalum and hafnium contents (which increases γ' strength) and the volume fraction of γ' phase increased the flow stress of alloys between room temperature and 900°C.

6.6. Relaxation tests and Strain-rate Cycling tests

From the similarity of the temperature dependence of the flow stress and athermal stress behaviour it is proposed that the temperature dependence of the flow stress results from the change of the athermal stress with temperature.

At high temperatures deformation in the alloys is strongly thermally activated, whereas at low temperatures the deformation is not strongly thermally activated. The likely rate-controlling mechanisms have been discussed.

Suggestions for further work

1. The present work has demonstrated the effect of hafnium on the strength of the alloys as a potential hardener through the solid solution hardening of γ' phase. However, further experimental investigation is needed to determine the effect of Hf on the strength of the alloys via solid solution in the β phase and Ni_3Hf.

   Although the crystal structure and lattice parameters of the intermetallic compound, α, (Ni_3Hf), have been determined, confirmation work is needed. The possible effect of the α phase as precipitate particles on the strength of the alloys should be investigated.

2. The higher strength of the γ' phase in the Al-rich side compared to the Ni-rich side has been attributed to the presence of the <111> oriented dislocations in the {110} and/or {112} possible slip planes in the Al-rich side of the γ' phase in the γ'/β phase region. The existence of the {110} and {112} possible slip planes should be confirmed.

3. Different fault systems have been observed to exist in the β phase martensite in the present work. It would be worth while to confirm especially the {210} and {012} fault system in any future work.

   Microprobe analysis has shown that in the γ'/β phases region the solid solution of tantalum in β phase is small. However, the potentiality of tantalum as a solid solution hardener in the single phase β region should be investigated; as tantalum is a good potent hardener in the γ' phase at every temperature tested, it might also be potent to improve the high temperature strength of the β phase.

ACKNOWLEDGEMENTS

I wish to thank my supervisors, Dr D.R.F. West and Dr R.D. Rawlings, for their stimulating discussions and continued encouragement throughout this study. I also wish to thank Dr. H.M. Flower for many discussions on some of the electron microscope results.

Finally, I am grateful to Professor J.G. Ball for the provision of research facilities in the Metallurgy and Materials Science Department and to the Ministry of Education of the Turkish Government for the financial support.

REFERENCES

1. GWYER, A.G.C., Z.Anorg.Chem., 1908, 57, p.113
2. BRADLEY, A.J. and TAYLOR, A., Proc.Roy.Soc. 159 (1937)
3. SCHRAM, J., 1941, Z.Metallk., 10, 347
4. HANSEN, M., Constitution of Binary Alloys, McGraw-Hill (1958)
5. GUARD, R.W. and TURKALO, A.M., 1960, in Mechanical Properties of Intermetallic Compounds (ed. Westbrook), Wiley, New York
6. BALL, A., Metal Sci. Journal, 1, 1967, 47
7. MOLLARD, F., et al, Z.Metall., 65, 1974, 461
8. KAUFMAN, L. and NESOR, H., Canadian Metall.Quart. 14, 1975, 221
9. MARKIV, V. Ya and BURNASHOVA, U.V., Izv,Acad.Nauk. SSR (Metally) 6, 1969, 181
10. AOKI, K and IZUMI, O., Phys.Stat.Sol.(a) 32, 657 (1975)
11. CURWICK, R., Ph.D. thesis, 1972, University of Minnesota, USA
12. GUARD, R.W. and WESTBROOK, J.H., Trans. of Met. Soc. of AIME, 215, 1959, 807
13. TAYLOR, A.and DOYLE, A.J., 1972, J.App.Cryst., 5, 201
14. STOECHINGER, G.R.S. and NEUMANN, J.P., J.App.Crys., 3, 32, (1970)
15. COOPER, M.J., (1963) Phil.Mag. 8, 805
16. WEST, G.W., 1964, Phil.Mag., 9, 979
17. WEST, G.W., 1973, Phys.Stat.Sol. (a), 20, 647
18. RAWLINGS, R.D. and STATON-BEVAN, A.E., J.Mat.Sci., 10, 505, (1975)
19. DAVIES, R.G. and STOLOFF, N.S., Trans.Met.Soc.AIME, 233, 714, (1965)
20. COPLEY, S.M. and KEAR, B.H., Trans.Met.Soc.AIME, 239, 977, (1967)
21. MUIR, G.P., Ph.D. thesis, University of Cambridge (1975)
22. ROSEN, S. and GOEBEL, J.A., Trans.Met.Soc.AIME, 242, 722, (1968)
23. ENAMI, K., NENNO, S. and SHIMIZU, K., Trans.Jap.Ins. Metals, 14, (1973) 161
24. CHANDRASEKARAN, M. and MUKHERJEE, K., Mat.Sci. and Eng., 13, (1974) 197

25. MOSKOVIC, R., 1974, Ph.D. thesis, University of Cambridge
26. SMIALEK, J.L. and HEHEMANN, R.F., Met. Transactions, 4, (1973) 1571
27. LITVINOV, V.S., ZELENIN, L.P. and SHKLYAR, R. Sh. Fiz.metal.metalloved, 31, No. 1, 138-142 (9171)
28. MOHANTY G.P. and WERT, J.J., Acta Met., 11. (1963) 217
29. MOHANTY G.P. and SCHMIDT, R.A., J. of App. Phys., 41 (1970) 3582
30. LITVINOV, V.S., ARKHANGEL'S KAYA A.A., and POLEVA, V.V., Fiz.metal.metalloved, 38, 383-388 (1974)
31. FLINN, A., Trans.Met.Soc.AIME., 218, (1960) 145
32. THORNTON, P.H., DAVIES, R.G. and JOHNSON, T.L., Met.Trans. 1, (1970) 207
33. WESTBROOK, J.H., J.Elec.Soc., 103, 54 (1956)
34. THORNTON, P.H., DAVIES, R.G. and JOHNSON, T.L., Met.Trans., 1, 207, (1970)
35. KEAR, B.H. and WILSDORF, H.G., Trans.Met.Soc.AIME, 224, 382 (1962)
36. STATON-BEVAN, A.E. and RAWLINGS, R.D., Phys.stat.sol. (a) 613, (1975)
37. SVETLOW, I.L. and TOLORAIYA, V.N., Fiz.metal.metalloved, 40, 409-414 (1975)
38. DOHERTY, J.E., KEAR, B.H. and GIAMEI, A.F., Journal of Metals, November (1971) 59
39. RAMASWAMY, V., HUMPREYS, F.J. and WEST, D.R.F., Private Communications unpublished report, Imperial College (1973)
40. AOKI, K. and IZUMI, O., J. of Japan Inst. Met. 39, 1975 (1282)
41. AOKI, K. and IZUMI, O., Phys.stat.sol. (a) 38, 587 (1976)
42. HIRSCH, P.B., Phil.Mag., 7, 67 (1962)
43. VIDOZ, A.E. and BROWN, L.N., Phil.Mag., 7, 1167 (1962)
44. KEAR, B.H., Acta Met. 14, 659 (1966)
45. STATON-BEVAN, A.E., Ph.D. thesis, Imperial College (London), 1973
46. GILMAN, J.J. and JOHNSTON, W.G., Sol.stat.Phys. (1962) 13, 147

47. RUSSELL, K.C. and EDINGTON, J.W., Metal.Sci. J., 6, 20 (1972)
48. TSIPAS, D., M.Sc thesis, Imperial College (1975)
49. BALL, A. and SMALLMAN, R.E., Acta Met. 14, 1517 (1966)
50. PASCOE, R.T. and NEWEY, C.W.A., Met.Sci. (1968), 2, 138
51. GRALA, E.M., 1960, in "Symp.Mech.Prop. of Intermetallic Compounds", (ed. Westbrook), Wiley, p. 353
52. SHAKLYAR, R. Sh., LITVINOV, V.S. and PANTSYEREVA, Ye.G., Fiz.Met.Metall., 32, No. 1, 181 (1971)
53. ARKHANGEL'S KAYA, A.A., BOGACHEV, I.N., LITVINOV, V.S. and PANTSYEREVA, Ye. G., Fiz.Metal.Metall., 34, 541-546, (1972)
54. KOECHLER, J.S. and SEITZ, F., J.Appl.Mech. A14, 219 (1947)
55. ARDLEY, G.W. and COTTRELL, A.H., Proc. Royal. Soc. A2 19, 328 (1953)
56. RACHINGER, W.A. and COTTRELL, A.H., Acta Met., 4, 109 (1956)
57. PASCOE, R.T., 1966, Ph.D. Thesis, University of London
58. PASCOE, R.T. and NEWEY, W.A., Phys.stat.sol. 29, 357 (1968)
59. BECKER, R., Physik Zeitz, 1925, 26, 919
60. CONRAD, H., Acta Met. 14, 1631-1633, 1966
61. EVANS, K.R., Trans. AIME, 242, 648-653, 1968
62. LITTLE, E.A., Journal of Sheffield University, Met. Soc., 13, 15-26, 1974
63. RANDALL, P., Ph.D. thesis, Imperial College (London) 1971
64. NICHOLLS, J.R., Ph.D. thesis, Imperial College (1974)
65. PASCOE, R.T. and NEWEY, C.W.A., Met.Sci.J., 1971, 5, 50
66. MASON, P.K., FROST, M.T. and REED, S.J.B., National Physical Lab./I.C. report Inorganic Metallic Structures, Ministry of Tech. (1969)
67. CHADWICK, G.A., Prog. Mater. Scie., 12, No. 2, 1963
68. REYNAUD, F., Scripta Met., 11, 765-770, 1977
69. BELL, W., ROSER, W.R. and THOMAS, G., Acta Met., 12, (1964) 1247
70. KEAR, B.H., Acta Met. 14, 659 (1966)

71. LI, J.C.M., Disc. Faraday Soc. No. 38 (1964) 138
72. TETELMAN, A.S., Acta Met., 10 (1962) 813
73. FELTHAM, P., Freiberger Forschungsh '8', 1965, 109, 29
74. FELTHAM, P., LEHMEN G. and MOISEL R., Acta Met. (1969), 17, 1305
75. KARG, A.V., FORNWALT, D.E. and KRIEGE, O.H., J. Inst. Metals 99 (1971) 301
76. KRIEGE, O.H. and BARIS, J.M., Trans. ASM 62 (1969) 195
77. FLEISCHER, R.L., Acta Met., 11 (1963) 203
78. KRAFT, R.W. and ALBRIGHT, D.L., Trans.Met.Soc.AIME, 221, 1961, 95
79. SUNDQUIST, B.E. and MONDOLFOR, L.F., Trans.Soc.AIME, 221 (1961) 607
80. KELLY and GROVES, Crystallography and Crystal Defects, Longman, 1970
81. KRAFT, R.W., Crystallography of Equilibrium Phase Interfaces in Al-$CuAl_2$ Eutectic Alloys, Trans.Met. Soc.AIME, 1962, 224, 65
82. COOKSEY, D.J.S., MUNSON, D., WILKONSON, M.P. and HELLAWELL, A., The Free Energy of Some Continuous Binary Eutectic Mixtures, Phil.Mag. 10, 745 (1964)
83. OKA, M. and WAYMAN, C.M., Trans TMS-AIME, 1968, 242, 337
84. SHIMIZU, K., OKA, M. and WAYMAN, C.M., Acta Met., 1971, 19, 1
85. CHRISTIAN, J.W., The Theory of Transformations in Metals and Alloys, Pergamon Press (1965)
86. ROSS, N.D.H. and CROCKER, A.G., Acta Met., 18, 1970, 405
87. SCHOEN, F.J. and OWEN, W.S., Scripta Met., 5, 315-318 (1971)
88. ACTON, A.F. and BEVIS, M., Mat.Sci.Eng., 1969, 5, 19
89. EASTERLING, K.E. and THOLÉN, Acta Met., 24, pp. 333-341, 1976
90. HIRSCH, P.B., HOWIE. A., NICHOLSON, R.B., PASCHELY, D.W. and WHELAN, M.J., Electron Microscopy of Thin Crystals, 1965, London, Butterworths
91. NABARRO, F.R.N., 1940, Proc.Phys.Soc., London, 52, 90

92. BOAS, W. and MACKENZIE, J.K., 1950, Prog. Met. Phys., 2, 90
93. TYPKIN, Yu.D. and GAVRILOVA, A.V., 1964, Soviet Physics-Cryst., 9, 166
94. ENAMI, K., HASUNUMA, J., NAGASAWA, A. and NENNO, S., Scripta Met., 10, 879-884 (1976)
95. ZENER, C., Phys.Rev. 71, 846 (1947)
96. Progg.Mat.Sci., 18, 1974, 55 Edit. by Chalmers, B., Christian, J.W. and Massalski, T.B.
97. MERCIER, O. and MELTON, K.N., Scripta Met., 1976, 10, pp. 1075-1080
98. WARLIMONT, H., "Microstructural, Crystal Structure, and Mechanical Properties of Martensite Phases in Copper Alloys", in "Physical Properties of Martensite and Bainite", Special Report 93
99. ROBERTSON, W.D., Martensite Transformation in terms of elastic Moduli, in "Physical Properties of Martensite and Bainite", Special Report 93, Iron and Steel Inst.
100. WASILEWSKI, R.J., Trans. AIME, 236, 1966, 455
101. AU, Y.K. and WAYMAN, C.M., Scripta Met., 6, pp. 1209-1214, 1974
102. WASILEWSKI, R.J., Met. Trans., 6A (1975) 1405
103. TAS, H., DELAEY, L. and DERUYTTERE, A., Met.Trans., 4, (1973) 2833
104. TAS, H., DELAEY, L. and DERUYTTERE, A., Scripta Met. 5, pp. 1117-1127, 1971
105. TAS, H., KRISHNAN, R.V. and DELAEY, L., Scripta Met., 7, pp. 183-188 (1973)
106. KAJIWARA, S., J. Phys. Soc. Japan, 30, (1971), 768
107. NISHIYAMA, S., KAKINOKI, J. and KAJIWARA, S., J.Phys. Soc. Japan, 20, (1965) 1192
108. KURDJUMOV, G.V., LOBODJIEK, W.A. and KHANDROS, L.G., Kristallographia USSR, 6, (1961) 210
109. SWANN, P.R. and WARLIMONT, H., Acta Met., 11, (1963) 511
110. KENON, N.F. and BOWLES, J.S., Acta Met. 17 (1969) 373
111. KELLY, P.M. and NUTTING, J., Jour. Iron and Steel Inst., March (1961) 199

112. MARDER, J.M. and MARDER, A.R., ASM Trans. 62, (1969) 1

113. PETTY, E.R., Martensite, Fundamentals and Technology, 1970, Longman

114. DAVIES, R.G. and MAGEE, C.L., Met. Trans., 2 (1971) 1939

115. KELLY, P.M. and NUTTING, J., Physical Properties of Martensite and Bainite I.S.I Special Report 93, p. 166 (1965)

116. HALL, E.O., The Deformation and Aging of Mild Steel: 111 Duscussion of Results, Proc.Phys.Soc. B64 (1951) 747

117. PETCH, N.J., The Cleavage Strength of Polycrystals, J.Iron Steel Inst., 174 (1953) 25

118. KOSTER, W. and SPEIDEL, M.O., Z.Metallk., 56 (1965) 585

119. SPEIDEAL, M.O. and WARLIMONT, H., Z.Metallk. 59, (1968) 841

120. KHAN, A.Q. and DELAEY, L., Z.Metallk., 60, 949 (1969)

121. KHAN, A.Q. and DELAEY, L., Scripta Met., 4, (1970) 981

122. RICHMAN, M., "Electron Microscopy of the Fine Structure in Fe-Ni-C Martensite", Ph.D. thesis, 1963, Department of Metallurgy, MIT

123. WINCHELL, P.G. and COHEN, M., Trans. ASM, 1962, 55, 374

124. WINCHELL, P.G. and COHEN M., "Electron Microscopy and Strength of Crystals", 995, (1962) Interscience

125. SPEICH, G.R. and SWANN, P.R., J.Iron Steel Inst., May 1965, 480

126. KELLY, P.M. and NUTTING, J., Proc.Roy.Soc. 1960, A259, 45

127. KELLY, A and NICHOLSON, R.B., Prog. in Mat.Sci. 10, (13), 149-391, 1963

128. PASCOE, R.T. and NEWEY, C.W.A., Phy.Stat.Sol., 29, (1968) 357

129. CHUNG, D.H. and BUESSEM, W.R., J.Appl.Phys., 38, Number 5, (1967) 2010

130. HOWIE, A. and WHELAN, M.J., Proc. Roy. Soc. 263A, (1961) 217

131. HOWIE, A. and WHELAN, M.J., Proc. Roy. Soc. 267A (1962) 206.
132. HEAD, A.K., LORETTO, M.H. and HUMBLE, P., Phys.stat. sol. 20, (1967) 505
133. HEAD, A.K., LORETTO, M.H. and HUMBLE, P., Phys. stat. sol. 20, (1967) 521
134. LORETTO, M.H. and FRANCE, L.K., Phys.stat.sol. 35, (1969) 167
135. OBLAK, J.M. and RAND, W.H., 1972, Proc. 30th Annual EMSA Meeting, p. 648
136. CHALMERS, B. and MARTIUS, U., Nature, April 28, 681 (1951)
137. CHALMERS, B. and MARTIUS, U., Proc. Roy. Soc. 1952, 213A, 175
138. FRANKEL, J., Z.Phys. 37, 572 (1962)
139. FOREMAN, J.E. and LOMER, W.M., Phil.Mag. 46, 73 (1955)
140. REID, C.N., Acta Met., 14, (1966) 13
141. FOREMAN, J.E., Acta Met., 3, 322 (1955)
142. HEAD, A.K., Phys.Stat.Sol. 6, 461 (1964a)
ibid 5, 51 (1946b)
143. ESHELBY, J.D., Phil.Mag., 40, 903 (1949)
144. NABARRO, F.R.N., 1952, Advances in Physics, 1, 35
145. KEAR, B.H., GIAMET, A.F., SILCOCK, J.M. and HAM, R.K., Scripta Met. 2, 285 (1968)
146. MIKKOLA, D.E. and COHEN, J.B., Acta Met., 14, 105 (1965)
147. KEAR, B.H., GIAMEI, A.F. and OBLAK, J.M., Scripta Met., 4, 567, 1970
148. DICKSON, R.W., WATCHMAN, J.B. and COPLEY, S.M., J.Appl.Phys., 40 (1969) 2276
149. ONO, K. and STERN, R., Trans.Met.AIME, 245 (1969) 171
150. HAZIF, R. Le. and POIRIER, J.P., Scripta Met., 6, 1972, 367
151. STEVENS, A.L. and POPE, L.E., Scripta Met., 5, (1971) 981
152. GRINGBERG, B.A., Fiz.Metal.Metallov., 15, No. 4, 486, 1963
153. POPOV, L. Ye., TERESHKO, I.V. and YEN'SHINA, N.A., Fiz.Metal.Metallov., 35, No. 1, 39, 1972
154. UNKEL, H., J.Inst.Metals, 61, 171 (1937)

155. CLAREBROUGH, L.M., Aust. J. of Scie. Research, 3, 1950, Series A, p. 72
156. FISCHMEISTER, H. and KARLSSON, Z.Metallkde., 68, 5 (1977) p.311
157. EVANS, A.G. and RAWLINGS, R.D., Phys.Stat.Sol., 34, (1969) 9
158. LI, J.C.M., Trans.Met.Soc. AIME, 233 (1965) 219
159. SCHOECK (1961) Mech. Behaviour of Materials at Elevated Temperatures, edit. Dorn., Wiley, p. 79
160. CORNWELL, L.R., PURDY, G.R. and EMBURY, J.D., Phys.Stat.Sol., 35, K1 (1969)
161. PAK, H.R., SABURI, T. and NENNO, S., Scripta Met., 10, (1976) 1081
162. LI, J.C.M., Can.J.Phys., 45, (1967) 493
163. RODRIGUEZ, P., J.Mat.Sci., 3, (1968) 98
164. GUIU, F. and PRATT, P.L., Phys.Stat.Sol. A6 (1964) 111
165. CULLITY, B.D., Elements of X-ray Diffraction, (Addison Wesley) (1967)
166. POPOV, L. Ye., YEN'SHINA, N.A. and KONEVA, N.A., Fiz. metal.metalloved., 40, No. 3, 465, 1975
167. NASH, PHILIP, Private communication (1978)
168. SERVI, I.S., NORTON, J.T. and GRANT, N.T., 1952, Trans. AIME, 194, 965
169. LAWLEY, A., Intermetallic Compounds, Ed. J.H. Westbrook, John Wiley and Sons, 1967, (p. 464)
170. SHUBERT, K., Kristallstrukturen Zweikomponent phases. Springer Verlag, Berlin, Gottingen, Heidelberg, 1964.
171. CROCKER, A.G., Acta Met., vol. 10, 1962 (113)
172. FLOWER, H.M., Private Communication (I.C.)
173. GEVERS, R., VANLANDUYT, J. and AMELINCKX, Phys. Status Solidi, 1966, vol. 18, p.343
174. FITZGERALD, G. and MANNAMI, M., Proc.Roy.Soc., 1966, vol. 293, p. 169
175. MOTT, N.F., and NABARRO, F.R.N., Proc. Phys. Soc., 52, 86 (1940)
176. MOTT, N.F. and NABARRO, F.R.N., "Report of the Conference on Strength of Solids", p.1, London, The Physical Society, 1948

177. COTTRELL, A.H., "Report of Conference on Strength of Solids", p. 30, London, The Physical Society, 1948
178. CRUSSARD, C., Metaux and COrrosion, 25, 203 (1950)
179. FLEISCHER, R.L., Acta Met., 9, 996 (1961)
180. POPOV, L. Ye., KONEVA, N.A., KOZLOV, E.V. and YEN'SHINA, N.A., Fiz. metal. metalloved, 38, No.1. 1974, 58
181. NABARRO, F.R.N., Proc. R. Soc. (A) 175, 519 (1940)
182. KRONER, E., Acta Met. 2, 302 (1954)
183. KHACHATURYAN, A.G. and HAIRAPETYAN, V.N., Phys. Status Solidi (B) 57, 801 (1973)
184. SCHWELLINGER, P., LEAMY, H.J. and WARLIMONT, H., Acta Met., Vol. 19, 1971, 421
185. ELLIOT, R., International Metals Review 1977, pp. 161-186
186. SUNDQUIST, B.F. and MONDOLFO, L.F., Trans. of AIME, 221, 1961, 157
187. MONDOLFO, L.F., J. Australian Inst. of Metals, 10, 2, 1965, 169
188. HOPKINS, R.H. and KRAFT, R.W., Trans. AIME, 1968, 242, 1627
189. CANTOR, B. and CHADWICK, G.A., J. Cryst. Growth, 1975, 30, 101
190. TILLER, W.A., Liquid Metals and Solidification, American Society for Metals, Cleveland, Ohio (1958)
191. BRADY, F.L., J. Inst. Met., 28, (1922) 369
192. PORTEVIN, A.M., ibid, 29, (1923) 239
193. SCHEIL, E., Z. Metallkunde, 45 (1954) 298
194. CROCKER, M.N. et al., J.Cryst. Growth, 30, 1975, 198
195. CHADWICK, G.A., Progr. Mat. Sci., 12, 1963, 97
196. SUNDQUIST, B.E., BRUSCATO, R. and MONDOLFO, L.F., J.Inst. Metals, 91, 1962, 204
197. SHAW, B.J., Acta Met. 15, 1169 (1967)
198. CLINE, H.E. and STEIN, D.F., Trans. TMS-AIME 245, 845 (1969)
199. THOMPSON, E.R., GEORGE, F.D. and BREINAN, E.M., Conference on "In-Situ" Composites, II, Publ. NMAB-308-II, P.71, Nat.Acad.Sci.-Nat. Acad.Engg., Washington, DC (1973)

200. DAVIES, I.G. and HELLAWELL, A., Phil. Mag., 19, 1285, (1969)

201. MARCINKOWSKI, M.J., BROWN, N. and FISHER, R.M., 1961, Acta Met., 9, 129

202. WOODFORD, D.A. and GLOVER, S.G., J.I.S.I. 201 (1963) 873

APPENDIX 1

The applied shear flow stress, , may be considered to consist of two components:

$$= \tau_\mu + \tau^* \qquad (1)$$

τ_μ is called the "athermal", "internal", "long range" or "back" stress. τ^* is the "thermal" or "effective" component of the flow stress and is determined by both temperature and strain-rate.

In general, short range forces from different obstacles are not additive; the strongest short range obstacles determine τ^* and are termed "rate controlling".

If a single thermally activated mechanism controls the deformation of a metal then:

$$\dot{\epsilon} = \dot{\epsilon}_o \exp\left(-\frac{\Delta G}{KT}\right) \qquad (2)$$

where $\dot{\epsilon}$ is the strain rate. KT has its usual meaning. ΔG is the activation energy for deformation. $\dot{\epsilon}_o$ is a constant effectively equal to the product of the frequency of thermal fluctuations large enough to produce slip multiplied by the strain produced by a single fluctuation.

It has been shown[157] that if the equation (2) is obeyed then

$$V^* = KT \left(\frac{\ln \dot{\epsilon}/\dot{\epsilon}_o}{\Delta \tau}\right)_T \qquad (3)$$

where the activation volume, V^*, is equal to the Burgers vector of the mobile dislocations multiplied by the length of the mobile dislocation multiplied by the distance over which thermal activation occurs. Equation (3) is only valid if dislocations of one type only are moving and $\Delta\tau$ is independent of strain.

APPENDIX 2

X-ray diffractometer analysis of the intermetallic compound in Alloy 4 (as-cast).

CuKα radiation.

The observed "d" values.

d (Å)	hkl	a (Å)	c (Å)
4,171	100	4,8165	-
3,027	002	-	6,054
2,027	201	4,9606	6,131
1,8275	103 ($\bar{1}$13)	4,912	6,071
1,6287	$\bar{1}$30 (3$\bar{2}$0)	4,9757	-
1,512	004	-	6,0488
1,4387	1$\bar{1}$4 (104)	4,9435	6,110
1,425	300	4,936	-
1,285	114	4,890	6,044